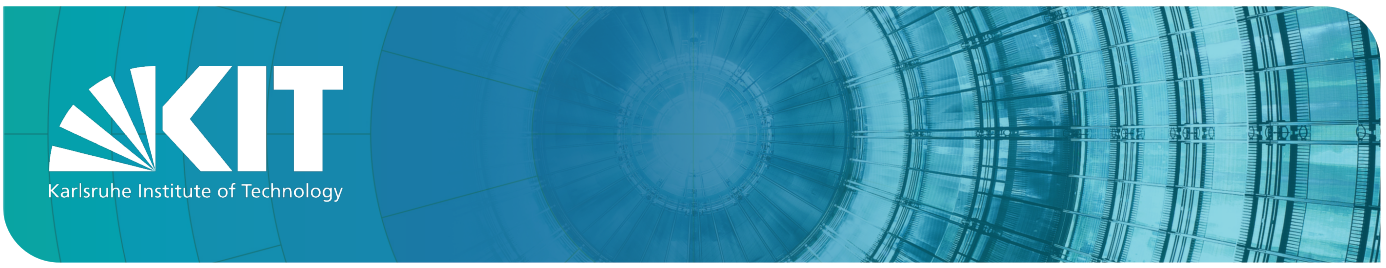

Combined neutrino-mass analysis of the first five KATRIN science runs

Zur Erlangung des akademischen Grades eines
Doktors der Naturwissenschaften (Dr. rer. nat.)
von der KIT-Fakultät für Physik
des Karlsruher Instituts für Technologie (KIT)
angenommene **Dissertation** von

M. Sc. Leonard Werner Köllenberger

aus Freiburg im Breisgau

Referent:	Prof. Dr. Kathrin Valerius
	Institut für Experimentelle Teilchenphysik, KIT
Korreferent:	Prof. Dr. Christian Weinheimer
	Institut für Kernphysik, WWU Münster

Tag der mündlichen Prüfung: 16.06.2023

Declaration of authorship Herewith I affirm that I wrote the current thesis on my own and without the usage of any other sources or tools than the cited ones and that this thesis has not been handed neither in this nor in equal form at any other official commission.

Erklärung der Selbstständigkeit Hiermit versichere ich, die vorliegende Arbeit selbstständig angefertigt zu haben und keine Hilfsmittel jenseits der kenntlich gemachten verwendet zu haben. Weiterhin habe ich weder diese noch eine äquivalente Version dieser Arbeit bei einer anderen Prüfungskommission vorgelegt.

Karlsruhe, May 14, 2023

Leonard Werner Köllenberger

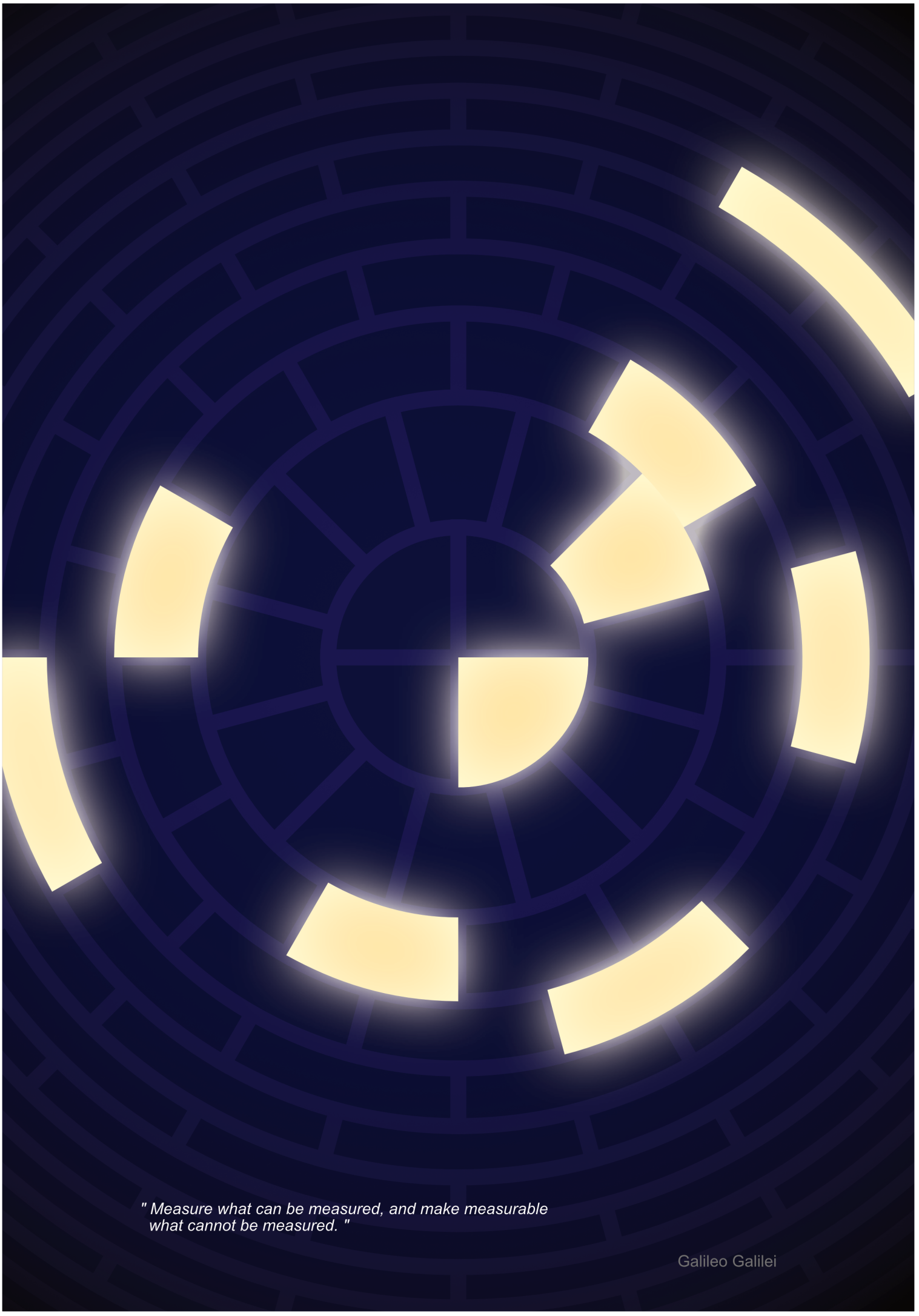
" Measure what can be measured, and make measurable
what cannot be measured. "
Galileo Galilei

Note on analysis changes after submission of the thesis

The results presented in the dissertation at hand were obtained in the unblinding procedure conducted by the KATRIN collaboration on the KATRIN science runs 1-5 in March 2023. After submission, review, and defence of this thesis, several refinements and corrections were applied to the neutrino mass analysis by the KATRIN collaboration as part of the journal publication [33]. It is crucial to underline that these adjustments were made after the initial data unblinding and do not affect the core findings, methods applied, or conclusions of the thesis. However, for the sake of transparency and consistency, the respective modifications are listed below, along with their estimated impact on the neutrino mass analysis. Aside from this note added during the publication process, all content of the dissertation is left unaltered compared to the submitted version.

Data combination: The KNM4 campaign data was divided into two distinct periods, KNM4a and KNM4b, based on the different measurement time distributions, to accommodate variations in effective endpoint values. This reclassification was necessitated by a drift in the starting potential within the source, resulting in an approximate shift in the squared neutrino mass value of the KNM4 campaign by about $|\Delta m_\nu^2| \sim 0.1\,\mathrm{eV}^2$. [33]

Column density: A re-evaluation of systematic parameters and measurements with a new electron gun led to a correction for the column density, accounting for the influence of the starting kinetic energy on the electron angles. This adjustment is considered as an additional independent uncertainty. The impact on the squared neutrino mass is estimated to be $|\Delta m_\nu^2| \sim 0.05\,\mathrm{eV}^2$. [33]

Energy loss function: Through calibration measurements with a new electron gun, possible discrepancies were identified between the integral and time-of-flight modes of energy loss determination [28]. Using different energy loss function models leads to a bias of $0.035\,\mathrm{eV}^2$ on the squared neutrino mass. To account for the possible bias, the covariance matrix was scaled by a factor of 80. [33]

Penning trap induced background: The background rate time-dependency model was changed from a linear to a quadratic function. This modification has an estimated impact of approximately $|\Delta m_\nu^2| \sim 0.05\,\mathrm{eV}^2$ on the squared neutrino mass. [33]

Rear wall background: Minor discrepancies in the rear-wall spectrum analysis were identified and corrected, with a negligible impact on the squared neutrino mass below $|\Delta m_\nu^2| \sim 0.001\,\mathrm{eV}^2$. [33]

The initial best-fit value for the squared neutrino mass of $m_\nu^2 = -0.05\,^{+0.11}_{-0.12}\,\mathrm{eV}^2/\mathrm{c}^4$, translating to an upper limit of $m_\nu < 0.43\,\mathrm{eV}/\mathrm{c}^2$ (90 % C.L.), changes to an updated final best-fit value of $m_\nu^2 = -0.14\,^{+0.13}_{-0.15}\,\mathrm{eV}^2/\mathrm{c}^4$, and an upper limit of $m_\nu < 0.45\,\mathrm{eV}/\mathrm{c}^2$ (90 % C.L.) [33]. These post-unblinding modifications were implemented without bias towards the neutrino mass estimations, preserving the objectivity of the analysis presented here.

12.04.2024

Abstract

The observation of neutrino oscillation proved that neutrinos possess a non-zero mass. Neutrinos are one of the most elusive particles, the absolute mass scale of neutrinos remains unknown until today. The KArlsruhe TRItium Neutrino (KATRIN) collaboration aims to measure the neutrino mass by precision spectroscopy of tritium β-decay with a design sensitivity of $0.2\,\mathrm{eV/c^2}$. To this end, KATRIN measures the endpoint region of the tritium β-electron spectrum. The first science run was taken in Spring 2019. Since then, more measurement campaigns have further improved the statistical precision. With an increasing number of campaigns, a combined analysis of all collected data becomes more challenging.

The main work presented in this thesis focuses on the neutrino-mass analysis of the first five neutrino-mass measurement campaigns. The combined analysis of the campaigns results in a best fit of $m_\nu^2 = -0.05\,^{+0.11}_{-0.12}\,\mathrm{eV^2/c^4}$, which translates to an upper limit of $m_\nu < 0.43\,\mathrm{eV/c^2}$ (90 % C.L.). This result improves on previous neutrino mass limits from kinematic measurements by about a factor of two and is the current leading model-independent limit.

Probing the neutrino mass is the main purpose of the KATRIN experiment. Beyond this, the ultra-precise measurement of the β-spectrum can be used for new physics searches. One such study is the search for extra (sterile) neutrino states. The result of the light sterile neutrino search at the eV mass scale is presented based on the first and second KATRIN measurement campaigns. No sterile neutrino signal was observed. The analysis excludes parts of the $(m_4^2, |U_{\mathrm{e}4}|^2)$ parameter space down to $|U_{\mathrm{e}4}|^2 = 6 \times 10^{-3}$ (95 % C.L.). The result improves on previous direct limits set by the Mainz and Troitsk experiments and excludes the large Δm_{41}^2 preferred by the reactor antineutrino anomaly and gallium anomaly.

Contents

Introduction

Neutrinos were first postulated by Wolfgang Pauli in 1930 to resolve unexpected observations from measurements of the β-decay spectrum [125]. With the postulate of their existence, Pauli already noted that neutrinos must possess a mass, which he expected to be small. The existence of a non-vanishing neutrino mass was eventually proven decades later with the discovery of neutrino oscillation. Since massive neutrinos are not included in the Standard Model, neutrino masses indicate that there is physics beyond the Standard Model. Furthermore, due to their extremely small interaction cross section, neutrino properties are extremely difficult to measure, including the determination of their mass.

In the past decades, several experiments, such as those at Mainz and Troitsk, were conducted to determine the neutrino mass from measurements of the β-decay spectrum of tritium. The neutrino mass is determined from the shape of the integrated β-spectrum close to the endpoint. With their measurements, these experiments provided a long-standing upper limit on the effective electron antineutrino mass of $2\,\mathrm{eV/c^2}$ at a 95 % confidence level [46, 121, 151]. Building upon the ideas of previous experiments like those conducted in Mainz, Troitsk, and Los Alamos, the KArlsruhe TRItium Neutrino experiment (KATRIN) is currently the leading approach for model-independent measurements of the neutrino mass. With kinematic measurements of the integrated β-spectrum, the KATRIN collaboration aims to determine the neutrino mass with a final sensitivity of $0.2\,\mathrm{eV/c^2}$ at a 90 % confidence level [39].

To reach this goal, the KATRIN experiment has been operated with gaseous tritium since the mid-2018 and started neutrino-mass operations in Spring 2019. To determine the neutrino mass from a continuously growing data sample, a precise understanding of the underlying model is required. Furthermore, to guarantee an unbiased result, correct treatment of systematic effects arising along the complex beamline is crucial. The increasing number of individual recorded spectra further requires the development of new analysis strategies. From the first and second campaign, KATRIN was already able to provide a more stringent limit on the neutrino mass with $0.8\,\mathrm{eV/c^2}$ (90 % C.L.) [25], with respect to previous experiments. With more data from additional campaigns, the sensitivity on the neutrino mass has improved further.

Alongside the three light active neutrinos, the Standard Model can be extended by additional right-handed sterile neutrinos. Using the same data as used in the neutrino mass determination, one can also search for the imprint of sterile neutrinos in the eV-mass range. A sterile neutrino would be manifested in a kink-like distortion of the spectrum. The search in the eV-mass range is interesting since direct kinematic measurements with KATRIN are complementary to oscillation experiments. KATRIN is furthermore able to probe the parameter space where experiments have previously observed hints for sterile neutrinos, such as the gallium anomaly (GA) or the reactor antineutrino anomaly (RAA) [53, 177].

This thesis has four main objectives that focus on the analysis of KATRIN data:

- Provide a detailed description of the physics model and analysis strategies as they are applied in the KATRIN data analysis.
- Outline the characterisation of systematic effects relevant to the analysis of the integrated β-spectrum.
- Present the neutrino-mass analysis of the data collected within the first five campaigns (2019 to 2021) and provide a new limit on the effective electron neutrino mass.
- And lastly, summarise the sterile neutrino analysis of the first and second campaign and provide an exclusion contour improving on other experiments.

The thesis in hand is structured as follows:

In chapter 1 a brief overview of neutrino physics is provided, including the historical background and the neutrinos' role in the Standard Model. Extensions to the Standard Model which could generate massive neutrinos are described. Furthermore, the principle of neutrino oscillation is introduced. Finally, an overview of different approaches to determine the neutrino mass, including cosmological observations, via neutrinoless double β-decay, or from kinematic measurements of the single β-decay is given. The last section of chapter 1 is a synopsis of the current status of eV-scale sterile neutrino searches.

In chapter 2, the KATRIN experiment is introduced. In this chapter, a general overview of the measurement concept is provided, followed by an in-depth description of the individual beamline sections and their function.

In chapter 3, the underlying physics model is summarised, describing the integrated β-spectrum that is measured with the KATRIN experiment. The core model is based on the theoretical description of the differential β-spectrum. It further includes effects, such as radiative corrections or Doppler broadening. An experimental response function reflects the transmission properties of the experimental setup. Lastly, significant systematic effects that contribute to the measured background or distort the measured spectrum are taken into account.

In chapter 4 an overview of the statistical methods and analysis tools that are applied in the KATRIN β-spectrum analysis is provided. This includes a definition of the likelihood, methods of how systematic effects and uncertainties are propagated, and further technical details on parameter estimation and limit setting.

In chapter 5 a summary is given of the five KATRIN neutrino-mass measurement campaigns. In this section, changes in the experimental setting and improvements between the measurement campaigns are described in more detail.

In chapter 6 an in-depth summary of the KATRIN neutrino mass and sterile neutrino analysis is given. As a basis, the methods of combining the data are introduced, together with the general fitting strategy. The neutrino-mass analysis of the first five campaigns is summarised, including a comprehensive set of systematic studies leading to an improved upper limit on m_ν^2. Lastly, the sterile neutrino analysis is presented, and the results are compared to other experiments.

The thesis is concluded with chapter 7, summarising both branches of the analysis and putting the results presented into the broader context of the field.

1. Neutrino physics

The first chapter of this thesis will give a general introduction and overview of neutrino physics. The history of how neutrinos was first theoretically postulated, and later experimentally confirmed, is outlined in section 1.1. In section 1.2, an overview of the neutrinos' role in the Standard Model will be given, which is further extended beyond the Standard Model in section 1.3, motivating how neutrino masses can be generated. The observations of neutrino oscillations are summarised in section 1.4, proving that neutrinos have a non-zero mass. Furthermore, in section 1.5, three different approaches are summarised that allow the determination of the absolute mass scale. The three methods cover the analysis of cosmological observations, estimation via the neutrinoless double β-decay, or from single β-decay spectra. The last section (section 1.6) of the chapter further provides a brief overview of the role of sterile neutrinos and the motivation to search for light sterile neutrinos in the eV-mass range.

1.1. History of neutrino physics

The first radioactive decays were observed by H. Becquerel in 1896, when investigating the phosphorescence of uranium [55]. In 1899 and 1913 E. Rutherford and F. Soddy later distinguished three types of radiation [209, 233]: α-, β-, and γ-radiation. In 1911, L. Meitner, O. Hahn, and O. von Baeyer discovered anomalies in their observations. However, it was only in 1914 when J. Chadwick was able to measure the β-spectrum of radium [70] with a Geiger counter[1]. Chadwick was able to prove that the measured β-spectrum is continuous. Until then, the spectrum was thought to correspond to a two-body decay and hence would be given by a characteristic monoenergetic line spectrum similar to the α- and γ-decay. The observation of a continuous spectrum violated conservation of energy and momentum according to the state of knowledge at the time.

The problem persisted for the next decades. W. Pauli resolved the discrepancy in 1930 by postulating a new particle, the "neutrino"[2]. In his famous letter to the "radioactive ladies and gentlemen" [189], Pauli was able to explain the continuous spectrum by adding a third decay constituent,

$$ {}^{A}_{Z}X \longrightarrow {}^{A}_{Z+1}Y + \mathrm{e} + \overline{\nu}_{\mathrm{e}}. \tag{1.1} $$

[1] The Geiger counter was developed by H. Geiger in 1908. With the Geiger counter, ionising radiation is detected when the ionising particles pass through a gas-filled chamber, producing an electric pulse.

[2] At the time, Pauli introduced the particle as "neutron". E. Fermi renamed the particle "neutrino" (little neutral one) in 1931 since "neutron" was already in use for the neutral nucleon named by W. Harkins in 1921 [125] and discovered by J. Chadwick in 1932 [71]

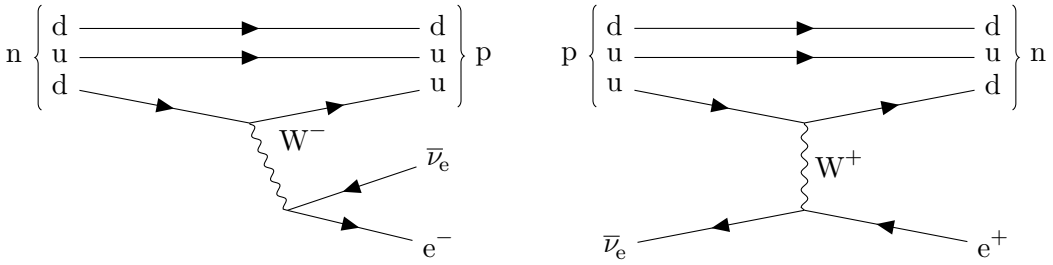

(a) β-decay **(b)** Inverse β-decay

Figure 1.1.: Feynman diagrams of the β-decay and the inverse β-decay on the quark level. (**a**) A neutron (ddu) decays into a proton (duu), and emitts an electron (e^-) and an electron antineutrino ($\overline{\nu}_e$) over a weak charged current interaction (W^-). (**b**) A proton (duu) interacts with an electron antineutrino ($\overline{\nu}_e$) via a W^+-boson exchange, resulting in a neutron (ddu) and a positron (e^+).

The new particle was characterised as a massive and electrically neutral particle with a spin of 1/2 to guarantee the conservation of charge, energy, momentum, and spin. At the time, Pauli already suggested that the neutrino must have a small mass to explain the spectrum's shape close to the endpoint.

In 1932, J. Chadwick experimentally measured the existence of a neutral nucleus constituent, the neutron [71]. Encouraged by the experimental findings of Chadwick and Pauli's theory, E. Fermi formulated the β-decay as a single-vertex three-body decay

$$n \longrightarrow p + e^- + \overline{\nu}_e. \tag{1.2}$$

In Fermi's theory [102], the heavy neutron (n) decays into a positive proton (p), an electron (e^-), and a massless neutral particle, the neutrino (ν), more precisely, the electron antineutrino ($\overline{\nu}_e$).[3] The β-decay process is illustrated in figure 1.1a.

Since neutrinos do not possess electric charge or colour charge, they only interact via the weak force, making them particularly difficult to measure. It took until 1942 when K. C. Wang suggested the inverse beta decay as a method to detect neutrinos [250]. The mechanism of the inverse β-decay is illustrated in figure 1.1b.

Subsequently, in 1956, C. Cowan and F. Reines experimentally observed the neutrino via the inverse beta decay in their setup for the first time [76]. This finding was honoured with the physics Nobel Prize in 1995 for Reines.[4] In the experiment named Poltergeist Project in the Los Alamos National Laboratory, an electron antineutrino is captured by a proton, resulting in a neutron and a positron. The positron annihilates with an ambient electron, emitting characteristic γ-rays. Additionally, the resulting neutron is captured by Cadmium within the solution, resulting in additional delayed γ-rays. The γ-rays from the annihilation, as well as the coincidence γ-rays, were then detected, prooving capture of a neutrino. In this experiment, only electron antineutrinos were detected.

It took another nine years until neutrinos with a different flavour were observed. At the Brookhaven National Laboratory, J. Steinberger, M. Schwartz, and L. Lederman measured

[3] Note that Fermi's theory described the β-decay with a four-fermion interaction model, which does not involve the exchange of a W-boson.

[4] Nobel prizes are not awarded posthumously. Only Reines was honoured with the prize, as Cowan had died in 1974.

the muon neutrino in 1962 [78], which also was rewarded with a physics Nobel Prize in 1988. The discovery was based on the decay of π-mesons:

$$\pi^+ \longrightarrow \mu^+ + \nu_\mu. \tag{1.3}$$

In the experiment, primary muons from the π decay were absorbed by a steel shielding, whereas the muon neutrinos passed through the shielding. Other particles were similarly stopped by this shielding. Subsequent interactions of the muon neutrinos with nucleons N in the aluminum detector led to charged current interactions, resulting in the production of secondary muons. These secondary muons were then detected in an aluminum target. The reaction can be described by the following equation, where X represents other particles produced in the interaction.[5]

$$\nu_\mu + N \longrightarrow \mu^- + X. \tag{1.4}$$

With the discovery of the tau lepton in 1975 [191], a third neutrino flavour was predicted. The measured decay width of the Z^0-boson further affirmed the assumption of three neutrino generations [81]. The existence of the ν_τ was provem in 2001 by measurements of the DONUT experiment at Fermilab [82].

1.2. Neutrinos in the Standard Model

The Standard Model of particle physics summarises the elementary building blocks of matter and the forces that govern their fundamental interactions. The forces described by the Standard Model are the weak, the strong, and the electromagnetic force. Not predicted by the Standard Model is the gravitational force. A graphical illustration of the Standard Model is presented in figure 1.2.

The Standard Model particles are divided into four fundamental groups. Each group is highlighted in a different colour in figure 1.2. The elementary particles are quarks (coloured in teal), leptons (coloured in light blue), gauge bosons (coloured in dark blue), and the scalar boson (coloured in purple). Quarks and leptons are both fermions, possessing spin of $1/2$. Compared to fermions, bosons, on the other hand, have integer spin values. Gauge bosons serve as the exchange particles of the fundamental forces and have spin of 1.

The fermions are grouped into three generations, each comprising two quarks and two leptons, according to their masses (marked by the roman numerals on top). There are six quark flavours: up (u), down (d), charm (c), strange (s), top (t), and bottom (b). Up-type quarks (u, c, and t) have an electric charge of $+2/3$, whereas down-type quarks (d, s, and b) have an electric charge of $-1/3$. The corresponding antiquarks have opposite charges. All quarks, in addition, have a colour charge. Leptons are categorised into charged leptons and neutral leptons. The charged leptons are the electron (e), the muon (μ), and the tau lepton (τ). The charged leptons all possess an electric charge of -1. To each charged lepton, there is a corresponding neutrino with the same flavour. The three neutinos are the electron neutrino (ν_e), the muon neutrino (ν_μ), and the tau neutrino (ν_τ).

The Standard Model is a quantum field theory that utilises a renormalised Lagrange formalism to explain the dynamics and interactions of particles. Within this framework, particles

[5] If only one type of neutrino existed, electrons and muons would have been produced in equal amounts. However, the observation of predominantly muons established the hypothesis of neutrino generations.

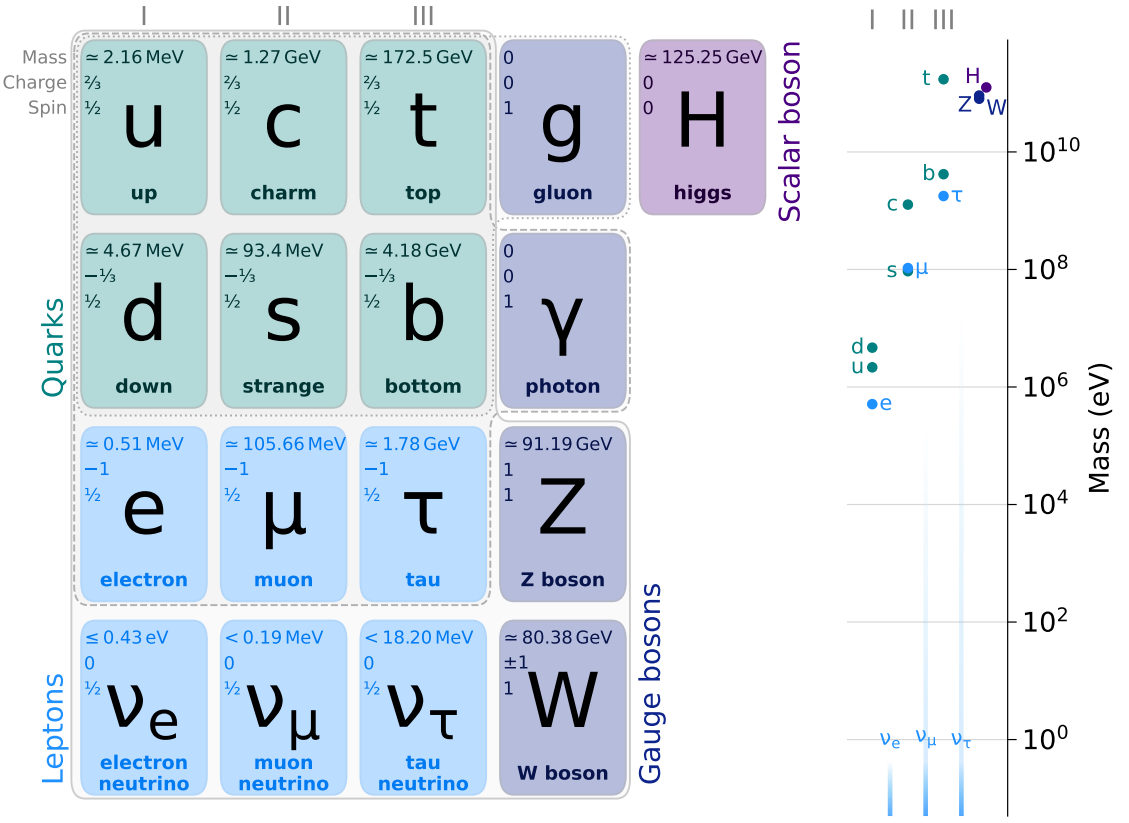

Figure 1.2.: (**Left**) Standard Model of particle physics with the extension of massive neutrinos. The Standard Model is divided into quarks (teal), leptons (light blue), gauge bosons (dark blue), and scalar bosons (purple). Particles interacting via the weak force are outlined by the solid grey line, particles interacting via the electromagnetic force are outlined by the dotted grey line, and particles interacting with the strong force are outlined by the dashed grey line. The fermions (teal and blue) are further grouped into three generations of matter. Note that the mass of the electron neutrino is based on the upper limit presented in this thesis (see section 4.4). All other masses are based on [257]. (**Right**) Comparison of the masses of the individual elementary particles. Since the masses of the three neutrino flavour eigenstates are only constrained by an upper limit, the neutrinos are marked as lines in the lower mass region.

are depicted as quantised fields, and their kinematics and interactions are encapsulated within a Lagrangian density $\mathcal{L}$. The Standard Model Lagrange density is invariant under the unitarity product group SU(3)×SU(2)×U(1). Therefore conservational quantities are the colour charge C, the weak isospin T_3, and the weak hypercharge Y. Quantum chromodynamics (QCD) defines the interactions between quarks and gluons through the SU(3) symmetry. Gluons (g) are the massless mediator particles of the strong force, coupling to the quarks.

The Weinberg-Salam SU(2)×U(1) [252] gauge group incorporates the electromagnetic and weak interactions, generated by the weak hypercharge[6]. Photons (γ) are massless particles,

[6]The weak hypercharge Y is explicitly defined by the difference of the electric charge Q and the weak isospin T_3, leading to $Y = 2(Q - T_3)$

mediating the electromagnetic force and coupling to all electrically charged fermions. Z and W bosons are the mediators of the weak force. The charged gauge bosons couple with left-handed particles and right-handed antiparticles. In weak interactions, the three bosons (Z^0, W^+, and W^-) transfer integer spin, and in the case of the W bosons, they also allow for charged-current interactions.

Experimental observations suggest neutrinos in the Standard Model exist solely as left-handed particles. The weak interaction is the only interaction violating the charge-parity (CP) symmetry. In the electroweak interaction theory, neutrinos are predicted to be massless, as only the left-handed neutrino is employed in the interaction, whereas the right-handed partner is not predicted to exist. Furthermore, the lepton number has to be conserved in interactions. Violating either of the aforementioned conditions and assuming positive, non-zero Yukawa coupling leads to a neutrino mass different to zero. The observation of neutrino oscillation (see section 1.4), on the contrary, suggests a non-vanishing neutrino mass. Therefore, the existence of the neutrino mass requires physics beyond the Standard Model. A possible mechanism to generate the neutrino mass is described in section 1.3, while also discussing the possible Majorana[7] nature of the neutrino.

The last component of the Standard Model is the Higgs boson. The Higgs boson is the manifestation of spontaneous symmetry breaking of the Higgs field ϕ. As a scalar boson, the Higgs boson has an integer spin of 0. The $W^{\pm}$ and the Z^0 mass are generated through spontaneous symmetry breaking, while the photon remain massless. All fermions obtain their mass by interacting with the Higgs field.

In the Standard Model Lagrangian $\mathcal{L}_{\mathrm{SM}}$, Dirac fermions obtain their masses through the mass term

$$\mathcal{L}_m = m_{\mathrm{D}} \bar{\psi} \psi. \tag{1.5}$$

This term is given by the Dirac mass m_{D} and the spinor ψ. The equation can be separated into the left-handed and right-handed Weyl spinors ψ_{L} and ψ_{R}.[8] The left-handed SU(2) doublets ψ_{L} are

$$\begin{pmatrix} \nu_{\mathrm{e}} \\ \mathrm{e}^- \end{pmatrix}_{\mathrm{L}} \quad \begin{pmatrix} \nu_{\mu} \\ \mu^- \end{pmatrix}_{\mathrm{L}} \quad \begin{pmatrix} \nu_{\tau} \\ \tau^- \end{pmatrix}_{\mathrm{L}}, \tag{1.6}$$

whereas the right-handed partners are the SU(2) singlets ψ_{R} with

$$\left(\mathrm{e}^-\right)_{\mathrm{R}} \quad \left(\mu^-\right)_{\mathrm{R}} \quad \left(\tau^-\right)_{\mathrm{R}}. \tag{1.7}$$

The particle masses are the result of coupling to the Higgs field

$$\phi = \begin{pmatrix} \phi^+ \\ \phi_0 \end{pmatrix}. \tag{1.8}$$

Electroweak symmetry-breaking shifts the vacuum expectation value v.[9] Expanding around

[7] Majorana particles are elementary particles, where the particle is its own antiparticle.

[8] Left and right-handedness refers to the particles' helicity. The helicity describes the relative direction of spin and momentum of a particle. For right-handed particles, both are aligned in the same direction, whereas the spin and momentum of left-handed particles point in opposite directions.

[9] The vacuum expectation value is connected to the mass of the W boson, m_{W}, and the weak isospin coupling g with $v = {}^{2m_{\mathrm{W}}}/_{g} \approx 246.22\,\mathrm{GeV}$.

the minimum, the vacuum Higgs field ϕ_0 is

$$\phi_0 = \frac{1}{\sqrt{2}} \begin{pmatrix} 0 \\ v \end{pmatrix}. \tag{1.9}$$

The mass contributions from the coupling of leptons (with flavour $\ell \in [\mathrm{e}, \mu, \tau]$) to the Lagrange density is described by the Yukawa coupling:

$$\mathcal{L}_{\mathrm{Yuk}} = -c_\ell \bar{\ell}_{\mathrm{R}} \phi^\dagger \begin{pmatrix} \nu_\ell \\ \ell \end{pmatrix}_{\mathrm{L}} + \mathrm{h.c.}, \tag{1.10}$$

applying the vacuum state of the Higgs field given by equation (1.9) leads to

$$\mathcal{L}_{\mathrm{Yuk}} = -c_\ell \frac{v}{\sqrt{2}} \left(\bar{\ell}_{\mathrm{R}} \ell_{\mathrm{L}} + \bar{\ell}_{\mathrm{L}} \ell_{\mathrm{R}} \right). \tag{1.11}$$

From this, one can see that a mass term for neutrinos is foreseen when introducing right-handed neutrinos. For charged leptons, the mass is determined by the coupling strength c_ℓ to the Higgs field. The first factor $c_\ell \frac{v}{\sqrt{2}}$ then gives rise to the lepton masses. The Dirac masses can not be predicted from theory and have to be measured experimentally. The measured masses for the three charged leptons are

$$m_{\mathrm{e}} = 0.511\,\mathrm{MeV}\ [240] \qquad m_\mu = 105.7\,\mathrm{MeV}\ [240] \qquad m_\tau = 1777\,\mathrm{MeV}\ [257]. \tag{1.12}$$

Note that the convention of setting the speed of light to $c = 1.0$ is used for the given masses.

1.3. Neutrino mass generation and physics beyond the Standard Model

The Standard Model only comprises left-handed neutrinos. Due to the lack of right-handed partners, neutrinos appear to be massless. This points to physics beyond the Standard Model, where additional processes give the neutrinos their mass. The approach outlined in the following is based on references [259, 260].

The first and simple approach is to add a right-handed neutrino into the Lagrangian, analogous to the other standard model particles. The right-handed partners would come as an additional set of SU(2) singlets with isospin $T_3 = 0$ and weak hypercharge $Y = 0$ (extending the singlets given in equation (1.7)). With this, the Lagrangian of the Yukawa coupling of equation (1.10) modifies to

$$\mathcal{L}_{\mathrm{Yuk}} = -c_\ell \bar{\ell}_{\mathrm{R}} \phi_0^\dagger \begin{pmatrix} \nu_\ell \\ \ell \end{pmatrix}_{\mathrm{L}} - c_{\nu_\ell} \bar{\nu}_{\ell \mathrm{R}} \tilde{\phi}_0^\dagger \begin{pmatrix} \nu_\ell \\ \ell \end{pmatrix}_{\mathrm{L}} + \mathrm{h.c.} \qquad \text{with}: \quad \tilde{\phi}_0 = \frac{1}{\sqrt{2}} \begin{pmatrix} v \\ 0 \end{pmatrix} \tag{1.13}$$

$$\mathcal{L}_{\mathrm{Yuk}} = -c_\ell \frac{v}{\sqrt{2}} \left(\bar{\ell}_{\mathrm{R}} \ell_{\mathrm{L}} + \bar{\ell}_{\mathrm{L}} \ell_{\mathrm{R}} \right) - c_{\nu_\ell} \frac{v}{\sqrt{2}} \left(\bar{\nu}_{\ell \mathrm{L}} \nu_{\ell \mathrm{R}} + \bar{\nu}_{\ell \mathrm{R}} \nu_{\ell \mathrm{L}} \right) \tag{1.14}$$

This extension results in a non-zero neutrino mass term within the Lagrangian. To explain the small neutrino masses (see figure 1.2 right), a small coupling constant is required with

$c_{\nu_\ell} \lesssim 10^{-11}$. This is at least five orders of magnitude smaller than the coupling strength of all other leptons. However, there is no explanation for why the neutrinos' coupling strength should be so vastly different.

An alternative approach is to consider neutrinos as Majorana particles ($\nu_L \equiv (\bar{\nu}_R)^C$ and $\nu_R \equiv (\bar{\nu}_L)^C$). The mass term in the Lagrangian equation (1.5) is then written with the charge-conjugated spinor ψ^C:

$$\mathcal{L}_m = m_\mathrm{D} \bar{\psi} \psi^C. \tag{1.15}$$

Separating this again into the left and right-handed two-component Weyl spinors leads to

$$\mathcal{L}_m = \frac{1}{2} m_\mathrm{D} \left(\bar{\psi}_\mathrm{L} \psi_\mathrm{R} + \bar{\psi}^C_\mathrm{L} \psi^C_\mathrm{R} \right) + \frac{1}{2} \left(m_\mathrm{L} \bar{\psi}_\mathrm{L} \psi^C_\mathrm{R} + m_\mathrm{R} \bar{\psi}^C_\mathrm{L} \psi_\mathrm{R} \right) + \mathrm{h.c.}. \tag{1.16}$$

This can further be expressed in its matrix representation, combining the Majorana and the Dirac mass terms

$$\mathcal{L}_m = \frac{1}{2} \begin{pmatrix} \bar{\psi}_\mathrm{L} & \bar{\psi}^C_\mathrm{L} \end{pmatrix} \begin{pmatrix} m_\mathrm{L} & m_\mathrm{D} \\ m_\mathrm{D} & m_\mathrm{R} \end{pmatrix} \begin{pmatrix} \psi^C_\mathrm{R} \\ \psi_\mathrm{R} \end{pmatrix}, \tag{1.17}$$

with one Dirac mass m_D and two Majorana masses m_R. Starting from this, there are different scenarios.

A common approach is to assume a vanishing left-handed mass $m_\mathrm{L} = 0$.

$$M = \begin{pmatrix} 0 & m_\mathrm{D} \\ m_\mathrm{D} & m_\mathrm{R} \end{pmatrix}. \tag{1.18}$$

In the minimal (type-I) seesaw mechanism [259] in addition, Majorana masses are much larger than the Dirac masses ($m_\mathrm{R} \gg m_\mathrm{D}$). The eigenvalues of M give two Majorana masses:

$$\lambda_1 = \frac{1}{2} \left(m_\mathrm{R} - \sqrt{m_\mathrm{R}^2 + 4 m_\mathrm{D}^2} \right) \approx -\frac{m_\mathrm{D}^2}{m_\mathrm{R}} \tag{1.19}$$

$$\lambda_2 = \frac{1}{2} \left(m_\mathrm{R} + \sqrt{m_\mathrm{R}^2 + 4 m_\mathrm{D}^2} \right) \approx m_\mathrm{R} \left(1 + \frac{m_\mathrm{D}^2}{m_\mathrm{R}^2} \right) \approx m_\mathrm{R}. \tag{1.20}$$

The two mass eigenvalues can be identified as a light "active" neutrino mass $m_{\nu_\mathrm{a}} = |\lambda_1| = m_\mathrm{D}^2 / m_\mathrm{R}$ and a heavy "sterile" neutrino mass $m_{\nu_\mathrm{s}} = |\lambda_2| = m_\mathrm{R}$. The left-handed neutrino participates in weak interactions and is therefore called "active". The right-handed neutrino, on the other hand, does not participate in weak interactions and is hence called "sterile". This also explains the name *seesaw mechanism*, where the active and sterile masses are inversely proportional to each other ($m_{\nu_\mathrm{a}} \propto m_{\nu_\mathrm{s}}^{-1}$). Hence, large masses of m_R (on the order of 10^2 GeV) and consequently large sterile masses can explain the small masses of the active neutrinos (on the order of 1 eV) [259]. Converting this into a mixing angle θ of the left-handed active neutrino with the right-handed sterile neutrino is

$$\theta \sim \frac{m_\mathrm{D}}{m_\mathrm{R}} = \sqrt{\frac{m_{\nu_\mathrm{a}}}{m_{\nu_\mathrm{s}}}}. \tag{1.21}$$

With a large mass difference, the active-to-sterile mixing angle θ is expected to be small. The

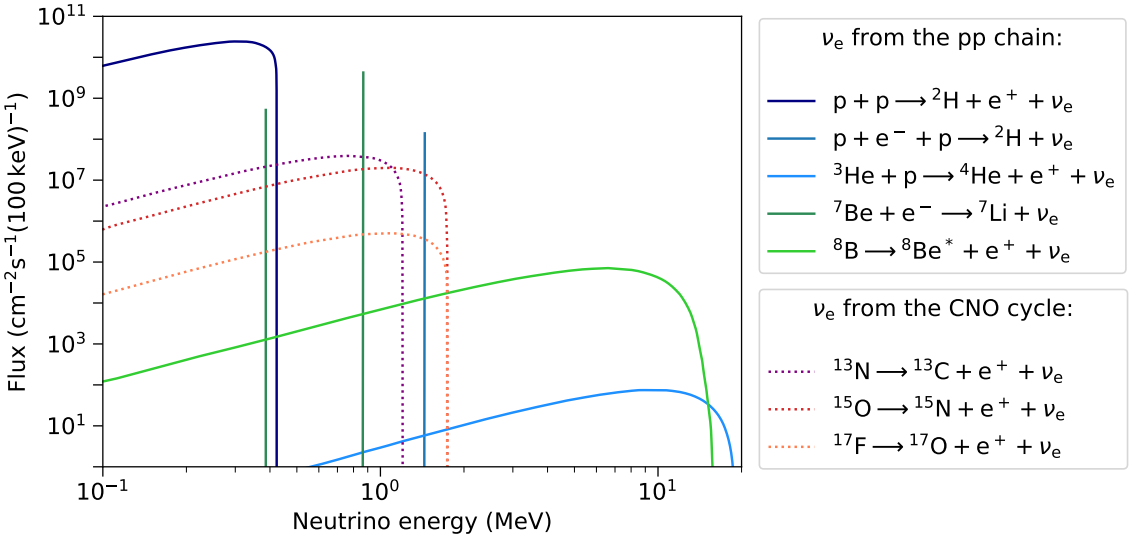

Figure 1.3.: Neutrino flux measured by the Borexino experiment. The plot is based on the phase-III data collected by Borexino [17]. The figure shows the neutrino flux per 100 keV bin generated in the pp chain (from pp, pep, hep, ^{7}Be, and ^{8}B) and emitted within the CNO cycle (from ^{13}N, ^{15}O, and ^{17}F decays). The energy spectra of ^{7}Be and pep are monoenergetic, as it is a two-body decay, all other spectra are continuous. Data extracted from [17].

problem of the small Yukawa coupling is also elegantly resolved by the see-saw mechanism.

There are also other theoretical processes besides the (type I) seesaw mechanism that could explain small neutrino masses. The (type II) seesaw mechanism explains massive neutrinos by introducing a Higgs triplet to the standard model [215]. Some of the theories are, for example, processes that involve additional radiative quantum corrections [170, 190], or models that assume approximate lepton number conservation [115, 72].

1.4. Neutrino oscillation

The Sun is the largest source of neutrinos in direct vicinity to the earth. Eight major reaction processes within the Sun contribute to the total observable neutrino flux. The most significant fraction of neutrinos is emitted from fusion processes of protons in the pp chain. A small fraction of neutrinos ($\sim 1\,\%$) stem from β^+-decays within the CNO cycle. The neutrinos emitted from both the fusion and β^+-decays are electron neutrinos with kinetic energies up to 18 MeV (see figure 1.3). The production ratio from the pp chain or the CNO cycle is usually determined by the core temperature. [13].[10] The measured neutrino flux of the pp chain (solid lines) and the CNO cycle (dotted lines) are displayed in figure 1.3. On Earth, around $\sim 6 \times 10^{10}$ neutrinos per second per cm^2 are observed at any moment. [17]

The first theoretical calculations of the expected neutrino flux were performed by J. Bahcall [49]. To confirm the theory, R. Davis Jr. designed the Homestake-Experiment with the aim of measuring the solar electron neutrino flux. The experiment operated between 1970

[10] Processes with higher nuclear charges are localised in regions of higher temperatur.

and 1994.[11] Surprisingly, the experiment only measured 1/3 of the number of neutrinos expected from the Sun [74], compared to the theoretical predictions by Bahcall. At the time, this discrepancy was known as the solar neutrino puzzle [50].

The findings subsequently motivated the construction of the Kamiokande-II experiment. The Kamiokande-II collaboration, independently measured a reduction of the number of neutrinos expected from the sun, releasing their results in 1988 [134]. The confirmation led to a number of follower experiments measuring additional neutrino flavours, such as the SuperKamiokande, and the Sudbury Neutrino Observatory (SNO) under the lead of A. McDonald. SNO measured the electron neutrino flux relative to the total neutrino flux.[12] The SNO results demonstrated clear evidence for neutrino oscillation, directly implying that neutrinos possess a non-zero mass. In 2015 T. Kajita and A. McDonald were awarded the Nobel prize in physics "for the discovery of neutrino oscillations, which shows that neutrinos have mass" [183].

The idea of neutrino oscillation was already introduced by Pontecorvo in 1957 [194], proposing the possibility of an admixture of neutrinos, allowing for oscillation. A more advanced theory was developed by Z. Maki, M. Nakagawa, and S. Sakata in 1962 [173], proposing an oscillation of the neutrino flavour eigenstates.

The three flavour eigenstates form an orthogonal basis of the observable neutrino states. The eigenbasis of these flavour eigenstates is formed by the three mass eigenstates. Neutrinos are propagated in their mass eigenstates while they interact via their flavour eigenstates. Due to the different masses of the mass eigenstates, the neutrino oscillates between different flavour eigenstates while propagating through space. The Pontecorvo-Maki-Nakagawa-Sakata neutrino mixing matrix (PMNS) connects the three flavour eigenstates with the three mass eigenstates as follows:

$$|\nu_\alpha\rangle = \sum_i U_{\alpha i} |\nu_i\rangle \quad \Leftrightarrow \quad \begin{pmatrix} \nu_\mathrm{e} \\ \nu_\mu \\ \nu_\tau \end{pmatrix} = \begin{pmatrix} U_{\mathrm{e}1} & U_{\mathrm{e}2} & U_{\mathrm{e}3} \\ U_{\mu 1} & U_{\mu 2} & U_{\mu 3} \\ U_{\tau 1} & U_{\tau 2} & U_{\tau 3} \end{pmatrix} \cdot \begin{pmatrix} \nu_1 \\ \nu_2 \\ \nu_3 \end{pmatrix}. \tag{1.22}$$

The PMNS-matrix U is given by the product of mixing between mass eigenstates ($|\nu_1\rangle \leftrightarrow |\nu_2\rangle$), ($|\nu_1\rangle \leftrightarrow |\nu_3\rangle$), and ($|\nu_2\rangle \leftrightarrow |\nu_3\rangle$), each given by a (3×3) matrix, resulting in

$$U = \begin{pmatrix} 1 & 0 & 0 \\ 0 & c_{23} & s_{23} \\ 0 & -s_{23} & c_{23} \end{pmatrix} \cdot \begin{pmatrix} c_{13} & 0 & s_{13} e^{-i\delta_{CP}} \\ 0 & 1 & 0 \\ -s_{13} e^{i\delta_{CP}} & 0 & c_{13} \end{pmatrix} \cdot \begin{pmatrix} c_{12} & s_{12} & 0 \\ -s_{12} & c_{12} & 0 \\ 0 & 0 & 1 \end{pmatrix} \tag{1.23}$$

$$= \begin{pmatrix} c_{12}c_{13} & s_{12}c_{13} & s_{13} e^{-i\delta_{CP}} \\ -s_{12}c_{23} - c_{12}s_{23}s_{13} e^{i\delta_{CP}} & c_{12}c_{23} - s_{12}s_{23}s_{13} e^{i\delta_{CP}} & s_{23}c_{13} \\ s_{12}s_{23} - c_{12}c_{23}s_{13} e^{i\delta_{CP}} & -c_{12}s_{23} - s_{12}c_{23}s_{13} e^{i\delta_{CP}} & c_{23}c_{13} \end{pmatrix}. \tag{1.24}$$

[11] The detection of neutrinos in the Homestake-Experiment was based on inverse β-decay, capturing an electron neutrino with chlorine: $\nu_\mathrm{e} + {}^{37}\mathrm{Cl} \longrightarrow {}^{37}\mathrm{Ar} + \mathrm{e}^-$. The chlorine was present in the form of tetrachloroethene. The resulting argon, with a half-life of 35 days, was purged from the system and captured. By observing the decay of the collected argon, the amount of captured electron neutrinos was estimated.

[12] With ∼1000 t of heavy water, SNO was able to detect charged current interactions, neutral current interactions, and elastic scattering of neutrinos with electrons.

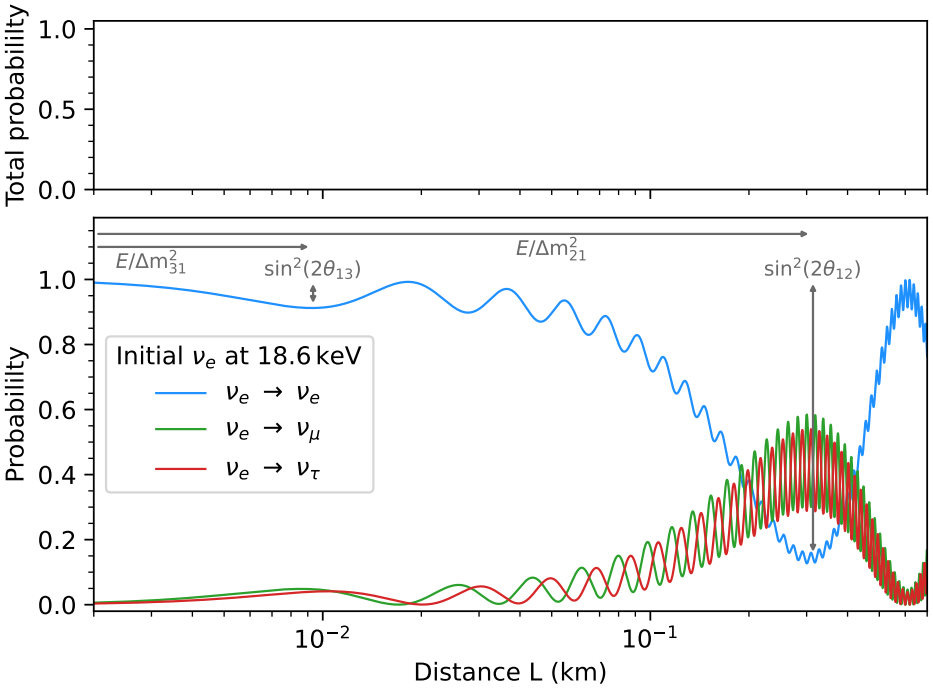

Figure 1.4.: Illustration of neutrino oscillation. The calculation is based on electron neutrinos with an initial energy of 18.6 keV. The inputs for the squared mass differences and mixing amplitudes are based on [257].

Hereby s_{ij} and c_{ij} are the abbreviated form of $\sin(\theta_{ij})$ and $\cos(\theta_{ij})$, with the corresponding mixing angle θ_{ij} between the mass eigenstates ν_i and ν_j. The relation further contains the CP-violating phase δ_{CP}. [252]

A neutrino with the energy $E_i = (Et - p_i x)$ starting in the flavour eigenstate ν_e at $t = 0$, oscillates over time with

$$|\nu_e(t > 0)\rangle = U^*_{e1} e^{-iE_1 t} |\nu_1\rangle + U^*_{e2} e^{-iE_2 t} |\nu_2\rangle + U^*_{e3} e^{-iE_3 t} |\nu_3\rangle \neq |\nu_e(t = 0)\rangle \,. \tag{1.25}$$

For highly relativistic neutrinos $v \approx c$ and $E_i = p_i$. The propagation time t can further be replaced by $t \approx {}^{L}/_{c} \overset{c=1}{=} L$, where L is the distance to the emission point. The probability of observing a neutrino starting with the flavour eigenstate $|\nu_\alpha\rangle$ in the flavour eigenstate $\left|\nu_\beta\right\rangle$ is given by

$$P(\nu_{\alpha\to\beta}(L, E)) = \sum_{k,l} U^*_{\alpha k} U_{\beta k} U_{\alpha l} U^*_{\beta l} e^{-i\left(\frac{\Delta m^2_{kl} \cdot L}{2E}\right)} \,. \text{ [260]} \tag{1.26}$$

Hence, measuring the oscillation behaviour allows one to determine the squared mass difference $\Delta m^2_{kl} = m^2_k - m^2_l$ between the mass eigenstates ν_k and ν_l. A visual representation of the neutrino oscillation is shown in figure 1.4. In the plot, the observation probability of the flavour eigenstates ν_e, ν_μ, and ν_τ is shown as a function of the distance L. The calculation is based on initial neutrinos in the electron flavour, emitted with an energy of 18.6 keV. The underlying low oscillation frequency is proportional to Δm_{21}, whereas the high-frequency oscillation is based on Δm_{31}. Similarly the low frequency oscillation

Table 1.1.: Summary of the results of neutrino mixing parameters, the mass differences of the neutrino mass eigenstates, and the CP violating phase. For $\sin^2(\theta_{23})$ and Δm^2_{32}, the scenarios of normal and inverted hierarchy are listed. All values are taken from [257].

Parameter	Value	Comments	References
$\sin^2(\theta_{12})$	0.307 ± 0.013	Results by KamLAND + global solar: Assuming 3ν	[5]
$\sin^2(\theta_{23})$ (IO) $\sin^2(\theta_{23})$ (NO)	0.539 ± 0.022 0.546 ± 0.021	PDG averaged: T2K, MINOS, NOνA, IceCube, and Super-Kamiokande	[1, 4, 6, 10, 11]
$\sin^2(\theta_{13})$	$(2.20 \pm 0.07) \times 10^{-2}$	PDG averaged: Daya Bay, RENO, and Double Chooz	[14, 37, 51, 145, 230]
Δm^2_{21}	$(7.53 \pm 0.18) \times 10^{-5}$ eV^2	Results by KamLAND + global solar + SBL + accelerator: Assuming 3ν	[113]
Δm^2_{32} (IO) Δm^2_{32} (NO)	$(-2.54 \pm 0.03) \times 10^{-3}$ eV^2 $(2.45 \pm 0.03) \times 10^{-3}$ eV^2	PDG averaged: T2K, MINOS, NOνA, IceCube, Super-Kamiokande, Daya Bay, and RENO	[1, 4, 6, 10, 11, 14, 51]
δ_{CP}	$(1.36^{+0.20}_{-0.16})\,\pi$ rad	PDG averaged: T2K, NOνA, and Super-Kamiokande	[6, 10, 4]

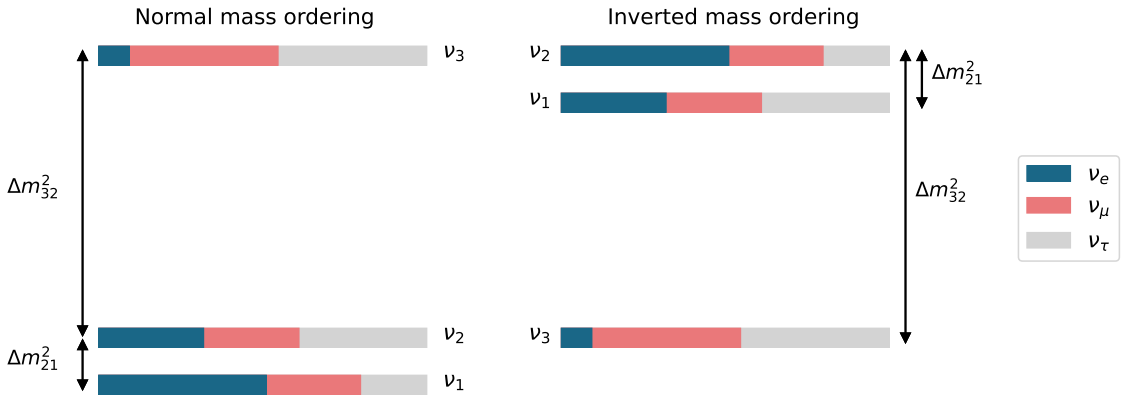

Figure 1.5.: Illustration of the neutrino mass ordering scenarios of the mass eigenstates. The mass eigenstates are composed of the three flavour eigenstates with a varying contributions. The two scenarios illustrated are the normal ordering (NO) and inverted ordering (IO). The composition of the individual mass eigenstates is based on the mixing listed in table 1.1.

amplitude is proportional to $\sin^2(2\theta_{12})$, and the high frequency oscillation amplitude is proportional to $\sin^2(2\theta_{13})$. In the top panel of figure 1.4, the combined total probability of all neutrino flavour eigenstates is shown, illustrating that the total flux of all flavour eigenstates remains constant. A summary of all oscillation parameters is presented in table 1.1.

The mass differences between the mass eigenstates were determined experimentally by analysing the oscillation frequency. Oscillation experiments are not able to give information about the absolute mass scale. There are two possible scenarios for the ordering of the mass eigenstates: the NO and the IO. The mass hierarchy also influences the sign of Δm^2_{32}

(positive for NO and negative for IO). In the normal mass hierarchy

$$\text{NO}: \quad m(\nu_1) < m(\nu_2) \ll m(\nu_3), \tag{1.27}$$

whereas in the inverted mass hierarchy

$$\text{IO}: \quad m(\nu_3) \ll m(\nu_1) < m(\nu_2). \tag{1.28}$$

Both hierarchy scenarios are illustrated in figure 1.5. Global analysis of oscillation experiments currently favours the normal ordering at $2.7\,\sigma$ over the inverted mass ordering [236].

1.5. Neutrino mass determination

Oscillation experiments give information about the relative scale of the mass eigenstates. The determination of the absolute scale ia an unresolved problem of modern physics until today. There are several approaches to determining the absolute scale. Generally, the methods can be divided into model-dependent and model-independent determination. The determination of the sum of neutrino masses from cosmological observations is considered to be dependent on the underlying model. Also, the neutrinoless double β-decay is categorised as a model-dependent determination since it depends on the presumption that neutrinos are Majorana particles. Model-independent approaches are based on kinematic measurements of β-decays. The expected spectrum is theoretically derived and does not contain prior assumptions. These different approaches are further sensitive to different observables, the sum of all neutrino masses $\sum m_\nu$ in cosmology, the effective Majorana mass $m_{\beta\beta}$ in neutrinoless double β-decays, and squared the effective neutrino mass m_ν in kinematic measurements of the β-spectrum. Therefore one must be cautious comparing results from different fields and analyses.

Cosmological observations: The minimal cosmological model Λ cold dark matter (ΛCDM) describes the evolution of the universe after the big bang. The model is composed of only six main parameters[13]. Cosmological models further predict relic neutrinos as a cosmic neutrino background (CνB). Similarly to the cosmic microwave background (CMB)[14], the neutrinos decoupled gradually, and are still present today ($n_\nu = 339.5\,\text{cm}^{-3}$ [257]). Due to the low energy and small cross section, relic neutrinos of the CνB have not yet been measured directly. The ΛCDM hence can be extended by including the additional parameter for the neutrino mass ΛCDM+$\sum m_i$.

Neutrinos have a characteristic influence on the formation and expansion of the universe. In the early universe, relativistic neutrinos behaved like radiation, enhancing the density of radiation. After decoupling, neutrinos contributed to the structure formation adding to the non-relativistic matter budget. Today, the average black body temperature of neutrinos is $T_\nu = 1.95\,\text{K} \approx 1.7 \times 10^{-4}\,\text{eV}$ [257]. This is smaller than two of the mass differences (see table 1.1). Therefore, at least two of the neutrino mass eigenstates are non-relativistic, contributing as hot dark matter. Neutrinos leave a detectable imprint that can be observed

[13] The parameters in the ΛCDM are: The baryon density Ω_b, the dark matter density Ω_c, the reionisation optical depth τ, the curvature fluctuation amplitude A_s, the scalar spectral index n_s, and the acoustic scalar angle θ_MC [62].

[14] The CMB is remanent from the primordial universe when the universe became transparent after nucleosynthesis.

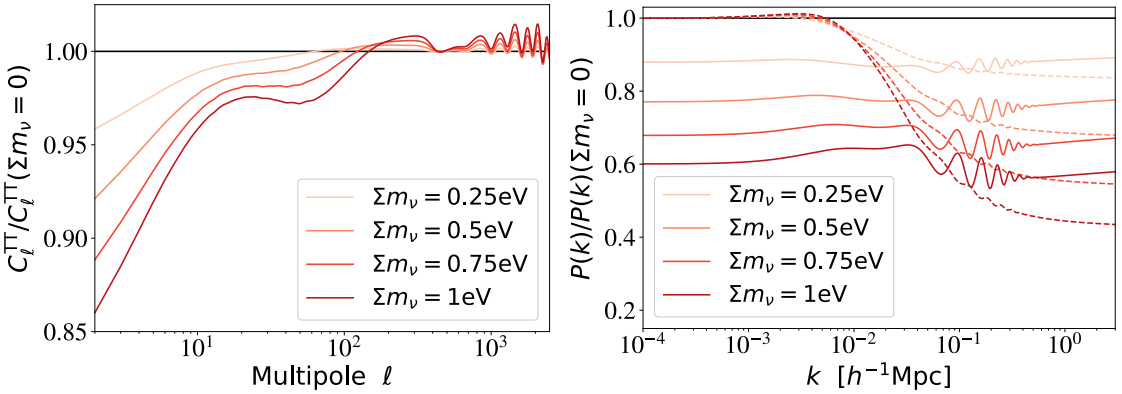

Figure 1.6.: Relative impact of the neutrino masses on the CMB TT polarised temperature spectrum C_ℓ^{TT} (left) and the matter power spectrum $P(k)$ (right). Figure taken from [257].

in cosmological data. Hereby, cosmology is sensitive to the neutrino density Ω_ν, the number of active neutrinos N_{eff}, and the sum of the neutrino mass eigenstates

$$\sum m_i := \sum_{i=1}^{3} m_i. \text{ [260]} \tag{1.29}$$

Cosmological observations, such as measurements of the CMB, allow us to infer the processes of large-scale structure formations, the distribution of galaxies, and the expansion rate of the universe. With their large abundance, neutrinos influence these processes and hence have to be taken into account. The neutrino density is given by

$$\Omega_\nu h^2 = \frac{\sum m_i}{93.14\,\text{eV}}, \tag{1.30}$$

with dimensionless Hubble parameter $h \equiv H_0/(100\,\text{kms}^{-1}\text{Mpc}^{-1})$ [260].[15] The effect of non-zero neutrino masses on the temperature spectrum C_ℓ^{TT} and the matter power spectrum $P(k)$ are depicted in figure 1.6.

The temperature spectrum of the CMB is measured for different polarisations (TT, TE, EE, TB, or BB), shown in the left panel of figure 1.6 is the influence on the TT polarisation mode over the multipole ℓ. The impact of the neutrino masses can be split into three regions. Increasing the neutrino masses results in a decrease of C_ℓ^{TT} for $\ell \lesssim 20$ due to changes in the late-time integrated Sachs-Wolfe effect (ISW) [156]. Influences of the neutrino masses to the pressure-to-density ratio of the universe become visible through the early ISW [156, 157], causing a reduction in the range of $20 \lesssim \ell \lesssim 200$. The oscillation patterns for $\ell \gtrsim 200$ are due to the effects of the neutrinos on the weak lensing induced by large-scale structures. [257, 260]

On the other hand is the influence on the matter power spectrum (right panel of figure 1.6). The neutrino masses affect the velocity dispersion in the universe due to their large free-streaming length. On large scales though, neutrinos cluster in similar ways as cold dark matter, contributing to the total background rather than density fluctuations [257]. The impact on $P(k)$ is shown for fixed Ω_b, Ω_c, Ω_Λ, where the dark matter density is adjusted

[15] Generally, densities are the ratio $\Omega_i \equiv \rho_i/\rho_{\text{crit}}$ with the critical density ρ_{crit}.

Table 1.2.: Overview over current limits on $\sum m_i$ from cosmology. The table shows the resulting limits when combining different datasets and likelihoods. This includes different polarisations of the Planck 2018 data, BAO data from BOSS, CMB lensing, and observation of 276 supernovae (Patheon). Combinations with lowℓ include multipoles with $\ell < 30$.

Datasets	**95 % C.L. limit**	**Ref.**
Planck18 (TT, lowℓ)	$< 0.54\,\mathrm{eV}$	[16]
Planck18 (TT, TE, EE, lowℓ)	$< 0.26\,\mathrm{eV}$	[16]
Planck18 (TT, TE, EE, lowℓ) + BAO	$< 0.13\,\mathrm{eV}$	[16]
Planck18 (TT, TE, EE, lowℓ) + BAO	$< 0.52\,\mathrm{eV}$	[245]*
Planck18 (TT, TE, EE, lowℓ) + Lensing	$< 0.24\,\mathrm{eV}$	[16]
Planck18 (TT, TE, EE, lowℓ) + BAO + Lensing + Patheon	$< 0.11\,\mathrm{eV}$	[16]
Planck18 (TT, TE, EE, lowℓ) + BAO + Lensing + Lyman-α	$< 0.11\,\mathrm{eV}$	[187]

*) In addition to the seven parameters in the ΛCDM+$\sum m_i$, the analysis accounts for the dark energy equation of state, the neutrino effective number, the running of the spectral index and the lensing amplitude [245].

along the neutrino density to keep the total dark matter density fixed (dashed lines in figure 1.6) [137, 158, 157]. In contrast, if the redshift of radiation-to-matter equality z_{eq} is kept fixed (solid lines), an increase of $\sum m_i$ is counteracted by an increase of h, resulting in a suppression of the large-scale power spectrum on the same order as the free-streaming effect, overall reducing the amplitude. The oscillation patterns are due to shifts of the baryon acoustic oscillations (BAO) scale [41].

In addition to the CMB temperature spectrum and the matter power spectrum, other cosmological observations can further constrain the neutrino mass. To name a view, there are measurements of BAO, the CMB lensing spectrum, supernovae surveys, and measurements of the Lyman-α forest.

Over the past 19 years, upper limits on $\sum m_i$ have shrunk by ~ 20. Table 1.2 summarises some of the current limits from cosmology. The Planck data is driving current cosmological constraints. The table also illustrates the many different possibilities of combining likelihoods, as well as the influence of additional free parameters in the fit. Despite the strong and competitive constraints given by cosmology, it has to be stressed that the results are strongly model dependent[16], highlighting the importance of model-independent laboratory experiments.

[16] Until today there are also unresolved issues in cosmology, such as the Hubble tension, which could imply physics beyond ΛCDM. The Hubble tension from direct and indirect determination is on the order of 5σ: $H_0 = (73.04 \pm 1.04)\,\mathrm{kms}^{-1}\mathrm{Mpc}^{-1}$ [202] compared to $H_0 = (67.4 \pm 0.5)\,\mathrm{kms}^{-1}\mathrm{Mpc}^{-1}$ [16].

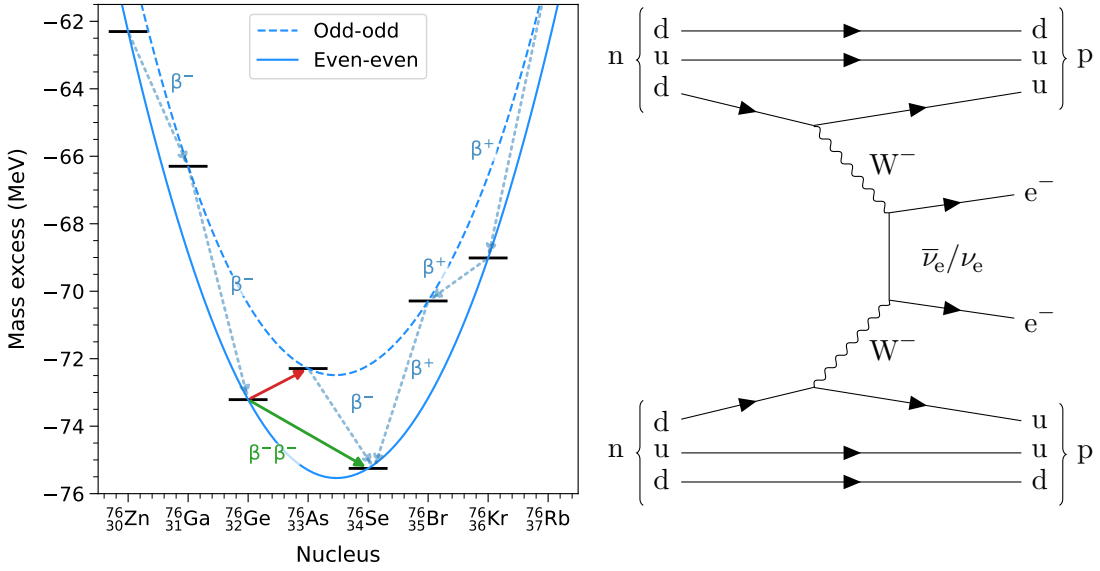

Figure 1.7.: (**Left**) Illustration of the ground state mass parabola for $Z = 76$. The dashed parabola connects all nuclei with an odd number of protons and an odd number of neutrons, the solid parabola connects nuclei with an even number of protons and neutrons. The shift of the odd-odd parabola is due to the nuclear pairing energy. In the case of ^{76}Ge, the decay into ^{76}As is energetically not allowed (red arrow). Only double β-decay of ^{76}Ge into ^{76}Se is allowed (green arrow). Mass excess data taken from [138]. (**Right**) Feynman diagram of the neutrinoless double β-decay. Two neutrons simultaneously decay by emitting two W^- bosons. Both of the W^- bosons decay into an electron (e^-) and an electron antineutrino ($\overline{\nu}_e$). The neutrinos absorbe each other. This process is only allowed if the neutrinos are Majorana particles ($\nu_e = \overline{\nu}_e$).

Neutrinoless double β-decay: Starting with the Bethe-Weizäcker formula, the binding energy of nuclei is calculated, resulting in a quadratic dependence of the binding energy to the proton number Z and $A = \text{const.}$.[17] The energy parabola determines the decay chain, striving for energetically preferred states. The parabolic shape of the binding energy is illustrated in the left panel of figure 1.7 for $A = 76$. The minimum of the parabola is the most stable nucleus for the respective Z.

The ordinary β-decay is a transition from nuclei with an odd number of protons and neutrons (odd-odd) to an even number of protons and neutrons (even-even) and vice versa (dashed blue arrows in figure 1.7). The single beta decay is a first-order weak interaction. Decays with an increase of Z are β^- decays, whereas decays where the proton number decreases are β^+ decays. The parabolas of odd-odd nuclei to even-even nuclei can be shifted to each other due to the nuclear pairing energy E_{Pairing}.

The possibility of simultaneous emission of two electrons from a nucleus was first discussed by M. Goeppert-Mayer in [118]. In the double β-decay ($2\nu\beta\beta$), two neutrons simultaneously

[17] The Bethe-Weizäcker formula is divided into five energy contributions:
$E_{\text{Binding}} = E_{\text{Volume}} - E_{\text{Surface}} - E_{\text{Coulomb}} - E_{\text{Asymmetry}} \pm E_{\text{Pairing}}$.

decay into two protons while releasing two electrons and two electron antineutrinos:[18]

$$(A, Z) \longrightarrow (A, Z+2) + 2\mathrm{e}^- + 2\overline{\nu}_\mathrm{e}. \tag{1.31}$$

In particular cases, the single β-decay is energetically forbidden since the binding energy of the daughter nucleus is higher (see red arrow in figure 1.7). In these cases, though, the transition with $\Delta Z = 2$ is energetically preferable (see green arrow in figure 1.7). The double β-decay is a second-order weak interaction. The $2\nu\beta\beta$ is a broad continuous electron spectrum.

Currently there are 35 known nuclei (such as ^{48}Ca, ^{76}Ge, ^{82}Se, ^{96}Zr, ^{100}Mo, ^{130}Cd, ^{130}Te, ^{136}Xe, and ^{150}Nd) able to decay via double β-decay, for 12 of these the double β-decay has been measured.

The idea of neutrinoless double β-decay ($0\nu\beta\beta$) was first published by G. Racah in 1937 [199]. A $0\nu\beta\beta$ is theoretically possible if neutrinos are Majorana particles ($\nu = \bar{\nu}$) [172]. Due to the Majorana nature, the neutrinos could consequently absorb each other, resulting in a β-decay where only electrons and protons are generated.

$$(A, Z) \longrightarrow (A, Z+2) + 2\mathrm{e}^-. \tag{1.32}$$

The corresponding Feynman diagram is shown in the right half of figure 1.7. $0\nu\beta\beta$ violates lepton number conservation by $\Delta L = 2$, which is prohibited in the Standard Model. Compared to $2\nu\beta\beta$, the energy spectrum of electrons is only a monoenergetic peak at the position of the Q-value. Furthermore, due to the small phase space, $0\nu\beta\beta$ is strongly suppressed.

In the last decades, several experiments[19] were designed to measure the neutrinoless double β-decay. In double β-decay experiments, the Majorana mass is determined from the half-life

$$\frac{1}{T_{0\nu\beta\beta}} = G_{0\nu\beta\beta} \cdot \left| M_{0\nu\beta\beta} \right|^2 \cdot \langle m_{\beta\beta} \rangle^2, \tag{1.33}$$

with the phase space factor $G_{0\nu\beta\beta}$ and the transition matrix element $M_{0\nu\beta\beta}$. The effective Majorana mass is given as the coherent sum of the mass eigenstates

$$\langle m_{\beta\beta} \rangle = \left| \sum_{i=1}^{3} U_{\mathrm{e}i}^2 m_i \right|. \text{ [204]} \tag{1.34}$$

Until today, no evidence for neutrinoless double β-decay has been observed [7, 18, 40]. Some of the current limits on the effective Majorana mass $m_{\beta\beta}$ from double β-decay experiments are

$$\text{GERDA } (^{76}\text{Ge}): \quad T_{0\nu\beta\beta} = 1.8 \times 10^{26}\,\text{y} \quad m_{\beta\beta} < (0.079 - 0.180)\,\text{eV} \quad [18], \tag{1.35}$$

$$\text{KamLAND-Zen } (^{136}\text{Xe}): \quad T_{0\nu\beta\beta} = 2.3 \times 10^{26}\,\text{y} \quad m_{\beta\beta} < (0.036 - 0.156)\,\text{eV} \quad [7], \tag{1.36}$$

$$\text{EXO200 } (^{136}\text{Xe}): \quad T_{0\nu\beta\beta} = 3.5 \times 10^{25}\,\text{y} \quad m_{\beta\beta} < (0.093 - 0.290)\,\text{eV} \quad [40]. \tag{1.37}$$

As the range of results already indicates, there is a strong dependence on the transition

[18] The same decay principle is also possible for two protons decaying into two neutrons, two positrons, and two electron neutrinos.

[19] Important experiments include the Heidelberg-Moscow experiment, GERDA, EXO, CUORE, and KamLAND-Zen.

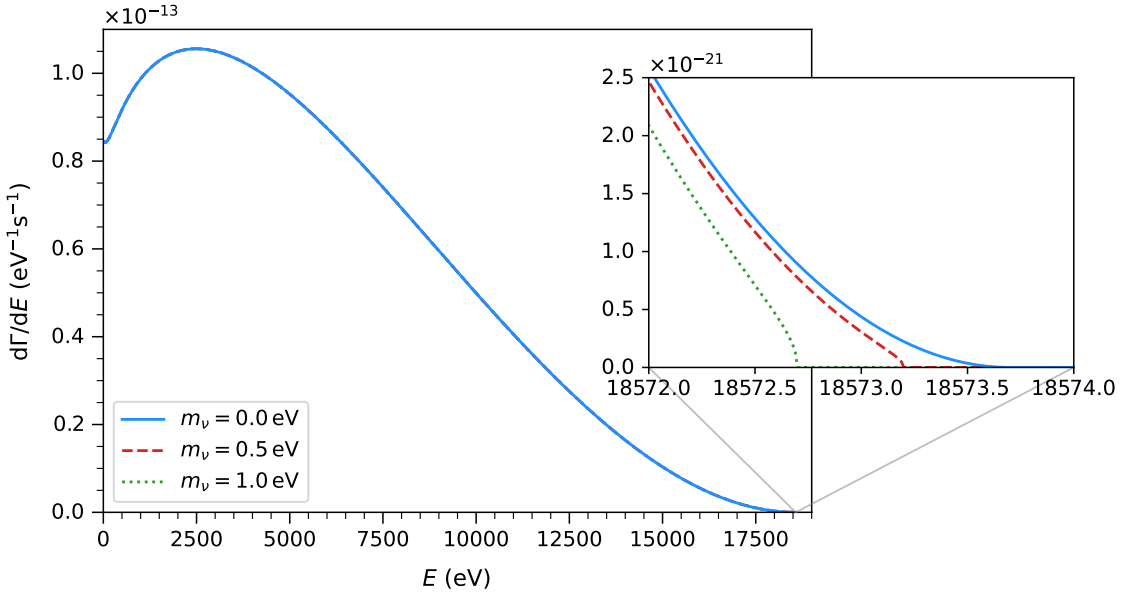

Figure 1.8.: Differential spectrum of the tritium β-decay. The neutrino mass mainly influences the spectral shape close to the endpoint. The plot illustrates the influence of three different neutrino masses.

matrix element $M_{0\nu\beta\beta}$, the phase space factor $G_{0\nu\beta\beta}$ and the connected theoretical uncertainties. This and the assumption of the Majorana nature of neutrinos underlines the strong model dependence of the results.

Single β-decay: A model-independent method to determine the neutrino mass is the kinematic measurement of the β-spectrum, by probing the spectral shape of the decay electrons close to the endpoint region. The corresponding decay Feynman diagram is shown in figure 1.1a. From the decay, the energy Q is distributed over the three decay constituents: the daughter nucleus, the electron, and the electron antineutrino. The daughter nucleus is recoiled with the energy E_{rec}, while the remaining energy E_0 is distributed over the electron and the neutrino

$$E_0 = Q - E_{\mathrm{rec}} = E_{\mathrm{e}} + E_{\overline{\nu}_{\mathrm{e}}}. \tag{1.38}$$

The neutrino hereby holds the energy

$$E_{\overline{\nu}_{\mathrm{e}}} = \sqrt{m_{\overline{\nu}_{\mathrm{e}}}^2 c^4 + p_{\overline{\nu}_{\mathrm{e}}}^2 c^2}. \tag{1.39}$$

Due to the non-zero rest mass of the neutrino, the energy remains $> 0.0\,\mathrm{eV}$ for $p_{\overline{\nu}_{\mathrm{e}}} = 0.0\,\mathrm{eVc}^{-1}$. This corresponds to the scenario where the electron carries the maximum momentum after the decay. The differential decay spectrum is well defined from theory (for more details, see chapter 3). The neutrino mass is manifested as a spectral distortion close to the endpoint. Figure 1.8 illustrates the impact of the neutrino mass on the differential spectrum of tritium. With larger neutrino masses, the spectrum is shifted by the neutrino mass, compared to the effective endpoint E_0 (in the case of tritium, the Q-value is 18.575 keV). The observable of the β-decay is the squared effective electron antineutrino mass m_ν^2, which is given by the incoherent sum of the squared neutrino mass

eigenstates

$$m_\nu^2 = \sum_{i=1}^{3} \left|U_{ei}\right|^2 m_i^2. \tag{1.40}$$

Tritium-based experiments such as the Mainz experiment, the Troitsk experiment and KATRIN use the MAC-E filter principle (more details in section 2.1) to measure the energy of the decay electrons. The Mainz experiment operated between 1991 and 2001. The Mainz collaboration was able to set an upper limit on the effective neutrino mass of $m_\nu < 2.3\,\text{eV}$ (90 % C.L.) [151]. The Troitsk experiment operated around the same time. From ten years of data taking (between 1994 and 2003), the collaboration set an upper limit of $m_\nu < 2.05\,\text{eV}$ (95 % C.L.) [46]. The KATRIN experiment was designed to reach a sesitivity of 0.2 eV at 90 % C.L.. As a successor experiment, KATRIN started data taking in 2018 and is currently in operation. From the first neutrino mass campaign, the previous limit was improved by almost a factor of two, setting an improved upper limit down to $m_\nu < 1.1\,\text{eV}$ (90 % C.L.) [22]. Combining the first two datasets yeilded a sub-eV limit of $m_\nu < 0.8\,\text{eV}$ (90 % C.L.) [25]. By combining the first five neutrino mass campaigns, the data provides even stronger constraints on the neutrino mass. The results are presented as part of this thesis (see section 6.3). The KATRIN experiment is currently giving the most stringent model-independent results for the neutrino mass.

Alternative to measurements of the β-decay spectrum tritium spectrum are measurements of the spectrum of electron capture. Measurements are based on ^{187}Re or ^{163}Ho. Both materials have small Q-values.

$$^{187}\text{Re} \longrightarrow {}^{187}\text{Os} + \text{e}^- + \overline{\nu}_\text{e} \qquad Q = 2.47\,\text{keV}\ [86], \tag{1.41}$$

$$^{163}\text{Ho} + \text{e}^- \longrightarrow {}^{163}\text{Dy} + \nu_\text{e} \qquad Q = 2.83\,\text{keV}\ [200]. \tag{1.42}$$

The setup is based on high-resolution microcalorimeters, where the embedded material functions simultaneously as the source and detector material. Also here, the neutrino mass can be determined from the spectral shape close to the endpoint, which is measured with microcalorimeters.[20] Experiments applying the principle are, for example, MIBETA, HOLMES, ECHo and MARE. The current limits based rhenium is $m_\nu < 15\,\text{eV}$ [86]. Holmium-based experiments were so far not able to set competitive limits.

The Project8 collaboration plans to measure the β-spectrum using the Cyclotron Radiation Emission Spectroscopy (CRES) technique in combination with an atomic tritium source. Decay of tritium in its atomic form within a cold trap avoids additional broadening of the spectrum due to the final state distribution (see section 3.3). Project8 is currently in the research and development phase, with the aim of reaching a sensitivity of 0.04 eV, which could probe the parameter space down to the inverted hierarchy [96]. The first frequency-based limit from demonstration measurements with the CRES method are $m_\nu < 155\,\text{eV}$ [97].

[20] In the case of the electron capture in holmium, the electron capture results in a subsequent de-excitation, by emission of an Auger electron or an X-ray photon. As the source material is embedded within an absorber, the emitted Auger electron or X-ray causes an increase in temperature. This temperature change can be measured with, for example, a transition-edge sensor (in the case of HOLMES) or a superconducting quantum interference device (SQUID) (in the case of ECHo as a magnetic microcalorimeter) [114, 184].

1.6. eV-scale sterile neutrinos

With the neutrino minimal extension of the Standard Model (νMSM), sterile neutrinos can be introduced to the standard model, allowing active neutrinos to possess non-vanishing masses. The most simple extension is the introduction of one additional neutrino mass eigenstate ν_4 and a sterile neutrino ν_N,

$$\begin{pmatrix} \nu_\mathrm{e} \\ \nu_\mu \\ \nu_\tau \\ \nu_N \end{pmatrix} = \begin{pmatrix} U_{\mathrm{e}1} & U_{\mathrm{e}2} & U_{\mathrm{e}3} & U_{\mathrm{e}4} \\ U_{\mu 1} & U_{\mu 2} & U_{\mu 3} & U_{\mu 4} \\ U_{\tau 1} & U_{\tau 2} & U_{\tau 3} & U_{\tau 4} \\ U_{N1} & U_{N2} & U_{N3} & U_{N4} \end{pmatrix} \cdot \begin{pmatrix} \nu_1 \\ \nu_2 \\ \nu_3 \\ \nu_4 \end{pmatrix}. \tag{1.43}$$

The sterile neutrino would mix (with a small fraction) with the other neutrino mass eigenstates. This would leave an imprint visible in the β-spectrum (for more details, see section 3.1).

Sterile neutrinos in different mass scales can help to solve different inconsistencies in particle physics and cosmology. To explain the small neutrino masses (as introduced in the (type-I) seesaw mechanism), the additional right-handed sterile neutrinos would need to have a mass comparable to the GUT scale. Sterile neutrinos in the GeV range, would act as a form of cold dark matter. If the mass of sterile neutrinos is on the keV scale, they could significantly contribute to the dark matter content in the universe as warm dark matter. This additional warm dark matter would be able to solve tensions on small cosmological scales and resolve the missing satellite problem [15, 169]. The third mass region is sterile neutrinos in the eV range. The search for eV scale sterile neutrinos is well motivated by long-standing anomalies in short-baseline neutrino oscillation experiments and in solar neutrino experiments.[21]

In the following, the current status of the eV-scale sterile neutrino search will be summarised. Different anomalies in this mass range have given rise to controversy in the past.

The first observations of anomalies were in short-baseline oscillation measurements (∼30 m) for the appearance of $\overline{\nu}_\mathrm{e}$ from a $\overline{\nu}_\mu$ beam by LSND in the 1990s. In the analysis, they found a $3.8\,\sigma$ excess of $\overline{\nu}_\mathrm{e}$ pointing towards a sterile neutrino in the eV range [20]. Testing the same region, MiniBooNE found an excess in a similar region [21]. Subsequent experiments such as KARMEN and NOMAD did not observe any signal and were able to exclude regions of the favoured parameter space [44, 47].

Independently, indications for sterile neutrinos were observed in 2011 in short-baseline (<100 m) reactor experiments known as the RAA [177]. Comparing evaluations of the expected reactor flux showed a lack of ν_e with $2.5\,\sigma$. In 2021 the $\overline{\nu}_\mathrm{e}$ flux model was again revisited, with additional fission spectra of ^{235}U and ^{239}Pu. These measurements showed a ∼5 % reduction in the expected flux, more compatible to previous observations [150]. The significance of the RAA is decreasing down to $1.1\,\sigma$ when comparing the flux to the re-evaluated model [116].

The solar neutrino experiments Gallium-Experiment (GALLEX) and SAGE were designed to measure the solar neutrino flux via the inverse β-decay on gallium.[22] During calibration measurements of both experiments (measurements with ^{51}Cr in GALLEX and

[21] Exclusion contours or claimed signals of most of the experiments listed here are shown in section 6.4.3.3.
[22] The neutrino capture results in $^{71}\mathrm{Ga} + \nu_\mathrm{e} \rightarrow {}^{71}\mathrm{Ge} + \mathrm{e}^-$.

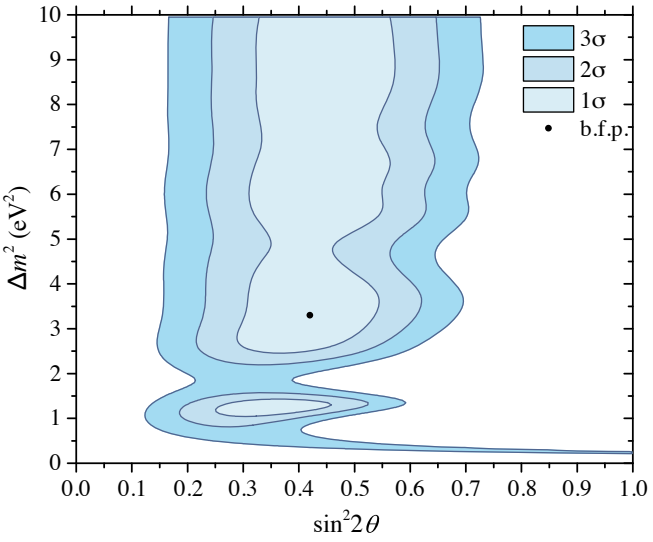

Figure 1.9.: Results from the BEST experiment. The oscillation measurements show a preference for sterile neutrinos with a best fit at $\Delta m^2_{41} = 3.3\,\mathrm{eV}^2$ and a mixing of $|U_{e4}|^2 = \sin^2(2\theta) = 0.42$. The measured region affirms previous observations by GALLEX and SAGE. Figure taken from [53].

measurements of ^{51}Cr and ^{37}Ar in SAGE) a lack of ν_e was measured [122, 123, 3]. Also here, the deficiency can be interpreted as additional mixing with a sterile neutrino. The SAGE experiment was upgraded in 2014 (now called BEST), to perform very-short-baseline ($\mathcal{O}(1\,\mathrm{m})$) neutrino oscillation measurements. Also the most recent results released by BEST in 2022 show a preffered region with $3\,\sigma$ in the range $> 1\,\mathrm{eV}^2$ [53], reaffirming the GA. The BEST contour is shown in figure 1.9.

Analysis of the data measured by the Neutrino-4 experiment claim to have measured a sterile neutrino with $2.9\,\sigma$ [228, 229]. Combining three datasets, the best fit was found for $\Delta m^2_{41} = 7.3\,\mathrm{eV}^2$ and of $\sin^2(2\theta) = 0.36$ [229]. The 2021 published analysis [229] surrounds a slightly wider region compared to [228]. The Neutrino-4 results are seen as the most controversial as it is partially already disfavoured by other experiments. Other publications have, for example, critiqued the negligence of efficiencies and Wilks' theorem [79].

In addition to the aforementioned experiments that have measured anomalies, there are also many short-baseline oscillation experiments that have not observed any signals. Experiments such as DANSS [80], Daya Bay [12], Double Chooz [9], PROSPECT [38], and STEREO [34, 35] were able to exclude regions with small Δm^2_{41} and large $\sin^2(2\theta)$.

Measurements of the β-decay provide the unique possibility to measure the active neutrino mass and search for sterile neutrinos. Theoretically, sterile neutrinos with masses up to 18.6 keV can be measured. The Mainz and Troitsk experiment were both able to exclude regions of the sterile parameter space for large masses and large mixing angles [59, 152]. In the same way, measurements of the tritium spectrum with KATRIN allow one to search for sterile neutrinos. The sterile neutrino exclusion contours of the first two KATRIN campaigns are published in [24, 26] and will be described in more detail as part of this thesis (see section 6.4).

2. The KATRIN exeriment

The KArlsruhe TRItium Neutrino experiment (KATRIN) is currently the most precise approach for direct neutrino-mass measurements. It is designed to measure the signature of the neutrino mass in the β-decay spectrum of tritium with high accuracy. The experimental setup combines a high-activity tritium source and a spectrometer of the magnetic adiabatic collimation with electrostatic (MAC-E) filter type. The main spectrometer is optimised to measure the β-electron spectrum close to the tritium endpoint with a high energy resolution. In the subsequent sections, the general working principle of KATRIN is outlined (section 2.1), followed by a description of the experimental setup (section 2.2). In the subsections of section 2.2, individual subsystems of the KATRIN beamline are explained in more detail. A full in-depth description of the KATRIN experiment can be found in [31, 39].

2.1. The MAC-E filter principle

Based on the work of Beamson et al. [54] and Kruit et al. [153], the MAC-E filter concept was originally introduced for the purpous of neutrino-mass measurement by Lobashev et al. in 1985 [162] and Picard et al. in 1992 [192]. The working principle of a MAC-E filter is based on a combination of magnetic and electric fields, functioning as a high-pass filter for charged particles. A schematic illustration of the working principle of the spectrometer is given in figure 2.1. Two superconducting solenoids generate a strong magnetic field on either end of the spectrometer vessel. In addition, an electric retarding potential is evoked by the vessel and the electrode system lining the inside of the vessel. The magnetic field strength is the smallest in the analysing plane[1] B_{ana} between the superconducting solenoids, increasing in both directions towards the solenoids. Due to the conservation of magnetic flux Φ by about four orders of magnitude,

$$\Phi = \int_A \vec{B} \cdot \mathrm{d}\vec{A} = \text{constant}, \tag{2.1}$$

the flux tube widens to its maximum between the magnets while reducing the magnetic field strength to its minimum value. The maximal electric potential U_{max} is present in the analysing plane, decreasing to either side to $U = 0\,\mathrm{V}$. Electrons are guided along the magnetic field lines, and the electrons' longitudinal energy $E_{\parallel} = p_{\parallel}^2/2m$ is filtered with the opposing retarding potential. To maintain magnetic guidance, the magnetic field strength decreases adiabatically to as small value $B_{\mathrm{ana}} \to 0\,\mathrm{T}$ in the analysing plane. [120, 39]

[1] The analysing plane is usually located near the centre of the spectrometer vessel. It describes the region where the flux tube is widened to its largest diameter. Here the magnetic field is at its minimum, and the electric potential is at its maximum.

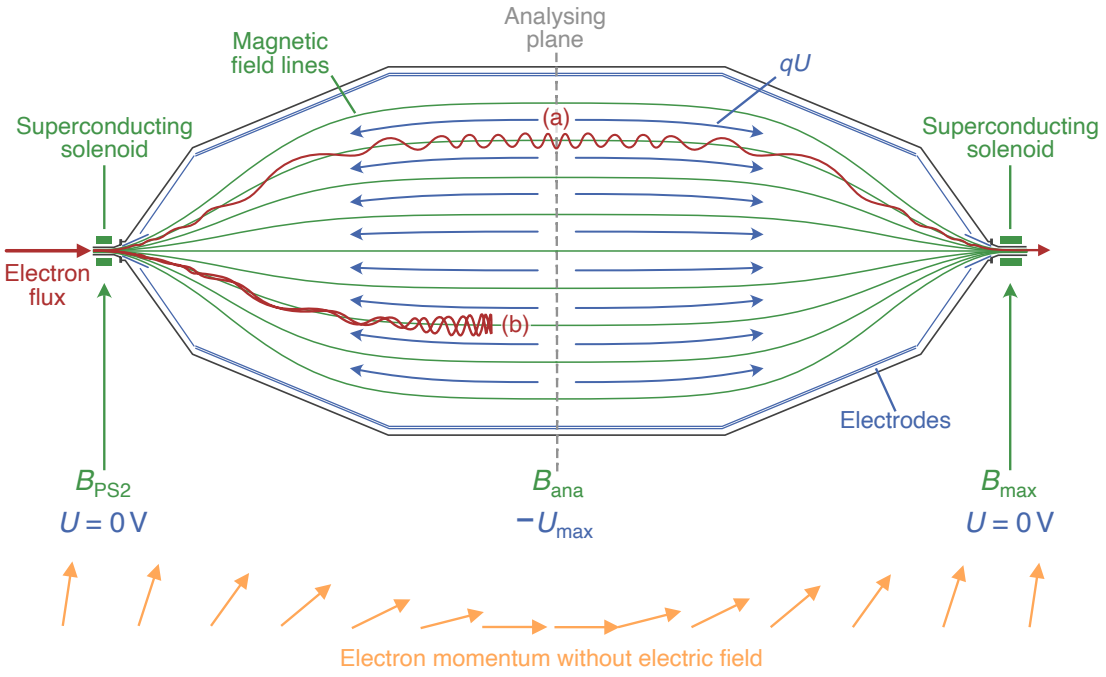

Figure 2.1.: Illustration of the working principle of a MAC-E filter. Superconducting magnets are located on both ends of the spectrometer, creating the stray magnetic field lines inside the vessel (green). Electric field lines are generated in parallel to the magnetic field lines by electrodes on the vessel's inner wall (blue). Electrons are guided in a cyclotron motion (red) along magnetic field lines. Those with an energy higher than the retarding energy are transmitted (a), while electrons with a lower energy are reflected (b).

Electrons with longitudinal energies larger than the retarding energy are transmitted, whereas electrons with lower energy are decelerated and reflected. The specific advantage of the MAC-E filter system is the collimation of transversal into longitudinal energy, allowing for a large angular acceptance[2] and high energy resolution at the same time.

In general, charged particles such as electrons in a magnetic field are guided along the field lines in a cyclotron motion. The total kinetic energy can therefore be described as the sum of an energy component in parallel $E_{\parallel}$ and an energy component transversal $E_{\perp}$ to the magnetic field lines,

$$E_{\mathrm{kin}} = E_{\perp} + E_{\parallel}. \tag{2.2}$$

Hence, the pitch angle of the electron relative to the field line is given by

$$\sin^2(\theta) = \frac{E_{\perp}}{E}. \tag{2.3}$$

The maximum longitudinal kinetic energy is reached when $E_{\perp} = 0\,\mathrm{eV}$. If the magnetic field B decreases adiabatically along the flightpath, the electron experiences a magnetic gradient force

$$\vec{F} = -\vec{\nabla}\left(\vec{\mu}\cdot\vec{B}\right), \tag{2.4}$$

[2] This is in particular important in the KATRIN experiment, since electons are emitted isotropically in the source.

with the magnetic moment

$$\mu = \frac{E_\perp}{B}. \tag{2.5}$$

The gradient force converts the transversal energy component into the longitudinal direction, under the prerequisite that the relative changes of the magnetic field are small in comparison to the cyclotron motion of the electron. [192]

Throughout the process, the adiabatic conversion, the product of the relativistic Lorentz factor γ and the magnetic moment is conserved ($\mu \cdot \gamma = \text{const.}$) [128]. For electrons close to the tritium endpoint (18.6 keV), the Lorentz factor is $\gamma = 1.04$. The collimation effect of the gradient magnetic field yields a high energy resolution for β-electrons with isotropic emission properties. The energy resolution of the system is limited by the non-vanishing magnetic field strength in the analysing plane and the maximum magnetic field of the setup, resulting in a small remaining transversal energy component that is not filtered by the retarding field. The energy resolution of the system is given by

$$\frac{\Delta E}{E} = \frac{B_{\text{ana}}}{B_{\text{max}}} \cdot \frac{\gamma + 1}{2}. \tag{2.6}$$

From the analysing plane towards the maximum magnetic field B_{max} at the outlet of the vessel, the momentum is converted back into the transversal component $E_\perp$, thus increasing the pitch angle. For large starting angles, $\theta \to 90°$, an increasing magnetic field results in a backreflection of electrons. The maximum acceptance angle θ_{max} is given by

$$\theta_{\text{max}} = \arcsin\left(\sqrt{\frac{B_{\text{src}}}{B_{\text{max}}}}\right) \text{ [153]}, \tag{2.7}$$

where B_{src} corresponds to the source magnetic field seen by the electrons when emitted in the tritium β-decay. [147]

In the KATRIN experiment, with $B_{\text{src}} = 2.51\,\text{T}$ and $B_{\text{max}} = 4.24\,\text{T}$, this leads to a maximum acceptance angle of $\theta_{\text{max}} = 50.30°$.

2.2. Experimental setup of the KATRIN experiment

In this section, the individual system components of KATRIN and their functions are described, focusing on the components relevant for neutrino-mass measurements. The 70 m long KATRIN experiment is located at Tritium Laboratory of the Karlsruhe Institute of Technology (KIT). The experimental setup, as illustrated in figure 2.2, can be subdivided into two major sections: the source and transport section (STS) and the spectrometer and detector section (SDS).

The STS comprises the windowless gaseous tritium source (WGTS) in the centre, where molecular tritium decays. Towards the spectrometer side, the WGTS is connected to the pumping section, which evacuates residual gas and ions and guides β-electrons through the beamline. The pumping section itself consists of a differential pumping section (DPS) and a cryogenic pumping section (CPS). To the rear side, the WGTS is connected to the rear section (RS), which houses monitoring and calibration systems.

The SDS, on the other hand, serves to determine and measure the emitted electrons' energy. This section combines a setup of three spectrometers and a detector system. The

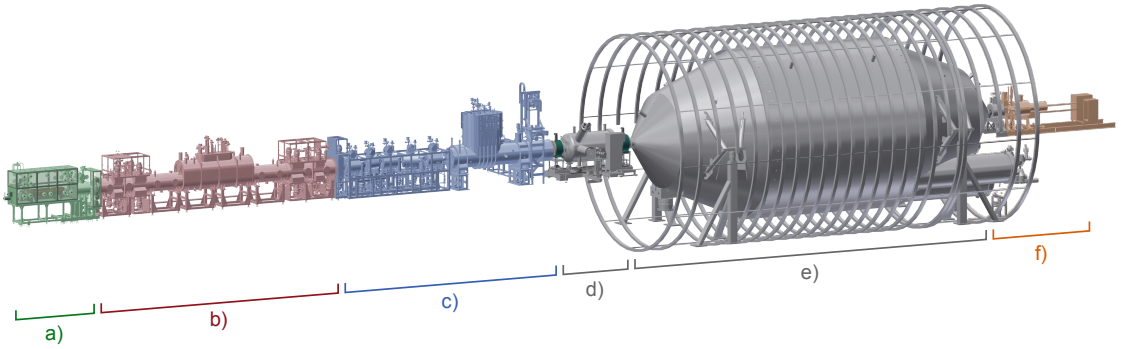

Figure 2.2.: Overview of the 70 m long KATRIN beamline. The KATRIN experiment is subdivided into different sections. The source and transport section (STS) consists of: a) the rear section (RS), b) the windowless gaseous tritium source (WGTS), c) a transport section containing the cryogenic pumping section (CPS) and differential pumping section (DPS). The spectrometer and detector section (SDS) consists of: d) the pre-spectrometer (PS), e) the main spectrometer (MS), and f) a detector system including the focal plane detector (FPD). β-decay electrons are emitted in the WGTS and guided along magnetic field lines towards the main spectrometer, where their energy is analysed. Electrons with high enough surplus energies are then counted at the detector system.

smaller pre-spectrometer (PS) is connected subsequent to the transport section, followed by the large main spectrometer (MS), which functions as a highpass filter for the β-decay electrons. The end of the beamline is constituted by the detector system, with the focal plane detector (FPD) as its core component. In parallel to the main spectrometer, an additional third spectrometer is coupled to the main spectrometer. This spectrometer can be used for high voltage monitoring and further functions as an additional test setup for future developments.

Hereafter the direction from the WGTS towards the FPD is denoted as downstream, and the direction from the FPD towards the WGTS as upstream.

2.2.1. Source and Transport Section

In the following subsections, the components of the STS are described in more detail. The STS is located inside the Tritium Laboratory Karlsruhe (TLK) to provide tritium handling and fulfil safety requirements. Components which are supplied with tritium are surrounded by negatively pressurised glove boxes to provide a two-stage containment system. Located in the centre of the STS is the WGTS, providing the KATRIN experiment with a high luminosity tritium source, needed to probe the endpoint region of the tritium spectrum (see section 2.2.1.1). Subsequent to the WGTS, pressure is reduced by 14 orders of magnitude. This is achieved by differential and cryogenic pumping sections (see section 2.2.1.3). In addition, the STS contains monitoring and calibration systems, both in the rear section and transport section, to calibrate the experimental setup (see section 2.2.1.2). In general, the beam tube on the STS side is grounded, so all electrons start at the similar potentials (close to 0 V).

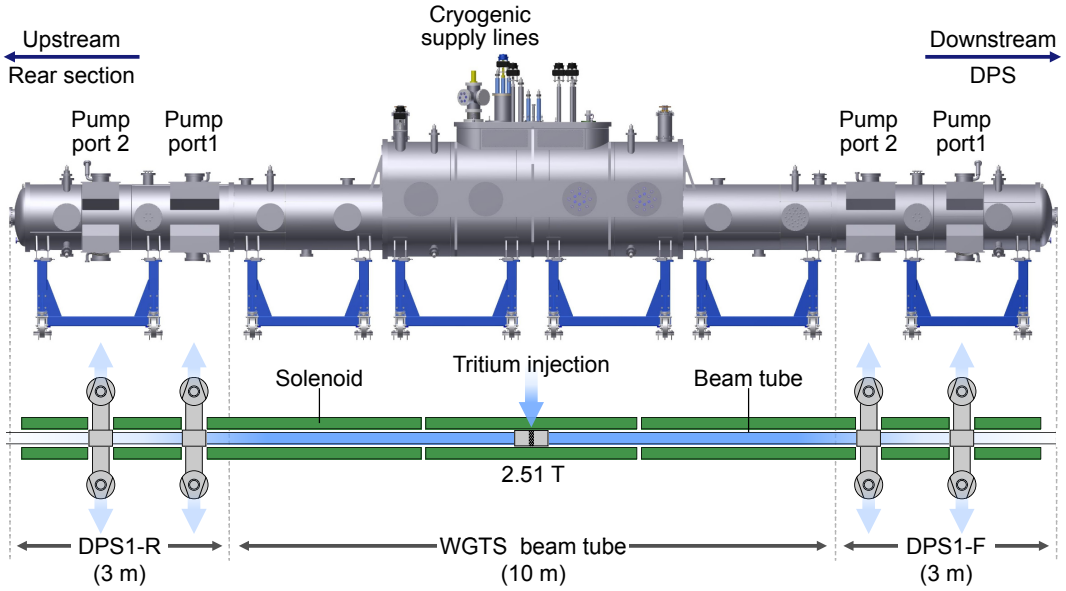

Figure 2.3.: Computer-aided design (CAD) drawing of the WGTS. Gaseous tritium is injected through capillaries into the centre of the source, diffusing towards both sides. Tritium is pumped out at each end with turbo-molecular pump (TMP)s (DPS1-R and DPS1-F), each connected to the beamline with two pump ports. The 10 m long central section of the WGTS is cooled by a two-stage neon cooling system, keeping the source temperature below 100 K. Figure adapted from [126].

2.2.1.1. Windowless gaseous tritium source

One of the most important core components in KATRIN is the WGTS. Within the source, tritium decays isotropically into helium, an electron, and an electron antineutrino:

$$T_2 \rightarrow THe^+ + e^- + \overline{\nu}_e. \tag{2.8}$$

A graphical representation of the WGTS is given in figure 2.3. Within the centre of the WGTS, inside a 10 m long and 90 mm in diameter beam tube, molecular gaseous tritium provides the experiment with a β-electron flux of 10^{11} Bq. The stainless steel beam tube is encapsulated by a 16 m long cryostat, containing a two-phase neon cooling system. To be maximally sensitive to the imprint of the neutrino mass, the requirements of the source are high throughput, high purity and stability, as well as small and well-understood systematic effects. [39]

The WGTS has to be operated with a temperature < 100 K to achieve a low beam tube conductance, allowing for an increased amount of tritium in the source. In addition, to achieve a sufficient amount of decays, a daily throughput of 40 g of molecular tritium is required [31]. Temperatures below 100 K furthermore have the advantage of less Doppler broadening of the tritium spectrum. In neutrino-mass measurements, the source is typically operated at 30 K or 80 K with a stability on the sub per mille level [175].

The WGTS is a system open to both ends (windowless), preventing energy losses of the β-electrons due to scattering. With an injection pressure of 3 µbar, gas is continuously injected through capillaries into the axial centre of the source tube flowing to each end. The injection

pressure stability of 0.0038 % exceeds the design stability of 0.1 %. Continuous injection allows for a nominal column density[3] ρd of $5 \times 10^{21}\,\mathrm{m}^{-2}$ at a beam tube temperature of 30 K. [175]

Connected to the WGTS is the loop system[4], continuously supplying the source with a stable amount of tritium [196, 197, 198]. Within the loop system, partially decayed tritium gas is purified and replaced. The system can maintain a constant tritium purity of $> 98\,\%$ throughout operation. As part of the inner loop system, the laser Raman spectroscopy system (LARA) continuously monitors the gas composition. Utilising the laser Raman spectrometer allows determination of the tritium purity as well as the ratio of the main impurities – HT and DT [141, 218].[5]

At each end of the WGTS, the beam tube is connected to a 3 m long pumping section. Each section, namely DPS1-R and DPS1-F, is connected to a TMP via two pump ports. These primary pumping sections reduce the pressure in a first step by $> 99.9\,\%$. Tritium gas that has been pumped out from these sections is reinjected into the inner loop system and recycled back into the source.[175]

Seven superconducting magnets are arranged along the WGTS beam tube length, with the beam tube itself in the centre of the warm bore of the seven superconducting magnets. The magnets generate a magnetic field of 2.51 T inside the beam tube. β-decay electrons emitted into downstream direction are consequently magnetically guided through the source towards the transport section (see section 2.2.1.3). Electrons emitted in the upstream direction are guided towards the rear wall (see section 2.2.1.2).

2.2.1.2. Rear section

The rear section (RS) is located at the upstream end of the KATRIN beamline. The 3.5 m long rear section contains three major components – the rear wall, the beta induced X-ray spectroscopy (BIXS) detector, and an electron-gun (e-gun) – which are described more in detail in the following. A graphical overview of the rear section is given in figure 2.4.

The rear wall is a 14.6 cm in diameter gold-coated stainless steel disc, which defines the physical termination of the flux tube. In addition, a 5 mm hole in the centre allows electrons from the e-gun to pass through into the WGTS. The rear wall is located in front of the rear section magnet, which is operated at 4.0 T, itself experiencing a magnetic field of 1.23 T. [31]

Electrons in the source that are emitted in upstream direction or are back reflected in the mainspectrometer are guided towards the rear wall and eventually terminated on the rear wall surface. As the rear wall is exposed to gaseous tritium, the surface is coated in gold, providing chemically inert behaviour with tritium [48]. Furthermore, gold provides a temporally stable work function Φ_{RW} [226]. Within the source, a low-density plasma is generated by ionisation of neutral gas molecules, such as T_2, with β-decay electrons,

[3] The column density, ρd, refers to the number of molecules per area when integrating over the source length.

[4] The tritium loop system of the TLK provides the KATRIN experiment with a constant stable supply of tritium. It is structured in a so-called inner loop and outer loop. The inner loop directly circulates tritium through the WGTS. The outer loop is connected to the TLK infrastructure and allows the injection and exhaustion of gas from the inner loop. [175]

[5] The laser Raman system not only measures tritium-related concentrations, but the general composition of the source.

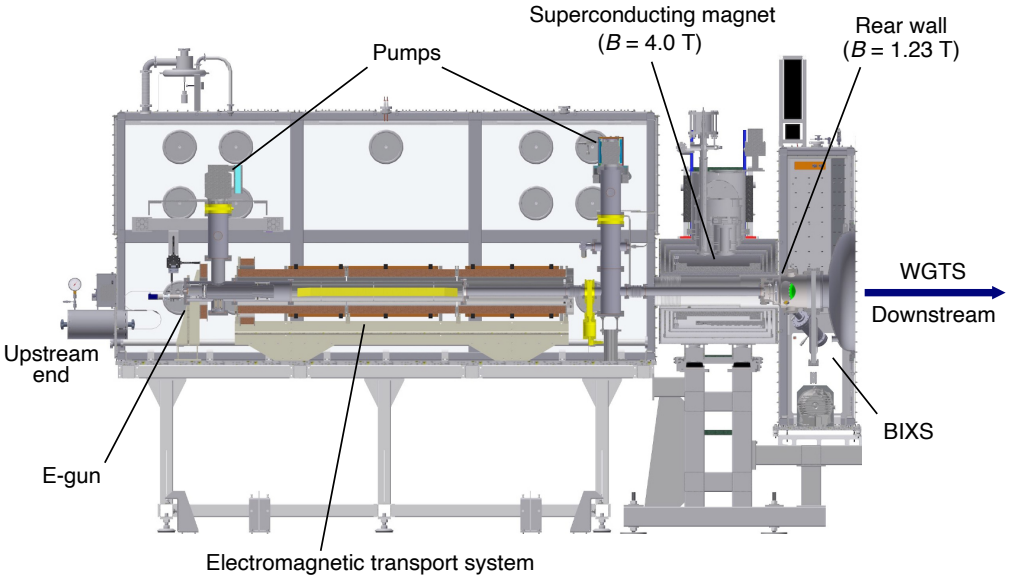

Figure 2.4.: Overview of the KATRIN rear section. The rear section is connected to the upstream end of the WGTS. The rear wall physically terminates the magnetic flux tube. Characteristic X-rays emitted from the rear wall are measured by the BIXS detector system to monitor the source activity. The rear section further contains an e-gun which can generate a quasi-monoenergetic pencil beam. Drift fields within the electromagnetic transport system allow for electron energies up to 21 keV. Figure adapted from [31].

resulting in free charges. The presence of a plasma changes the initial starting potential of β-electrons when generated. As the plasma can have radial or longitudinal variation, the initial electron energy can depend on its location when being generated. [154, 171]

The magnetic flux, which directly maps to the rear wall, couples the source plasma to the rear wall and defines the ground potential of the cold plasma. To improve longitudinal and radial plasma inhomogeneities, both the rear wall and the stainless steel beam tube can be biased externally [154]. For the reduction of longitudinal plasma effects, the rear wall voltage is optimised to provide the best possible coupling conditions.

The total β-decay electron flux from the source, seen by the rear wall, is approximately $10^{11}\,\mathrm{e}^{-}/\mathrm{s}$. Electrons penetrating the rear wall surface emit a characteristic X-ray line spectrum. Utilising the X-ray spectrum of these electrons, the relative source stability can be monitored. The BIXS detector system measures these X-rays continuously with a precision of 0.1 % in 100 s intervals [31]. The system consists of two X-ray sensors that are located in two pump ports, branching off-axis from the rear wall chamber. Each of the X-ray sensors is located behind a gold-coated beryllium window. The beryllium windows shield the sensors from residual gas, preventing tritium contamination.

The third component, the so-called electron-gun (e-gun), is a high-resolution angular selected, quasi-monoenergetic photoelectron source. The e-gun produces a pencil beam with a diameter of 60 µm that is used for calibration measurements along the entire beamline, such as measuring magnetic fields, the source column density, or the energy loss characteristics within the source. [28, 65, 216]

To generate the photoelectrons, UV light is coupled into a 200 µm thick optical fibre, whose

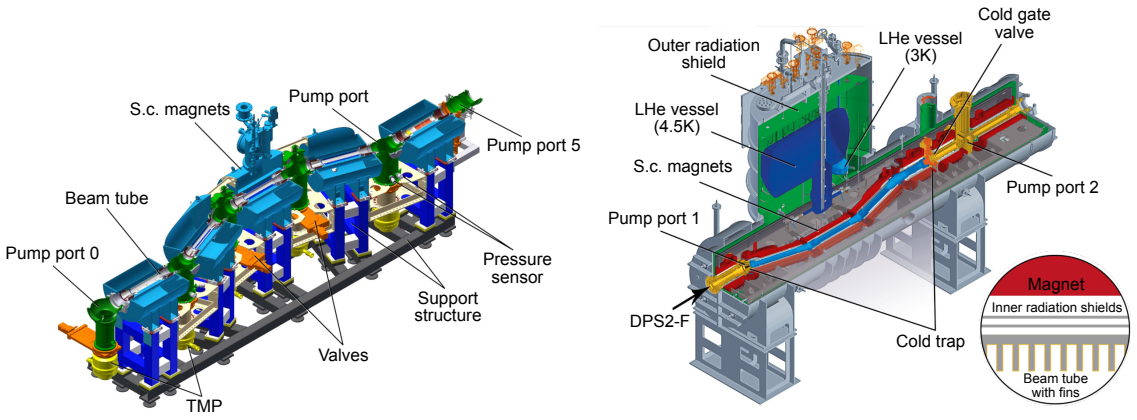

(a) DPS2-F. **(b)** CPS.

Figure 2.5.: (a) CAD model of the differential pumping section DPS2-F, which is connected to the differential pumping section DPS1-F of the WGTS. (b) CAD model of the cryogenic pumping section CPS. With both DPS and CPS it is possible to reduce the pressure by a factor of 10^{14} in comparison to the pressure inside the WGTS. A more detailed description of the sections and their components is given in the text. Figures adapted from [109].

end is coated with a 30 nm gold layer [58]. This layer functions as the photocathode. The electrons are emitted between two 10 cm round capacitor plates that are spaced 10 mm apart. An applied voltage between the plates accelerates the electrons towards the front plate. The electrons can then exit through a 6 mm hole in the centre of the front plate. In order to change the pitch angle of electrons to the magnetic field lines, both capacitor plates can be tilted. Subsequent to the initial acceleration, electrons are further accelerated by a cascade of cylinder electrodes to up to 21 keV. The e-gun setup in this configuration is able to produce an electron rate of up to 10^4 counts per second (cps). [28]

2.2.1.3. Transport section

Connected to the downstream end of the WGTS is the transport section. The main task of the transport section is to adiabatically guide β-decay electrons from the source towards the spectrometer section, while further reducing the amount of residual gas, as well as blocking ions. The transport section reduces the pressure to an ultra-high vacuum in a two-stage approach. First is a differential pumping section, followed by further pressure reduction via cryogenic pumping. Combining both, a pressure lower than 10^{-11} mbar can be achieved with a maximum partial tritium pressure of 10^{-20} mbar. The ultra-high vacuum vacuum is requiered for a loss free tranport of electrons.

The differential pumping section (DPS) refers to the second stage differential pumping section (DPS2-F) connected to the first stage DPS1-F as part of the WGTS. A graphical representation of the DPS is given in figure 2.5a. The DPS beam tube is split into five sections. The central three segments are tilted by 20° to each other, oriented in a chicane configuration. Each of the five segments is located inside the bore of superconducting magnets. Charged particles are guided along the magnetic field lines, while neutral gas scatters with the walls and is pumped out. There are five pump ports located between

the WGTS and the DPS and between the superconducting magnets. Connected to each of the pump ports are TMPs evacuating residual gas. The TMPs reduce the pressure by five orders of magnitude. The evacuated gas is recirculated into the outer loop system[6]. Charged particles are guided along magnetic field lines. Therefore only neutral gas will scatter with the beam tube walls and is pumped out through the pump ports. Positive ions such as He^+ from the β-decay are unaffected by the differential pumping and remain in the magnetic flux tube. In order to block magnetically guided ions, a system of dipole electrodes and a ring electrode are installed inside the beam tube. The dipole electrodes utilise the $(\vec{E} \times \vec{B})$-drift of ions towards the inside of the beam tube. As the mass of electrons is much smaller, they are less affected by the drift inside the electrodes. In addition, a ring electrode is installed at the end of the DPS, which is set to a 100 V positive blocking potential. [31, 149]

The cryogenic pumping section (CPS) is located downstream from DPS. As TMPs undergo back-diffusion in the pumps, they are not sufficient to further reduce the pressure following the DPS. The 7 m long CPS is therefore designed to utilise cryosorption of tritium molecules to further reduce the tritium flow in downstream direction. It is designed to reduce the pressure by seven orders of magnitude. A graphical representation of the CPS is given in figure 2.5b. The beam tube is subdivided into seven sections, each surrounded by a superconducting magnet. The superconducting magnets allow for adiabatic transport of electrons into the spectrometer section. In addition, the CPS contains two pump ports, where the second pump port includes an additional port open to the forward beam monitor (FBM) (see section 2.2.1.4) and a condensed krypton source. The inside of each of the beam tube segments is coated with gold, as it is chemically inert with tritium. Similar to the DPS, the second, third, and fourth segments are each tilted by 15° to each other, forming a chicane[7] and increasing the probability of collisions of neutral gas molecules with the beam tube walls. Segments 2 to 5 are operated as a cold trap, cooled by liquid helium to 3 K. Furthermore, an argon frost layer is prepared on the inside of the beam tube walls, increasing the surface and hence the adsorption probabilities of gas molecules. The 3 K environment, on the other hand, increases the desorption time of molecules. To additionally increase the wall surface by a factor of three, the insides of beam tube sections 2-4 are covered with 90 2 mm long fins. Over time the argon frost layer accumulates tritium and, when saturated, is regenerated. To regenerate the condensed gas layer, the CPS is warmed up to 80 K. Next, the contaminated argon is pumped out, followed by a purging cycle with helium. After this, a new condensed argon layer is prepared on the walls, with full cryogenic pumping capacity. The regeneration is required roughly every 60 days during operation of continuous tritium circulation. [31, 208]

2.2.1.4. Foraward beam monitor

The forward beam monitor (FBM) system is designed to continuously monitor the source activity. The aim is to measure the source activity with a precision of 0.1 % on a 60 s time scale [39]. The FBM system is connected to pump port 2 of the CPS. It is attached to a movable arm inside a 2 m bellow. The detector board can be inserted into the magnetic

[6] Inside the outer loop system, different isotopes are separated and recovered tritium is reinjected into the inner loop system.

[7] The chicane of the CPS diverges the beam tube to the opposite direction compared to the DPS (see figure 2.5).

flux tube to measure the intensity of the electron flux at different locations within the beam tube. The detector plate can be positioned with a precision of 0.1 mm by a set of stepper motors. Horizontal positioning is achieved by insertion and retraction into the beam tube, whereas vertical positioning is accomplished by rotation of the detector board. Both movements combined allow for the mapping of the entire flux tube cross section. During neutrino-mass measurements, the monitoring position is located in the outer 7 mm brim of the flux tube to avoid shadowing of any FPD pixels. In this position an electron flux of $\sim 10^6\,\mathrm{e}^-/\mathrm{s\,mm}^2$ is expected. [31, 88]

During the neutrino mass campaigns relevant to the thesis at hand, two generations of FBM detector boards have been used for monitoring. Each of the detector boards includes a temperature gauge to monitor the board temperature.

The first generation FBM combines two silicon positive intrinsic negative (PIN) diodes[8] with an energy resolution of about 2 keV at 59.5 keV[9]. The diodes have a sensitive area of $0.031\,\mathrm{mm}^2$ and $0.12\,\mathrm{mm}^2$ leading to the 0.1 % precision within 60 s. In addition to the diodes, the detector board contains a hall sensor to measure the magnetic field. [88]

The FBM detector was upgraded in the middle of 2019. The second generation FBM is based on the seven-pixel detector prototype of the TRISTAN detector upgrade[10]. The detector design is based on a silicon drift detector (SDD) segmented into seven hexagonal pixels with an active area of $0.34\,\mathrm{mm}^2$. The detector design delivers an improved energy resolution of 139 eV at 5.9 keV[11] [180]. Apart from this, the detector allows for measurements of higher rates compared to the first generation. In the current setting, the FBM collects 56 kcps per pixel. With the upgraded FBM detector, the goal precision of 0.1 % can be reached within 20 s. [244]

2.2.2. Spectrometer and Detector Section

The spectrometer and detector section (SDS) includes a total of three spectrometers, the pre-, main, and monitor spectrometer, as well as the detector system. The pre-spectrometer (see section 2.2.2.2) and main spectrometer (see section 2.2.2.1) are an integral part of the KATRIN beamline. The monitor spectrometer (see section 2.2.2.4) is installed in parallel with an underground electric connection to the main spectrometer. Electrons are guided through the beamline by four superconducting magnets and a large air coil system while being filtered by the spectrometers. Transmitted electrons are then measured by the focal plane detector (FPD), which forms the end of the beamline. The FPD is the centrepiece of the detector system (see section 2.2.2.3). In the following subsections, the main SDS components and their functions are described in detail, focussing on their functions during neutrino-mass measurements.

[8] A silicon PIN diode is a diode with an undoped intrinsic layer between a p-type and n-type doped semiconductor.

[9] The calibration of the PIN diode detector is based on the ^{241}Am peak at 59.5 keV.

[10] The seven-pixel TRISTAN detector prototype was produced by the Halbleiter Labor (HLL) of the Max-Planck-Society in Munich. The goal of the tritium beta decay to search for sterile neutrinos (TRISTAN) sub-project is to develop a new detector and read-out system designed to handle high count rates. In addition, the upgrade allows one to search for sterile neutrinos in the keV range with the KATRIN experiment.

[11] The full width half maximum (FWHM) value is based on calibration mesurements with ^{55}Fe.

2.2.2.1. Main spectrometer

The KATRIN collaboration designed and commissioned the main spectrometer with a length of 23.3 m and a diameter of 10 m, following the MAC-E filter principle. The design fulfils the conditions for magnetic adiabatic collimation of the electrons with a target energy resolution of 1 eV [39]. The main spectrometer is located between the pre-spectrometer and detector section (see figure 2.2). With a volume of 1240 m^3, the main spectrometer is the largest spectrometer vessel ever built [126].

To prevent collisions of electrons with residual gas molecules and to minimise the production of background electrons, the main spectrometer volume is evacuated to ultra-high vacuum conditions. To meet the requirements, the pressure is on the order of 10^{-11} mbar. The ultra-high vacuum is realised by a combination of turbo-molecular pumps (TMP) and non-evaporating getter pumps (NEG), located in two of the three downstream pump ports[12]. The operation of three TMPs in addition to the NEGs is necessary to realise the first stage of initial vacuum and pump non-getterable gases such as noble gases. However, the NEG material comes with the disadvantage of radio-impurities, leading to the emanation of radon from the NEGs. For this reason, the vacuum system is placed behind a liquid nitrogen-cooled cryogenic baffle, where radon (and H_2O) sticks to the cold copper baffle surface. To reduce the background and improve the vacuum conditions, a crucial step before the operation is the baking of the main spectrometer. Hereby the main spectrometer is heated up to 200 °C. The baking, on the one hand, activates the getter pumps, and on the other hand, causes desorption of hydrogen and water molecules from the inner wall surfaces. In addition, accumulated radon on the baffles surfaces inside the pump ports is outgassed and pumped out. [31, 42]

The magnetic field inside the main spectrometer is mainly evoked by stray fields of the superconducting downstream pre-spectrometer magnet (PS2) and the superconducting pinch magnet (located at the beginning of the detector section). During neutrino-mass measurements, PS2 is set to 3.1 T, whereas the pinch magnet (designed for a maximum nominal magnetic field of 6 T) is operated at 4.2 T. The pinch magnetic field corresponds to the maximum field strength throughout the beamline ($B_{\mathrm{pch}} = B_{\mathrm{max}}$). Due to the conservation of magnetic flux as described by equation (2.1), the flux tube widens in the spectrometer vessel[13]. The flux tube can widen up to 9 m in diameter in the analysing plane within the vessel's physical dimension of 10 m. With a vessel length of 23.3 m, it is possible to realise a low magnetic field gradient, allowing for adiabatic guidance of electrons with small surplus energies. During neutrino-mass measurements, the minimum magnetic field in the analysing plane is around 6×10^{-4} T (for more detailed numbers, the reader is referred to section 5.2.1). Assuming the non-relativistic case, the main spectrometer energy resolution at the endpoint during nominal neutrino mass settings is

$$\Delta E = \frac{B_{\mathrm{ana}}}{B_{\mathrm{max}}} \cdot E = \frac{6 \times 10^{-4}\,\mathrm{T}}{4.2\,\mathrm{T}} \cdot 18\,575\,\mathrm{eV} = 2.65\,\mathrm{eV}. \tag{2.9}$$

In order to fine shape the magnetic field inside the spectrometer vessel, the main spectrometer is surrounded by a large volume air coil system, comprised of the low-field correction system (LFCS) and the earth magnetic field compensation system (EMCS). With a diameter of 12.6 m, the coaxial LFCS was originally designed with 14 normal conducting air

[12] Due to radon-induced background caused by the getter pumps, it was decided to only install the vacuum system in two of the three main spectrometer pump ports. [31]

[13] With a source magnetic field of 2.51 T, the magnetic flux is $\Phi = 153\,\mathrm{T\,cm^2}$.

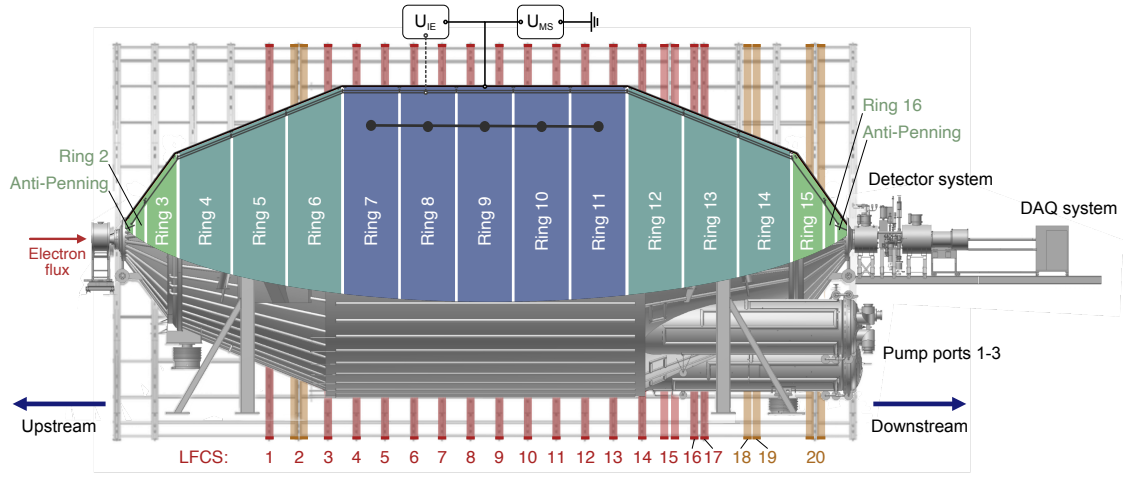

Figure 2.6.: Schematic illustration of the main spectrometer, inner electrode system, and LFCS. The main spectrometer vessel is connected to high voltage. On top of this potential, the inner electrodes shape the electric field inside the main spectrometer. The inner wire electrode system is segmented into three groups: steep cone (rings 2, 3, 15, 16, coloured in green), flat cone (rings 4, 5, 6, 12, 13, 14, coloured in teal) and central part (rings 7, 8, 9, 10, 11, coloured in blue). Rings 7-11 are short-circuited to provide a homogeneous electric field. In contrast, the first and last segments are solid electrodes. The LFCS (original: red; extension: orange) consists of a set of 20 normal conducting air coils, which allow fine-shaping of the flux tube inside the spectrometer vessel.

coils (red in figure 2.6) [117]. In 2020 the LFCS was extended with five additional air coils (orange in figure 2.6) while also dividing one of the original air coils into two, leading to a total of 20 coils[14] [239]. By adjusting the current applied to each coil in interplay with the vessel potential, the magnetic flux tube, field gradient and position of the analysing plane are adjusted precisely. The LFCS coils are also set to prevent flux tube collisions with the spectrometer walls while reducing the background via magnetic shielding [31]. In addition to the 20 vertical LFCS air coils, 10 EMCS air coils are installed horizontally. The EMCS coils are divided into two sets of dipole coils. The purpose of the EMCS is to compensate for the terrestrial magnetic field and avoid flux tube collisions with the spectrometer walls on the underside. The applied LFCS and EMCS settings relevant to this thesis are listed in table A.2. [31, 65, 93, 117]

The main spectrometer retarding potential is regulated by a system of high voltage supplies, high voltage dividers, and digital voltmeters capable of potentials down to $-35\,\mathrm{kV}$[15]. One of the main background contributions is electrons emitted from the walls. These electrons can be induced by interactions of the cosmic muon flux or gamma rays inside the vessel walls, or can originate from the decay of radioactive isotopes implanted inside the stainless steel. To prevent electrons from entering the sensitive volume, a system of wire electrodes is installed inside the spectrometer vessel, parallel to the spectrometer walls. The inner electrodes are set to a more negative voltage, relative to the walls, repelling emitted electrons, thus

[14] In addition, the extension included an upgrade of air coils 3-11 from 8 to 14 windings [239].

[15] The operation down to $-35\,\mathrm{kV}$ is necessary for measurements of the $^{83\mathrm{m}}$Kr spectrum. For measurements of the tritium spectrum, a retarding voltage around $-18.4\,\mathrm{kV}$ is applied.

shielding the inner volume and reducing the background coming from the walls. [247]

The inner electrode system is usually operated at around −200 V relative to the spectrometer tank. Together with the vessel potential, the retarding potential sums up to around 18.6 kV for measurements of the tritium spectrum. The inner electrode system is divided into three groups (see figure 2.6): steep cones (coloured in green), flat cones (coloured in teal), and the central part (coloured in blue). The segments are further subdivided into rings, which are biased with individual voltages. The inner electrode system allows for fine-shaping of the electric field inside the vessel volume. Both the flat cone and central inner electrodes consist of two wire layers, whereas the steep cone electrodes consist of a single layer. In addition, the central rings (highlighted in blue) are short-circuited to provide a more homogeneous field. The applied inner electrode settings relevant to this thesis are listed in table A.1. [31, 126, 246]

2.2.2.2. Pre-spectrometer

The CPS and the main spectrometer are connected by the pre-spectrometer (PS). Similar to the main spectrometer (see section 2.2.2.1), it uses the MAC-E filter principle (see section 2.1). The 3.4 m long and 1.7 m diameter PS originally served as a prototype, and test setup for the development of the main spectrometer [119, 179, 249]. In the current setup, the PS can function as a prefilter, allowing to reduce the flux of incoming electrons by about six orders of magnitude. Like the main spectrometer, ultra-high vacuum conditions are present inside the PS, which are achieved by a combination of TMPs and non-evaporating getter pumps. A superconducting magnet is installed at the inlet and outlet of the spectrometer vessel, the upstream pre-spectrometer magnet (PS1) and the downstream pre-spectrometer magnet (PS2). During neutrino-mass measurements, both PS1 and PS2 are operated at 3.1 T. The flux tube inside the PS expands to ~ 1 m, resulting in an energy resolution of about 70 eV in the PS analysing plane [126]. When applied, the retarding potential is mainly given by the high voltage applied to the vessel walls. In addition, an inner electrode system allows for refined adjustments of the electric field [247]. Fast switching of the main spectrometer potential in combination with switching of the PS potential allows for dedicated time of flight (TOF) measurements [39].

If the main and pre-spectrometer are both operated on high voltage, the combination of increasing electric potential to both sides and magnetic guidance within the flux tube can lead to the creation of a Penning trap between the spectrometers [195, 247]. Over time electrons are stored within the Penning trap, leading to a slowly increasing background rate (more details given in section 3.8.3). In the worst case, stored electrons can cause spontaneous Penning discharges. For this reason, in between scan steps, free charges can be collected with a so-called Penning wiper, emptying the stored charges in the Penning trap.

During neutrino-mass measurements relevant to this thesis, the PS was operated in two different settings. First, the PS was operated at −10 kV. It was found that the background caused by trapped Penning electrons leads to an increased systematic uncertainty. As a consequence, the PS was set to 0 V to eliminate the Penning trap and hence remove the systematic effect on the neutrino mass. For more details and the impact on the neutrino mass, the reader is referred to sections 3.8.3 and 6.3.3.

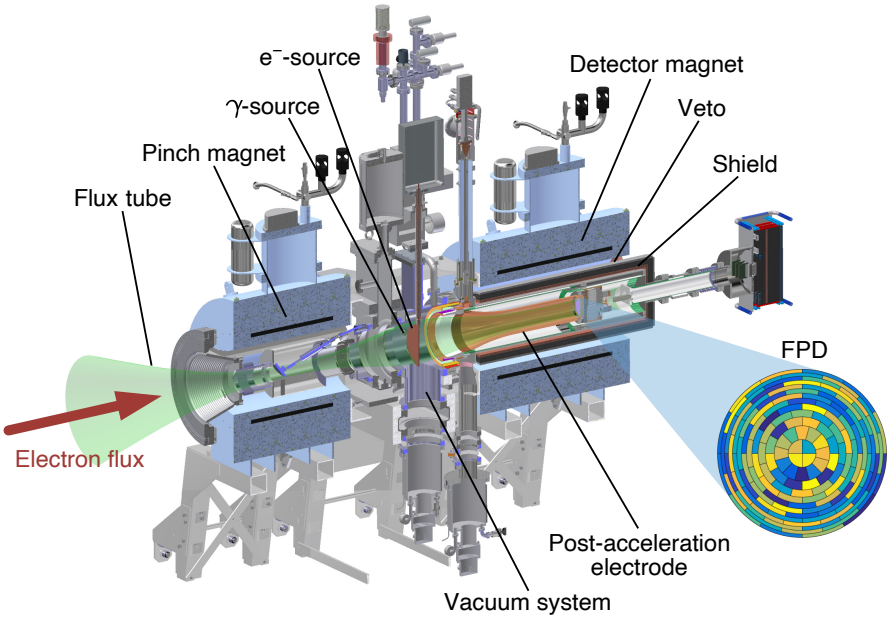

Figure 2.7.: CAD drawing of the focal plane detector system. The magnetic flux tube is narrowed by the pinch magnet, guiding electrons from the main spectrometer towards the FPD. In addition, electrons are accelerated with 10 kV post acceleration. The FPD is located in the centre of the detector magnet, surrounded by a muon veto system. Figure adapted from [36].

2.2.2.3. Detector system

To measure the β-electrons that are transmitted by the main spectrometer, a detector system is installed at the downstream end of the KATRIN setup. A graphical illustration of the detector system components is given in figure 2.7. The detector system includes two superconducting solenoids: the pinch magnet, narrowing the flux tube after the main spectrometer, followed by a second superconducting magnet, the detector magnet. The combination of both magnets allows adiabatic transport of electrons towards the detector. Since the detector section is open towards the main spectrometer, the system needs to fulfil similar ultra-high vacuum requirements as present inside the main spectrometer. Therefore a pressure $< 10^{-9}$ mbar is required [31]. To evacuate the detector section, a pump port is located between the solenoids.

The centrepiece of the detector system is the focal plane detector (FPD), a monolithic silicon wafer with a sensitive area of 90 mm in diameter. The FPD wafer has a thickness of 500 µm, with a dead layer thickness of 100 nm, and functions as a PIN diode. The FPD is segmented into 148 pixels of equal surface area (43 mm^2). The pixels are arranged in a concentric formation, with four pixels in the centre (bullseye), surrounded by twelve rings, each containing twelve pixels. The detector pixels have an energy resolution on the order of 2.2 keV to 2.6 keV [126, 133]. The FPD is located in the bore of the detector magnet. By setting the detector magnetic field to 2.5 T (which is similar to the source magnetic field), the flux tube is narrowed and mapped onto the sensitive detector area. To count the incoming electrons, the electron signals are processed by custom readout electronics and a data acquisition system (DAQ). Detector calibrations can be performed with a γ- and e^--source that is located between the two magnets. An ^{241}Am source functions as a

γ-emitter, allowing calibration of the detector independent of the dead layer thickness. For calibrations with electrons, photoelectrons between 0 keV and 25 keV can be generated by UV illumination of a titanium plate that can be placed in front of the detector. Since both γ- and e^--source are installed inside the vacuum environment, detector calibrations are performed without venting the high vacuum system. [31, 36]

To reduce the background originating from cosmic rays, the detector is surrounded by an active and passive background suppression system. Active attenuation of the background is achieved by a muon veto system in the outer layer around the detector. With this veto system, composed of 20 mm thick plastic scintillators, incoming muons can be tagged and matched to coinciding detector signals. Passive background suppression is accomplished by nested cylindrical layers of lead and copper shielding. The 3.0 cm lead shield reduces the γ-background, and the 1.27 cm copper shields the detector from X-rays emitted by the lead. [31]

Additionally, to improve electron detection, the guided electrons are boosted by applying an accelerating potential at the post acceleration electrode (PAE). The PAE is set to 10 kV during neutrino-mass measurements. Boosting the electron momenta has the advantage of shifting the electron signal into a region of lower intrinsic detector background. Furthermore, the acceleration decreases the pitch angle, reducing the probability of electrons being backscattering from the detector and decreasing losses in the dead-layed. [36]

2.2.2.4. Monitor spectrometer

The third spectrometer in the KATRIN setup, the monitor spectrometer, is located parallel to the beamline in a building next to the main spectrometer hall. This spectrometer was the MAC-E filter setup in the former Mainz experiment, which operated between 1991 and 2001 [151]. With a length of ~ 4 m and a diameter of 1 m, the setup comprises two 6 T superconducting magnets, achieving an energy resolution on the order of 1 eV. Similarly to the main spectrometer setup, the monitor spectrometer includes a set of normal conducting coils as well as an EMCS. Both the main spectrometer and monitor spectrometer are directly connected and can therefore be kept at the same potential. By continuous observation of the quasi-monoenergetic K32 calibration line of ^{83}Kr, subtle differences in the high voltage stability and drifts of the potential can be monitored. [92, 231, 232]

If not connected to the main spectrometer, the monitor spectrometer can be used as an additional test and commissioning setup. For example, e-gun systems [58, 221] were commissioned at the monitor spectrometer before being installed in the main KATRIN beamline. Additionally, new TRISTAN detector prototypes are tested and characterised there [180, 243].

3. Physics model

The main objective of this thesis is the analysis of the tritium β-spectrum measured with the KATRIN experiment. The model used to analyse the data is described in more detail in the following sections. The model is based on the differential β-decay spectru of molecular tritium (sections 3.1 to 3.3), and precisely calculates the transport and transmission properties of the experimental setup including the WGTS and MAC-E filter (sections 3.4.1 to 3.4.3). In addition, effects that affect the measured spectrum including Doppler broadening (section 3.5), inhomogenities of the source potential (section 3.7), or the detector response (section 3.10), are taken into account. Since the MAC-E filter principle results in the measurement of the integrated β-decay rate, the different components are combined to compose a physics model for the integrated β-spectrum (section 3.6). In addition, a background model is included (sections 3.8 and 3.9). The focus of this chapter is to provide an overview of the model in the exact configuration as it is used in the analysis.

From here on, the KATRIN measurement campaigns are referred to as KATRIN neutrino-mass measurement (KNM). More details about all of the campaigns and data combinations are given in chapter 5.

3.1. Differential β-decay spectrum

Initially, a description of the differential nuclear β-decay of tritium is given. Tritium decays to helium via β-decay, thereby emitting an electron and an electron antineutrino,

$$\mathrm{T} \rightarrow \mathrm{He}^{+} + \mathrm{e}^{-} + \overline{\nu}_{\mathrm{e}}. \tag{3.1}$$

For the dirivation of the decay rate, Fermi's golden rule [102] is applied to describe the decay process. For a more in-depth description, the reader is referred to [186]. The decay probability Γ from the initial state $\langle i|$ into the final state $|f\rangle$ is derived using first-order perturbation theory[1],

$$\Gamma_{i \rightarrow f} = 2\pi \cdot |\langle f| M |i\rangle|^2, \tag{3.2}$$

where $|M_{fi}|$ is the transition matrix element between the initial and final state. The matrix element includes leptonic as well as nuclear transitions. Using the ansatz of equation (3.2)

[1] The convention $\hbar = c = 1.0$ is used.

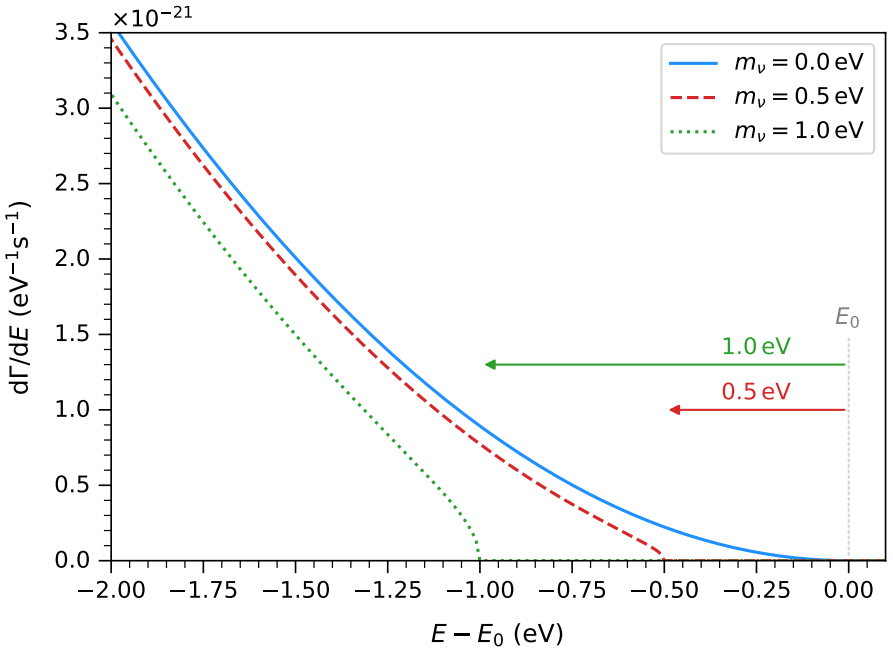

Figure 3.1.: Imprint of the neutrino mass on the differential spectrum. The spectrum is calculated according to equation (3.3). The plot includes three different neutrino mass scenarios: $m_\nu = 0.0\,\text{eV}$ (blue), $m_\nu = 0.5\,\text{eV}$ (red), and $m_\nu = 1.0\,\text{eV}$ (green). With increasing neutrino mass, the differential rate is reduced near the endpoint and the end of the spectrum is shifted to lower energies – away from the effective endpoint (grey).

the differential decay rate of a tritium nucleus is:

$$\begin{aligned}\left(\frac{\mathrm{d}\Gamma}{\mathrm{d}E}\right)_{\text{nucl.}} =& \frac{G_\text{F}\cos^2(\Theta_\text{C})}{2\pi^3}\cdot|M_\text{nucl.}|^2\cdot F\left(Z',E\right)\cdot p\left(E+m_\text{e}\right)\\ &\cdot\sum_i|U_{ei}|^2\cdot(E_0-E)\cdot\sqrt{(E_0-E)^2-m_i^2}\cdot\Theta\left(E_0-E-m_i\right).\end{aligned} \tag{3.3}$$

In this equation, E_0 is the endpoint of the tritium spectrum and m_e is the electron mass. Properties belonging to the matrix element are connected to nuclear and leptonic transitions. $M_\text{nucl.}$ corresponds to the matrix element for nuclear transitions and can further be divided into a vector (g_V) and axial-vector coupling (g_A). The nuclear matrix element is $|M_\text{nucl.}|^2 = g_\text{V}^2 + 3g_\text{A}^2$. The differential spectrum further contains the Fermi coupling constant G_F, which is projected onto the (u, d) coupling with $\cos(\Theta_\text{C})$, where Θ_C is, the Cabibbo angle. The momentum of the electron is calculated with the phase space factor $p\left(E+m_\text{e}\right)$. Connected to leptonic matrix element is the Fermi function $F\left(Z',E\right)$,

$$F\left(Z',E\right) = \frac{2\pi\eta}{1-\exp(-2\pi\eta)}, \quad \text{with} \quad \eta = \frac{\alpha Z'}{\beta}. \tag{3.4}$$

The Fermi function serves as a correction due to electromagnetic interactions of electrons with the daughter nucleus. The Sommerfeld parameter η contains the fine structure constant α, and β is the ratio of velocity and speed of light. In the case of decaying tritium,

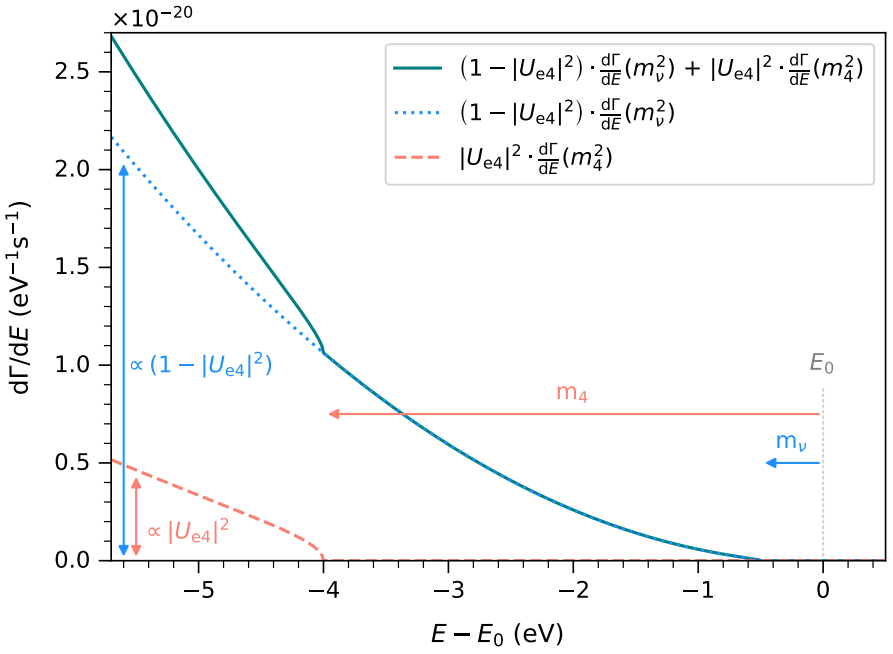

Figure 3.2.: Imprint of sterile neutrinos on the differential spectrum. In the plot, the total differential spectrum (teal), as well as the active (blue) and sterile branch (orange), are displayed separately. Inputs to the calculated spectrum are an effective active neutrino mass of $m_\nu = 0.5\,\mathrm{eV}$, a sterile mass of $m_4 = 4.0\,\mathrm{eV}$ and a large mixing amplitude of $|U_{e4}|^2 = 0.25$. Similarlz to the case of the active neutrino, the sterile branch of the spectrum is shifted by the sterile mass m_4 towards smaller energies and in addition, is scaled by the sterile mixing amplitude $|U_{e4}|^2$.

the daughter nucleus He^+ has the atomic number $Z' = 2$. The differential spectrum is further confined to a physical solution by the Heavyside function Θ, which ensures energy conservation. Hereby a neutrino can only be generated if the energy is larger than the mass of the neutrino. [186, 147]

The mass splitting can not be resolved by the KATRIN experiment, therefore the observable is the squared effective electron neutrino mass m_ν^2. With the assumption of unitarity of the neutrino mass eigenstates $\sum_i |U_{ei}|^2 = 1$, the effective mass is defined as a superposition of the three mass eigenstates m_i, weighted with the elements U_{ei} of the 3×3 PMNS. The squared effective neutrino mass is then given by

$$m_\nu^2 = \sum_{i=1}^{3} |U_{ei}|^2 m_i^2. \tag{3.5}$$

The differential spectrum, as described by equation (3.3), is displayed in figure 3.1. The plot includes three different effective neutrino mass scenarios – $m_\nu = 0.0\,\mathrm{eV}$ (blue), $m_\nu = 0.5\,\mathrm{eV}$ (red), and $m_\nu = 1.0\,\mathrm{eV}$ (green), to illustrate the impact a non-zero neutrino mass has on the differential spectrum. With larger masses, the spectrum is shifted from the effective endpoint towards lower energies.

The formulation of the differential spectrum can also be adapted to account for sterile neutrinos. In this case, the sum over the mass eigenstates is extended to also include the

heavy, sterile eigenstates:

$$\text{active, light:} \quad \sum_{i,\text{active}} |U_{ei}|^2 =: \cos^2(\theta) \tag{3.6}$$

$$\text{sterile, heavy:} \quad \sum_{i,\text{sterile}} |U_{ei}|^2 = 1 - \sum_{i,\text{active}} |U_{ei}|^2 =: \sin^2(\theta). \tag{3.7}$$

Assuming that unitarity is conserved, the sum of active and sterile branches adds up to $\sin^2(\theta) + \cos^2(\theta) = 1$. In the most simple case, the Standard Model is extended by one sterile neutrino ($3\nu + 1$). In this case, the additional spectrum is characterised by an active-to-sterile mixing amplitude $|U_{e4}|^2$ and the mass of the fourth mass eigenstate m_4. Measurements of the Z^0 resonance support the existence of only three active neutrinos [237], therefore a fourth heavy neutrino would mainly be composed of a sterile neutrino, not participating in the weak interaction. The differential spectrum can be separated into an active and sterile branch, leading to

$$\begin{aligned} \frac{\mathrm{d}\Gamma}{\mathrm{d}E} &= \cos^2(\theta) \cdot \frac{\mathrm{d}\Gamma}{\mathrm{d}E}\left(m^2_{\nu_{\text{active}}}\right) + \sin^2(\theta) \cdot \frac{\mathrm{d}\Gamma}{\mathrm{d}E}\left(m^2_{\nu_{\text{sterile}}}\right) \\ &= (1 - |U_{e4}|^2) \cdot \frac{\mathrm{d}\Gamma}{\mathrm{d}E}\left(m^2_{\nu}\right) + |U_{e4}|^2 \cdot \frac{\mathrm{d}\Gamma}{\mathrm{d}E}\left(m^2_{4}\right). \end{aligned} \tag{3.8}$$

In comparison to KATRIN, oscillation experiments are sensitive to $\sin^2(2\theta_{ee})$ and Δm^2_{41}. Hereby $|U_{e4}|^2$ and m^2_4 are transformed as follows:

$$\sin^2(2\theta_{ee}) = 4|U_{e4}|^2 \cdot \left(1 - |U_{e4}|^2\right) \tag{3.9}$$

$$\Delta m^2_{41} \approx m^2_4 - m^2_\nu. \tag{3.10}$$

A sterile neutrino manifests itself as a kink-like signature within the β-spectrum (see figure 3.2). The kink position is given by $(E_0 - m^2_4)$. The active-to-sterile mixing amplitude determines the magnitude of the kink feature. For comparison to oscillation experiments, it is sensible to only probe $|U_{e4}|^2$ down to 0.5, as $4|U_{e4}|^2 \cdot \left(1 - |U_{e4}|^2\right)$ reaches a maximal value of 1.0 at this active-to-sterile mixing.

3.2. Radiative corrections

To account for contributions from both real and virtual photons during the decay, the differential spectrum is multiplied by a radiative correction factor (G_{rad}). The energy-dependent formulation for tritium decay has been derived by W. Repko and C. Wu [201] and is implemented as

$$\begin{aligned} G_{\text{rad}}(E, E_0) = (E_0 - E)^{\frac{2\alpha}{\pi} t(\beta)} \cdot \Bigg[1 + \frac{2\alpha}{\pi} \cdot \Bigg[t(\beta) \cdot \left(\ln(2) - \frac{3}{2} + \frac{E_0 - E}{E} \right) \\ + \frac{1}{4} \cdot (t(\beta) + 1) \cdot \left(2\left(1 + \beta^2\right) + 2\ln(1 - \beta) + \frac{(E_0 - E)^2}{6E^2} \right) \\ - 2 + \frac{1}{2}\beta - \frac{17}{36}\beta^2 + \frac{5}{6}\beta^3 \Bigg] \Bigg]. \end{aligned} \tag{3.11}$$

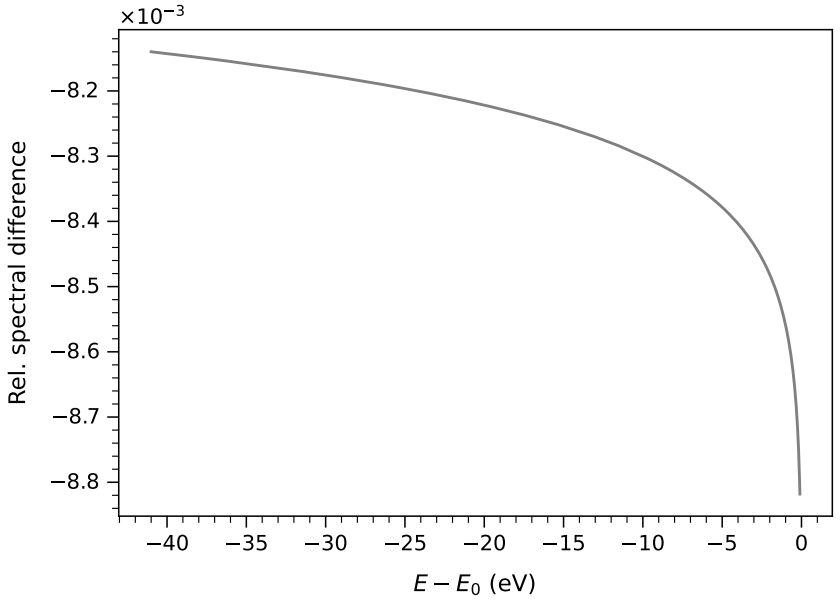

Figure 3.3.: Relative spectral difference after applying radiative corrections to the differential spectrum. The addition of radiation corrections increases the decay rate energy dependent on the order of 1 %.

Hereby $t(\beta)$ is calculated by

$$t(\beta) = \frac{1}{\beta} \cdot \tanh^{-1}(\beta) - 1. \tag{3.12}$$

The relative influence on the differential decay rate is illustrated in figure 3.3. When including the contributions from both virtual and real photons, the decay rate overall decreases close to the endpoint with an additional energy dependency. If not taken into account in the neutrino-mass analysis, the energy-dependent correction can lead to a bias $\mathcal{O}(2 \times 10^{-2}\,\mathrm{eV}^2)$ [73].

3.3. Molecular final state distribution

As an extension to the single nucleus decay description in the previous section, molecular excitation is also taken into account, as gaseous molecular tritium is decaying in the sourc,

$$\mathrm{T}_2 \rightarrow \mathrm{THe}^+ + \mathrm{e}^- + \overline{\nu}_\mathrm{e} + Q(\mathrm{T}_2). \tag{3.13}$$

In this decay, Q represents the electronic binding energy difference between molecular and atomic tritium. The endpoint of molecular tritium is given by the difference in Q and the recoil energy E_rec. The maximum recoil energy for THe^+ is 1.72 eV. [186]

The transition probability $\Gamma_{i\rightarrow f}$ from equation (3.2) is modified by the phase space density $\rho(E_f)$ of the final states,

$$\Gamma_{i\rightarrow f} = 2\pi \cdot \rho(E_f) \cdot |\langle f|\, M\, |i\rangle|^2 = 2\pi \cdot \rho(E_f) \cdot |M_{if}|^2. \tag{3.14}$$

To get the total decay rate, it is necessary to integrate over the transition probabilities

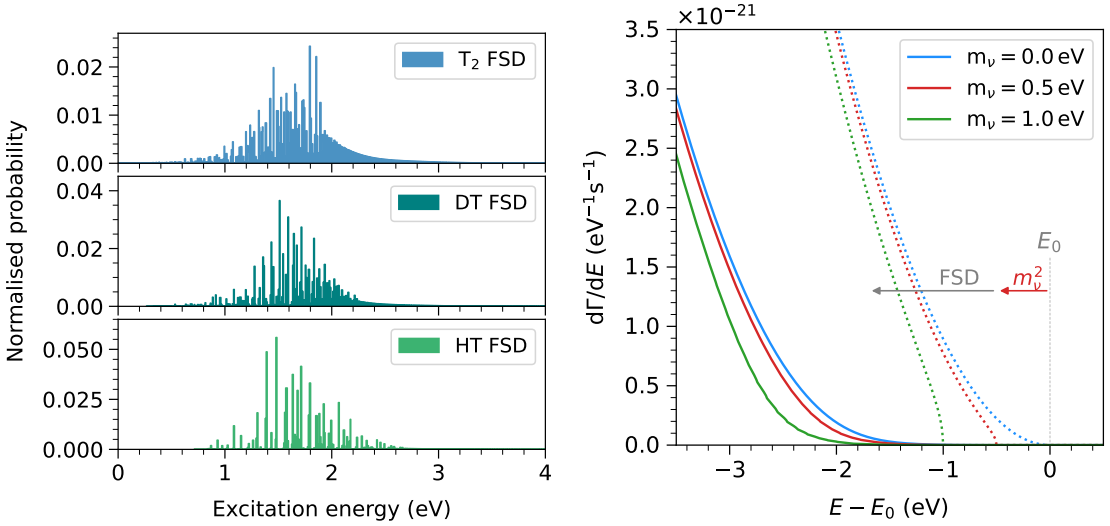

(a) KATRIN FSD. **(b)** Differential spectrum.

Figure 3.4.: (a) FSDs applied in the KATRIN neutrino-mass analysis. The three different FSDs (for T_2, DT, and HT) are summed, weighted by the gas composition. Here the energy range is zoomed into the region of the ground states as this region covers most of the excitation probabilities and has the largest impact in the neutrino-mass analysis. (b) Impact of the FSD on the differential spectrum. The differential spectrum without FSD is plotted with dotted lines, and spectra including the FSD are plotted with solid lines. Since some of the transition energy is deposited in (mainly) the ground state of the resulting daughter molecule, the energy of the emitted electron $\varepsilon_f(E) = E_0 - E_f - E$ is shifted towards lower energies. Additionally, the summation over all final states f washes out the distinct imprint of the neutrino mass close to the endpoint.

$\Gamma_{i\to f}$ of all final states. For discrete final states, this leads to a summation of all molecular final states f, weighted by their final state probability ζ_f. Consequently, the differential spectrum as given by equation (3.3) is modified to:

$$\begin{aligned}\frac{\mathrm{d}\Gamma}{\mathrm{d}E} =& \frac{G_\mathrm{F}\cos^2(\Theta_\mathrm{C})}{2\pi^3}\cdot|M_\mathrm{nucl}|^2\cdot F\left(Z',E\right)\cdot p\left(E+m_\mathrm{e}\right)\\ &\cdot\sum_f \zeta_f\cdot\varepsilon_f\cdot\sqrt{\varepsilon_f^2-m_\nu^2}\cdot\Theta\left(\varepsilon_f-m_\nu\right).\end{aligned} \tag{3.15}$$

The energy scale is hereby expressed by $\varepsilon_f(E) = E_0 - E_f - E$. This further shifts the spectra by E_f. [147] The final states distribution (FSD)[2] includes recoil excitation of rotational final states, vibrational final states, and excitations of the electronic shells [83, 84, 211, 212].

The impact on the shape of the differential spectrum is displayed in figure 3.4b. The summation of all final states shifts the spectrum towards lower energies and washes out the distinct shape distortion of the neutrino mass close to the endpoint.

In figure 3.4a, the different FSDs applied in the KATRIN analysis are displayed. The

[2]The FSD describes the excitation probability of each final state over energy.

FSDs correspond to excitation of T_2, DT, and HT. The three FSDs are combined when calculating the differential spectrum. Each of the FSDs is weighted by the fraction within the gas composition and summed into one effective final state distribution. The combined final state distribution is mainly dominated by T_2, as $> 98\,\%$ of the gas inside the source is molecular tritium.

3.4. Experimental response function

To model the transmission properties of electrons through the experimental setup, an experimental response function has to be calculated. The Response function combines the energy loss characteristics in the source (section 3.4.2) as well as transmission properties of the spectrometer section (section 3.4.1). Cobining both leads to the response function (section 3.4.3). The following subsections will outline how the components are derived and how the final response function is composed.

3.4.1. Transmission function

The transmission properties of the main spectrometer in KATRIN are described by the transmission function $T(E, \theta_{\mathrm{src}}, U)$. The transmission function describes the probability for electrons with energy E and emission angle θ_{src} relative to the source magnetic field B_{src} to overcome the potential U in the analysing plane. The transmission function is given as follows:

$$\begin{aligned} T(E,U) &= \int_{\theta_{\mathrm{src}}=0}^{\theta_{\mathrm{max}}} \mathcal{T}(E,\theta,U_i)\sin\theta \mathrm{d}\theta_{\mathrm{src}} \\ &= \begin{cases} 0 & , \; E - qU < 0 \\ 1 - \sqrt{1 - \frac{E-qU}{E}\frac{B_{\mathrm{src}}}{B_{\mathrm{ana}}}\frac{2}{\gamma+1}} & , \; 0 \leq E - qU \leq \Delta E \\ 1 - \sqrt{1 - \frac{B_{\mathrm{src}}}{B_{\mathrm{max}}}} & , \; E - qU > \Delta E. \end{cases} \end{aligned} \tag{3.16}$$

B_{ana} is the magnetic field in the analysing plane and B_{pch} is the maximum magnetic field located in the pinch magnet. This assumes that electrons are isotropically emitted in the source, resulting in the integration of θ_{src} in the range $\theta \in [0, \theta_{\mathrm{max}}]$ over the solid angle. [23, 58, 147]

An example of the transmission function as it is applied in the neutrino-mass analysis is displayed in figure 3.5. The transmission function has three characteristic regions. If the electron's energy is below the retarding energy $E < qU$, electrons are reflected and have a transmission probability of 0 (figure 3.5 (left)). The second part is the so-called transmission edge and describes the partial transmission of electrons between surplus energies of zero and ΔE (figure 3.5 (centre)). In this region, the transmission probability depends on the emission angle of electrons in the source. Due to conservation of the total energy,

$$E_{\perp}(B) = E_{\perp}(B_{\mathrm{src}}) \cdot \frac{B}{B_{\mathrm{src}}}, \tag{3.17}$$

the angle is colimated when lowering the magnetic field by $B_{\mathrm{ana}}/B_{\mathrm{src}}$. Electrons that are emitted with larger θ_{src} have less longitudinal momentum and hence need more surplus

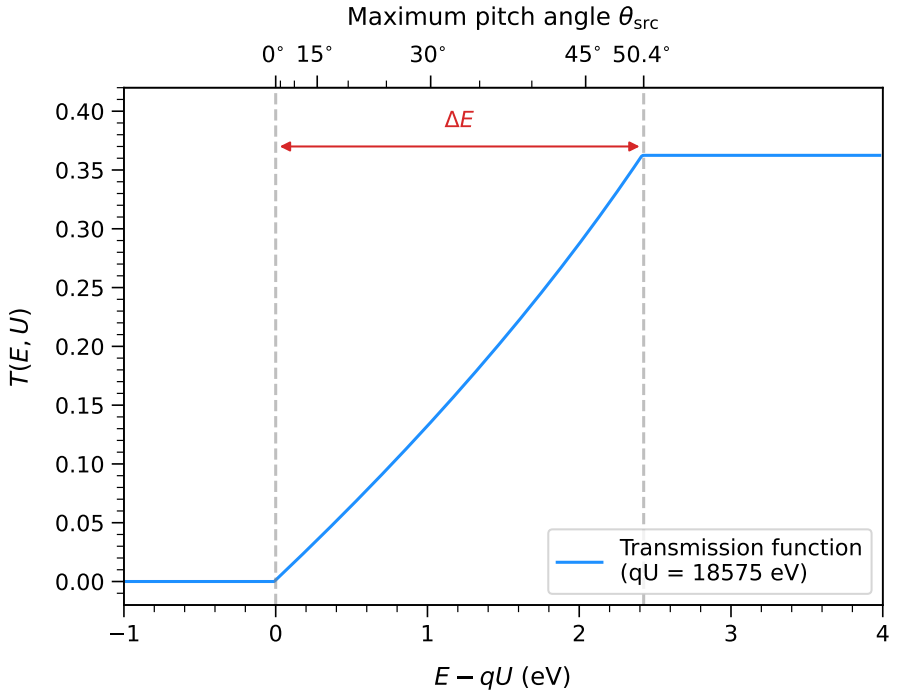

Figure 3.5.: Transmission function of the KATRIN main spectrometer given for the surplus energy $E - qU$. The transmission function is calculated for a retarding energy of 18 575 eV according to equation (3.16). Isotropic electron emission in the source is assumed. The transmission is split into three characteristic sections. Electrons with energies below the retarding energy are backreflected (left). In the region of the transmission edge (centre), electrons are transmitted depending on their starting pitch angle. Electrons below a pitch angle of θ_{src} are transmitted. Electrons with an energy larger than ΔE are fully transmitted up to the am maximum pitch angle of $\theta_{max} = 50.4°$ (right).

energy to overcome the retarding potential. Electrons can only overcome the retarding potential when

$$E - E \cdot \frac{B_{ana}}{B_{src}} \frac{\gamma + 1}{2} \cdot \sin^2(\theta_{src}) - qU \geq 0. \tag{3.18}$$

From this, the maximum accepted angle of electrons emitted in the source θ_{src} is derived for the corresponding retarding potential qU, and electron energy E,

$$\theta_{src} \leq \arcsin\left(\sqrt{\frac{E - qU}{E} \frac{B_{src}}{B_{ana}} \frac{2}{\gamma + 1}}\right). \tag{3.19}$$

Using the relation $\cos(\arcsin\sqrt{x}) = \sqrt{1 - \sin(\arcsin(\sqrt{x}))^2} = \sqrt{1 - x}$ the transmission edge formulation of equation (3.16) is derived. [147]

The third region (figure 3.5 (right)) is characterised by the maximum acceptance angle:

$$\theta_{max} = \arcsin\left(\sqrt{\frac{B_{src}}{B_{max}}}\right). \tag{3.20}$$

By increasing the magnetic field, $B_{max} > B_{src}$, the longitudinal energy is reduced to a point

where it vanishes; this effect is known as the magnetic mirror effect. Only electrons below the maximum acceptance angle are fully transmitted. Electrons with a pitch angle greater than θ_{max} are magnetically backreflected. For this reason, the transmission function is < 1 in the full transmission region.

The energy resolution ΔE of the MAC-E filter setup directly corresponds to the ratio of the maximum magnetic field B_{max} and the magnetic field in the analysing plane B_{ana},

$$\Delta E = E \cdot \frac{B_{\mathrm{ana}}}{B_{\mathrm{max}}} \cdot \frac{\gamma + 1}{2}. \tag{3.21}$$

In two of the typical magnetic field settings used during neutrino-mass measurements, the main spectrometer has an energy resolution between 2.42 eV and 2.76 eV at the endpoint.[3] Equation (3.21) is given using the relativistic Lorentz factor γ. The last fraction is an approximation for $\frac{\gamma_{\mathrm{src}}+1}{\gamma_{\mathrm{ana}}+1} \approx \frac{\gamma+1}{2}$. At the endpoint applying the relativistic Lorentz factor has an impact on the order of 1.8 %. From here on we denote γ_{src} as $\gamma = \frac{E+mc^2}{mc^2}$.

The transmission function applied in the neutrino-mass analysis is further renormalised to the full transmission region and is then given by:

$$T(E,U) = \begin{cases} 0 & , \; E - qU < 0 \\ \dfrac{1-\sqrt{1-\frac{E-qU}{E}\frac{B_{\mathrm{src}}}{B_{\mathrm{ana}}}\frac{2}{\gamma+1}}}{1-\sqrt{1-\frac{B_{\mathrm{src}}}{B_{\mathrm{max}}}}} & , \; 0 \leq E - qU \geq \Delta E \\ 1 & , \; E - qU > \Delta E. \end{cases} \tag{3.22}$$

As electrons are transported on helical paths along the magnetic field lines, energy losses due to synchrotron radiation must be considered to describe the transmission behaviour fully. The energy loss due to synchrotron radiation ΔE_{sync} is given by

$$\Delta E_{\mathrm{sync}} = \frac{-\mu_0}{3\pi c}\frac{q^4}{m^3} \cdot B^3 \cdot E_{\perp} \cdot \frac{\gamma + 1}{2} \cdot t, \tag{3.23}$$

where μ_0 is the vacuum magnetic permeability. The time, t, electrons take to propagate through the sections depends on their velocity v, $t = \frac{s}{\cos(\theta)v}$. The synchrotron loss further depends on external magnetic field, B, that the electron is propagating through.

In different sections of the KATRIN experiment different magnetic fields are present, therefore the energy loss is split up into synchrotron losses in the source $\Delta E_{\mathrm{sync}}^{\mathrm{WGTS}}$ and in the transport section $\Delta E_{\mathrm{sync}}^{\mathrm{transport}}$:

$$\Delta E_{\mathrm{sync}} = \Delta E_{\mathrm{sync}}^{\mathrm{WGTS}} + \Delta E_{\mathrm{sync}}^{\mathrm{transport}} \; [120]. \tag{3.24}$$

The mean magnetic field in the source is 2.51 T, whereas the magnetic field present in the transport section is 3.60 T, with $s_{\mathrm{WGTS}} = 5.04\,\mathrm{m}$ as the mean source length for $\Delta E_{\mathrm{sync}}^{\mathrm{WGTS}}$ and $s_{\mathrm{transport}} = 14.00\,\mathrm{m}$ in the case of $\Delta E_{\mathrm{sync}}^{\mathrm{transport}}$. Synchrotron radiation losses for electrons

[3] The two configurations reffer to the nominal analysing plane (NAP) configuration and shifted analysing plane (SAP) configuration (more details in section 5.2). For the NAP setting, the estimation is based on a mean magnetic field of $\langle B_{\mathrm{ana}} \rangle = 6.31 \times 10^{-4}\,\mathrm{T}$ in the analysing plane and $\langle B_{\mathrm{max}} \rangle = 4.24\,\mathrm{T}$ in the pinch magnet. For the SAP configuration, the estimation is based on a mean magnetic field of $\langle B_{\mathrm{ana}} \rangle = 5.53 \times 10^{-4}\,\mathrm{T}$ in the analysing plane and $\langle B_{\mathrm{max}} \rangle = 4.24\,\mathrm{T}$ in the pinch magnet.

emitted with energies colse to the endpoint is around 0.04 eV. As a consequence when including synchrotron radiation losses, the normalised transmission function (equation (3.22)) is modified to:

$$T_{\mathrm{sync}}(E,\theta,U) = \begin{cases} 0 & , \; E - qU < 0 \\ T(E - \Delta E_{\mathrm{sync}}(\theta,z),\theta,U) & , \; 0 \leq E - qU \geq \Delta E \\ 1 & , \; E - qU > \Delta E. \end{cases} \tag{3.25}$$

The combined energy resolution, including the synchrotron radiation hence modifies to

$$\Delta E = E \cdot \frac{B_{\mathrm{ana}}}{B_{\mathrm{max}}} \frac{\gamma + 1}{2} + \Delta E_{\mathrm{sync}}(\theta_{\mathrm{max}}, z). \tag{3.26}$$

3.4.2. Energy loss function

Given the high column density of $\rho \mathrm{d} \sim 5 \times 10^{21}\,\mathrm{m}^{-2}$, present in the WGTS, scattering processes with molecular tritium is a important systematic that has to be taken into account. Energy losses result in distortions of the β-spectrum, where measured electrons are shifted towards lower energies in the spectrum according to their experienced energy loss. In general, the scattering processes are subdivided into elastic and inelastic scattering. [28, 216]

When elastic scattering occurs, the molecule is not excited, and due to coulomb interaction, only the electron's angle is changed[4]. The initial energy of the electron is reduced due to the momentum transfer of the deflected electron to the molecule. Elastic scattering results in a median scattering angle of $\overline{\theta}_{\mathrm{scat}} = 2.1°$ [147]. This translates to a median energy loss of $\overline{\Delta E} = 2.3\,\mathrm{meV}$ [147]. The energy loss due to elastic scattering is given by:

$$\Delta E_{\mathrm{el}} = 2 \cdot \frac{m_e}{M_{\mathrm{T_2}}} \cdot E_{\mathrm{kin}} \cdot (1 - \cos(\theta_{\mathrm{scat}}))\,. \tag{3.27}$$

According to [159], the elastic scattering cross section of molecular hydrogen can be parametrised following the first Born approximation,

$$\sigma_{\mathrm{el}}(E_{\mathrm{kin}}) = \frac{\pi a_0^2 R}{E_{\mathrm{kin}}} \left(4.2106 - \frac{2R}{E_{\mathrm{kin}}}\right), \tag{3.28}$$

where E_{kin} is the kinetic electron energy[5], $a_0 = 5.29 \times 10^{-11}\,\mathrm{m}$ is the Bohr radius, and $R = 13.61\,\mathrm{eV}$ is the Rydberg energy . [159, 216] The elastic scattering cross section for relativistic electrons at the tritium endpoint is $\sigma_{\mathrm{el}}(18.6\,\mathrm{keV}) = 2.86 \times 10^{-23}\,\mathrm{m}^2$. The elastic scattering is negligible for the neutrino-mass analysis.

In contrast, inelastic scattering processes can result in different excitations of the tritium molecule. Hereby the following have to be accounted for: rotational excitation, vibrational excitation, electronic excitation, ionisation, and dissociation. For a detailed description of all listed processes, the reader is referred to [28, 216].

[4] This type of scattering is also known as Rutherford scattering.

[5] For electrons with energies close to the endpoint (∼18.6 keV) it is necessary to use the relativistic kinetic energy.

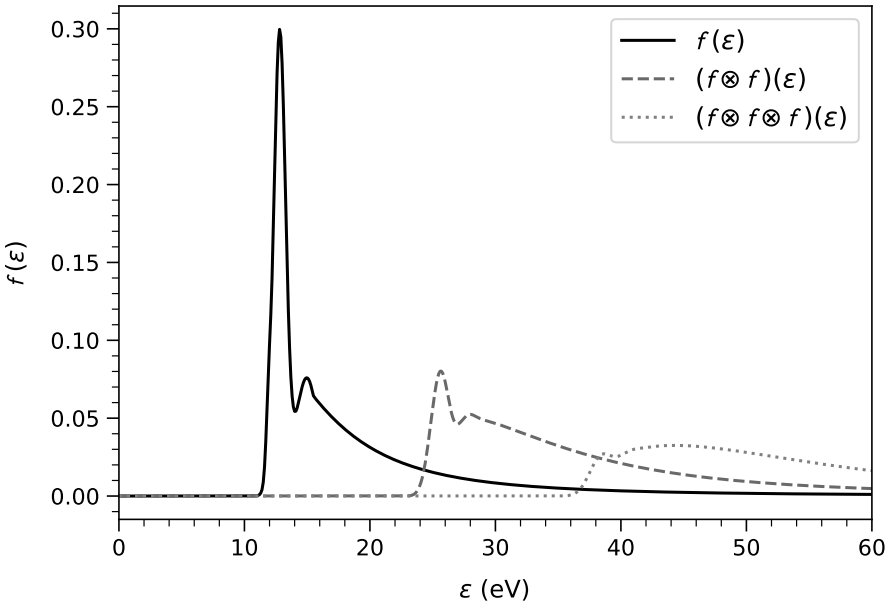

Figure 3.6.: Energy loss probability $f(\varepsilon)$ as it is applied in the neutrino mas analysis. The function is composed of a set of three Gaussians combined with a binary-encounter-dipole (BED) model to describe the ionisation continuum. The plot shows the energy loss probability for two-fold scattering (dashed line) and three-fold scattering (dotted line). The s-fold scattering energy loss probability is calculated by convolving the energy loss function s times with itself.

Based on [160, 159, 139], a parametrisation of the total inelastic scattering cross section has been derived by F. Glück (KIT) and is given as:

$$\sigma_{\text{inel}}(E_{\text{kin}}) = \frac{4\pi a_0^2 R}{E_{\text{kin}}} \left(M_{\text{total}}^2 \cdot \ln\left(4c_{\text{tot}} \cdot \frac{E_{\text{kin}}}{R} \right) - 0.0097 \right), \tag{3.29}$$

with $M_{\text{total}}^2 = 1.5356$ and $c_{\text{tot}} = 1.18$. For electrons at the endpoint, the total inelastic scattering cross section of molecular hydrogen is $\sigma_{\text{inel}}(18.6\,\text{keV}) = 3.64 \times 10^{-22}\,\text{m}^2$, which is larger by an order of magnitude compared to the elastic scattering cross section.

To describe the energy loss probability of inelastic scattering process with gaseous tritium, a semi-empirical model has been developed – the so-called energy loss function $f(\epsilon)$ [28]. In figure 3.6, the energy loss probability is plotted as a function of energy loss ε. The energy loss function used in the KATRIN neutrino-mass analysis is an improved parametrisation based on the work of Abdurashitov et al. [2], and Aseev et al. [45]. The function is composed of a set of three Gaussians combined with a relativistic binary-encounter-dipole (BED) model beyond the ionisation threshold $E_{\text{ionisation}}$. For tritium the ionisation threshold is $E_{\text{ionisation}}(\text{T}_2) = 15.486\,\text{eV}$ [251].

Combining both the Gaussians and BED model, the energy loss function is calculated with

$$f(\varepsilon) = \begin{cases} \sum_{j=1}^{3} a_j \exp\left(-\frac{(\varepsilon-\mu_j)^2}{2\sigma_j^2}\right) & , \varepsilon \leq E_{\text{ionisation}} \\ \frac{f(E_{\text{ionisation}})}{f_{\text{BED}}(E_{\text{ionisation}})} \cdot f_{\text{BED}}(\varepsilon) & , \varepsilon > E_{\text{ionisation}}. \end{cases} \tag{3.30}$$

The mean and width of each Gaussian are given by μ_j and σ_j. Furthermore, a_j are the amplitudes of the Gaussians. The three Gaussian components each approximate one group of molecular final states and are mainly centred in a region between 11 eV to 15 eV. Above the ionisation threshold, the BED model $f_{\text{BED}}(E_{\text{ionisation}})$ describes the ionisation continuum, which is based on [146]. To guarantee that both regions of the model are continuous, the BED function is normalised to the Gaussian sum at the ionisation threshold $f(E_{\text{ionisation}})$. [28] All function parameters are summarised in table 3.1.

Table 3.1.: Parameters and uncertainties of the energy loss function as it is used in the neutrino-mass analysis. The corresponding correlations can be found in appendix E.1. [28, 217]

Parameter	**Value**
μ_1	(11.919 ± 0.008) eV
μ_2	(12.805 ± 0.002) eV
μ_3	(14.968 ± 0.004) eV
σ_1	(0.184 ± 0.007) eV
σ_2	(0.468 ± 0.002) eV
σ_3	(0.907 ± 0.013) eV
a_1	(0.033 ± 0.001) eV^{-1}
a_2	(0.296 ± 0.001) eV^{-1}
a_3	(0.0757 ± 0.0003) eV^{-1}

The energy loss function parameters are determined from in-situ measurements performed with the e-gun. In these measurements, the transmission characteristics of mono-energetic electrons through the filled WGTS are measured, from which the parameters of the energy loss function are obtained. [28]

To describe the energy loss probability of multiple scatterings, the energy loss function is convolved with itself. In the case of s-fold scattering, the energy loss function is convolved s times to obtain $f_s(\varepsilon)$:

$$\begin{aligned} f_0(\varepsilon) &= \delta(\varepsilon) \\ f_1(\varepsilon) &= f(\varepsilon) \\ f_s(\varepsilon) &= (f \otimes f \otimes \ldots)(\varepsilon). \end{aligned} \tag{3.31}$$

The effect of the manifold scattering is illustrated for two and three scatterings in figure 3.6. In the standard neutrino-mass analysis, up to seven scatterings are taken into account.

3.4.3. Response function

Combining the transmission behaviour for electrons from the source through the main spectrometer with the energy loss due to scattering leads to the experimental response function $R(E,U)$. The response function is written as follows:

$$R(E,U) = T(\varepsilon,\theta,U) \otimes (P_0 \cdot \delta(\varepsilon) + P_1 \cdot f(\varepsilon) + P_2 \cdot (f \otimes f)(\varepsilon) + \dots). \tag{3.32}$$

Here, $T(\varepsilon,\theta,U)$ and $f(\varepsilon)$ correspond to the transmission function and energy loss function as described in sections 3.4.1 and 3.4.2. P_s are the scattering probabilities for s-fold scattering of the electrons. As electrons travel through the gas column within the WGTS, the scattering probabilities are strongly dependent on the column density ρd. Since the rest of the beamline is evacuated and hence has reduced pressure by more than five orders of magnitude, only scattering within the source is accounted for. The scattering probabilities are calculated from

$$P_s(z,\theta) = \frac{(\mathcal{N}(z,\theta)\cdot\sigma_{\text{inel}})^s}{s!} \cdot e^{-\mathcal{N}(z,\theta)\cdot\sigma_{\text{inel}}}. \text{ [147]} \tag{3.33}$$

This includes the integrated column density, $\mathcal{N}(z,\theta)$, that electrons starting at position z travel through. The WGTS has a length of $L = 10\,\text{m}$. The scattering probabilities up to the 7^{th} scattering are listed in table 3.2, illustrated for three different column densities.

Since electrons with large starting pitch angles θ travel on longer trajectories within the source, the integrated column density is angle dependent. The integrated column density is then given as

$$\mathcal{N}(z,\theta) = \frac{1}{\cos\theta} \int_z^L \rho\left(z'\right) \mathrm{d}z' \,. \tag{3.34}$$

Assuming that on average electrons start in the centre of the source (where $z = 0$) and see an effective source length of $L = {}^{\mathrm{d}}/_2$, this leads to

$$\mathcal{N}_{\text{eff}}(\theta) = \frac{1}{\cos\theta} \int_0^{\mathrm{d}/2} \rho \,\mathrm{d}z' = \frac{1}{\cos\theta} \cdot \frac{\rho\mathrm{d}}{2}. \tag{3.35}$$

The inputs for ρd are experimentally estimated from measurements with the e-gun. To first order it is assumed, that electrons within the acceptance angle θ_{max} are emitted isotropically, leading to an additional angular weighting of the scattering probabilities over the solid angle with $\omega(\theta) = \sin(\theta)$. The s^{th} scattering probability from equation (3.33) hence modifies to

$$\overline{P}_s = \int_0^{2\pi} P_s(z,\theta) \cdot \omega(\theta) \,\mathrm{d}\theta \tag{3.36}$$

$$= \frac{1}{1-\cos\left(\theta_{\text{max}}\right)} \int_0^{\theta_{\text{max}}} P_s(z,\theta) \cdot \sin(\theta) \,\mathrm{d}\theta \,. \tag{3.37}$$

Including the additional modification of isotropic weighting of the scattering probabilities,

Table 3.2.: Scattering probabilities up to $s = 7$ scatterings. Corresponding to the different conditions during neutrino-mass measurements, the probabilities are given for 22.2 %, 75.5 %, and 84.5 % of the nominal column density. In these configurations, the probability for electrons to experience no scattering is the largest. In comparison, one can see how one- and two-fold scattering significantly increase with column density.

Nominal ρd	P_0	P_1	P_2	P_3	P_4	P_5	P_6	P_7
22.2 %	78.67 %	18.01 %	2.91 %	0.37 %	0.04 %	0.00 %	0.00 %	0.00 %
75.5 %	47.99 %	29.62 %	14.27 %	5.59 %	1.84 %	0.52 %	0.13 %	0.03 %
84.5 %	44.75 %	29.60 %	15.53 %	6.67 %	2.42 %	0.76 %	0.21 %	0.05 %

the response function is written as:

$$\begin{aligned} R\left(E, qU\right) = &\int_{\theta=0}^{\theta_{\max}} \int_{\varepsilon=0}^{E-qU} \mathcal{T}\left(E-\varepsilon, \theta, qU\right) \cdot \sin(\theta) \\ &\cdot \left(P_0(\theta) \cdot \delta(\varepsilon) + P_1(\theta) \cdot f(\varepsilon) + P_2(\theta) \cdot (f \otimes f)(\varepsilon) + \dots\right) \mathrm{d}\theta \, \mathrm{d}\varepsilon \,. \end{aligned} \tag{3.38}$$

As applied in the neutrino-mass analysis, the response function is illustrated in figure figure 3.7. The function is given for a retarding energy of $qU = 18\,575\,\mathrm{eV}$. In addition, the components corresponding to s-fold scattering are highlighted in different shades of blue. Figure 3.7 (right) further includes a comparison of the scattering probabilities at $\theta_{\max}$ corresponding to the values listed in table 3.2.

So far, isotropic emission is assumed for electrons that are emitted within the source. Suppose electrons scatter; their angular distribution changes. Hence the angular distribution is non-isotropic after scattering. For this reason, the transmission function derived in section 3.4.1 is adapted for scattered electrons. The assumption $\omega(\theta) = \sin(\theta)$ modifies as follows for s-fold scattered electrons

$$\omega_s(\theta) = P_s \cdot \sin(\theta). \tag{3.39}$$

Propagating this into the transmission function leads to the individual, non-isotropic transmission functions $T_s^*(E, U)$ for s scatterings,

$$T_s^*(E,U) = \begin{cases} 0 & , \; E - qU < 0 \\ \int_0^{\theta_{\mathrm{tr}}(E,U)} \frac{P_s \cdot \sin(\theta)}{\overline{P}_s \cdot (1-\cos(\theta))} & , \; 0 \leq E - qU \geq \Delta E \\ 1 & , \; E - qU > \Delta E. \end{cases} \tag{3.40}$$

The factor $1/\overline{P}_s \cdot (1-\cos(\theta))$ is added normalising the transmission function. The transmission polar angle θ_{tr} is limited to

$$\theta_{\mathrm{tr}} \leq \arcsin\left(\sqrt{\frac{E-qU}{E} \frac{B_{\mathrm{src}}}{B_{\mathrm{ana}}} \frac{2}{\gamma+1}}\right). \tag{3.41}$$

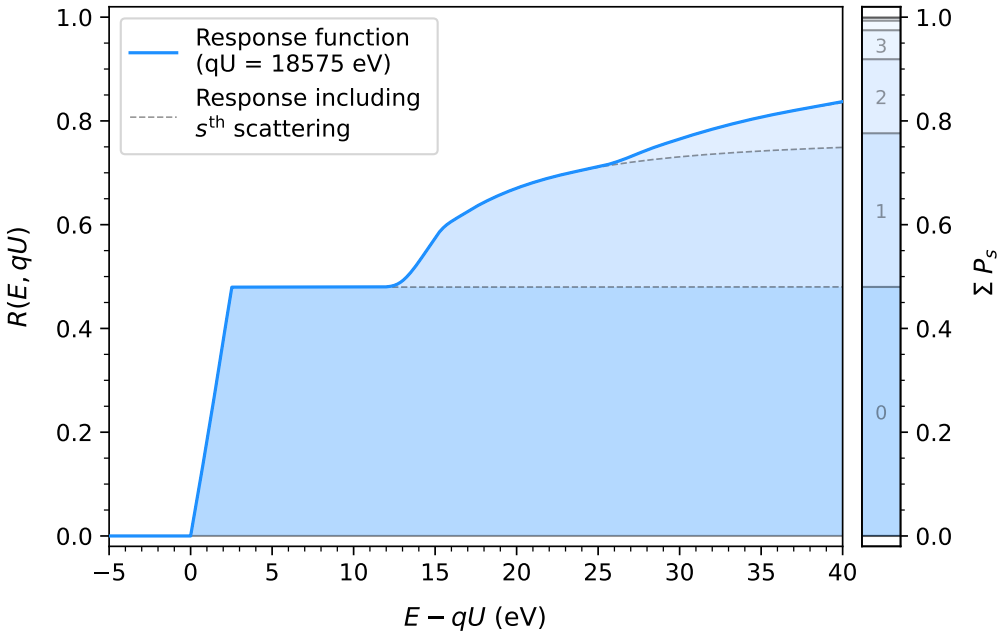

Figure 3.7.: Response function of the KATRIN experiment over surplus energy $E - qU$ (left). The response function is calculated for a retarding energy of 18 575 eV. Isotropic electron emission in the source is assumed. The individual components of s-fold scattering contributing to the response function are highlighted in different shades of blue. Corresponding to this, the cumulative scattering probabilities are illustrated in the right subplot (values given in table 3.2). The response function and scattering probabilities are calculated based on KNM5 with 75 % of the nominal column density. In both subplots, it is apparent that in this configuration, the majority of electrons (47.9 %) reach the detector unscattered. In comparison components corresponding to multiple scatterings s contribute less to the response function.

To avoid a potential bias on the squared neutrino mass on the order of $1 \times 10^{-2}\,\text{eV}^2$, the non-isotropic transmission function is taken into account in the analysis. As the additional integral can significantly increases the computation time it is only applied up to the first scattering. [120]

3.5. Doppler effect

Since the gaseous molecular tritium within the source is in thermal motion, the energy distribution is broadened due to the Doppler effect. This additional broadening is expressed as a convolution of the integrated tritium spectrum with a Gaussian kernel. The Gaussian kernel g follows[6] [136]

$$g(E-\varepsilon) = \frac{1}{\sigma_E\sqrt{2\pi}} e^{-\frac{1}{2}\left(\frac{(E-\varepsilon)-U_b}{\sigma_e}\right)^2} \quad \text{with} \quad \sigma_E = \sqrt{\frac{2Ek_\text{B}Tm_\text{e}}{M_{\text{T}_2}}}, \tag{3.42}$$

[6]The distribution is applied to the integrated spectrum in its non-relativistic approximation.

with an additional energy shift $U_b \approx v_u\sqrt{2Em_e}$. The additional shift is due to the gas flow with velocity v_u from the centre of the WGTS towards the pump ports on either end. The distribution is given for the kinetic electron energy E in the tritium molecule rest frame, and ε is the energy in the laboratory rest frame. The kernel, in addition, depends on the Boltzmann constant k_B, the source temperature T, the electron mass m_e, and the mass of the tritium molecule M_{T_2}. The Doppler broadening is applied as follows:

$$\left(g \otimes \frac{\mathrm{d}\Gamma}{\mathrm{d}E}\right)(E) = \int_{-\infty}^{+\infty} g(E-\epsilon)\frac{\mathrm{d}\Gamma}{\mathrm{d}E}\mathrm{d}\epsilon. \text{ [147]} \tag{3.43}$$

As the convolution involves an additional integration over the energy, the convolution has to be performed in each iteration when fitting the tritium data. In general, convolutions are associative. Using this knowledge, we write the final form of the integrated spectrum as a convolution of the integrated spectrum with the final state distribution, allowing us to apply the Gaussian convolution to the final state distribution,

$$g \otimes \frac{\mathrm{d}\Gamma}{\mathrm{d}E} = g \otimes \left(\frac{\mathrm{d}\Gamma}{\mathrm{d}E_f} \otimes \mathrm{FSD}\right) = \frac{\mathrm{d}\Gamma}{\mathrm{d}E_f} \otimes (g \otimes \mathrm{FSD})\,. \tag{3.44}$$

In this formulation, the Gaussian convolution only has to be performed once in the beginning. In fitting, only the broadened final state distribution is used when calculating the integrated tritium spectrum, making the calculation computationally much more efficient.

3.6. Integrated β-decay spectrum

Combining the response function $R(E, qU)$ (equation (3.38)) to describe the transport through the KATRIN beamline and the predicted differential β-decay spectrum of molecular tritium (equation (3.14)), the integrated β-spectrum $\dot{N}_{\mathrm{sig}}(qU)$ is calculated. The measured integrated β-electron rate for a given retarding energy qU is defined as:

$$\dot{N}_{\mathrm{sig}}(qU) = \mathrm{Sig} \cdot N_T \cdot \frac{\Omega}{4\pi} \int_{qU}^{E_0} \frac{\mathrm{d}\Gamma}{\mathrm{d}E} \cdot R(E, qU)\,\mathrm{d}E\,. \tag{3.45}$$

The rate is scaled by the number of tritium nuclei within the magnetic flux tube N_T. The number of tritium atoms in the source is given by the product of tritium purity ε_T, column density $\rho\mathrm{d}$ and the effective cross section A of the WGTS

$$N_T = 2 \cdot \varepsilon_T \cdot \rho\mathrm{d} \cdot A. \tag{3.46}$$

Furthermore, an additional signal factor (Sig) scales the model amplitude.[7] As electrons with a pitch angle larger than θ_{max} are magnetically reflected, only electrons within the solid angle Ω, contribute to the measured rate. The solid angle is given by

$$\Omega = \frac{2\pi}{1 - \cos(\theta_{\mathrm{max}})}. \tag{3.47}$$

[7] The signal factor is close to 1.0 and is added to account for potential scaling effects, for example, when applying different detector readout cuts to the measured energy spectrum (more information in section 3.10).

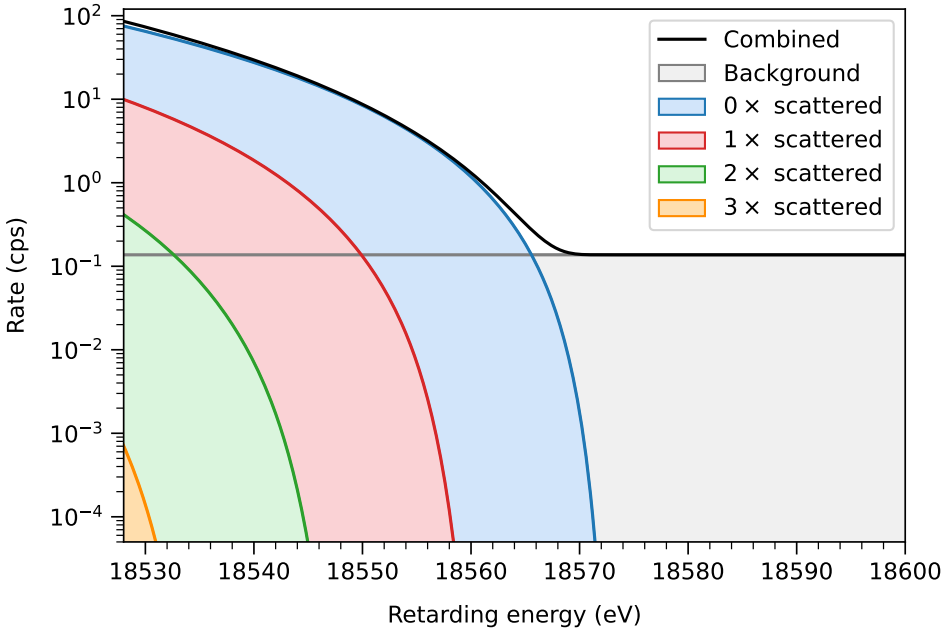

Figure 3.8.: Contribution of scattered electrons to the combined integrated tritium β-spectrum. The combined spectrum, including up to 7-fold scattering, is plotted in black. The measurement interval (40 eV below the endpoint), used for the neutrino-mass analysis, is mainly dominated by unscattered electrons (blue). Furthermore, 1× and 2× scattering (red and green) have a significant impact on the spectral shape. Higher orders of scattering have less impact on the final spectrum. Here only up to the 3× scattered electrons are depicted (orange). In addition, a background level of 136 cps (grey) is added to the spectrum. The inputs to the calculation are based on KNM5 with 75.5 % nominal column density.

In figure 3.8 the integrated β-spectrum is shown alongside a breakdown of the spectrum into its components of scattered electrons. As described in section 3.4.3, the figure illustrates that mainly unscattered electrons contribute to the spectrum.

Two examples of the integrated spectrum are displayed in figures 3.9 and 3.10. In figure 3.9, the signal imprint of the neutrino mass is displayed. The neutrino mass mainly changes the spectral shape close to the endpoint. Therefore, the imprint becomes most pronounced when looking at the relative difference to a spectrum with a zero neutrino mass. In addition, figure 3.10 includes the impact of sterile neutrinos on the spectral shape. Unlike active neutrinos, sterile neutrinos can cause a broader spectral shape difference, depending on the sterile neutrinos' mass. The active-to-sterile mixing amplitude changes the magnitude of the kink-like shape distortion. Both integrated spectra have been calculated including background. More details about the background are given in section 3.8. In the displayed comparison, the spectra have been generated with the same signal, endpoint and background. Only the neutrino mass is set to different values. In general, it should be noted that when fitting data, in addition to the squared neutrino mass, the signal, the background, and the endpoint are free parameters, making the imprint less pronounced when looking at the relative difference.

To calculate the predicted number of counts N_{sig}, the integrated count rate is further

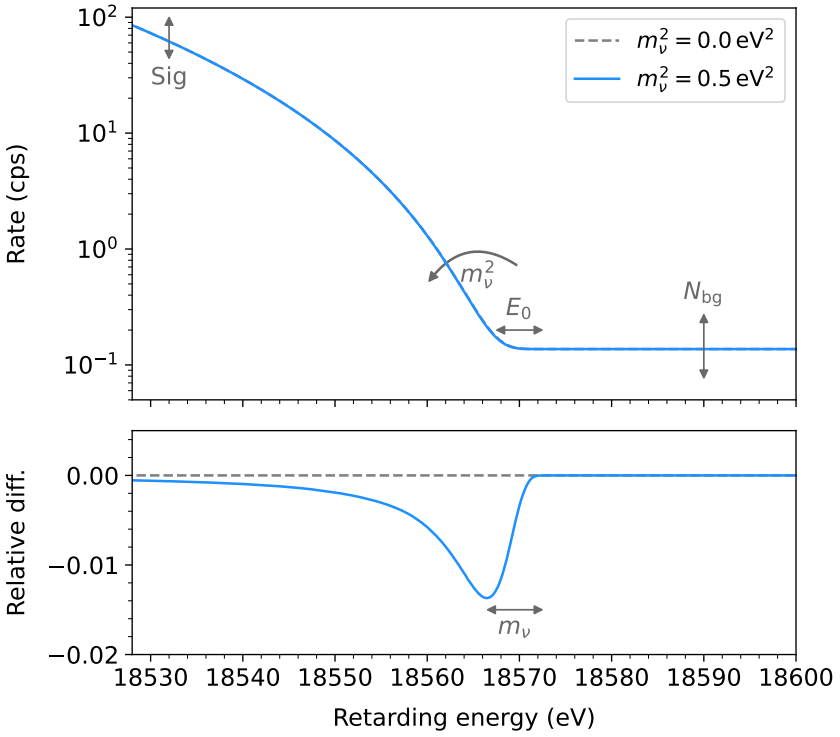

Figure 3.9.: Imprint of the neutrino mass on the integrated spectrum. In the top panel, the integrated spectrum is displayed over the retarding energy. In the most simple case, the spectrum is characterised by a signal Sig, endpoint E_0, background N_bg, and the squared neutrino mass m_ν^2. Hereby the imprint of the neutrino mass is most visible close to the endpoint. To enhance the feature, the relative difference of the spectrum with a neutrino mass, in comparison to a spectrum with a zero neutrino mass is displayed in the bottom panel.

integrated over the measurement time at a set retarding energy $t(qU)$. As KATRIN provides stable conditions, the integral reduces to a product of measurement time and integral rate. The measured number of decay electrons of scan step i is written as

$$N_\mathrm{sig}\left(qU_i\right) = \int_0^{t(qU_i)} \dot{N}_\mathrm{sig}\left(qU_i\right) \mathrm{d}t = \dot{N}_\mathrm{sig}\left(qU_i\right) \cdot t\left(qU_i\right). \tag{3.48}$$

3.7. Source potential effects

Due to the presence of low energy electrons and ionised molecules, a cold-magnetised plasma is created inside the WGTS. Considering the plasma within the source is especially important when measuring at higher column densities. The effects of the source plasma are differentiated into spatial and temporal variations. In this section, spatial and temporal variations are addressed. These can cause longitudinal or radial inhomogeneities. Time-dependent effects can result in slow drifts of the absolute source potential or high-frequency instabilities.

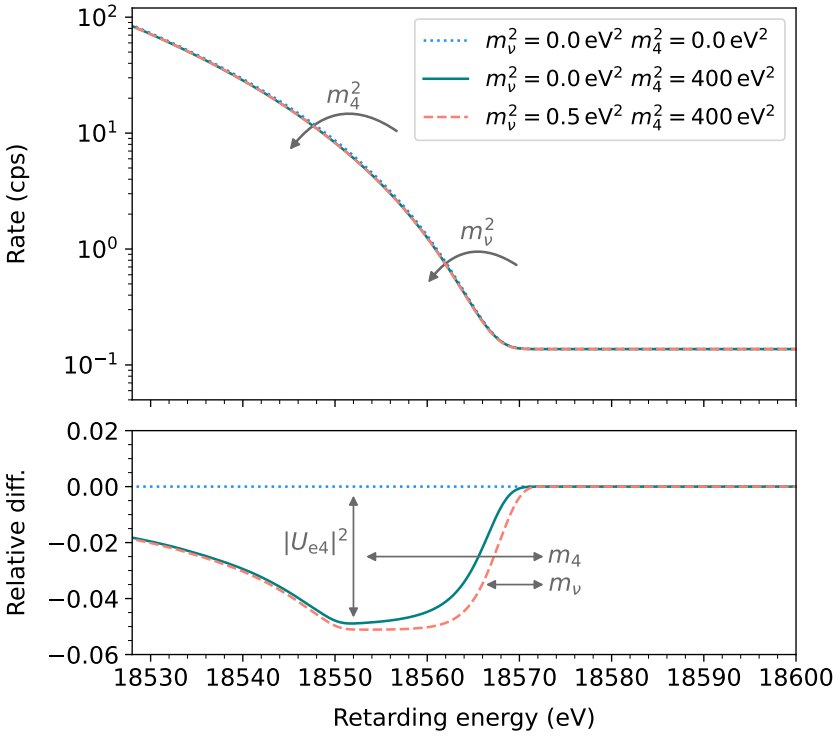

Figure 3.10.: Imprint of sterile neutrinos on the integrated spectrum. Here, a spectrum with no sterile neutrino and with a zero active neutrino mass is compared to a spectrum with only a sterile neutrino and one with both active and sterile neutrinos. The spectra including a sterile neutrino have been calculated with $m_4^2 = 400\,\mathrm{eV}^2$ and $|U_{e4}|^2 = 0.05$. The spectrum, including an active neutrino mass, has been calculated with $m_\nu^2 = 0.5\,\mathrm{eV}^2$. When looking at the relative difference (bottom), the imprint of sterile neutrinos impacts the entire spectral shape (teal). The magnitude of the imprint is given by the active-to-sterile mixing amplitude $|U_{e4}|^2$. In addition, an active neutrino (orange) impacts the shape difference close to the endpoint.

On the one hand, assuming stable plasma conditions, the absolute potential of the plasma has a negligible effect on the measured spectral shape. It is absorbed by free effective endpoint E_0 in the fit. On the other hand, radial variations are accounted for by allowing a radially varying endpoint in the fit. Longitudinal inhomogeneities and drifts of the plasma potential over time have to be taken into account within the model. [25]

If not taken into account, longitudinal plasma inhomogeneities can lead to a neutrino mass bias, following the quantitative equation

$$\Delta m_\nu^2 = -2\sigma_0^2 - \sum_i \epsilon_i \Delta_{i0}. \tag{3.49}$$

σ_0 is the weighted[8] spectral broadening caused by the inhomogeneous source potential, Δ_{i0} is the relative energy scale shift of the i^{th} scattering compared to unscattered electrons, multiplied with constant factors ϵ_i.

Within the model, the additional broadening due to the plasma is simply added to the

[8] The weighting is applied based on the spatial probability density function (pdf) of unscattered electrons.

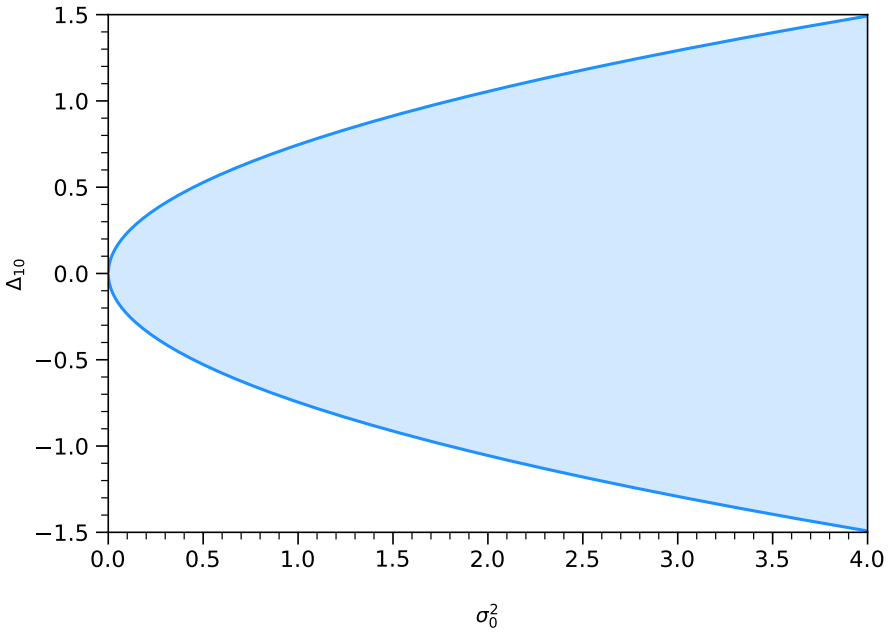

Figure 3.11.: Illustration of the mathematically allowed region for the energy loss shift Δ_{10} (outlined in blue). The allowed regions are given by the inequality in equation (3.51) spanning over the range $[-\kappa_i\sigma_0, +\kappa_i\sigma_0]$. The illustration is based on KNM2 with $\sigma_0^2 = (0.88 \pm 0.88) \times 10^{-3}\,\mathrm{eV}^2$ and $\kappa_1 = 0.746$.

doppler broadening σ_E as described in section 3.5. The longitudinal asymmetry results in an energy shift of the spectrum of scattered electrons relative to the spectrum of unscattered electrons.[9] This shift of the energy scale is propagated by a shift of the i^{th} energy loss function $f_i(\varepsilon)$ (section 3.4.2) leading to the shifted energy loss function $f_i(\varepsilon + \Delta_{i0})$. The relation of the plasma broadening σ_0 and the energy loss shift Δ_{i0} of the i^{th} scattering is given by the potential antisymmetry factor $\hat{\rho}_i$ and a constant κ_i[10] [171],

$$\Delta_{i0} = \hat{\rho}_i \kappa_i \sigma_0. \tag{3.50}$$

For a given inhomogeneity σ_0 of the potential, those potentials which are antisymmetric ($|\rho| = 1$) produce the largest $|\Delta_{i0}|$. In general, the mean antisymmetry factor $\hat{\rho}_i$ is therefore constrained and only allows a certain region. For the energy loss shift of each scattering relative unscattered electrons Δ_{i0}, the antisymmetric factor is limited to $\hat{\rho}_i = [-1, 1]$. The mathematically allowed region leads to the inequality derived by M. Machatschek [171],

$$|\Delta_{i0}| \leq \kappa_i \sigma_0. \tag{3.51}$$

The plasma broadening is extracted experimentally from calibration measurements with gaseous krypton. Analysis of the linewidth of quasi-monoenergetic conversion lines of $^{83\mathrm{m}}$Kr reveals information about σ_0. An example of such an $N_{2,3}$ line analysis is given in figure 3.12. The displayed data was collected during KNM5 in patch 0. The figure also

[9] Electrons that experience scattering are mainly generated in the upstream end of the source since these electrons have to travel through more gas. Electrons that are able to leave the source unscattered are mainly dominated by electrons generated in the downstream end of the WGTS. As a consequence, electrons of different scattering probabilities start in a different source potential.

[10] κ_i is dependent on the column density and hence is different for each measurement campaign.

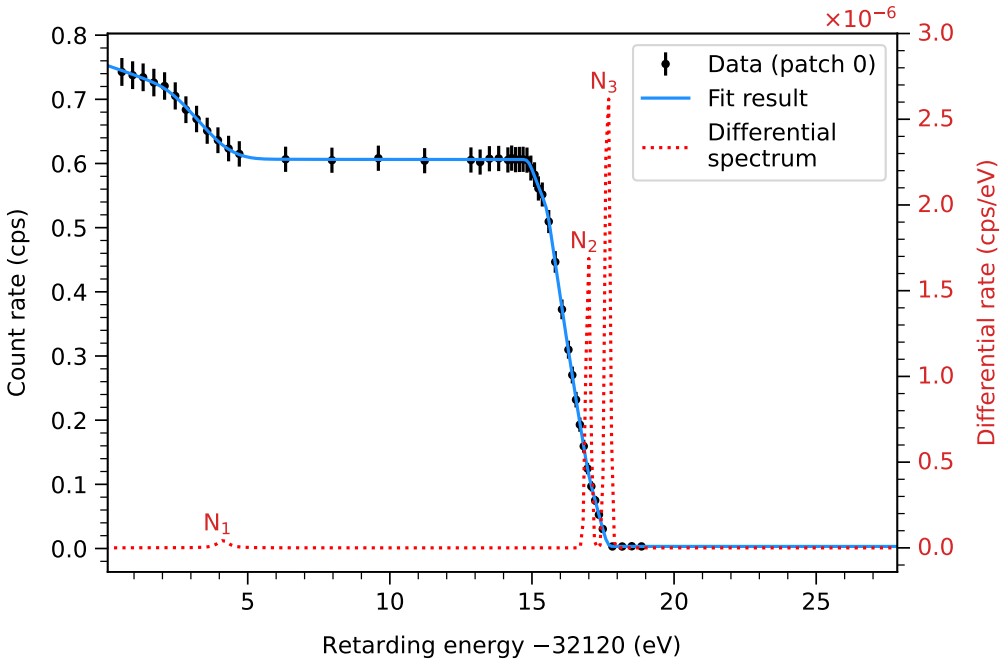

Figure 3.12.: Example of a N_{23}-line spectra of ^{83m}Kr measured with KATRIN (black) as well as a fit to the data (blue). In addition, the plot contains the differential spectrum where one can see the distinct N_1, N_2, and N_3 lines (red). The data shown was collected during KNM5 and corresponds to patch 0. A fit to the data provides information about the broadening σ_0, and energy loss shifts Δ_{i0}, due to the longitudinal plasma profile. Data and fit result provided by M. Machatschek.

includes the fit result in blue and the differential spectrum in red. The differential spectrum shows the positions and amplitudes of the N_1, N_2, and N_3 lines.

In particular, the N_2-32 and N_3-32 doublet and the L_3-32 transition are suitable to determine the broadening.[11] The $N_{2,3}$ lines have negligible natural linewidth compared to spectral broadening due to the plasma. However, the intensity is comparatively lower. The L_3 line, in comparison, offers the advantage of higher intensity but also has the disadvantage that the natural line width is not precisely known. In the dedicated calibration measurements, krypton is co-circulated with tritium at $\sim 80\,\mathrm{K}$.[12] It is assumed that the longitudinal plasma profile within the source is not affected by the admixture of trace amounts of krypton.

During measurement campaigns, slow shifts and drifts in the plasma potential can occur due to changes in the rear wall bias voltage, changes in the work function, and plasma conditions. The maximum possible plasma potential shift and drift are obtained from the broadening of the endpoint distribution over the scans and is determined from fits on "window blind" data.[13] The broadening on the endpoint fit result is taken into account in

[11] The energy of conversion electrons of the N_2-32 and N_3-32 doublet is around 32.137 eV and 32.137 eV. The energy of electrons from the L_3-32 transition is around 30.472 eV. [248]

[12] Calibration measurements including krypton have to be performed at around 80 K to avoid condensation of krypton.

[13] "Window blind" data refers to scans that exclude the spectral data points that are used for the neutrino-mass analysis in order to avoid double usage of data.

the neutrino-mass analysis via an additional broadening parameter $\sigma^2_{\text{shift,drift}}$.

From the scan-wise endpoints the mean weighted endpoint is given as

$$\langle E_0 \rangle = \frac{\sum w_i \cdot E_{0,i}}{\sum w_i}. \tag{3.52}$$

In order to account for different scan lengths, the endpoint results are weighted with the corresponding effective measurement time of each scan $w_i = t_i$. The weighted standard deviation is calculated as

$$\sigma_{E_0} = \sqrt{\frac{\sum w_i \cdot \left(E_{0,i} - \langle E_0 \rangle\right)^2}{\sum w_i}}. \tag{3.53}$$

Furthermore, the expected statistical uncertainty is given by

$$\langle \sigma_{E_0,\text{stat.}} \rangle = \frac{\sum w_i \cdot \sigma_{E_0,i}}{\sum w_i}. \tag{3.54}$$

The variance is then calculated as the difference (in quadrature) between the width and the expected width,

$$\sigma^2_{\text{shift,drift}} = \sigma^2_{E_0} - \langle \sigma_{E_0,\text{stat.}} \rangle^2. \tag{3.55}$$

This variance $\sigma^2_{\text{shift,drift}}$ is interpreted as the additional broadening due to shifts or drifts of the plasma conditions or other unknown effects. Similarly to the broadening due to a longitudinal plasma profile, the shift and drift broadening is added to the Doppler broadening σ_E and applied to the FSD as described in section 3.5

3.8. Spectrometer background

One of the most important things to account for within the model is the background contribution, which influences the neutrino mass sensitivity and, if not correctly modelled, can lead to a bias of the neutrino mass. The background model is composed of three major components: A flat background base $N_{\text{bg}}^{\text{base}}$, a potential qU-dependence of the background $N_{\text{bg}}^{\text{slope}}(qU_i)$, as well as a component increasing within the measurement time of a single scan step $N_{\text{bg}}^{\text{Penning}}(t(qU_i))$. The total expected background counts are hence written as

$$N_{\text{bg}}^{\text{total}}(qU_i) = N_{\text{bg}}^{\text{base}} + N_{\text{bg}}^{\text{slope}}(qU_i) + N_{\text{bg}}^{\text{Penning}}(t(qU_i)). \tag{3.56}$$

All three components are described in the following sections 3.8.1 to 3.8.3. An example for each component and the resulting total background rate is seen in figure 3.13.

3.8.1. Flat background

The main component of the background originating from the main spectrometer is

$$N_{\text{bg},i}^{\text{base}} = \text{Bg} \cdot t_i. \tag{3.57}$$

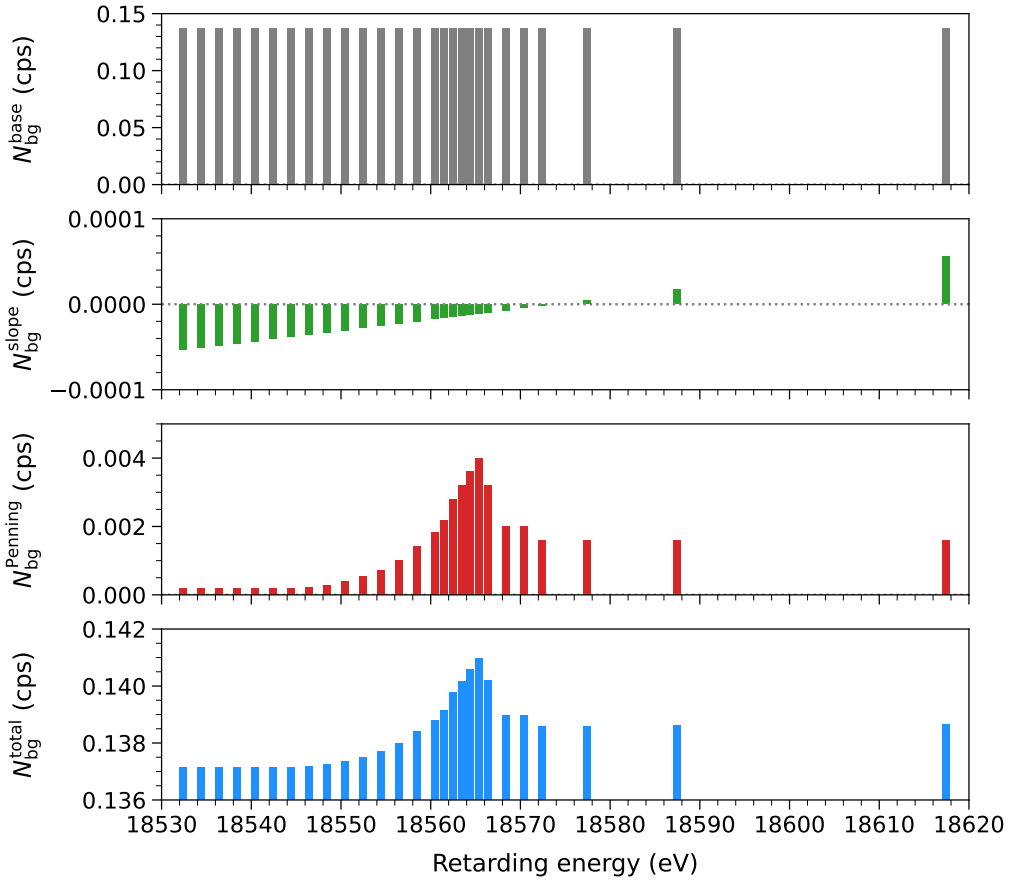

Figure 3.13.: Example composition of the background model. The background model comprises three major components: A flat background base N_{bg}^{base}, a potential high voltage-dependent background slope $N_{bg}^{slope}(qU_i)$, and an over measurement time increasing background $N_{bg}^{Penning}(t(qU_i))$. All three components result in the total background rate $N_{bg}^{total}(qU_i)$. The values used in this figure correspond to the inputs used in the KNM3a analysis.

The number of expected background electrons is given by the background rate Bg multiplied by the measurement time t_i of the i^{th} scan step. This background is created by a variety of processes.

Contributions due to cosmic muons or gamma rays interacting with the stainless steel walls [126] are reduced by the inner electron system (see section 2.2.2.1) as well as a veto system (see section 3.10).

The dominant source of the background is due to polonium and radon. On the one hand, α-decays of ^{210}Po implanted within the spectrometer walls, create a recoiling ^{206}Pb ion which can result in the sputtering of atoms from the vessel surface. These sputtered atoms can be released in excited states – so-called Rydberg states.[14] Rydberg atoms are electrically neutral and can propagate freely. Such highly excited atoms can propagate into

[14] As a leading contributor, hydrogen is assumed to be the primary Rydberg atom species. In addition, other atom species can be sputtered from the surface. Since oxygen is abundant on the steel surface, it is an interesting Rydberg candidate. The dissociation of oxygen molecules with light can result in autoionising oxygen states and free background electrons. [133]

the sensitive flux tube volume and can be ionised by black-body-radiation, isotropically creating very low energetic electrons in the sensitive volume. [108, 242, 214, 133]

On the other hand, the second major background source is due to radon isotopes such as ^{220}Rn present in the spectrometer surface and ^{219}Rn that is emanated from the NEG and can not fully be retained by the cooled baffle system. The radon subsequently decays in the main spectrometer, creating primary electrons within the magnetic flux tube. These electrons are most likely magnetically trapped, ionising residual gas within the magnetic flux tube [107, 178]. The background due to radon increases the overall background and results in coinciding electrons, creating a non-Poissoninan background component.

The low energy electrons from all processes described above are accelerated by the retarding potential within the volume downstream of the analysing plane towards the FPD. These measured background electrons are indistinguishable from signal β-electrons and hence are accounted for in the model. ß In addition to the spectrometer background, the detector has an intrinsic background which is between 13 mcps to 21 mcps[15] [133], contributing to the flat background base.

3.8.2. High voltage-dependent background slope

Previous measurements investigating the high voltage-dependence of the background have been presented in [126, 242, 133]. Hereby, in particular, a smooth high voltage-dependence has been found for retarding energies $qU < 10\,\text{keV}$. The high voltage-dependence is assumed to level out for larger retarding potentials. Nevertheless, it can not be fully excluded that a small high voltage-dependence remains. Electrons, for example originating from radon decay, are created with different surplus energies, hence leading to different trapping probabilities, which could be a reason for a remaining retarding voltage-dependency. An additional component is added to the background model to account for the possible existence of this qU dependence. The high voltage-dependent background $N_{\text{bg}}^{\text{slope}}(qU)$ is described by

$$N_{\text{bg}}^{\text{slope}}(qU) = a \cdot (qU - qU_{\text{ref}}). \tag{3.58}$$

The background slope is implemented pivoting around the reference retarding potential qU_{ref}. The reference retarding potential is introduced to offset the additional background slope contribution to be zero, 15 eV above the T_2 endpoint.[16] This means qU_{ref} is chosen to be 18 588.7 eV. As illustrated in figure 3.13, the impact of a potential background slope is small compared to the Penning trap induced background (see section 3.8.3).

3.8.3. Penning trap induced background

The third component of the background model is induced by the filling of a Penning trap. As described in section 2.2.2.2, if both pre- and main spectrometers are operated on high voltage, a Penning trap is created between the spectrometers inside superconducting magnet PS2. [195, 247]

[15] The intrinsic detector background depends on the region of interest cut applied to FPD data (ROI) and increases with wider ROIs. The values given here refer to the intrinsic backgrounds of an ROI of 14 keV to 32 keV and a broader region of 22 keV to 34 keV.

[16] The position of the pivot point is arbitrary. Setting the position close to the endpoint makes the interpretation of the fit absolute background scale easier.

This trap is gradually filled with an increasing number of low energetic electrons that are not able to overcome either of the retarding potentials. Stored electrons propagate through the trap, eventually scattering on residual gas, producing a positive ion as well as secondary electrons. Secondary electrons fill the trap over time, enhancing the mechanism. The positive ions, on the other hand, are accelerated by the electric potential towards the vessel walls and can result in sputtering on the spectrometer surface. Between scan steps, the stored electrons are removed from the Penning trap with the so-called Penning wiper, resetting the trap before the next scan step. This leads to a background component that increases over the measurement time within one scan step. The increasing scan-step-duration-dependent background component is given by integral of the increasing background rate s over time, resulting in

$$N_{\mathrm{bg}}^{\mathrm{Penning}}(t_i) = \frac{1}{t_i} \int_0^{t_i} s \cdot t \mathrm{d}t = \frac{1}{2} \cdot s \cdot t_i. \tag{3.59}$$

Here, t_i denotes the weighted mean length of a single scan step. The weighted length of scan step i, is given by summing over all I scans taken within one measurement campaign:

$$t_i = \frac{\sum_j^I t_{i,j} \cdot t_{i,j}}{\sum_j^I t_{i,j}}. \tag{3.60}$$

As seen in figure 3.13, the scan-step-duration-dependent background component strongly resembles the measurement time distribution and is not equally high in each scan step. Scan steps with longer measurement time result in a larger expected additional background.[17]

3.9. Rear wall spectrum

As tritium is continuously pumped through the WGTS, it is deposited on the surface of the rear wall. This accumulating tritium creates an additional underlying tritium spectrum that is measured with the FPD during neutrino-mass measurements. If not accounted for, the imprint of the secondary spectrum leads to a negative bias of the measured neutrino mass $\mathcal{O}(1 \times 10^{-2}\,\mathrm{eV}^2)$. The impact of an additional rear wall spectrum is illustrated in figure 3.14. The secondary tritium spectrum contributes significantly, also when compared to the total background rate. When looking at the relative impact of the rear wall spectrum, the expected negative bias is explained by the overdispersion of electrons in the endpoint region.

The rear wall spectrum is included in the model following the same description as the β-decay spectrum of electrons originating from gaseous tritium in the WGTS. Both spectra share most parameters when performing the analysis with some exceptions.

As rear wall electrons start outside the WGTS magnetic field, their starting magnetic field is mainly generated by the superconducting magnet behind the rear wall, leading to a field strength of 1.23 T at the position of the rear wall. This reduced magnetic field leads to an increased flux tube size, as well as a reduced acceptance angle θ_{max} of electrons.

[17] It should be noted that the scan-step-duration-dependent background only needs to be added when the prespectrometer was operated. From KNM5 onwards, the prespectrometer was set to a very small voltage (grounded vessel, and with the inner electrodes partially set to ∼100 V) in order to eliminate the Penning trap.

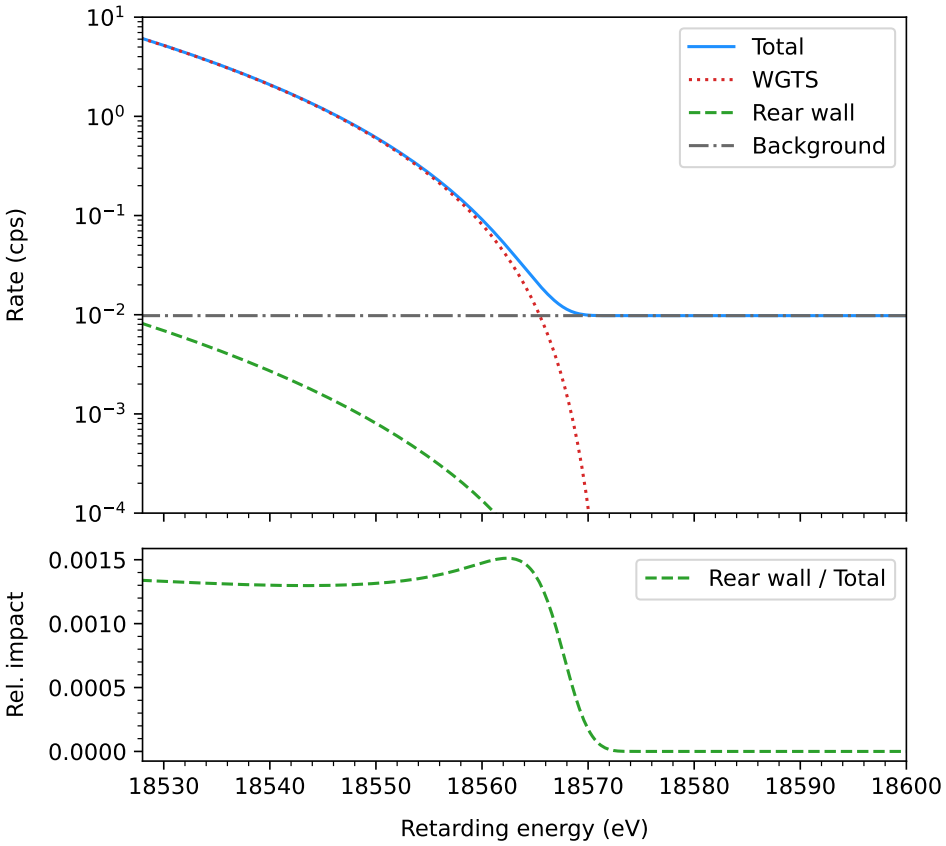

Figure 3.14.: llustration of an additional rear wall spectrum contribution. **Top:** The total combined spectrum (solid blue) comprises three components: The WGTS spectrum (dotted red), a background (dash-dotted grey), and an additional decay spectrum originating from the rear wall (dashed green). Compared to WGTS electrons, electrons originating from the rear wall are more likely to scatter as they have to traverse the entire length of the WGTS.
Bottom: Display of the relative impact of the rear wall spectrum in comparison to the total spectrum. An unaccounted rear wall spectrum would result in an overdispersion of electrons in the endpoint region which would cause a negative bias of the squared neutrino mass. The here displayed spectra are based on KNM5 with a rear wall signal of around 0.2 % and a rear wall endpoint of 18 575.98 eV.

Additionally, the rear wall spectrum is defined by a separate normalisation $\mathrm{Sig_{rw}}$ factor, a separate endpoint $\mathrm{E_{0,rw}}$, and the FSD shape parameter $w_{\mathrm{GS,rw}}$ which allows for additional uncertainty on the $\mathrm{T_2}$ FSD (for more details, see section 6.3.3.1). As electrons are emitted from the rear wall surface, they experience different work function conditions, which is directly reflected in the comparatively increased endpoint.

β-electrons from the rear wall are transmitted from the upstream end of the WGTS. Hence all electrons have to traverse the entire source length, leading to increased scattering probabilities. This increase is taken into account by integrating equation 3.35 over the entire source length $\mathrm{d} = 10\,\mathrm{m}$.

3.10. Detection efficiency

The combined detection efficiency $\varepsilon_{\mathrm{det}}$ results from a variety of detector effects that are taken into account and are described in the following. The detection efficiency is

$$\varepsilon_{\mathrm{det}} = \varepsilon_{\mathrm{const}} \cdot \varepsilon_{\mathrm{pu}}\left(\dot{N}\right) \cdot \varepsilon_{\mathrm{bs}}\left(qU\right) \cdot \varepsilon_{\mathrm{ROI}}\left(qU\right). \tag{3.61}$$

To first order, the detector is interpreted with a constant, energy-independent detection efficiency $\varepsilon_{\mathrm{const}}$. This base efficiency is 95 %. In addition to this, rate, energy, and anglular-dependent efficiency corrections are accounted for in the analysis. The corrections are distinguished into a rate-dependent pile-up correction $\varepsilon_{\mathrm{pu}}$ and two energy-dependent corrections, $\varepsilon_{\mathrm{bs}}$ and $\varepsilon_{\mathrm{ROI}}$. Since tritium β-electrons are indistinguishable from background electrons in the integrated spectrum, the combined detection efficiency is multiplied to both, the signal counts (see equation (3.48)) and background counts (see equation (3.56)) of each scan step i, leading to

$$N_{\mathrm{total}}\left(qU_i\right) = \varepsilon_{\mathrm{det}}\left(qU_i\right) \cdot \left(N_{\mathrm{sig}}\left(qU_i\right) + N_{\mathrm{bg}}^{\mathrm{total}}\left(qU_i\right)\right). \tag{3.62}$$

In addition to this, an anglular-dependent detection efficiency $\varepsilon_{\mathrm{ang}}(\theta_{\mathrm{src}})$ is applied to the response function, described in section 3.10.4.

3.10.1. Pileup

The readout of electrons arriving at the focal plane detector is based on a DAQ system that relies on a two-level trigger system. Electrons that impact on the detector cause a step-like detector response, proportional to the electron energy. Subsequently, two trapezoidal filters detect the signal. [36, 227] The filters are characterised by the shaping length $L = 1.6\,\mu\mathrm{s}$ and the gap length $G = 200\,\mathrm{ns}$. With the shaping length and the gap length, the event window length is calculated with

$$W = L + G + 26\,\mathrm{ns}. \tag{3.63}$$

This leads to an event window length of $W = 1.826\,\mu\mathrm{s}$. An additional semi-empirical correction of 26 ns is added to account for a slight gradual increase at the beginning of the trapezoidal filters and an exponential decay effect after charge accumulation.

If high electron rates are recorded at the FPD, electrons arrive within short time intervals. If the arrival time of two electrons is not long enough, only one trigger is recognised, and rather than two electrons, one single electron is recognised with an energy that corresponds to the combined energy of both electrons. These pile-up events lead to a distortion of the recorded spectrum. To correct for the distortion, a rate-dependent detection efficiency is multiplied with the integrated spectrum. The pile-up correction is calculated with the following,

$$\varepsilon_{\mathrm{pu}}(\dot{N}) = \left(1 - \frac{\alpha}{2}\right) \cdot \exp\left(-2\dot{N} \cdot W\right) + \frac{\alpha}{2}, \tag{3.64}$$

where the he scale factor α is $\alpha = 0.215$. [91]

The effect pile-up has on the measured energy spectrum can be seen in the exemple detector response displayed in figure 3.15. Multiplicity events result in the characteristic pileup spectrum above the main peak.

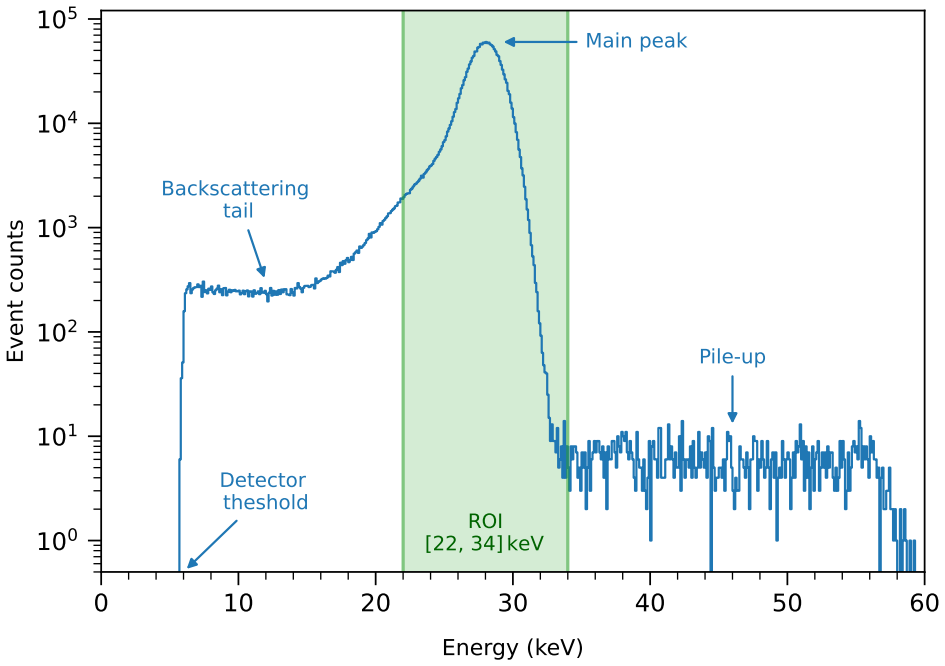

Figure 3.15.: Characteristics of the energy spectrum measured by the FPD. The energy histogram corresponds to a retarding voltage setpoint of 18 281 eV which is taken as a reference measurement for every scan. The data was taken during KNM5 (run 68567) and is displayed for patch 0. Electrons are only detected above the detection threshold. The majority of electrons are able to deposit their entire energy and are contained in the main peak within the ROI. The peak position is shifted by 10 keV due to the post-acceleration voltage. Electrons that are backscattered only deposit a fraction of their energy, resulting in a low-energy backscattering tail. Multiplicity events result in the characteristic pile-up structure above the main peak. Here the pile-up structure is dominated by two coinciding electron events.

3.10.2. Backscattering

Electrons hitting the detector deposit their energy by elastic and inelastic interactions in the silicon bulk of the FPD. Depending on the energy and impact angle, the impinging electrons can also only partially deposit energy in the detector and are backscattered. The backscattering probability is mainly dominated by the electron incident angle θ_{FPD}. The effect of partial energy deposition followed by backscattering can be seen in the detector response depicted in figure 3.15. Backscattering results in a tail-like distortion of the measured energy spectrum towards lower energies. To counteract this effect and decrease the backscattering probability, electrons are collimated towards steeper angles by a boosting post acceleration voltage of $U_{\mathrm{PAE}} = 10\,\mathrm{kV}$.

Backscattered electrons are likely to be backreflected towards the detector. The backreflection can either be invoked by the detector magnetic field, the pinch magnetic field, the post-acceleration electrode potential or even the potential of the main spectrometer. If electrons are backreflected within a short time span and within the same detector pixel, the second energy deposition piles up with the first deposition of energy, leading to a single measured electron event. On the other hand, electrons with small escape angles are unlikely

to be magnetically backreflected. With low probability, if the backscattering energy is larger than the main spectrometer retarding potential, a small number of electrons can even overcome the retarding potential and are lost. As a consequence, part of the initial electron energy is lost.

Based on simulations, this results in an estimated energy-dependent backscattering loss of $\varepsilon_{\mathrm{bs}} \sim 0.1\,\%\mathrm{keV}^{-1}$ which is taken into account in the analysis [91].

3.10.3. Region of interest cut

To improve the data quality, only electrons within a certain region of interest cut applied to FPD data (ROI) are summed and used for the neutrino-mass analysis. The ROI is applied to optimise the signal-to-background ratio and reduce the number of pile-up events, and is specific to individual detector wavers. In measurements of the β-spectrum, the ROI is typically chosen to be either in a fixed wide range of [14, 32] keV or in a fixed narrow range of [22, 34] keV.

The ROI remains constant for all scan steps within a scan and throughout a measurement campaign. As shown in figure 3.15, the ROI spans over the width of the main peak. As the shape of the measured energy spectrum slightly distorts with the retarding potential, the data coverage consequently depends on the main spectrometer retarding potential. To correct for the high voltage-dependent coverage, an additional detection efficiency $\varepsilon_{\mathrm{ROI}}$ is applied to the model.

Ideally, the ROI efficiency would be calculated by comparing the coverage at scan step qU_i compared to the coverage at the endpoint:

$$\varepsilon_{\mathrm{ROI}} = \frac{N_{qU_i}[\min(\mathrm{ROI}),\, \max(\mathrm{ROI})]}{N_{E_0}[\min(\mathrm{ROI}),\, \max(\mathrm{ROI})]}. \tag{3.65}$$

Technically this is challenging, as rates at the endpoint are small, and the reference coverage value would strongly fluctuate for the endpoint or require long measurement times.

As a proxy, the correction is estimated based on reference measurements taken at the beginning of every scan.[18] To emulate the losses due to the energy histogram distortion, the events within a shifted ROI are compared to the reference energy spectrum. The sliding ROI is shifted by $\Delta qU_i = E_0 - qU_i$. The ratio then gives the efficiency,

$$\varepsilon_{\mathrm{ROI}} = \frac{N[(\min(\mathrm{ROI}) + \Delta qU_i), (\max(\mathrm{ROI}) + \Delta qU_i)]}{N[\min(\mathrm{ROI}),\, \max(\mathrm{ROI})]}. \tag{3.66}$$

In general, this correction is small for the typical neutrino-mass analysis window, for completeness it is nevertheless applied to the model.

3.10.4. Angular-dependent detection efficiency

The fourth detector-related correction concerns the relative efficiency of electrons with respect to the detector incident angle θ_{FPD}. Based on simulation, it was observed that the

[18] The reference detector response is measured at ∼300 eV below the endpoint. Regular reference measurements furthermore allow for the monitoring of different detector properties over time, such as changing energy resolution or drifting peak positions. These can drift with temperature changes of the detector or the readout electronics.

measured energy spectrum distorts depending on θ_{FPD}. This pitch angle dependence also leads to different ROI coverage, which distorts the overall transmission function shape. If not considered, this would lead to a bias of the neutrino mass on the $10^{-4}\,\mathrm{eV}^2$ level. [176]

The correction is based on the simulation of mono-energetic and mono-angular electrons hitting a silicon body.[19] As described in section 3.10.2, with large pitch angles, more electrons are expected to backscatter, proportionally increasing the backscattering tail of the energy spectrum. Energy spectra for different simulated WGTS emission angles θ_{src} were then added, weighted by the solid angle, up to the cut-off angle [176]. From this, the calculated mono-angular detection efficiency is approximated by a polynomial of second order,

$$f(\theta_{\mathrm{src}}) = c_0 \left(1 + \frac{c_2}{c_0} \cdot \theta_{\mathrm{src}}^2\right). \tag{3.67}$$

c_0 is the zero angle efficiency and strongly depends on the ROI as this determines the cut-off angle up to which the spectra are summed. The angular relative efficiency is the fraction c_2/c_0. Since the model describes the integrated β-electron rate that is emitted isotropically, the mono-angular detection efficiency (equation (3.67)) has to be integrated over the source angle, weighted by the solid angle. This leads to the following expression:

$$\varepsilon_{\mathrm{ang}}(\theta_{\mathrm{src}}) = \frac{\int_0^{\theta_{\mathrm{src}}} c_0 \left(1 + \frac{c_2}{c_0} \cdot \theta_{\mathrm{src}}^2\right) \cdot \sin(\theta)\mathrm{d}\theta}{\int_0^{\theta_{\mathrm{src}}} \sin(\theta)\mathrm{d}\theta} \tag{3.68}$$

$$= c_0 \cdot \left(1 - \frac{c_2}{c_0} \cdot \left(2 - \theta_{\mathrm{src}}^2 - \frac{\theta_{\mathrm{src}} \cdot (2 \cdot \sin(\theta_{\mathrm{src}}) - \theta_{\mathrm{src}})}{(1 - \cos(\theta_{\mathrm{src}}))}\right)\right). \tag{3.69}$$

The weighted angular detection efficiency $\varepsilon_{\mathrm{ang}}(\theta_{\mathrm{src}})$ is further renormalised with the weighted angular detection efficiency of the maximum pitch angle $\varepsilon_{\mathrm{ang}}(\theta_{\mathrm{max}})$. To apply the normalised efficiency, the transmission probability (see equation (3.22)) is multiplied by the efficiency before integration.

[19] Simulations are performed using a Monte Carlo simulation code for low-energy electron interactions in silicon detectors (KATRIN electron silicon scattering (`KESS`)). The resulting energy spectra were then propagated into the detector readout simulation (`DRIPS`) code. The derived angular detection efficiencies are based on simulations of 28.6 keV electrons.

4. Statistical methods and analysis tools

This chapter summarises the analysis tools and statistical methods applied in the analysis and studies of the integral β-spectrum in the context of this thesis.

To fit the measured data, the Likelihood is constructed, which is then reformulated into a χ^2 (see section 4.1). In this particular analysis, both normal and Poissonian probability density functions are combined. For the analyses, the treatment of systematics is crucial. Here, two different methods were applied (sections 4.2.1 and 4.2.2).

Different methods of parameter estimation and uncertainties are outlined in section 4.3. Finally, upper limits are set if a central value is found that includes zero within the range of uncertainties or in the case of negative squared neutrino mass results. This is illustrated in section 4.4.

The main neutrino-mass analysis and sterile neutrino analysis presented in this thesis are performed with `KaFit` (section 4.5.2), which is part of the `KASPER` suite (section 4.5). Model calculations are based on the source and spectrum calculation code `SSC` (section 4.5.1).

> In the context of this thesis, a variety of extensions have been implemented in the `KASPER` framework. Within `KaFit` this includes the addition of a combined χ^2 function that allows for a combination of a normal and Poisson different probability density functions. This is an essential requirement for the combined analysis of the first five KATRIN science runs. The first analysis with the combined χ^2 was published in [25]. Different treatments of systematic effects have been included in the neutrino-mass analysis, such as the covariance matrix approach and the pull-term approach. This work further included code developments for: χ^2 profiling, parameter grid searches, the construction of different confidence belts, and limit calculations. Furthermore, two Python-based libraries were added to the `KASPER` framework, which allow for easy visualisation and interpretation of fit results (`KaFigure`), and the analysis of slow control parameters (`KaFitSlowControlAnalysis`). Lastly, the Bayesian analysis tool `katrin-MCMC` was developed for the analysis of tritium and krypton spectra with `KaFit`.

4.1. Likelihood definition

A likelihood function is defined to estimate parameter values. The likelihood function $\mathcal{L}(\vec{\Theta}|\vec{N}_{\text{obs}})$ is a mathematical evaluation to calculate the probability of how likely the proposed parameter set $\vec{\Theta}$ is, with respect to the observed data $\vec{N}_{\text{obs}}$. This formulation is

equivalent to the probability $\mathcal{P}(\vec{N}_{\mathrm{obs}}|\vec{\Theta})$ of observing the measured data $\vec{N}_{\mathrm{obs}}$, given the parameter set $\vec{\Theta}$,

$$\mathcal{L}(\vec{\Theta}|\vec{N}_{\mathrm{obs}}) = \mathcal{P}(\vec{N}_{\mathrm{obs}}|\vec{\Theta}) = \prod_{i=0}^{I} f(N_{\mathrm{obs},i}|N_{\mathrm{theo}}(qU_i, \vec{\Theta})). \tag{4.1}$$

As the likelihood $\mathcal{L}(\vec{\Theta}|\vec{N}_{\mathrm{obs}})$ is evaluated for each datapoint in the analysis, it is given by the product of probability density functions (pdf) f. The single pdfs provide the probability of an individual data point i to be observed under the assumption of the parameter vector $\vec{\Theta}$.

In the specific case of KATRIN, the pdf is written with the observed number of electrons $N_{\mathrm{obs},i}$ and the theoretically expected number of electrons $N_{\mathrm{theo},i}$. The index i indicates the i^{th} scan step at retarding energy qU_i. The total theoretical number of electrons for scan step i further consists of β-decay electrons as well as background electrons,

$$N_{\mathrm{theo},i} = N_{\mathrm{sig},i} + N_{\mathrm{bg},i}. \tag{4.2}$$

The parameter vector is composed of the squared neutrino mass m_ν^2, as well as additional nuisance parameters[1]: $\vec{\Theta} = (m_\nu^2, E_0, \mathrm{Sig}, \mathrm{Bg}, B_{\mathrm{src}}, B_{\mathrm{ana}}, \dots)$. The set of parameters is required to describe the full integrated β-spectrum, including the experimental response behaviour, as well as the background model. In the minimal description, the parameter vector can be reduced to the neutrino mass and the three basic nuisance parameters, endpoint, signal, and background rate: $\vec{\Theta} = (m_\nu^2, E_0, \mathrm{Sig}, \mathrm{Bg})$.

To get the best estimate of the parameter vector, the process of maximum likelihood estimation (MLE) is applied to find the parameter set that maximises the probability prediction of the data. Typically, in statistics and optimization algorithms, the convention is to minimize a function value rather than maximize the likelihood $\mathcal{L}$. Therefore, it is more efficient to minimize the $-\log(\mathcal{L})$ to find $\vec{\Theta}_{\mathrm{best}}$.

$$\frac{\mathrm{d}}{\mathrm{d}\vec{\Theta}} \left(-\log\left(\mathcal{L}(\vec{\Theta}|\vec{N}_{\mathrm{obs}}) \right) \right) \Bigg|_{\vec{\Theta}_{\mathrm{best}}} = 0. \tag{4.3}$$

Furthermore, when transforming the likelihood into log-space, the product is turned into a sum which is computationally more efficient to handle.

In the case of sufficiently large statistics, the pdf f is given by a normal distribution,

$$\mathcal{N}(\mu, \sigma) = \frac{1}{\sigma\sqrt{2\pi}} e^{-\frac{1}{2}\left(\frac{x-\mu}{\sigma}\right)^2}. \tag{4.4}$$

Translating this for the expected and observed number of electrons, $x = N_{\mathrm{obs},i}$ and $\mu = N_{\mathrm{theo},i}$, the uncertainty becomes

$$\sigma(N_{\mathrm{theo},i}) = \sqrt{\sigma(N_{\mathrm{sig},i})^2 + \sigma(N_{\mathrm{bg},i})^2} = \sqrt{N_{\mathrm{sig},i} + N_{\mathrm{bg},i}} = \sqrt{N_{\mathrm{theo},i}}. \tag{4.5}$$

Inserting the Gaussian distribution into the $-\log(\mathcal{L})$, the product is reformulated into a

[1] A set of nuisance parameters describes parameters that are not of primary interest but are accounted for. The parameters are kept free as there is not sufficient information to constrain them.

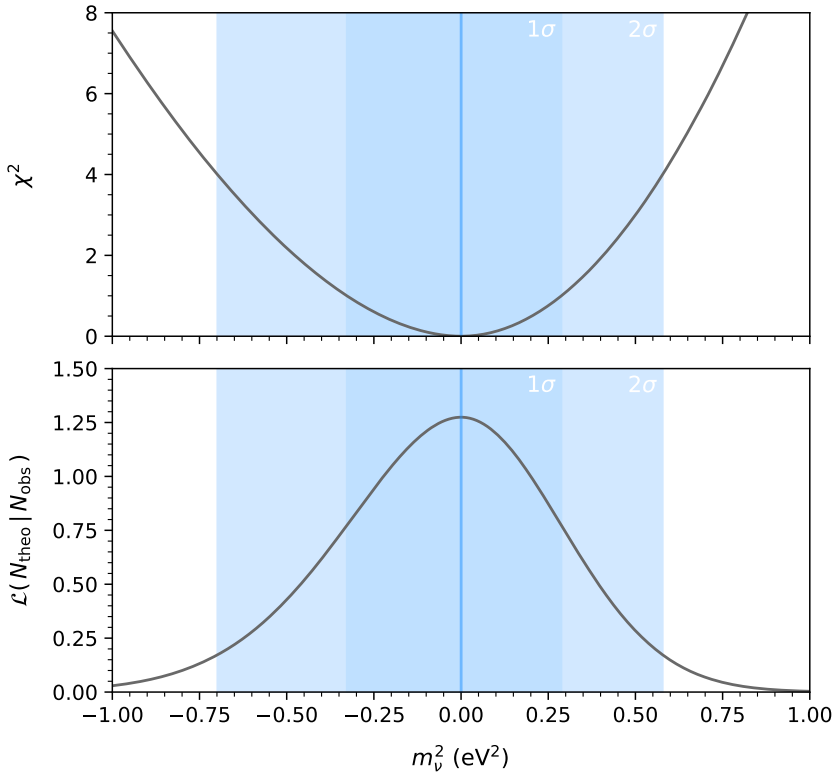

Figure 4.1.: Exemple χ^2 and likelihood profile over m_ν^2. The plot is based on a simulated spectrum with statistics similar to KNM2. The χ^2 profile has been calculated for given fixed m_ν^2 (top panel). The χ^2 can further be translated into $\mathcal{L}$ applying equation (4.6) (bottom panel). Here the likelihood is renormalised, that ($\int_{-\infty}^{\infty} \mathcal{L}\, \mathrm{d}m = 1$). In both cases, one can see the asymmetric nature of the profile, where the χ^2 is less steep for negative m_ν^2. The 1σ and 2σ confidence intervals have been highlighted in shades of blue. The vertical blue line marks the minimum χ^2. Note that the χ^2 minimum is at ≈ 0.0, as the simulated spectrum does not contain statistical fluctuations.

sum, leading to Pearson's chi-square statistic (χ^2) [193],

$$\begin{aligned} -2\log\mathcal{L}(\vec{\Theta}) &= -2\log\prod_{i=0}^{I} f(N_{\mathrm{obs},i}|N_{\mathrm{theo}}(qU_i,\vec{\Theta})) \\ &= -2\sum_{i=0}^{I}\log\Big(f(N_{\mathrm{obs},i}|N_{\mathrm{theo}}(qU_i,\vec{\Theta}))\Big) + \mathrm{h.c.} = \chi^2. \end{aligned} \tag{4.6}$$

To illustrate the connection between the χ^2 and the likelihood $\mathcal{L}$, they are compared in figure 4.1 as a function of m_ν^2.

The χ^2 function, assuming a normal distribution, hence becomes

$$\begin{aligned} \chi^2_{\mathrm{N}}\left(\vec{N}_{\mathrm{theo}}(\vec{\Theta}),\vec{N}_{\mathrm{obs}}\right) &= \sum_{i=0}^{I}\frac{\left(N_{\mathrm{theo},i}-N_{\mathrm{obs},i}\right)^2}{N_{\mathrm{theo},i}} \\ &= \left(\vec{N}_{\mathrm{theo}}-\vec{N}_{\mathrm{obs}}\right) C_{\mathrm{stat}}^{-1}\left(\vec{N}_{\mathrm{theo}}-\vec{N}_{\mathrm{obs}}\right)^{\mathrm{T}}. \end{aligned} \tag{4.7}$$

In the last step, the sum is rewritten as a matrix operation with the inverse covariance matrix C_{stat}^{-1}. The covariance matrix, in this case, contains the variances $\sigma_i^2 = N_{\text{theo},i}$ on the diagonal elements.[2]

Following the generalised χ^2 for a Poissonian pdf presented by S. Baker and R. D. Cousins [52], the Poissonian likelihood χ^2_λ for KATRIN is given by:

$$\chi^2_\lambda \left(\vec{N}_{\text{theo}}(\vec{\Theta}), \vec{N}_{\text{obs}}\right) = 2 \cdot \left[\sum_{i=0}^{I} N_{\text{theo},i} - N_{\text{obs},i} + N_{\text{obs},i} \cdot \log\left(\frac{N_{\text{obs},i}}{N_{\text{theo},i}}\right)\right]. \tag{4.8}$$

Including a Poissonian pdf is especially necessary with smaller statistics ($N_{\text{theo}}, i < \mathcal{O}(10^3)$), as the pdf approximation by a Gaussian is not sufficiently accurate and can result in a bias of fit parameters and, thus, a biased neutrino mass result. The bias introduced by Gaussian pdf approximation for small-statistics datasets is discussed in more detail in appendix B.1.

The total χ^2_{total} can also be composed of a combination of χ^2_λ and χ^2_{N}:

$$\chi^2_{\text{total}} = \sum_i \chi^2_{\lambda,i} + \sum_j \chi^2_{\text{N},j}. \tag{4.9}$$

In this case, scan steps i are described by a Poissonian pdf, and scan steps j are characterised by a normal pdf according to the respective number of counts in each scan step. This combination can for example be applied if scan steps j or particular spectra have sufficient statistics to be approximated by the normal pdf. Furthermore, non-Poissoninan overdispersions of the measured data can be accounted for by broadening the normal pdf (for more details see section 6.3.3.1).

4.2. Treatment of systematic uncertainties

Systematic uncertainties arising from different parts along the beamline are propagated into the analysis to provide robust and unbiased neutrino mass results. With increasing collected statistics over time, and hence continuously decreasing statistical uncertainty, precise modelling and the correct treatment of systematics are crucial.

For the analyses and studies performed in the course of this thesis, two different treatments of systematics are of particular interest, namely the covariance matrix approach and the pull-term approach. Either method comes with certain advantages and disadvantages. The following subsections will present both methods and elaborate on their respective pros and cons.

4.2.1. Covariance matrix approach

The covariance matrix approach is an a priori estimation of systematic uncertainties on the spectral shape. To construct the covariance matrix representing systematic uncertainties, Monte Carlo spectra are generated while fluctuating a systematic parameter according to its respective pdf. Correlations between different systematics are propagated by simultaneously sampling the correlated parameters from their joint pdf. Independent systematic parameters

[2] This description becomes advantageous when propagating systematics via covariance matrices (for more details, see section 4.2.1).

or model components (such as spectral systematics and background systematics) are sampled separately, and the individual covariance matrices are summed to represent the combined systematic impact. Correlated systematics are sampled together according to their multivariate distribution. Covariance matrices are typically based on $\mathcal{O}(10^4)$ simulated tritium spectra. From all K simulated spectra, elements ij of the rate covariance matrix V are constructed with

$$V_{ij} = \mathrm{cov}(\dot{N}_i, \dot{N}_j) = \frac{1}{K} \sum_{k=0}^{K} \left(\dot{N}_{i,k} - \left\langle \dot{N}_i \right\rangle \right) \cdot \left(\dot{N}_{j,k} - \left\langle \dot{N}_j \right\rangle \right). \tag{4.10}$$

The indices i and j correspond to the scan steps of the k^{th} simulated spectrum. Hence the covariance matrix has the dimension of the number of retarding potential scan steps. Off-diagonal elements of the matrix represent correlations between the scan steps. Since we perform a shape analysis of the spectrum, a covariance matrix representing the relative uncertainties rather than the absolute uncertainty is applied in the analysis. Therefore the covariance matrix is normalised by the mean spectral rate

$$R_k = \frac{\sum_i \dot{N}_{i,k}}{\sum_{i,k} \dot{N}_{i,k}}. \tag{4.11}$$

Equation (4.10) modifies to:

$$V_{ij}^{\text{shape}} = \frac{1}{K} \sum_{k=0}^{K} \left(\frac{\dot{N}_{i,k}}{R_k} - \left\langle \frac{\dot{N}_i}{R_k} \right\rangle \right) \cdot \left(\frac{\dot{N}_{j,k}}{R_k} - \left\langle \frac{\dot{N}_j}{R_k} \right\rangle \right). \tag{4.12}$$

In the last step, this normalised covariance matrix, applicable to the count rate, is scaled by the measurement time:

$$C_{\text{syst},ij} = V_{ij}^{\text{shape}} \cdot t_i \cdot t_j. \tag{4.13}$$

This covariance matrix, in units of absolute counts, can now be added to the covariance matrix C_{stat}, which comprises the statistical variance on the diagonal elements. The combined covariance matrix C_{total} is then given by

$$C_{\text{total}} = \sum_{\text{syst}} C_{\text{syst}} + C_{\text{stat}}, \tag{4.14}$$

where the sum is overall independent systematic covariance matrices. C_{total} is then used to evaluate the χ^2 as described in equation (4.7).

A significant advantage of the covariance matrix approach is that the matrices can be precalculated once a priori, and no additional nuisance parameters are added to the fit [219]. Thus, the approach does not increase in fitting computation time when including systematics. On the other hand, the covariance matrix method comes with the disadvantage that no additional information is gained from the data on the systematic parameter. Also, biased inputs are not compensated by the model. Covariance matrices can furthermore only be applied for Gaussian pdf (equation (4.7)), thus are only applicable for sufficiently sized datasets.

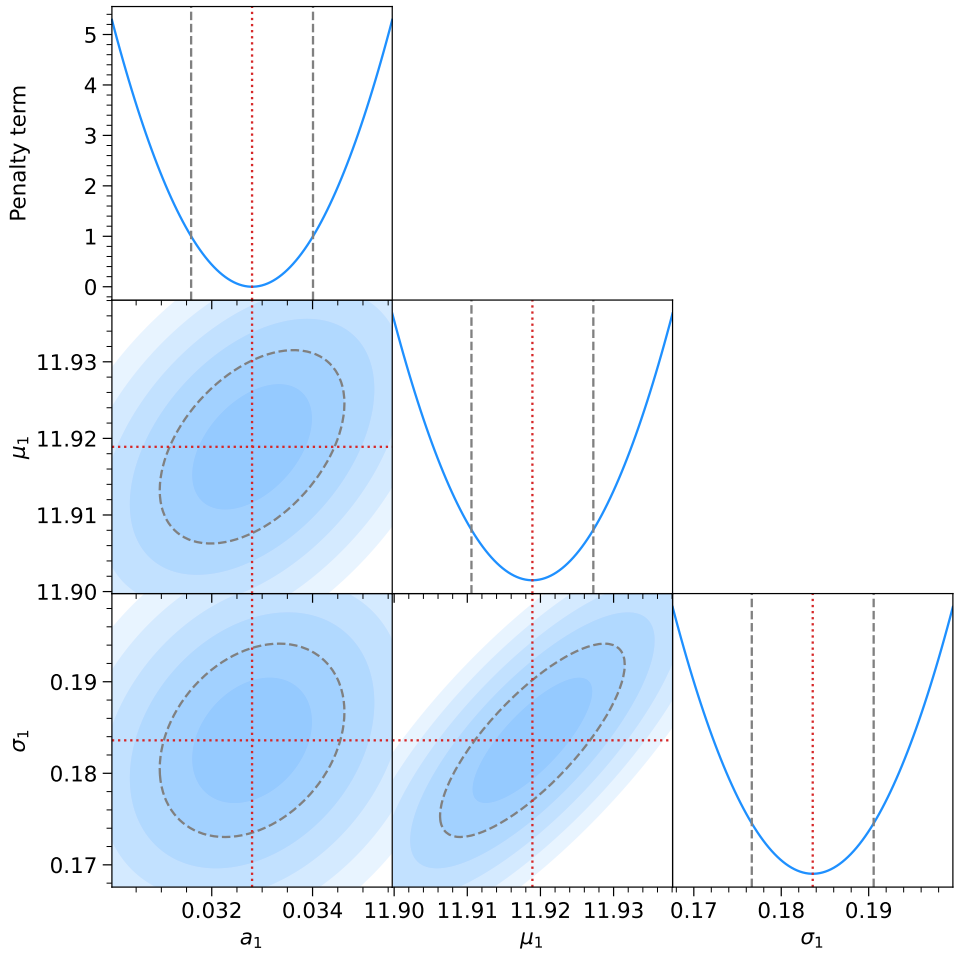

Figure 4.2.: Illustration of multivariate Gaussian penalty terms. Penalty terms are added to constrain additional fit parameters. To account for inter-period correlations, inter-patch correlations, or correlations between different parameters, the penalty terms are generated via a multivariate normal distribution. In the figure, the penalty terms for three of the nine energy loss parameters are illustrated (the central values, uncertainties, and correlations are according to [28]). The plots on top of each column give the profile of the single penalties. The 1 σ interval is indicated by dashed grey lines. The central value of the penalty term is highlighted in red. In the subplots on the lower left, the penalties are displayed with respect to two parameters. Hereby one can also observe, that strongly correlated penalties result in more narrow and tilted ellipsoids (for example, σ_1 and μ_1).

4.2.2. Pull-term approach

In the statistics-only case, free parameters in the optimisation are the squared neutrino mass and the additional nuisance parameters – endpoint, signal, and background rate. Hence the parameter vector is given by $\vec{\Theta} = (m_\nu^2, E_0, \mathrm{Sig}, \mathrm{Bg})$. Systematics, $\vec{\eta}$, following a Gaussian pdf, are accounted for by introducing so-called pull terms[3]. When adding pull terms, the parameter vector is extended by the systematic parameters as additional

[3]Pull terms are sometimes also called penalty terms.

nuisance parameters $\vec{\Theta} = (m_\nu^2, E_0, \mathrm{Sig}, \mathrm{Bg}, \eta_1, \eta_2, \dots)$. In addition to this, the χ^2 evaluation (equation (4.9)) is extended by additional penalty terms:

$$\chi^2_{\text{stat \& syst}}(m_\nu^2, E_0, \mathrm{Sig}, \mathrm{Bg}, \eta_1, \eta_2, \dots) = \chi^2_{\text{total}}(m_\nu^2, E_0, \mathrm{Sig}, \mathrm{Bg}, \eta_1, \eta_2, \dots) + \underbrace{\left(\vec{\hat{\eta}} - \vec{\eta}\right) \Sigma^{-1} \left(\vec{\hat{\eta}} - \vec{\eta}\right)^{\mathrm{T}}}_{\text{Multivariate Gaussian penalty term}} . \tag{4.15}$$

In this formulation, the systematic parameters $\vec{\eta}$ are compared to the expected systematic mean values $\vec{\hat{\eta}}$. Uncertainties and correlations between the systematics are contained in the covariance matrix Σ. The diagonal elements of the covariance matrix are given by the variance $\Sigma_{ii} = \sigma_{\eta,i}^2$ and the off-diagonal elements take into account correlations between parameters $\Sigma_{ij} = \sigma_{\eta,i} \cdot \sigma_{\eta,j} \cdot \rho_{\eta,ij}$. Syststematic mean values $\hat{\eta}$, uncertainties σ_η, and correlations $\rho_{\eta,ij}$ are constrained from external measurements. An illustration of the multivariate penalty term is presented in figure 4.2. The plot shows the correlated pull term of three of the nine energy loss function parameters. The plots on top of each column represent the profile over only a single parameter, which is parabolic due to the Gaussian nature of the pull term. The subplots on the lower left illustrate the penalty for two parameters together. If parameters are strongly correlated, the ellipsoid becomes more narrow (see, for example, parameters σ_1 and μ_1).

The advantage of the pull-term approach is that additional information coming from the data is naturally taken into account by the resulting correlation to other parameters and the addition of nuisance parameters. If, for example, the data contains further information than the constraints from external measurements, the initial central values can change, and uncertainties on η improve. On the other hand, the pull-term approach introduces additional free parameters in the minimisation, which is computationally more expensive.

An example of the application and effect of pull terms is illustrated in figure 4.3. From the plot, it becomes obvious how the introduction of additional nuisance parameters widens the χ^2, consequently increasing the uncertainties.

4.3. Parameter estimation

The difference between the theoreticap model and the experimental data is minimised when optimising a parameter set. Traditionally parameter optimisation is described as χ^2 minimisation, or maximum likelihood estimation. Both optimisation methods describe the same and they can be transformed into each other. From this point onward, the terminology of χ^2 minimisation is used.

4.3.1. Frequentist inference

Minimisation: Frequentist inference refers to the statistical analysis of a set of parameters based on the frequentist probability. As illustrated in equation (4.3), the χ^2 reaches a stationary minimum if $\mathrm{d}\chi^2/\mathrm{d}\vec{\Theta} = 0$. Consequently, to perform the parameter inference, the χ^2 (as defined in equations (4.9) and (4.15)) is minimised for the parameter vector $\vec{\Theta}$.

Frequentist analyses presented in this work are based on the `MINUIT`[4] class provided by the

[4] `ROOT:TMinuit` class: https://root.cern.ch/doc/master/classTMinuit.html.

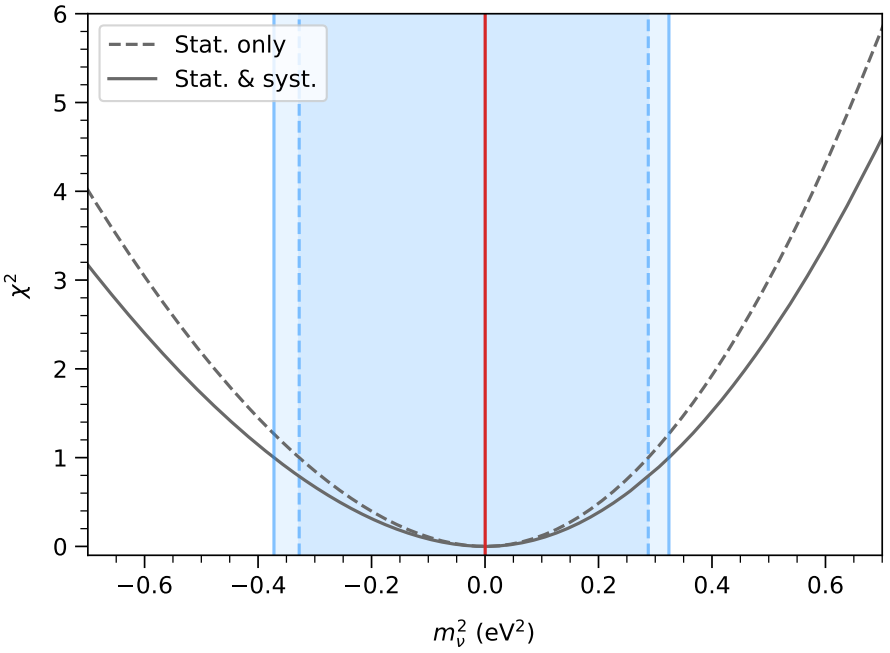

Figure 4.3.: Impact of systematics on the χ^2. The plot is based on a simulated spectrum ($m_\nu^2 = 0.0\,\mathrm{eV}^2$) with statistics similar to KNM2 and systematics equivalent to the ones applied in the neutrino-mass analysis. The graph includes the χ^2 profile when only accounting for statistic uncertainties (dashed), as well as a profile when including additional systematics via pull terms (solid). The minimal χ^2 is marked in red. The corresponding 1σ uncertainties are shaded in blue. By giving the model additional freedom, the uncertainty increases when adding systematics.

`ROOT`[5] library. `MINUIT` provides fast and efficient function minimisation routines and hence is ideal for the parameter space at hand. The core analysis utilises the `MIGRAD` subroutine. `MIGRAD` is based on inexact line search while checking that the first derivatives are positive definite. The first and second derivatives are calculated numerically. The descending direction and step size are determined using the Broyden–Fletcher–Goldfarb–Shanno (BFGS) algorithm for the Hesse matrix[6]. [140]

Estimation of uncertainties: Uncertainties and correlations on fit parameters are further provided by `MINUIT`. To first order, if the pdf is assumed to be Gaussian and therefore the χ^2 parabolic, the uncertainty and correlations are directly provided by the inverse Hesse matrix. To illustrate this with a simple example, the diagonal elements of the Hesse matrix are given by

$$\frac{\partial^2 \chi^2}{\partial \Theta_i \partial \Theta_i} = \frac{2}{\sigma_i^2}, \qquad \text{where} \quad \chi^2(\Theta_i) = \frac{(\Theta_i - \hat{\Theta})_i^2}{\sigma_i^2}. \tag{4.16}$$

To evaluate the Hesse matrix numerically, `ROOT` provides the `HESSE` routine. However, the Hesse matrix has the disadvantage of only providing symmetric uncertainties based on the second derivative at the minimum. This can therefore be susceptible to numerical noise,

[5] `ROOT` data analysis framework: https://root.cern.ch.
[6] The Hesse matrix contains the second partial derivative.

making the uncertainties less reliable.

A common technique is to profile the χ^2 over the multidimensional parameter space to obtain more precise uncertainties and reflect asymmetric errors. Profiling is a constructive approach to derive the confidence level on a particular parameter of interest. To extract the asymmetric error, `MINUIT` further provides subroutines such as the `MINOS` algorithm. After successfully minimising the χ^2 function, `MINOS` iteratively probes the parameter space for the 1σ upper and lower errors. This is in general computationally more expensive, but correctly takes into account correlations between parameters and asymmetries of the χ^2 profile. The upper and lower uncertainties are defined by a $\Delta\chi^2 = 1$ (at 68.3 % confidence level (C.L.)) with respect to the minimum. The estimation of uncertainties from the $\Delta\chi^2$ follows Wilks' theorem [256]. Wilks' theorem builds on the likelihood ratio $\lambda = {}^{\mathcal{L}(\theta)}/_{\mathcal{L}(\hat{\theta})}$, where $-2\log\lambda$ is approximated by the χ^2 distribution. The critical $\Delta\chi^2$ is calculated for an arbitrary confidence level α by integrating the χ^2 distribution f for n degrees of freedom

$$\int_0^{\Delta\chi^2} f_n(\chi)\mathrm{d}\chi = \alpha. \tag{4.17}$$

Impact of systematics on uncertainties: To estimate the impact of systematic effects on the squared neutrino mass, the statistical uncertainty σ_{stat} is usually compared to the uncertainty including both statistical and systematic uncertainties, $\sigma_{\text{stat \& syst}}$. The asymmetric uncertainties are computed using the `MINOS` algorithm. For the comparison, σ refers to the mean uncertainty of the upper and lower error:

$$\sigma = \frac{|\sigma_{\text{lower}}| + |\sigma_{\text{upper}}|}{2}. \tag{4.18}$$

The systematic impact is calculated by subtracting the statistical uncertainty in quadrature

$$\sigma_{\text{syst}} = \sqrt{\sigma^2_{\text{stat \& syst}} - \sigma^2_{\text{stat}}}. \tag{4.19}$$

4.3.2. Bayesian inference

Both frequentist and Bayesian inference are mathematically consistent with each other. Bayesian inference allows the extraction of final probability distributions for the model parameters which are of interest – giving us the probability of the hypothesis after observing the data. In addition, Bayes' theorem allows us to propagate additional prior assumptions into the analysis. Bayes' theorem is given as:

$$P(\vec{\Theta}|\vec{N}_{\text{obs}}) = \frac{\pi(\vec{\Theta}) \cdot \mathcal{L}(\vec{\Theta}|\vec{N}_{\text{obs}})}{p(\vec{N}_{\text{obs}})}. \tag{4.20}$$

For consistency, this formulation uses the same nomenclature as before, where $\vec{\Theta}$ is the vector of parameters and $\vec{N}_{\text{obs}}$ is the vector of observed data points. $\mathcal{L}(\vec{\Theta}|\vec{N}_{\text{obs}})$ is the likelihood function as defined in equation (4.1), giving the conditional probability to observe the data $\vec{N}_{\text{obs}}$ if the parameter set $\vec{\Theta}$ is true. $p(\vec{N}_{\text{obs}})$ is the evidence or marginal probability of observing $\vec{N}_{\text{obs}}$. This marginal probability acts as a normalisation, summarising the total probability of the observed data independent from any parameter set. This normalisation factor is technically difficult to compute and even becomes intractable with a higher number of dimensions. $\pi(\vec{\Theta})$ is the prior probability which takes prior assumptions on the

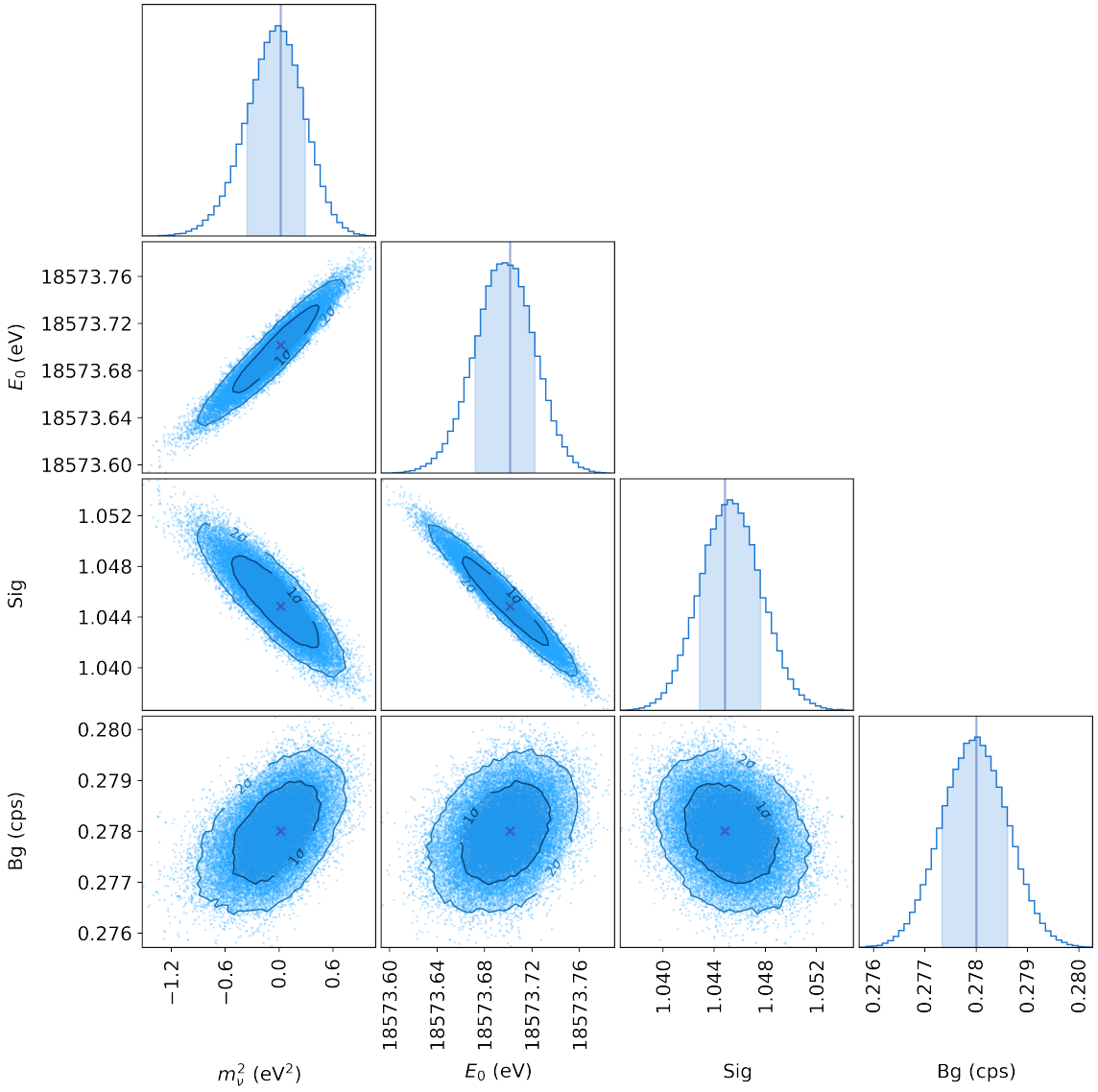

Figure 4.4.: Illustration of the posterior probability density distribution illustration. The figure is based on a simulated spectrum with statistics similar to KNM2. The plot consists of the one-dimensional marginalised posterior distributions (diagonal subplots) and two-dimensional posterior distributions (lower left subplots) when accounting only for statistical uncertainties. The crosses and vertical lines mark the global mode for each parameter. Credibility intervals (here the highest density interval (hdi)) are outlined and highlighted in different shades of blue. Markov chains were run with the `katrin-mcmc` toolkit using the `emcee` sampler (more details in section 4.5.2) with eight walkers and 5×10^5 samples per walker.

parameters into account. Applying Bayes' theorem results in the posterior distribution $P(\vec{\Theta}|\vec{N}_{\text{obs}})$. The posterior probability distribution reflects the probability of the inferred parameters $\vec{\Theta}$ after observing the dataset $\vec{N}_{\text{obs}}$.

As mentioned before, it can become technically difficult to calculate $p(\vec{N}_{\mathrm{obs}})$ for a higher number of dimensions. Therefore techniques such as Markov Chain Monte Carlo (MCMC) sampling methods have been developed to circumvent the computational difficulties. MCMC sampling methods only compute various punctual statistics, which in combination approximate the distributions. In general Bayesian inference with MCMC requires a comparatively large number of samples and hence many function evaluations. Moreover, the number of likelihood evaluations grows with increasing number of parameters.

Prior: The ability to apply prior knowledge and assumptions is especially advantageous for the purpose of avoiding unphysical regions of the parameter space. In these cases, one can define prior functions such as

$$\pi(x) = \begin{cases} 1 & \text{if } x = \text{physical} \\ 0 & \text{if } x = \text{unphysical.} \end{cases} \tag{4.21}$$

The prior pdf can take any shape and is not restricted to be flat or Gaussian but can, for example, be the posterior delivered by another experiment or previous data sets.

Posterior: The result of a Bayesian analysis is the multidimensional posterior probability distribution function itself. An illustration for such a posterior probability distribution is shown in figure 4.4. After convergence, this pdf is extracted by histogramming all MCMC samples. From the posterior distribution, various quantities can be extracted. To quote a central value, it is most common to use the global mode. The global mode is the sample with the smallest χ^2 or largest likelihood (marked by the crosses and vertical lines in figure 4.4). With a sufficiently large number of samples, the global mode is equivalent to the minimisation result of the frequentist approach. Credibility intervals are usually extracted from the marginalised posterior distribution (shaded in blue in figure 4.4). It is common practice to quote the highest density interval (hdi). In addition, the two-dimensional distributions give direct information about the correlation between parameters.

4.4. Limit setting techniques

In frequentist analyses in KATRIN, three commonly used statistical methods can be applied to construct the upper limit on a parameter. These belt construction, and hence limit setting methods, are the Neyman construction [182], the Feldman-Cousins [101] construction, and the Lokhov-Tkachov construction [166]. All three methods guarantee a conserved coverage[7]. An illustration of the three construction methods is shown in figure 4.5. In KATRIN usually the 90 % C.L. limit is quoted, therefore the following descriptions are based on this particular choice of C.L. The same construction principle can also be applied to any other C.L.

The most simple belt construction is the standard construction by J. Neyman [182]. An example of the Neyman belt is shown in figure 4.5 (dotted green). Probability distributions are calculated for different *true* m_ν^2. The distributions can either be calculated from fluctuated Monte Carlo spectra or from the profile likelihood based on Asimov spectra. For

[7] Coverage represents the fraction, α, that a parameter of interest is obtained when repeating the same experiment many times.

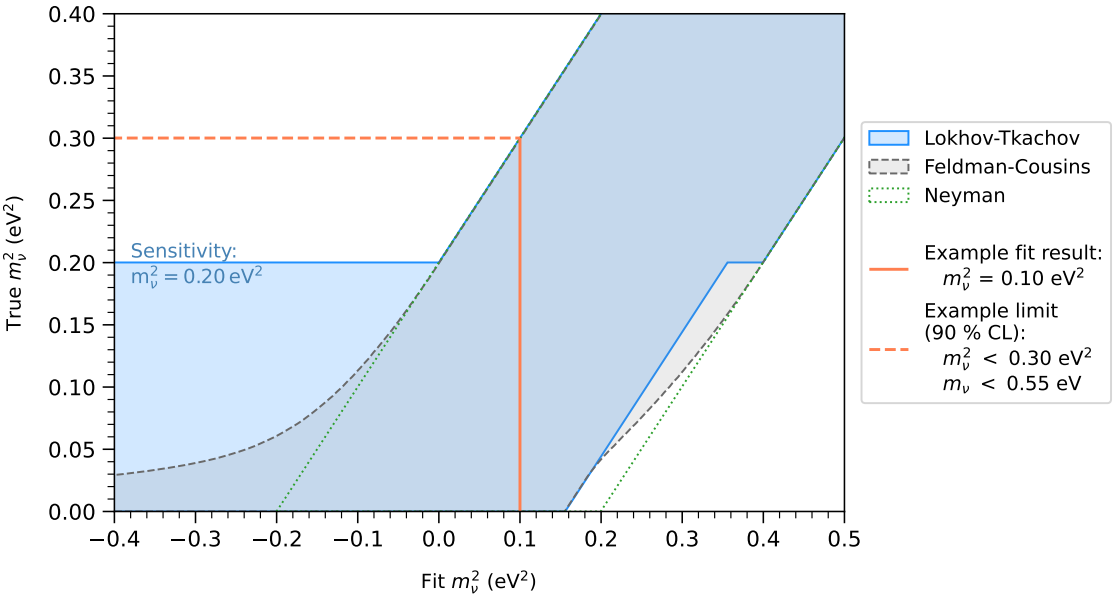

Figure 4.5.: Example Lokhov-Tkachov belt (solid blue), Feldman-Cousins belt (dashed grey) construction, and Neyman belt (dotted green) for neutrino-mass limit construction. The belts are based on a 1σ sensitivity of $122\,\mathrm{meV}^2$ which translates to a 90 % C.L. sensitivity of $0.2\,\mathrm{eV}^2$. The plot illustrates the construction of the upper limit for an example measurement result of $0.10\,\mathrm{eV}^2$. From this example, the upper limit on m_ν^2 is $0.30\,\mathrm{eV}^2$ at 90 % C.L.. In this case, this translates to a neutrino mass limit of 0.55 eV at 90 % C.L..

each *true* m_ν^2 the two-sided $\alpha = 90\,\%$ C.L. upper and lower bounds are constructed, such that

$$\alpha = \int_{m^2_{\nu,\mathrm{lower}}}^{m^2_{\nu,\mathrm{upper}}} \mathcal{L}\left(m^2_{\nu,\,\mathrm{fit}} \middle| m^2_{\nu,\,\mathrm{true}}\right). \tag{4.22}$$

To construct the acceptance region, samples are, for example, sorted by their likelihood $\mathcal{L}$ and the hdi is extracted. Connecting the lower bounds of all *true* m_ν^2 and upper bounds of all *true* m_ν^2 gives the Neyman belt. The upper limit on m_ν^2 is then extracted by calculating the lower belt edge at the *fit* m_ν^2 from the fit to the data. This construction has the undesirable disadvantage that for large unphysical negative values that lie outside the belt, the construction would need to be changed to a one-sided interval construction after looking at the data to avoid the effect of flip-flopping. In other words, flip-flopping describes a vertical deformation of the confidence belt, resulting in and leading to incorrect coverage for different *true* m_ν^2 [101]. To avoid this, the Lokhov-Tkachov and Feldman-Cousins belt constructions follow a modified approach.

The unified approach by G. J. Feldman and D. Cousins [101] introduces an alternative ordering compared to the Neyman construction. For each *true* m_ν^2 the probed likelihood

entries are ordered by the likelihood ratio

$$R\left(m^2_{\nu,\,\mathrm{fit}}\middle|m^2_{\nu,\,\mathrm{true}}\right) = \frac{\mathcal{L}\left(m^2_{\nu,\,\mathrm{fit}}\middle|m^2_{\nu,\,\mathrm{true}}\right)}{\mathcal{L}\left(m^2_{\nu,\,\mathrm{fit}}\middle|\max\left(m^2_{\nu,\,\mathrm{true}}, 0.0\right)\right)}. \tag{4.23}$$

Similar to the Neyman construction, probabilities are subsequently summed until 90 % coverage is reached. Also, in this case, all upper and lower bounds of the accepted regions are connected to construct the belt. An example of the Feldman-Cousins belt is shown in figure 4.5 (dashed grey). Again, the upper limit on m^2_ν is then extracted by calculating the lower belt edge at the *fit* m^2_ν. The unified Feldman-Cousins approach has the advantage that it gives a smooth transition from a two-sided to a one-sided confidence interval while guaranteeing appropriate coverage.

The third construction method was introduced by A. V. Lokhov and F. V. Tkachov [166]. Similar to the previous method, the Lokhov-Tkachov construction also provides conserved coverage. This belt construction is split into two distinct regions, which are given by a two-sided and a one-sided confidence interval, given as a horizontal deformation.[8] As long as the lower bound of the acceptance region for each *fit* m^2_ν is $\geq 0.0\,\mathrm{eV}^2$ the two-sided region is chosen. For negative *fit* m^2_ν, the acceptance region is only defined by an upper bound. This method returns the expected sensitivity for *fit* $m^2_\nu < 0.0\,\mathrm{eV}^2$. The advantage of the Lokhov-Tkachov approach is that there is no misleading benefit when obtaining more negative squared neutrino mass results in the unphysical region.

In figure 4.6, a direct comparison between the limit expectation for the two different scenarios of Lokhov-Tkachov and Feldman-Cousins is presented. The study is based on the expected final KATRIN sensitivity of 200 meV (at 90 % C.L.), which translates to a sensitivity of $0.04\,\mathrm{eV}^2$ on m^2_ν. Both belt constructions are shown in the upper left plot. The plot further includes the largest *fit* m^2_ν, which would result in an upper limit on m^2_ν. Results above this point would be quoted as a central value with uncertainties. The two scenarios compared (lower right) further represent statistically fluctuated results with a central value of $\langle m^2_\nu\rangle = 0.0\,\mathrm{eV}^2$ (grey) and $\langle m^2_\nu\rangle = 0.02\,\mathrm{eV}^2$ (green). Sampling from each distribution leads to a set of limits based on the Lokhov-Tkachov belt (upper right) and Feldman-Cousins belt (lower right). Again, distributions in grey correspond to the first scenario and in green to the second. Both limit distributions are equivalent above the expected sensitivity of $0.04\,\mathrm{eV}^2$ and are cut off at $0.07\,\mathrm{eV}^2$ (dotted orange lines), from which point a central value and uncertainty would be quoted.

As described above, in the case of Lokhov-Tkachov, *fit* $m^2_\nu < 0.0\,\mathrm{eV}^2$ returns the sensitivity. For the first scenario ($\langle m^2_\nu\rangle = 0.0\,\mathrm{eV}^2$), 56 % of limits are given by the sensitivity. For the second scenario ($\langle m^2_\nu\rangle = 0.02\,\mathrm{eV}^2$) around 30 % of limits are represented by the sensitivity. The modes of both distributions are also given by the expected sensitivity (grey and green triangles).

In the case of Feldman-Cousins (lower right), the expected limits spread further down as more negative values result in lower limits. The modes of both distributions are also different from each other. The mode of the grey distribution lies below the expected sensitivity, whereas the mode of the green distribution lies above the expected sensitivity.

[8] In contrast to flip-flopping, when introducing horizontal deformations, the correct coverage for all *true* m^2_ν is obtained. [166]

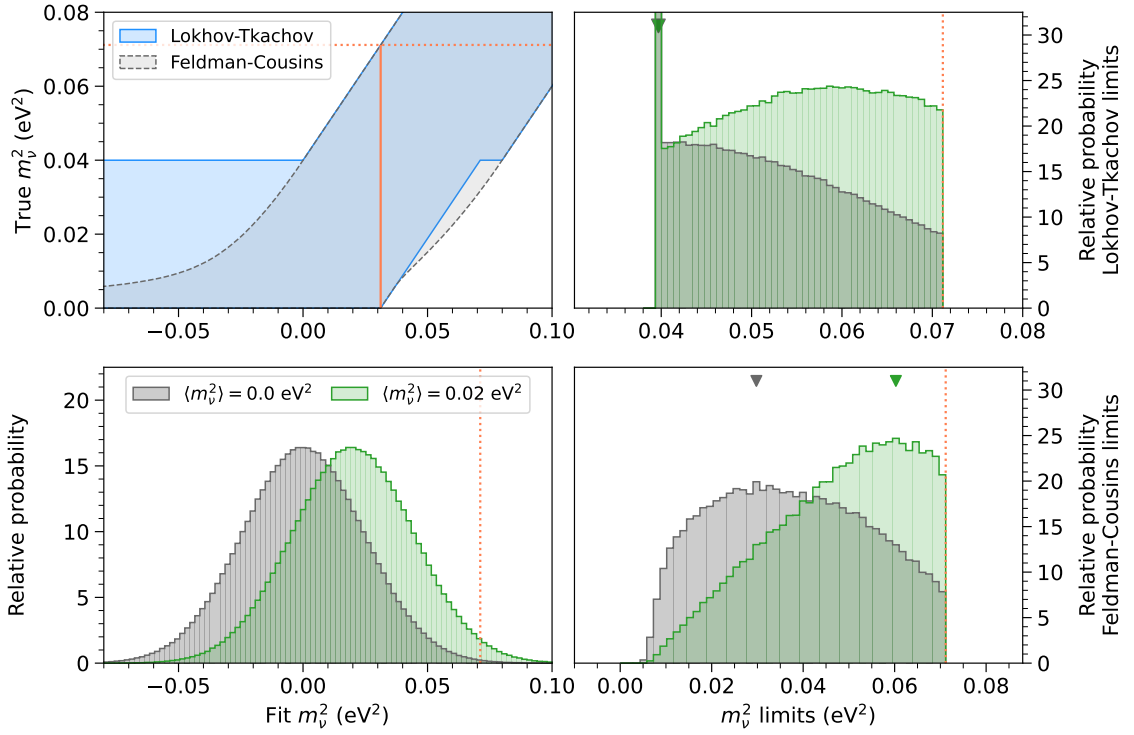

Figure 4.6.: Illustration of limit expectation for two different scenarios. The Lokhov-Tkachov and Feldman-Cousins belts have been constructed based on a 90 % C.L. sensitivity of 0.2 eV (upper left). The simulation investigates the expected distribution of limits for the neutrino mass scenarios of $m_\nu^2 = 0.0\,\text{eV}$ and $m_\nu^2 = 0.02\,\text{eV}$ (lower left). In both cases, the limits have been calculated based on a statistically fluctuated distribution around the mode m_ν^2 values. From the fluctuated distributions, the resulting Lokhov-Tkachov limits have been histogramed (upper right), as well as the resulting Feldman-Cousins limits (lower right). The distribution modes are marked by green and grey triangles. For the distribution of Lokhov-Tkachov limits, around 56 % of limits are given by the sensitivity for the scenario of $m_\nu^2 = 0.0\,\text{eV}$ and around 30 % of limits are represented by the sensitivity in the case of $m_\nu^2 = 0.02\,\text{eV}$. Note that the x-scale differs for the latter two plots. The maximum given limit is marked by the dotted orange line, given by the minimum value of the upper belt edge.

For Bayesian analyses, upper limits on m_ν^2 are extracted by applying a flat positive prior on m_ν^2. Then, from the posterior distribution, the limit is calculated without any additional construction or Monte Carlo. From the marginalised posterior probability distribution, the hdi is integrated, resulting in the uncertainties or upper limit on the squared neutrino mass. An upper limit is given when the lower bound of the hdi coincides with the smallest m_ν^2 obtained from the chain.

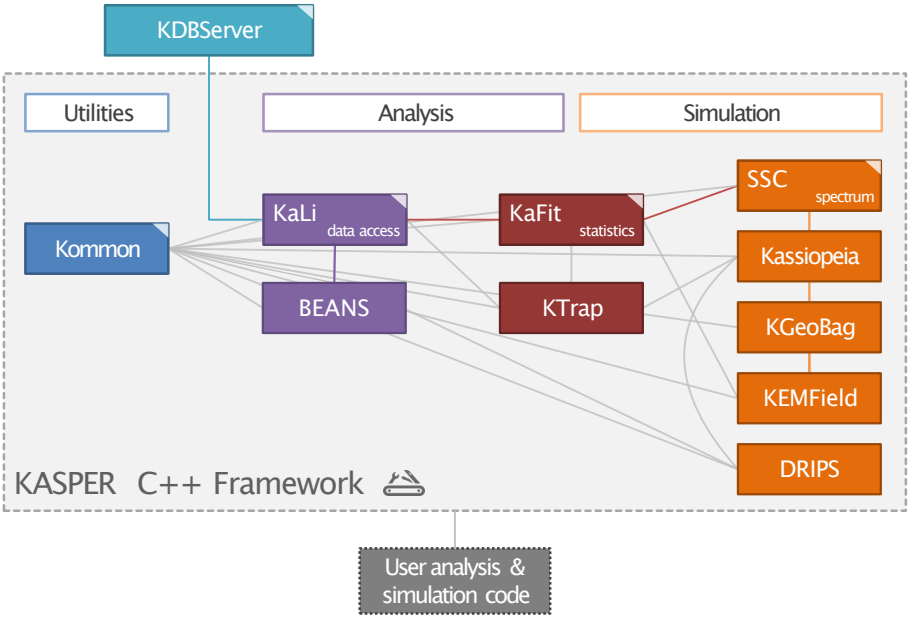

Figure 4.7.: Overview of the KASPER framework and its components. The framework is subdivided into utilities, analysis, and simulation tools. More details to each component in the text. Figure adapted from [148].

4.5. The KASPER framework

The KATRIN C++ software package (KASPER) is a collection of libraries and tools that allow simulation, data access, and data processing, as well as a variety of analyses developed for the KATRIN experiment. The software package is in active development and contains some of the main C++ tools used within the KATRIN collaboration. The KASPER suit is divided into several main components that are grouped into three classes: utilities, analysis and simulation. An overview of the main components and their connections is illustrated in figure 4.7. In the following paragraphs, the individual modules and their key features are briefly summarised. For more information on the individual components, the reader is referred to [111, 112, 120, 148]. The SSC package and KaFit toolkit are of particular interest in the context of this thesis, both are described in more detail in sections 4.5.1 and 4.5.2.

KASPER-common (Kommon) is the most basic KASPER module. All modules and libraries described in the following depend on Kommon. The Kommon module includes headers of basic C++ classes (such as boost[9]) and also provides general functionalities such as logging mechanisms, input/output passing, as well as general mathematical operations and algorithms. In addition, Kommon contains physical constants used by all other KASPER modules.

KATRIN library (KaLi) acts as a data access class library. During operation, all KATRIN data is stored in the database. With KaLi, the KATRIN database can be accessed, and data can be committed. It can handle network data transfer, including automatic offline

[9] Boost C++ libraries: https://www.boost.org

caching. The database can, for example, be accessed through a combined web interface, allowing access to runs and slow control parameters in real-time. In connection with the intermediate data layer (IDLE) system, preprocessed scans (so-called run summaries) can be downloaded.

BEANS provides a collection of analysis logic. The library is included in Detector Section Analysis Suite – Temporary Evaluation Revision (DeSASTER), which is a collection of libraries for detector data analysis and detector readout simulation (see paragraph DRIPS). BEANS allows the user to combine logic elements and mechanisms to build analysis programs. The KATRIN data can be accessed with BEANS through KaLi. BEANS analysis elements are applied to generate the run summaries used for neutrino-mass analysis.

Source and Spectrum Calculation (SSC) package of the KASPER suite provides elements to describe the experimental setup mathematically and calculate the integrated tritium β-decay spectrum. This includes modelling of the source as well as transmission behaviour through the experiment. The SSC package is discussed in more detail in section 4.5.1. [136, 148]

Kassiopeia is one of the major components of KASPER. The Kassiopeia software serves as a simulation tool for tracking of charged particles (such as electrons) through static electric and magnetic fields in complex geometries. The tracking simulation package was, in particular, developed by the KATRIN collaboration for the design of components, optimisation of experimental settings, and simulation of experimental conditions. Kassiopeia utilises features of many different libraries such as: boost, ROOT, GSL[10], VTK[11], or FFTW[12]. The simulation package is publically availabel under https://github.com/KATRIN-Experiment/Kassiopeia. [112, 238]

KGeoBag provides a set of basic shapes and surfaces that can be included in field simulations or tracking simulations within Kassiopeia. The KGeoBag collection further includes complex polysurfaces of physical components that are commonly encountered in experimental setups (such as vacuum pump ports or beam tube surfaces). [111, 120]

KEMField allows the computation of static electric and magnetic fields for a given setup or geometry. KEMField includes a zonal harmonic field solver (for axial symmetric configurations) and a fast multipole field solver (for three-dimensional problems). The computed magnetic and electric fields can also be used as inputs to Kassiopeia simulations. [75]

Detector readout simulation (DRIPS) is also part of the DeSASTER toolkit. It is a detector readout simulation library. The DRIPS code allows simulation of the DAQ chain as it is implemented in the KATRIN setup. By simulating processes that emulate the DAQ system, effects such as pile-up, the efficiency of the trapezoidal filters, or noise effects are investigated.

[10] GNU Scientific Library: https://www.gnu.org/software/gsl/.
[11] The visualisation toolkit: https://vtk.org.
[12] Fastest Fourier Transform in the West.: http://www.fftw.org.

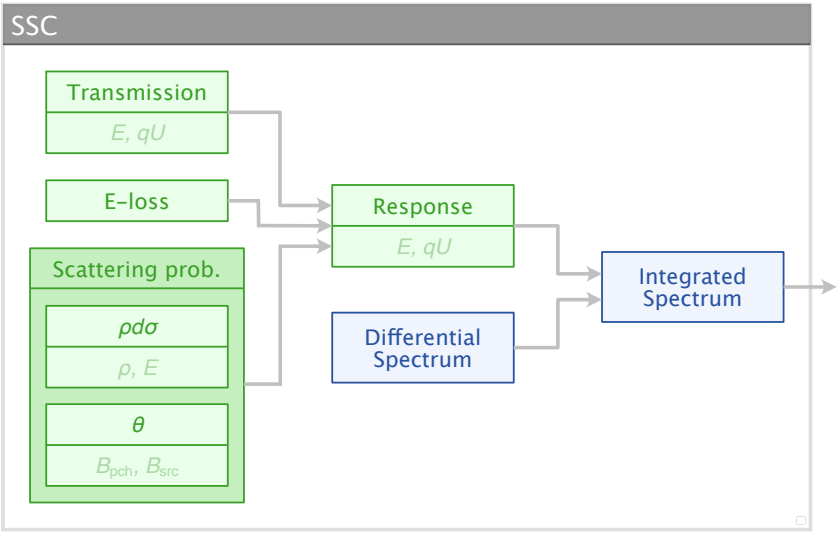

Figure 4.8.: Schematic overview over the `SSC` structure and components. The `SSC` code is composed of different modules that are combined into the integrated β-spectrum. Model components are combined (symbolised by the grey arrows). Components that are highlighted in green include caching capability. Components highlighted in blue are evaluated in each calculation of the spectrum.

Fit environment for KATRIN-spectra (`KaFit`) is used to analyse spectra. The `KaFit` code is used to perform sensitivity studies and analyse data measured with the KATRIN experiment. The model evaluation is connected to the `SSC` package and is compatible with both Krypton and Tritium spectra. Combining the model and data, a likelihood is constructed to optimise the parameters of interest. `KaFit` furthermore includes different fitting tools and minimisation methods, such as `MINUIT` or MCMC. A more in-depth description is given in section 4.5.2. [148]

KATRIN transmission analysing package (`KTrap`) combines different analysis and simulation tools of the `KASPER` suit to investigate transmission properties of the main spectrometer of the KATRIN setup. For more details, see [120].

4.5.1. Source and spectrum calculation

`SSC` is C++-based code and comes as one of the key parts of `KASPER`. The software package was developed to calculate the integrated β-spectrum for given retarding potentials qU, representing electromagnetic and gas dynamic settings in the experimental setup of KATRIN.

Unlike in `Kassiopeia`, where single electron trajectories are simulated through the experimental setup, in `SSC`, the entire kinematic β-spectrum is calculated and convolved with the analytical description of the response function. The components composing the integrated spectrum are calculated following the theoretical description of chapter 3, and integrations are performed numerically. Furthermore, the package can compute both tritium and krypton spectra [171].

SSC is designed in a modular way, allowing one to combine different spectra, source, transmission, or response models. The SSC model is composed through xml configuration files. An example for the ssc.xml applied in the neutrino mass, and sterile neutrino analysis is in appendix D.2. From the configuration, one can see the distinction between different model components: Source model, final state model, differential spectrum, energy loss function, transmission function, response function, detector, and finally, combining all into the integrated spectrum. Figure 4.8 gives an overview of the different model components and how these are connected. The package allows for easy and flexible configuration and comes with additional corrections and different gas dynamic models, which are not applied in the following analysis. More details on many of the features can be found in [120, 136, 142, 148]. As can be seen in figure 4.7, SSC is further connected and embedded into other KASPER modules. For example, transmission simulations from Kassiopeia can serve as inputs to SSC calculations.

The SSC model defines over 173 model parameters. All parameters come with default values and can be set accordingly to represent the experimental conditions and further be optimised during the fit. Spectral distortions of the neutrino mass result in comparatively small distortions of the spectrum; precise and numerically stable computation of the spectral shape is mandatory. As mentioned before, integrals are evaluated numerically. This is realised by binning the functions whilst satisfying a certain integration precision. The integration precision is further refined by either using Simpson's rule, Romberg's method [207], or the Legendre-Gauss quadrature. [148]

Integration is computationally expensive, SSC was optimised by W. Xu to rely on extensive caching of many model components [258]. In addition, the precomputation of specific quantities prevents redundant computation if SSC model parameters are not changing. The caching structure is illustrated in figure 4.8. Components that can currently be cached are highlighted in green. The boxes further include information about the parameter space the components are cached over. By adding caching and parallelisation features, the evaluation of the model becomes much faster, leading to evaluation times similar to approaches using multidimensional interpolation via neural nets [143] without the need for pre-calculation or training.

4.5.2. The KaFit framework

KaFit is a C++-based fitting framework used for sensitivity studies and the analysis of measured KATRIN data. The framework was mainly built to apply frequentist analysis methods (based on the MINUIT class of ROOT) but also includes Markov Chain Monte Carlo (MCMC) algorithms for Bayesian analysis (such as Metropolis-Hastings algorithm [127], or the sampling algorithm described in [103]).

Similarly to SSC, KaFit is configured with xml configuration files. An example for the kafit.xml applied in the neutrino mass, and sterile neutrino analysis can be found in the appendix (appendix D.1). The main fitting application coming with KaFit is called kafit-fitter. A simplified overview of the KaFit workflow when running kafit-fitter is illustrated in figure 4.9. The configuration file sets up how data is handled in the fit, how to configure the model, and furthermore links to the parameter definitions and constraints.

Measured data is summarised into run summaries. As described previously, run summaries are generated using BEANS routines to post-process the stored detector data. The information of slow control parameters on a scan basis and the measured counts are summarised in

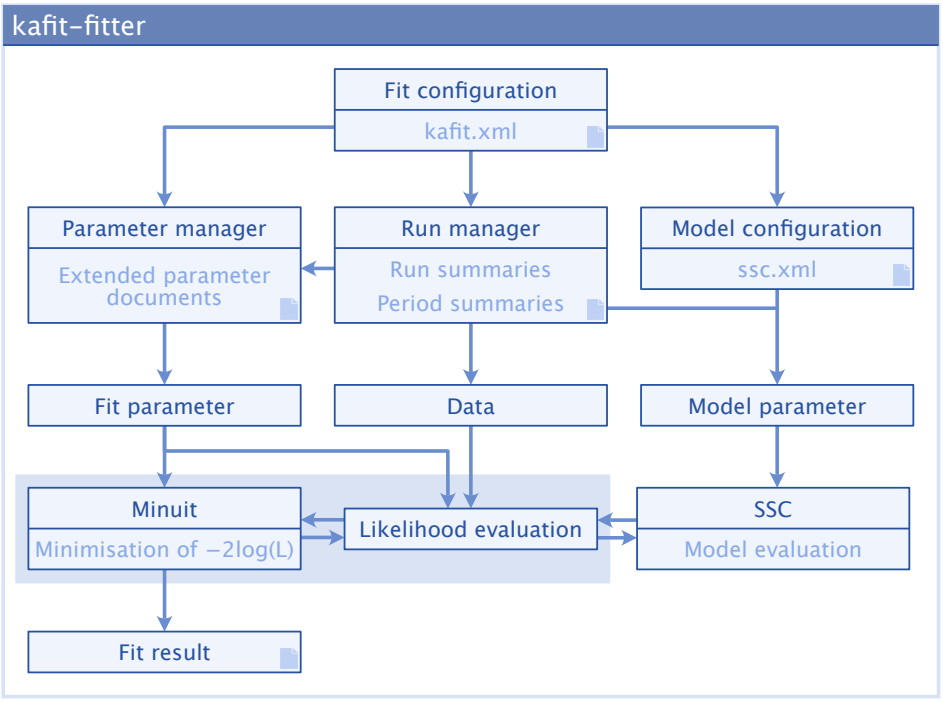

Figure 4.9.: Simplified schematic overview of `KaFit` when fitting KATRIN data with `kafit-fitter`. The fit is set up with the `kafit.xml` configuration file. Additional files define the fit parameter configuration and the `SSC` model from this. The data is collected from run and period summaries. The likelihood is evaluated during minimisation by comparing the model to the data. The minimisation itself is performed with `Minuit`, minimising the $-2 \log \mathcal{L}$. Once convergence criteria are satisfied, the result is written to a `root` file.

a single run summary. Parameters that apply to extended time periods or entire campaigns are collected in period summaries. All data going into the fit is listed in run registers. The `xml` run register links the corresponding files and defines which pixels are rejected for the analysis, how to group the data, and the relevant retarding potential cuts. The run register configuration looks as follows:

```
<kafit>
    <RunSummary
      Name="myRunSummary0"
      VarianceModel="Poissonian"
      RelativeEfficiency="true"
      PixelCuts="myPixelCutsKNM1"
      Patches="myPatchesUniform"
      QUCuts="myQUCuts"
      Segmentation="[seg:pixel]" >
        <Source Name="file:RunSummary.json"/>
        <Source Name="file:TritiumPeriodSummary-SolenoidCurrents.ktf"/>
        <Source Name="file:PeriodSummary.ktf" />
```

```
    </RunSummary>
    ...
</kafit>
```

Data from run summaries can also be combined in different ways. The options of run/campaign-wise data, appended data, and data stacking are possible. Usually, all scans of a campaign are stacked into a single spectrum, averaging the slow control parameters.

In parallel to this, the `SSC` model is initialised according to the model configuration file (see section 4.5.1). Information from the run manager determines how many models are initialised to match the number of spectra given in the data.

On the other side is the parameter manager. The parameter manager also relies on input from the run manager, giving information about the number of models. The parameters themselves are configured with so-called extended parameter documents. In a basic four-parameter fit, the `json` parameter doc would look like the following:

```
{ "ParameterDescription": {
  "Parameter": [
    { "KaFitIndex": 0, "Name": "mnu2",
      "RunCombination": "common", "PixelCombination": "uniform",
      "StartValue": "mnu2start", "StartError": 0.03, "Fixed": true,
      "LowerLimit": "none", "UpperLimit": "none" },
    { "KaFitIndex": 1, "Name": "E0",
      "RunCombination": "common", "PixelCombination": "uniform",
      "StartValue": 18573.7, "StartError": 0.002, "Fixed": false,
      "LowerLimit": "none", "UpperLimit": "none"},
    { "KaFitIndex": 2, "Name": "Sig",
      "RunCombination": "common", "PixelCombination": "uniform",
      "StartValue": 1.0, "StartError": 0.0003, "Fixed": false,
      "LowerLimit": "none", "UpperLimit": "none"},
    { "KaFitIndex": 3, "Name": "Bg",
      "RunCombination": "common", "PixelCombination": "uniform",
      "StartValue": 0.15, "StartError": 1e-06, "Fixed": false,
      "LowerLimit": "none", "UpperLimit": "none"}]
  }
}
```

This initialises each parameter with a specific start value and initial start error. The parameter configuration also configures parameter bounds and gives information if parameters are fixed or free. In addition, different options can be set for `RunCombination` and `PixelCombination`. Parameters can, for example, either be `common` for all scans or on a `run` basis. The same principle also applies for detector segments, assigning parameters `uniform`, `ring`-, `pixel`-, or `patch`-wise.

The extended parameter documents allow one to configure Gaussian penalty terms:

```
"Penalty": [
  { "KaFitIndex": 60, "PenaltyType": "Gauss",
    "Mean": 0.0328, "Sigma": 0.0012 }
]
```

The penalties are applied as a multivariate penalty when adding correlations:

```
"ParameterCorrelation": [
    { "KaFitIndex1": 1, "KaFitIndex2": 2, "Coefficient": 0.5 }
]
```

If a parameter is not considered as `uniform` or `common`, the parameter can be further correlated over different segments or runs. This correlation is established with additional `MINUIT` correlation terms:

```
"MinuitParameterCorrelation": [
  { "MinuitIndex1": 1, "MinuitIndex2": 2, "Coefficient": 0.5 }
]
```

Once parameters, data, and model are initialised, the fitting routine is executed. During optimisation, the minimiser (in this case `MINUIT`) passes different parameter proposals to the likelihood evaluator. As the name suggests, the likelihood evaluator sets the parameters in the model, the $-\log \mathcal{L}$ is calculated, which is then returned to the minimiser. Finally, the likelihood is implemented following the description in sections 4.1 and 4.2.2. Once the fit converges, results are written to `root` result files. In the case of other analysis types, such as a bayesian analysis, the minimiser is replaced by a Markov Chain sampler, and each chain step is written to a `h5` file.

The `KaFit` toolkit further comes with additional applications and modules:

The `kafit-runsummarygenerator` is used to produce Monte Carlo pseudo experiments or Asimov datasets[13]. These simulated datasets can be based on actual run summaries and allow systematic studies or testing of fitting routines before applying the analysis to real data.

The `kafit-runsummarymerger` allows one to pre-merge of datasets, so only one single pre-merged run summary must be read-in when starting the fit, rather than many hundreds of run summaries for each fit. In addition, the merging routine can stack the data and average each slow control parameter in a time-weighted manner.

A large part of the neutrino-mass analysis is usually the investigation of spectral features, biases, or spatial and temporal behaviour of parameters. To simplify such investigations, `KaFit` includes the visualisation tool `kafigure`. The application returns model components or spectra based on fit results or configuration files. The installation includes python

[13]The term is inspired by the short story "Franchise" by I. Asimov. An Asimov dataset describes the concept of a simulated dataset that does not contain statistical fluctuations [77], hence is an ideal representation of the model.

visualisation utilities and a python `KaFigure` module. The python utilities offer different visualisation options for spectra, fit results, model components, and direct comparison of different configurations.

The last feature is `KaFitpython` bindings. These provide a python interface to the C++ code, allowing one to obtain likelihood evaluations with python. This feature is, for example, used by the `katrin-MCMC` tool. `katrin-MCMC` is a modular Bayesian tool written in python. The tool is currently mainly based on the `KaFit` likelihood evaluation and combines MCMC samplers such as emcee. The Bayesian tool is optimised to perform studies with different priors and sampling methods, with the goal of performing a Bayesian analysis of the final KATRIN dataset, including different prior scenarios.

5. KATRIN measurement campaigns

The KATRIN experiment has been operating with tritium since the First Tritium campaign in June 2018 [32]. Since then, statistics have continuously been collected, gradually improving the sensitivity on the squared neutrino mass. Until today, there have been nine successful neutrino mass campaigns, with intermediate breaks for maintenance, systematics measurements, and improvements of experimental conditions. The campaigns follow the naming scheme KATRIN neutrino-mass measurement (KNM)x. From both the first and second neutrino mass campaigns, the KATRIN collaboration was able to set new best upper limits on the neutrino mass [22, 25], as well as improved exclusion bounds in the sterile neutrino parameter space [24, 26]. The first five neutrino-mass measurement campaigns are relevant to the thesis in hand. An overview of these campaigns is given in the following and in table 5.1.

Table 5.1.: Overview of KNM1 to KNM5. The respective duration of the first five KATRIN neutrino-mass measurement campaigns and the number of individually recorded scans are listed. The three columns (up, down, random) further split the scans by their respective scan direction. In the last column the relative amount of time spent to measure the background region is summarised.

Campaign	**Campaign duration**	**Number of scans**				t_{bg}
		Total	**Up**	**Down**	**Random**	
KNM1	2019, April to May	274	140	134	–	26 %
KNM2	2019, September to October	361	187	174	–	26 %
KNM3a	2020, June to July	114	48	47	19	21 %
KNM3b	2020, July	116	38	38	40	20 %
KNM4	2020, September to November	470	156	156	158	21 %
KNM5	2021, March to July	422	144	137	141	21 %

The KNM3 campaign is split into two parts (KNM3a and KNM3b) due to the fact that a new electromagnetic field setting has been tested in KNM3a (more details in section 5.2.1). In this chapter, a summary of the campaigns is presented. This includes an overview of the different applied measurement time distributions (section 5.1). Furthermore, the experimental conditions of each campaign are described more in detail (section 5.2), including in particular improvements of the background level by optimisation of the

electromagnetic field settings (section 5.2.1). In addition, the collected statistics are summarised, highlighting the improvements in the signal-to-background ratio.

> In the framework of this thesis, the data quality has been evaluated and monitored for different parameters on a scan and scan-step basis. This contributed to the identification of data quality cuts and the final scan selection used in the neutrino-mass and sterile neutrino analysis. Similar studies, investigating pixel dependent influences, and energy dependencies from the detector region of interest, contributed to the established pixel selections and provided justification for the applied region of interest cut. Additionally, a concept for "remote analysis shifts" was developed for the KATRIN collaboration to enable near-real-time problem identification. In combination with an online tool, this is now in use during neutrino mass operation.

5.1. Measurement time distribution

To optimise the sensitivity on the neutrino mass, dedicated measuring time distributions (MTDs) have been developed. The measurement time for a single scan is divided over different scan steps with varying lengths. In figure 5.1, an overview of the total cumulated measurement time during KNM1 to KNM5 is given. The plot shows the retarding voltage range down to 40 eV below the endpoint. The resulting MTD consists of 27 or 28 scan steps. Scan steps close to the endpoint are spaced with 1 eV, scan steps in the $\sim$ 15 eV to 40 eV window below the endpoint are spaced with 2 eV. Additional scan steps are taken beyond this range[1], which are used to monitor the stability and to quantify the impact of individual systematic effects. To investigate and avoid biases based on the scan direction, scan steps are usually performed in an upwards, downwards, and random fashion[2]. The ratios of up, down, and random scans are listed in table 5.1. As can be seen from the figure, slight adaptations and optimisations have been applied to the MTD over time. Many details on MTD optimisations can be found in [148, 221]. In general, longer measurement times are required for scan steps with expected low rates or in the background region.

Due to the limited knowledge of the neutrino mass and effective endpoint during the first campaigns, a conservative and broad MTD was chosen. The MTDs of KNM1 to KNM3b resemble this conservative distribution. The characteristic shape allows measurement of the spectrum with roughly equal statistics in scan steps close to the endpoint [131]. It was designed with the intent to achieve at least one count per pixel per scan step [132]. The five most upper scan steps are background points. It is essential to have good knowledge about the underlying background rate to be more sensitive to the neutrino mass [130]. Table 5.1 summarises the fraction of time spent in the background region. Modifications from KNM1 to KNM3b included small shifts to compensate for the potential depression in the analysing plane correctly and due to an overall lower background level [129].

During the course of KNM4 the MTD has been further adapted to reduce the impact of the time-dependent Penning trap induced background component (see section 3.8.3). In this case, 24 % (111 scans) of the campaign was taken with scan step blocks of only 100 s length, with regular intermittent emptying of the Penning trap with the Penning wiper[3] [222].

[1] The additional measurement points are evenly spaced in 5 eV steps down to 90 eV below the endpoint. There are one to two calibration points around 200 eV or 300 eV below the endpoint.

[2] The random scan direction was introduced from KNM3 onwards.

[3] The MTD with 100 s blocks became obsolete after grounding of the prespectrometer and hence eliminating the Penning trap.

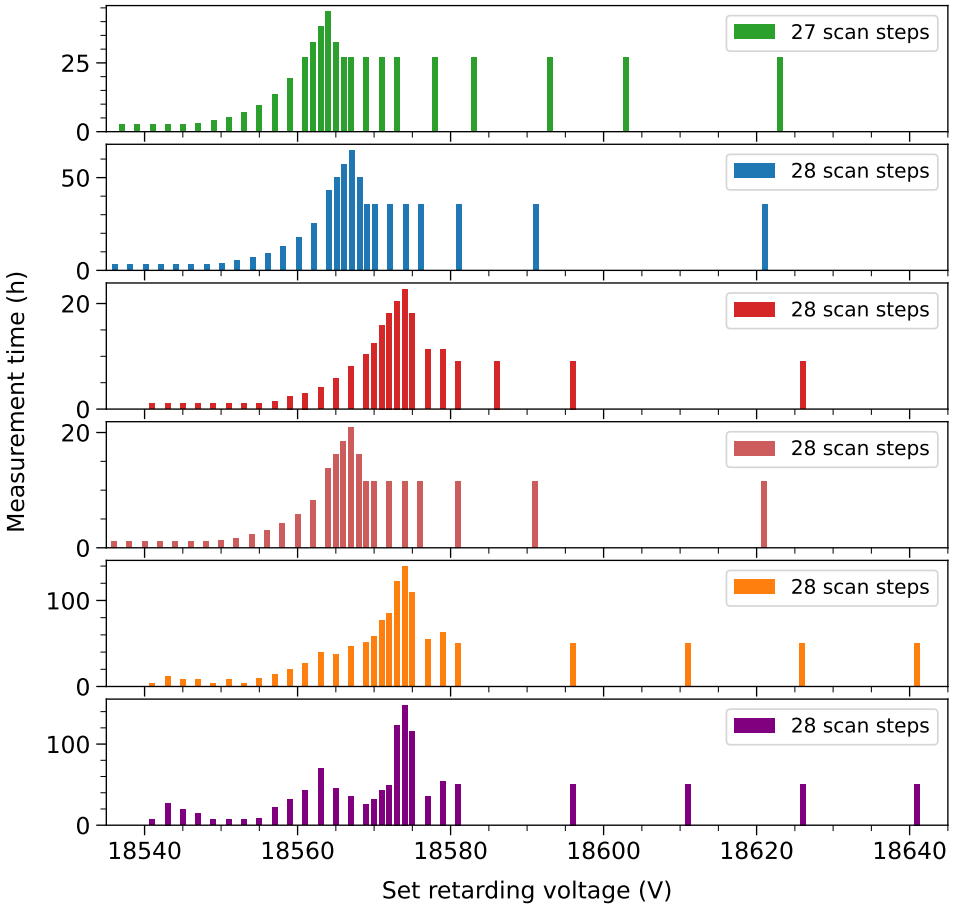

Figure 5.1.: KNMx measurement time distributions used for neutrino mass data taking. The distributions include a range down to 40 eV below the endpoint. Most of the measurement time is spent in the endpoint region for optimised sensitivity. Note that the plots are zoomed in for better illustration. KNM2, KNM3a, and KNM3b contain one additional background point at around 135 eV above the endpoint (at around 18 711 V and 18 716 V).

Before this, the emptying of the Penning trap was performed between scan steps of varying lengths. The last 39 scans of KNM4 were measured with a grounded prespectrometer, and varying scan-step duration.

According to the work presented in [148], the most optimised MTD consists of only four distinct points that characterise the neutrino mass, endpoint, signal, and background.[4] With uncertainties on these parameters and additional systematic effects, the measurement times of the four points are stretched out over a wider region, resulting in three peaks in the spectral region and an evenly spaced flat distribution in the background region. The even spacing of the background points achieves a robust sensitivity on a potential background slope.

The last MTD of KNM5 resembles this optimisation [221]. One can see the three peaks to disentangle the signal, the endpoint, and the neutrino mass. The background region is evenly-spaced. [223]

[4]This highly optimised MTD assumes that all parameters are perfectly known.

Table 5.2.: Experimantal conditions during neutrino-mass measurements. The table summarises the most significant changes in operation and data taking. The second column indicates the field setting. The third and fourth columns give an overview of the source conditions. The last two columns are detector related and show the applied region of interest cut on the measured data, as well as if a muon veto is applied to the detected electrons.

Campaign	Field setting	Source		Detector	
		$\rho d\sigma$	Temperature (K)	ROI (keV)	μ-veto
KNM1	NAP	0.397	30.1	[14, 32]	No
KNM2	NAP	1.539	30.1	[14, 32]	No
KNM3a	SAP	0.751	78.8	[22, 34]	Yes
KNM3b	NAP	1.357	78.8	[22, 34]	Yes
KNM4	SAP	1.377	78.8	[22, 34]	Yes
KNM5	SAP	1.379	78.8	[22, 34]	Yes

5.2. Experimental conditions

Experimental settings have been changed and optimised between measurement campaigns to improve the collected statistics and data quality. In this section, the main changes and improvements are summarised. KNM1, KNM2, and KNM3b have been measured in the nominal analysing plane (NAP) mode, whereas spectra of KNM3a, KNM4, and KNM5 were measured in the improved shifted analysing plane (SAP) mode. The two electromagnetic field settings are described in more detail in section 5.2.1. In addition to this, the stability of parameters is reviewed, describing what implication some of the parameters have in the context of systematics on the neutrino mass (see section 5.2.2).

The most significant applied changes in data taking are summarised with table 5.2. From this, one can see the evolution of the experimental conditions over time.

In the KNM1 campaign, the KATRIN experiment was operated for the first time with T_2 and a source temperature of 30.1 K, to demonstrate the functionality of all system components. Radiochemical reactions of T_2 with previously unexposed components and outgassing from the turbo molecular pumps led to freeze-out of a mixture of hydrogen, methane, and air in the injection capillaries, restricting the WGTS preassure to $1.09 \times 10^{21}\,\mathrm{m}^{-2}$ [175, 22]. This corresponds to 22 % of the designed nominal column density and a tritium throughput of 4.9 g/day. After a successful first campaign and reaching an equilibrium state of the metal surface conditions, the column density was increased to 85 % nominal in the second campaign. After KNM2, a new circulation mode was introduced that allowed the cocirculation of tritium and krypton. The cocirculation of krypton is particularly advantageous as it allows for direct measurements of the plasma conditions without extrapolations from different temperatures or column densities. However, measurements with krypton are not possible at 30 K as the krypton would start to condense. For this reason, the source temperature was raised to 78.8 K from KNM3 onwards. Again, to test the new circulation system, the source was not operated at full capacity during KNM3a but with a column density of $2.07 \times 10^{21}\,\mathrm{m}^{-2}$ (41 % nominal). From KNM3b onward, the WGTS is set

between 75 % and 76 % nominal column density at a temperature of 78.8 K.

On the detector system side, there have been two significant changes throughout the measurement campaigns. The data going into the neutrino-mass analysis of KNM1 and KNM2 corresponds to a detector ROI of [14, 32] keV. The FPD wafer was exchanged after KNM2. Therefore a more conservative ROI cut of [22, 34] keV is applied to the measured detector histogram. The upper edge of the ROI (34 keV) is motivated due to a different peak position and energy resolution of the replacement detector wafer. The narrow ROI cut is more conservative since a smaller amount of background electrons are recorded, which also cuts off background effects such as the additional ion peak below 22 keV. Since KNM3, additional background reduction is achieved, using data from the muon veto system. This reduces the background rate by $\sim 1\,\mathrm{cps/keV}$[5] and consequently improves the overall signal to background ratio [90].

5.2.1. Field configuration of the main spectrometer

One of the most significant changes was the introduction of improved field configuration of the main spectrometer. An overview of the two magnetic field configurations relevant to the neutrino-mass measurements is depicted in figure 5.2. The KNM1 and KNM2 campaigns were both performed in the nominal analysing plane (NAP) field configuration. The NAP fluxtube (figure 5.2 top – blue) has its analysing plane positioned in the centre of the main spectrometer vessel. Here, the minimum magnetic field in the analysing plane is $6.13 \times 10^{-4}\,\mathrm{T}$ with a maximum spread of $0.26 \times 10^{-4}\,\mathrm{T}$ (figure 5.2 centre left). This translates to a mean energy resolution of 2.76 eV at the endpoint.

Since the overall background significantly impacts the neutrino mass sensitivity, measures to reduce the background level are beneficial. The overall background rate is mainly composed of a volume-dependent component (77 %) originating from radon decays [163]. Hence, reducing the fluxtube volume between the analysing plane and the detector is advantageous. [167]

With KNM3, the shifted analysing plane (SAP) setting (figure 5.2 top – orange) was introduced by C. Weinheimer et al. [253] based on the work presented in [87]. In this setting, the electric potential maximum and magnetic field minimum are shifted towards the downstream end of the main spectrometer.[6] This effectively reduces the fluxtube volume (shaded orange) downstream of the analysing plane to $56\,\mathrm{m}^3$ compared to the NAP setting with $160\,\mathrm{m}^3$ (shaded blue) [167]. Furthermore, from figure 5.2 (top), one can also see that the analysing plane is deformed into a two-dimensional parabola.

The SAP has a mean analysing magnetic field of $5.53 \times 10^{-4}\,\mathrm{T}$ (figure 5.2 centre right) with an average energy resolution of 2.43 eV. Compared to the NAP setting, the magnetic field thus ranges over $1.66 \times 10^{-4}\,\mathrm{T}$ comparing the inner to the outer pixels. This consequently leads to a variation in energy resolution by 0.72 eV.

Alongside the changes in magnetic fields, the potential depression[7] ΔU_{ana} (see figure 5.2 bottom) is affected by the positional change of the analysing plane. The NAP setting

[5] For the narrow ROI this translates to a background reduction of ∼12 cps and for the wide ROI to ∼20 cps.

[6] The positioning and shaping of the analysing plane are limited by the vessel walls, as well as the inner electrode system and the air coil system surrounding the main spectrometer vessel.

[7] The potential depression describes the potential difference compared to the retarding potential set to the inner electrode system. The potential depression is given relative to a value of 18 600 V and reflects the effective retarding potential experienced by the electrons when traversing the main spectrometer.

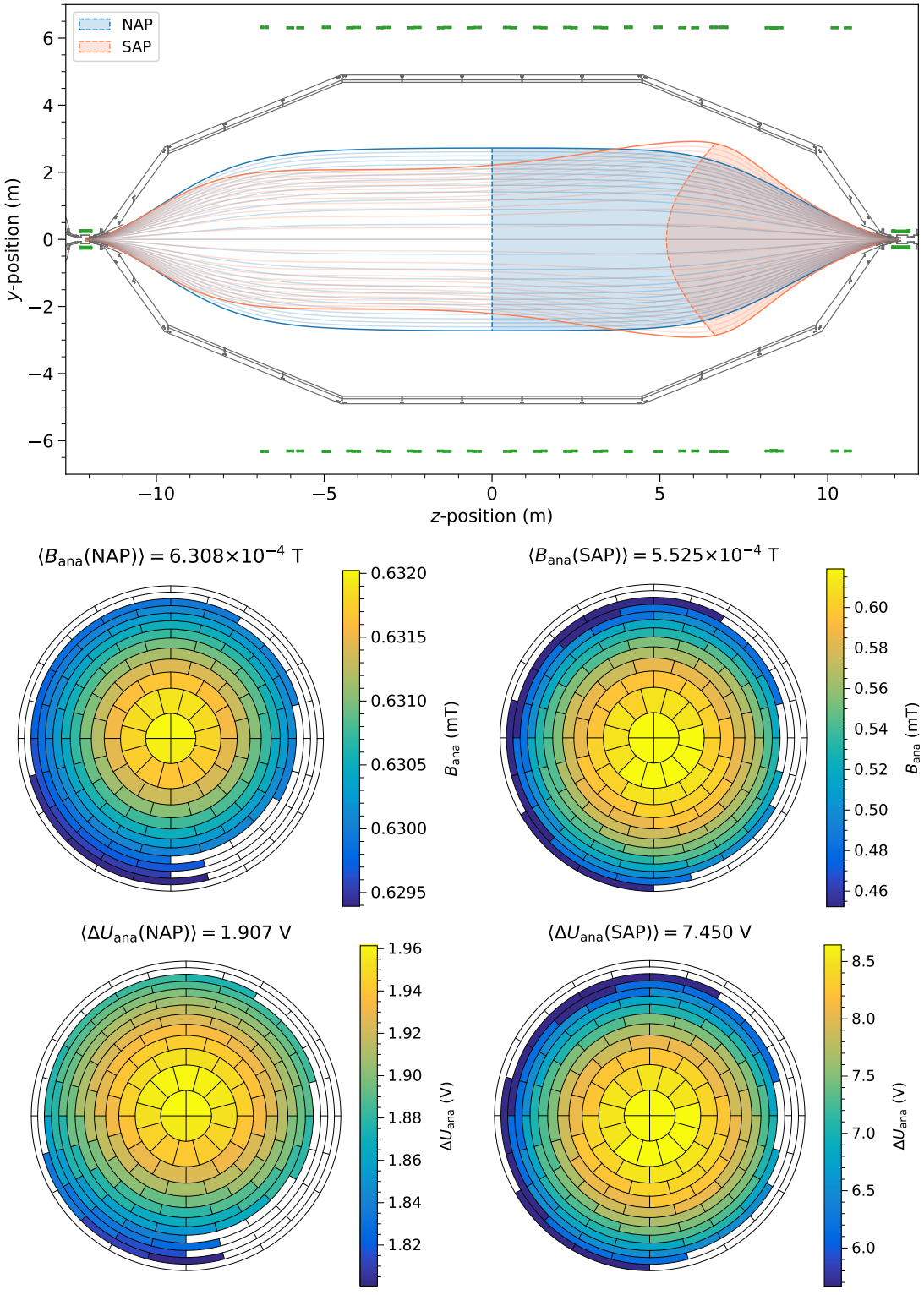

Figure 5.2.: Overview of the NAP and SAP field settings. **Top:** Simulated field lines of the NAP (blue) and SAP (orange) field settings. The lines correspond to field lines starting on the pixel edges. Dashed lines mark the analysing planes. The fluxtube volume between the analysing plane and the main spectrometer exit is shaded in blue and orange. Field line simulations provided by D. Hinz. **Centre:** Magnetic field strength in the analysing plane of KNM2 (left) and KNM5 (right). **Bottom:** Potential depression in the analysing plane of KNM2 (left) and KNM5 (right).

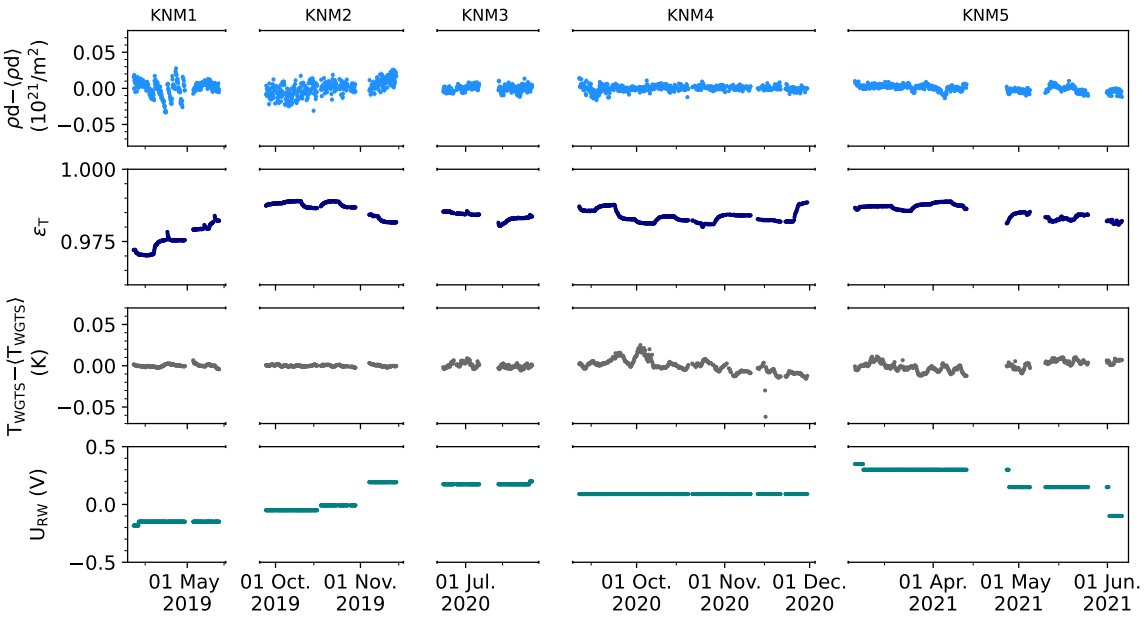

Figure 5.3.: Experimental source conditions over time. The relative column density ($\rho\mathrm{d} - \langle\rho\mathrm{d}\rangle$), tritium purity ($\varepsilon_\mathrm{T}$), relative temperature variations ($T_\mathrm{WGTS} - \langle T_\mathrm{WGTS}\rangle$), and rear wall bias voltage (U_RW). Each data point represents an individual β-scan.

exhibits a mean potential depression of 1.91 V relative to the set potential of the inner electrode system, while the SAP has a more pronounced potential depression of 7.54 V. Also, the spread of the retarding potential varies more in the SAP setting, with a maximal difference of 3.01 V from the outer to the inner pixels, compared to only 0.16 V in the NAP setting.

Both the large variations in the magnetic field and differences in the retarding potential in the analysing plane do not allow combination of all detector pixels into a single spectrum without significant sensitivity losses. Hence, for the analysis of campaigns in the SAP mode, pixels with similar transmission conditions are grouped into detector patches (for more details, see section 6.1.2).

5.2.2. Parameter stability

Stable operation is essential to the precise measuring of the tritium spectrum. Hence only small adjustments and minor fluctuations are expected throughout a measurement campaign. Larger changes that directly influence the neutrino mass have to be propagated as systematic uncertainties (for more details, see section 6.3.3). In figure 5.3, four major source-related parameters are shown, summarising the conditions within the WGTS.

The absolute values of the column density have been presented in table 5.2. One can observe two distinct features by looking at the relative column density fluctuations (figure 5.3, light blue). First, during KNM1, freezing in the injection capillaries restricted the maximum throughput and resulted in a conductance change of the injection capillaries, leading to drifts. With regular increases in the injection pressure, the column density was stabilised throughout the campaign. Despite the drifts, the relative changes in column density during

KNM1 are on the order of 0.08 ‰. The second feature can be observed at the beginning of KNM4. These fluctuations are solely due to a shorter length of the monitoring point for the first 95 scans, leading to a more considerable statistical uncertainty of the estimated column density. For KNM2 to KNM5 the measured column density varies with a standard deviation of only 0.01 ‰ to 0.02 ‰. Uncertainties on the column density, including the fluctuation, are discussed in more detail in section 6.3.3.1.

The source composition is characterised by the tritium purity ε_{T} (dark blue), which is mainly composed of T_2 and a small fraction of DT and HT.[8] The isotopologue HT results from the outgasing of hydrogen from the steel surfaces, and the fraction of DT is a residual remainder from the isotope separation process. The tritium purity is between 97.0 % and 98.9 %.[9] The amount of T_2 is ∼95 % for KNM1 and ∼97 % for all other campaigns. The second largest contribution is HT, which is on the order of 1.5 % to 3.5 %. Only a small fraction of around ∼1 % is DT. One can observe several kinks and steps when plotting the tritium purity over time. These features indicate a refilling of the inner loop system with a new batch of purified tritium [22]. Since each batch has a slightly different composition, refilling results in a changed equilibrium of the circulated gas. Variations of the tritium purity have a negligible effect when stacking scans, as they are absorbed in the signal normalisation.

As mentioned in the previous section, two operation temperatures (30.1 K and 78.8 K) were set during the measurement campaigns. It is important to mention the extremely high stability of the source temperature. In the 30.1 K setting during KNM1 and KNM2, the source temperature varied by only 2 mK and 1 mK, respectively. In the 78.8 K setting, the absolute variations are slightly larger with a standard deviation between 2 mK and 3 mK in KNM3, and the largest deviations with 8 mK and 6 mK in KNM4 and KNM5, respectively. The temperature fluctuations impact the broadening of the spectrum due to the Doppler effect and can be considered negligible compared to other broadening effects in the analysis.

As the rear wall defines the physical termination of the fluxtube, changes in the rear wall bias voltage, U_{RW}, directly impact the absolute starting potential of electrons in the WGTS. The bias voltage (figure 5.3, teal) is typically set to a small potential on the order of 100 mV. In the neutrino-mass analysis, the effective endpoint directly absorbs the mean rear wall potential. This mean rear wall bias voltage is lowest for KNM1 at −0.15 V, and largest for KNM5 at 0.23 V. During each measurement campaign, the voltage was reset several times to improve the coupling of the source plasma to the rear wall. These resulting offsets hence are also visible in the measured endpoint over time, effectively broadening the spectrum when stacking scans. Significant changes in U_{RW} are present during KNM2 and KNM5 with a maximum difference of 0.24 V and 0.45 V, respectively. This additional broadening due to the bias voltage is considered in the analysis. For more details, the reader is referred to section 6.3.3.1.

[8] The tritium purity is the number of tritium atoms in comparison to the overall amount of gas in the WGTS. The tritium purity is below 100 % due to the presence of a small fraction other isotopologues such eas DT and HT.

[9] During KNM1 the tritium purity was lower (in a range between 97.0 % and 98.4 %), whereas, in all subsequent campaigns, the tritium purity was ≥ 98.0 %.

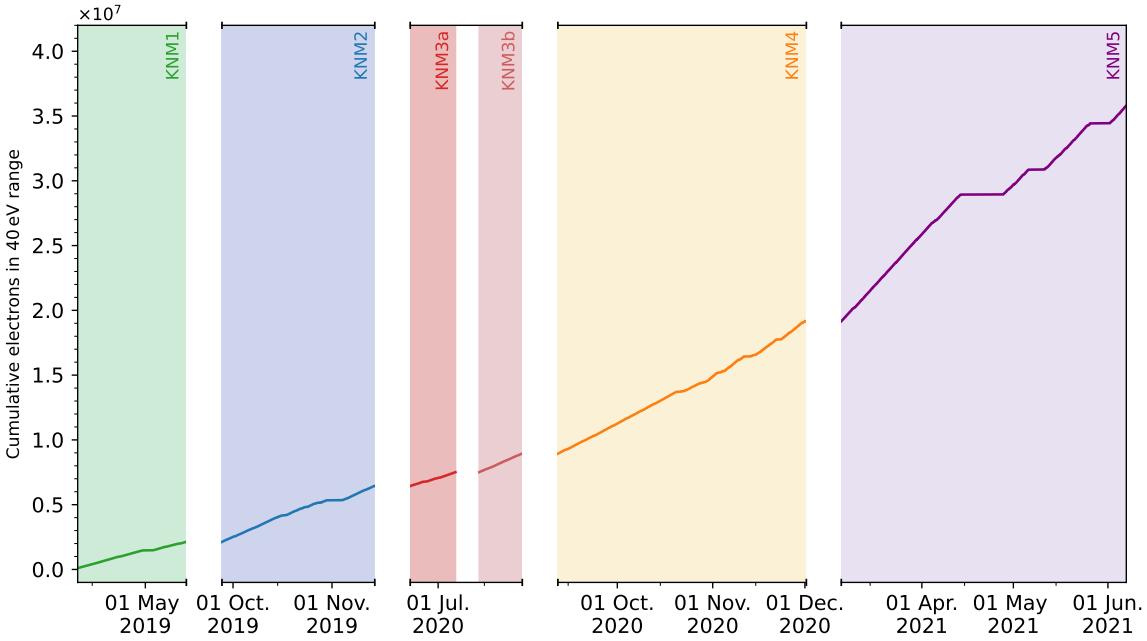

Figure 5.4.: Collected statistics during neutrino-mass measurements over time. Collected electrons that are combined into a dataset are highlighted in the corresponding colour. Overall 3.58×10^7 electrons were collected within the 40 eV analysis energy range during KNM1-5.

5.3. Collected statistics

As can be seen in figure 5.4, over the first five campaigns data taking with KATRIN continuously improved, leading to KNM4 and KNM5 being the longest measurement campaigns out of the set considered here. In figure 5.4, the cumulated number of electrons used in the analysis is given. One can also see that the increase in statistics over time is improving over campaigns, leading to a much steeper increase in KNM5.

A more detailed analysis of the statistics is summarised in table 5.3. Here, KNM3a and KNM3b are considered independently, as their spectra are also analysed separately. This campaign overall has fewer runs and net measurement time, as the feasibility of the SAP setting and the increase of the source temperature to 78.8 K were tested, followed by the introduction of a new circulation mode post KNM3. KNM4 and KNM5 have the largest net measurement time, as the operation was more automated, and improved post-regulation settings leading to faster high voltage stabilisation and shorter wait times when switching high voltage set points.

The number of active detector pixels, taken into account in the neutrino-mass analysis, increased from 117 pixels to 126 pixels between KNM2 and KNM3a. This was due to a different alignment, the detector wafer exchange post KNM2, and an improved position of the FBM within the CPS beam tube.

Separating the collected number of electrons into signal and background electrons, the major improvements and measures in background reduction are visible. Between KNM1 and KNM2, baking of the main spectrometer at 200 °C for approximately two weeks improved the vacuum conditions and resulted in a background reduction of 25 %. The introduction

Table 5.3.: KATRIN neutrino-mass measurement – statistics summary. All values refer to the energy range down to 40 eV below the endpoint. This is the same data selection as used for the neutrino-mass analysis. The number of background electrons approximated based on the five background scan setps.

Campaign	Scans	Scan steps	Active pixels	Net meas. time (h)	Signal electrons	Background electrons	Total	Sig./Bg.
KNM1 *	274	27	117	521.7	1.48×10^6	5.47×10^5	2.03×10^6	2.71
KNM2 *	361	28	117	694.3	3.76×10^6	5.54×10^5	4.31×10^6	6.79
KNM3a †	114	28	126	220.2	9.77×10^5	0.93×10^5	1.07×10^6	10.49
KNM3b *	116	28	126	224.1	1.25×10^6	1.80×10^5	1.43×10^6	6.92
KNM4 †	470	28	126	1266.6	9.63×10^6	5.89×10^5	1.02×10^7	16.36
KNM5 †	422	28	126	1225.6	1.60×10^7	6.05×10^5	1.67×10^7	26.53

* Normal analysing plane (NAP)
† Shifted analysing plane (SAP)

of the SAP field setting reduced the background rate by an additional 51 %. This is also reflected in the improved signal-to-background ratio in KNM3a.

Alongside this, changes of the MTD also directly impact the signal-to-background ratio. This is most pronounced when comparing the ratio of measured β-electrons to the number of recorded background electrons of KNM4 to KNM5 (Sig./Bg. = 16.36 compared to Sig./Bg. = 26.53). Here, the total measurement time remained at a similar length, while the collected statistics of signal electrons increased by 66 %. This is due to the redistribution of measurement time in the optimised MTD, with increased time spent deeper in the spectrum to be more sensitive to the signal amplitude.

6. Data analysis

In this chapter, the analyses of measured KATRIN data from KNM1 to KNM5 are presented in detail. First, the concepts of data combination and model fitting are outlined (sections 6.1 and 6.2). In the following two sections the neutrino-mass analysis of KNM1-5 data (section 6.3) and the search for sterile neutrinos by analysis of KNM1-2 data is presented (section 6.4). Each section will give detail on the applied fitting procedures, the systematic inputs and the influence of systematics, as well as the results.

With the work that went into this thesis, the combined fitting strategy was established, which is now used as the standard fit strategy for the combined analysis of measurement campaigns. This can simultaneously incorporate periods with uniformly analysed detector data and periods in which segmented detector data (e.g. pixels or patches as pixel groups) are considered. Within this thesis, the influence of various systematic effects was investigated in depth: First, the inputs modeling the additional rear wall spectrum were estimated from the analysis of dedicated rear wall measurements. Second, the systematic uncertainty from potential shifts and drifts was estimated from a scan-wise analysis of the measured β-spectrum. Before executing the neutrino-mass analysis, systematic uncertainties were implemented and tested in the analysis framework throughout comprehensive sensitivity studies on simulated spectra.

Different analysis environments were established for each campaign and the combined analysis, respectively. Due to the high degree of complexity of the analysis, automated handling of parameter inputs, uncertainties, and correlations was implemented for configuring of the model. Intermediate analyses of the KNM1 and KNM2 datasets, to which the work at hand has contributed, were published in [22, 25], resulting in successive improvements of the upper limit on the neutrino mass. Furthermore, the full KNM1-5 neutrino-mass analysis was performed. This analysis is the main result presented in the thesis in hand.

In addition, I was responsible for both preparing the released data that accompanied [25] and for preparing the release of KATRIN data, that will be published alongside the KNM1-5 analysis.

Extending the neutrino-mass analysis, also the search for light sterile neutrinos was conducted within the framework of this thesis. The sterile neutrino analysis of KNM1 presented here served as a crosscheck for the result published in [24]. The KNM2 sterile neutrino analysis was published in [26], where I serve as one of the three corresponding authors on behalf of the collaboration.

6.1. Data combination

From KNM1 to KNM5 included, a total number of 68 237 individual scan steps were recorded within the analysis window. Each of the 148 FPD pixels recorded incoming electrons separately, leading to 8.4×10^6 data points for all active pixels. Fitting all data points individually is computationally unfeasible; hence datasets are grouped and combined without consequently introducing a bias of the neutrino mass or sacrificing sensitivity. In the following two subsections, the temporal and spatial combination of datasets is discussed, as well as a short description of model modifications due to averaging of parameters (see section 6.1.2).

6.1.1. Scan combination

To group the data, simple criteria are applied. If the experimental conditions are stable, scan groups are formed. Typically experimental conditions throughout a measurement campaign are not changed, allowing grouping by measurement campaign. In the case of KNM3, the campaign is split into measurements in the NAP and SAP settings, leading to a scan grouping of KNM3a and KNM3b.

The grouped scans are then combined into one spectrum while averaging the slow control parameters present within the recorded data. For example, for the tritium purity, one would calculate the mean[1] tritium purity of all scans, propagating this value into the model. The individual spectral data points can then further be combined in several ways. Hereby, one can either append the data points of all individual scan steps or single scan steps of all scans are stacked into one combined scan step while averaging the corresponding retarding potential for the step. As high voltage reproducibility is on the ppm-level [205], stacking of scan steps is feasible, reducing the number of scan steps from 6×10^4 to only 167 scan steps for all campaigns combined. For the individual campaigns, scan steps the order of 10^3–10^4 are reduced to 27 or 28 scan steps.

6.1.2. Pixel combination

Similarly to the scan combination, the data of individual detector pixels are stacked if the spatial conditions are similar. Spectra of different pixels can be used individually (pixel-wise), as detector rings (ring-wise or radial), as patches (for example, radial patches or quarters), or combined into a uniform detector. When combining detector pixels into segments, spatially varying parameters are averaged over the corresponding pixels.[2] Spatially varying parameters are, for example, magnetic fields or electric potentials. Systematic inputs are given, varying over the detector segments.

The transmission function is calculated based on the mean magnetic field values in the analysis. If combined pixels show significant differences in the magnetic field, representing the transmission behaviour with an average magnetic field would lead to a bias on the neutrino mass. A better approach is the individual calculation of transmission functions of each pixel and subsequent averaging of the pixel-wise transmission functions. This

[1] Here, the weighted mean is calculated where the slow control parameters of individual scans are weighted by the scan duration. In this way, scans of varying lengths can be correctly combined.

[2] For the average, no weighting is needed, as all pixels have the same area.

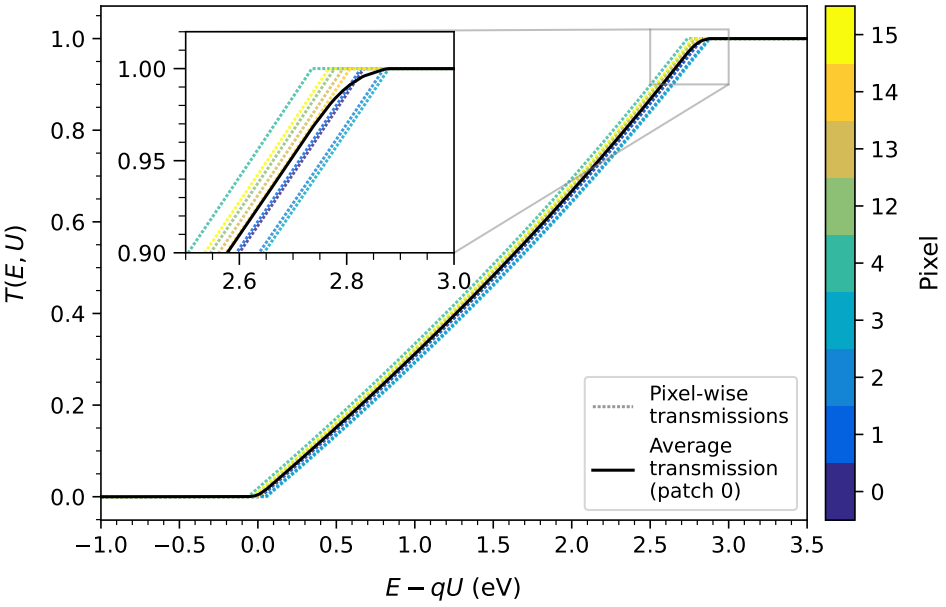

Figure 6.1.: Illustration of the transmission function broadening. In the SAP setting, the differences in the transmission characteristics are comparatively large. Combining different pixels (dotted) into patches is best represented by the average transmission function (black). The averaging effectively results in a broadening which smoothens the sharp transition of the transmission edge. Here, the effect is illustrated with patch 0 and its corresponding pixels. The magnetic field settings are those of the SAP configuration present during KNM5.

effectively leads to a broadened transmission function as illustrated in figure 6.1. However, the averaging of pixel-wise transmission functions comes with the downside of additional computation time. To reflect the broadening behaviour of the transmission function, an additional transmission broadening parameter σ_{ana} is introduced. This transmission broadening component is applied alongside other broadening effects by convolution of a Gaussian kernel (see section 3.5).

As a criterion for the pixel grouping, the similarity in transmission characteristics is evaluated[3]. This justifies a grouping to a uniform detector for each campaign in the NAP setting and grouping into 14 detector patches [165] of each campaign in the SAP setting. The 14 SAP patches each consist of nine pixels as illustrated in figure 6.2. Furthermore, all pixel numbers and the corresponding patches are listed in detail appendix C.2.

The patches are in first order radially aligned due to the strong radial dependence of the electric potential and magnetic field in the analysing plane. Due to the misalignment of the flux tube, the flux tube centre is mapped slightly towards the lower right in the front-face illustration chosen in figure 6.2. This slight misalignment is taken into account, leading to the patch definition displayed in figure 6.2.

[3]The position of 50 % transmission ($qU(T = 1/2)$) was chosen to quantify the similarity of the transmission between pixels.

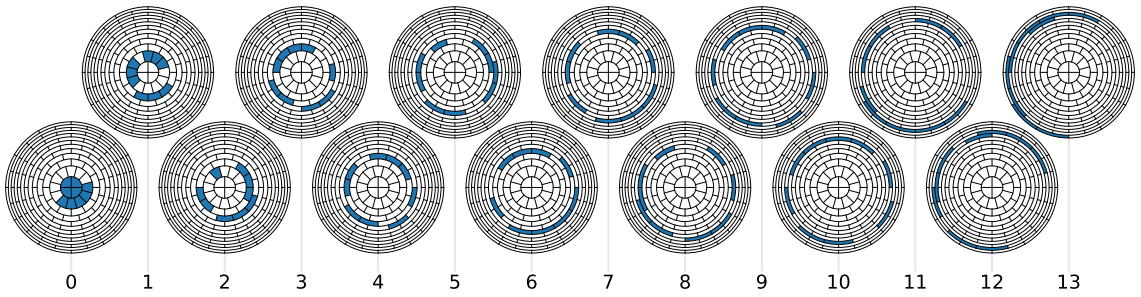

Figure 6.2.: SAP patch configuration. The active golden detector pixels are divided into 14 patches, each consisting of 9 pixels. Pixels are grouped into patches based on their transmission characteristics. A list of pixel numbers within a patch and the golden pixel selection can be found in appendices C.1 and C.2.

6.2. Combined fitting strategy

The concept of multi-fitting describes the combined fitting of datasets of, for example, different campaigns, scans, or detector segments, including parameters that are shared across models (such as m_ν^2). For the combined analysis of KATRIN data collected in KNM1-5 the χ^2 is constructed according to equations (4.9) and (4.15), leading to

$$\begin{aligned}\chi^2_{\text{multi}}\left(\vec{\Theta}\right) = &\sum_{\substack{i\in\\[1,2,3b]}} \chi^2_{\text{N},i}\left(m_\nu^2, E_{0i}, \text{Sig}_i, \text{Bg}_i, \vec{\eta}\right) \\ &+ \sum_{\substack{j\in\\[3a,4,5]}} \sum_{p=0}^{13} \chi^2_{\lambda,jp}\left(m_\nu^2, E_{0jp}, \text{Sig}_{jp}, \text{Bg}_{jp}, \vec{\eta}\right) \\ &+ \left(\vec{\eta}-\vec{\eta}\right)\Sigma^{-1}\left(\vec{\eta}-\vec{\eta}\right)^{\text{T}}.\end{aligned} \tag{6.1}$$

The defined χ^2_{multi}-function consists of three components. Note that only relevant entries of the parameter vector $\vec{\Theta}$ are used in each component.

First, we encounter a sum over the χ^2_{N} functions of all i NAP campaigns. The equation (4.7) is defined assuming a Gaussian pdf. The spectra are each defined with campaign-specific endpoint, signal normalisation, and background, but all share a common m_ν^2. In the case of systematics, also campaign-relevant elements of $\vec{\eta}$ are set during the χ^2 evaluation.

The second component is given for those spectra where Poisson pdfs are applied. As previously discussed, this is necessary for datasets with lower statistics. Due to the large radial differences and fractioning of data into patches, this affects all patch-wise spectra of SAP campaigns. For this reason, the χ^2_λ functions (according to equation (4.8)) are summed over all j SAP campaigns and also all 14 detector patches p.

The last contribution to the χ^2_{multi} are the penalty terms (see equation (4.15)). Here the multiplication with the covariance matrix Σ propagates correlations between entries of the nuisance parameter vector $\vec{\eta}$ naturally.

When analysing individual campaigns, only one of the the χ^2 components is required

Table 6.1.: Summary of the number of data points and the number of fit parameters per campaign. The number of constrained fit parameters is also given. Numbers are provided for both the statistics-only analysis and the total analysis which includes all systematics.

Campaign	No. of spectra	No. of data points	Stat. only			Total		
			Fit param.	Constr.	dof	Fit param.	Constr.	dof
KNM1	1	27	4	0	23	23	19	23
KNM2	1	28	4	0	24	23	19	24
KNM3a	14	392	43	0	349	105	62	349
KNM3b	1	28	4	0	24	26	22	24
KNM4	14	391	43	0	348	105	62	349
KNM5	14	392	43	0	349	104	61	349
KNM1-5	45	1259	136	0	1123	281	145	1123

(χ^2_{N} for NAP and χ^2_{λ} for SAP). For SAP campaigns, the summation over patches is still required.

For the analyses presented in this chapter, a summary of the parameter configuration and the number of data points is shown in table 6.1. The table is split into a section summarising the parameter setup of the statistics-only analysis and the total analysis which includes systematics. The number of degrees of freedom (dof) are calculated with

$$\mathrm{dof} = N_{\text{data points}} - N_{\text{free param.}} \qquad \text{where: } N_{\text{free param.}} = N_{\text{fit param.}} - N_{\text{constr}}, \tag{6.2}$$

and remain constant when adding systematics via pull terms. The analysis of individual campaigns is based on 1 or 14 spectra, respectively, with 4 free fit parameters in NAP campaigns and $1 + 14 \times 3 = 43$ free fit parameters for SAP campaigns. The free, unconstrained parameters of each campaign are solely composed of m^2_ν, E_0, Sig, and Bg. In the combined analysis, 1259 data points of 45 spectra are fit simultaneously while sharing one common m^2_ν. When adding systematics, 145 constrained nuisance parameters are added to account for systematic uncertainties. In the minimisation, 136 parameters are completely free.

6.3. Neutrino mass analysis

This section summarises the neutrino-mass analysis performed on the KNM1 to KNM5 datasets. In addition, general information about the fit setup, from a hardware and software standpoint, is summarised in section 6.3.1. To obtain unbiased results, a blinding procedure is applied (see section 6.3.2). Furthermore, having good knowledge about sources of systematic effects is essential. Therefore, the systematic effects are constrained by external measurements or simulations. The summary of all applied systematic inputs with central values and uncertainties is presented in section 6.3.3. Here, the methods and procedures for obtaining the external constraints are outlined. Further information about correlations between parameters, especially inter-campaign correlations applied in the combined analysis is given in this section. A breakdown of the effect of each systematic on the uncertainty and the central values is presented in section 6.3.3.2. The results and goodness-of-fit are

discussed in section 6.3.4. Additional studies on the time-dependence of the parameters, spatial dependencies, and effects of the scan direction are given in sections 6.3.4.1 to 6.3.4.3. Furthermore, fit range dependencies are discussed in section 6.3.4.4 Finally, results of the belt constructions using the Lokhov-Tkachov method and the Feldman-Cousins approach are presented in section 4.4.

6.3.1. Fit setup

The fit results presented in the following sections were performed with the `KaFit/SSC` framework (see section 4.5). The model and fit are set up according to the configurations displayed in appendices D.1 and D.2.

The fits are run on the local IAP cluster. The computing cluster is based on `Intel(R) Xeon(R) Gold 6230 CPUs` with 85 cores. The machines are operated with `Ubuntu 20.04.5 LTS`.

The `KASPER` code is compiled with `boost 1.71`, and C++ `9.4.0`. The version of `Root` used for the minimisation is `6.24`. Numerical minimisation is done with `MINUIT`, where asymmetric error estimation is done with the `MINOS` profiling algorithm.

The code is also compiled with `OpenMP` to allow for multithreading and hence reduce the fitting time. When compiled with `OpenMP` all spectra in the multi-fit are calculated in parallel.

The fit results have a numerical accuracy of the fit neutrino mass squared on the order of $10^{-4}\,\mathrm{eV}^2$ to $10^{-5}\,\mathrm{eV}^2$. Additional information about numerical stability and reproducibility is shown in appendix B.2.

6.3.2. Blinding scheme

The analysis follows a strict blinding scheme to guarantee a robust analysis and reliable, unbiased neutrino mass results. The model blinding scheme was introduced with KNM1 as described in [128]. The blinding follows a three-staged approach. In the first stage, model blinding is applied by broadening the final state distribution. In this stage, the electronic ground state of the final state distribution is replaced by a Gaussian, which is broadened or narrowed by an unknown value. Next, investigations on individual campaigns are performed with individually blinded FSDs. The combined analysis utilises a separate blinded FSD. The FSD smearing has the advantage that only the central value of the squared neutrino mass is affected by the model blinding, which can shift to both positive and negative values by an arbitrary, unknown amount, therefore eliminating potential biases due to the knowledge of the central value [128]. Other fit parameters, such as the signal, endpoint, and background are, on the other hand, unaffected by the FSD blinding procedure. Furthermore, the sensitivity of the neutrino mass is identical since the data remains unchanged.

In the first stage, studies on data are only performed with a neutrino mass fixed to zero. Testing of the analysis code and investigations with a free m_ν^2 are performed on simulated Asimov datasets. The datasets are generated based on inputs from individual scans to closely mimic the expected data. The analysis is performed by independent teams with different analysis codes in parallel.

After the agreement of the different teams, the actual data is fit in unblinding step two. Again, analysis is only performed with the blinded FSDs, which shifts the neutrino mass squared by an unknown value. In this step, additional investigations can be performed on the data, giving insight into relative effects, such as radial dependencies, of the observed m_ν^2.

In the third and final unblinding step, the data is fit with the actual unblinded FSD without allowing any further changes to the analysis procedure. Since all campaigns are blinded separately, unblinding of individual campaigns is possible without unblinding the entire dataset.

6.3.3. Systematics effects

It is crucial to correctly account for systematic uncertainties to fit an unbiased value for the neutrino mass and to obtain a reliable uncertainty estimation. For the neutrino mass analyses presented in this chapter, systematics are propagated into the analysis by introducing additional constrained fit parameters. The inputs are estimated and provided by dedicated subsystem expert groups. In the following, sections 6.3.3.1 and 6.3.3.2 will give an overview of the systematic inputs that go into the analysis, as well as the impact of the described systematics on the neutrino mass. In the following paragraphs, a summary of each systematic effect is given, summarising what the respective values and uncertainties are based upon.

6.3.3.1. Systematic inputs

Table 6.2 gives a general overview of the systematic inputs used in the neutrino-mass analysis. The systematic inputs are divided into ten groups:

Overdispersion of the background due to non-Poisson events	Background related
Time-dependent background	
Retarding potential dependent background	
Additional β-spectrum from the rear wall	
Source plasma related	Source related
Column density	
Energy loss function	
Analysing plane	Transmission related
Source magnetic field	
Pinch magnetic field	

The values in the table represent the input for each campaign. If inputs are valid for more than a single campaign, the correlated campaigns are marked with a) or b). To keep the overview table compact, patch-wise values and uncertainties (marked by the asterisk) are averaged and only the mean value and mean uncertainty are listed in the table. Each of the inputs and their uncertainties is described in more detail in this section.

Table 6.2.: Summary of parameter inputs applied in the neutrino-mass analysis. The parameters are sorted by their impact on the neutrino mass in the combined analysis. Each column contains central values and uncertainties for a single campaign. If a systematic is not present, negligible, or eliminated in a campaign, it is marked with n.a. Some of the inputs are taken into account as patch-wise values in the analysis; in this case, the mean value and mean uncertainty are listed. Central values and uncertainties of the energy loss function parameters have been omitted, they can be found in table 3.1.

Parameter	Unit	KNM1	KNM2	KNM3a	KNM3b	KNM4	KNM5
$\boldsymbol{\sigma_0^2}$	(10^{-3} eV^2)	0.900 ± 0.900	0.880 ± 0.880	0.890 ± 0.150	[a)] 0.890 ± 0.190	[a)] 0.890 ± 0.190	[a)] 0.890 ± 0.190
$\boldsymbol{\Delta_{10,\mathrm{eff}}^{\dagger}}$	(mV)	0.000 ± 18.730	0.000 ± 22.950	0.000 ± 18.930	[a)] 0.000 ± 21.040	[a)] 0.000 ± 21.040	[a)] 0.000 ± 21.040
$\boldsymbol{\sigma^2_{\mathrm{shift,drift}}}$	(10^{-3} eV^2)	-1.990 ± 1.695	3.782 ± 0.758	0.111 ± 1.286	-1.317 ± 0.650	0.659 ± 0.176	8.594 ± 0.876
$\mathbf{Bg^{\dagger}_{Penning}}\dagger$	(μcps/s)	-2.783 ± 5.439	3.795 ± 3.795	11.135 ± 4.417	13.191 ± 6.308	10.102 ± 1.879	n.a.
$\boldsymbol{\rho \mathrm{d}\sigma}$		0.397 ± 0.003	1.539 ± 0.006	0.751 ± 0.003	1.357 ± 0.006	1.377 ± 0.006	1.379 ± 0.005
$\mathbf{Bg^{\dagger}_{slope}}\dagger$	(μcps/eV)	[a)] 1.057 ± 3.759	[a)] 1.057 ± 3.759	[b)] 1.292 ± 0.822	[a)] 1.057 ± 3.759	[b)] 1.292 ± 0.822	[b)] 1.292 ± 0.822
$\boldsymbol{B_{\mathrm{ana}}}$	(10^{-4} T)	6.306 ± 0.063	6.308 ± 0.063	[a)*)] 5.355 ± 0.263	6.289 ± 0.063	[a)*)] 5.355 ± 0.263	[*)] 5.525 ± 0.011
$\boldsymbol{\sigma^2_{\mathrm{ana}}}$	(10^{-3} eV^2)	1.202	1.306	[a)*)] 54.715 ± 51.162	1.130	[a)*)] 54.715 ± 51.162	[*)] 13.346 ± 1.190
$\boldsymbol{B_{\mathrm{src}}}$	(T)	[a)] 2.506 ± 0.006	[a)] 2.506 ± 0.006	[a)] 2.506 ± 0.006	[a)] 2.506 ± 0.006	[a)] 2.506 ± 0.006	[a)] 2.506 ± 0.006
E-loss				Parametrs and uncertainties provided in table 4.1.			
$\boldsymbol{B_{\mathrm{pch}}}$	(T)	4.240 ± 0.004	4.239 ± 0.004	[a)*)] 4.242 ± 0.004	4.241 ± 0.004	[a)*)] 4.242 ± 0.004	[a)*)] 4.242 ± 0.004
$\mathbf{Sig_{rw}}$	(10^{-3})	n.a.	n.a.	[a)] 4.522 ± 0.106	2.850 ± 0.040	[a)] 4.109 ± 0.034	2.283 ± 0.034
$\boldsymbol{E_{0,\mathrm{rw}} - 18575}$	(eV)	n.a.	n.a.	[a)] 1.140 ± 0.360	[a)] 1.140 ± 0.360	[a)] 1.230 ± 0.360	0.980 ± 0.500
$\boldsymbol{w_{\mathrm{GS,rw}}}$		n.a.	n.a.	[a)] -0.110 ± 0.033	[a)] -0.110 ± 0.033	[a)] -0.110 ± 0.033	-0.134 ± 0.046
$\mathbf{Bg_{non\text{-}Poi}}$		1.064	1.112	n.a.	1.106	n.a.	n.a.

[a)b)] Values or uncertainties of this parameter are correlated between campaigns. More details can be found in the text.

[*)] Values are patch wise, here the mean is given.

[†] $\Delta_{10,\mathrm{eff}}$ is here given as an effective value, representative for the individual Δ_{i0} which would lead to an equivalent systematic error in the 40 eV fit range.

[††] The input values for the Penning trap induced background and the high voltage dependent background slope are scaled to the area of 148 pixels.

The systematic effects described in this section are sorted corresponding to their impact (which will be discussed in section 6.3.3.2).

For KNM1 and KNM2, the systematic inputs presented in this section are reevaluated compared to [22, 25]. The updated inputs come from new measurements and calibrations, as described in the following.

Source potential: Plasma effects[4] on the source potential are measured in dedicated krypton campaigns. Plasma effects are manifested in the spectrum as an additional broadening and relative energy shifts of the energy loss function. The parameters are extracted from the analysis of the N_{23} conversion electron lines of ^{83m}Kr at around 32 keV. The integrated spectrum of ^{83m}Kr is described as follows:

$$\dot{N}(qU) = \int_0^\infty \int_0^{E-qU} \int_0^{\theta_{\max}} \sum_s \mathcal{T}\left(E - \Delta E_{\text{sync}} - \varepsilon, qU, \theta, B_{\text{ana}}\right) \cdot \sin\theta \cdot P_s\left(\theta, \rho\text{d}\right) \cdot f_s(\varepsilon - \Delta_{s0}) \cdot D(E) \cdot \text{d}E\, \text{d}\varepsilon\, \text{d}\theta + \text{Bg}. \tag{6.3}$$

Similarly to the integrated spectrum of tritium (equation (3.45)), the integrated krypton spectrum is composed of the transmission function $\mathcal{T}$ including synchrotron losses ΔE_{sync}, the scattering probabilities P_s for the s-fold scattering, the s-fold energy loss function f_s, the differential krypton spectrum $D(E)$, as well as the addition of a background component Bg [171]. Note that the energy loss function includes the additional parameter Δ_{s0}, reflecting the shift of the s^{th} energy loss function as a result of plasma effects. The differential line spectrum of krypton is the sum of individual lines,

$$D(E) = A_2 \cdot V\left(E_2, \sigma^2, \Gamma_2^2\right) + \sum_i R_{i2} \cdot A_2 \cdot V\left(E_2 + \Delta E_{i2}, \sigma^2, \Gamma_i^2\right). \tag{6.4}$$

The spectrum is hereby centred around the N_2 line at E_2, with the addition of i other lines that are shifted by ΔE_2 to the N_2 line.[5] The line spectra are multiplied by a normalisation factor A_2 and relative amplitude ratios R_{i2}. The krypton line itself is described by the Voigt function V with a Lorentzian width of Γ.[6] The characteristic broadening caused by the presence of plasma is included in the differential spectrum through the additional broadening parameter σ^2. When fitting krypton spectra, the broadening parameter σ^2 also includes other broadening effects. The additional broadening can come from high voltage fluctuations σ^2_{HV} and Doppler broadening σ^2_E (section 3.5). The broadening only due to plasma σ^2_0 is then given by:

$$\sigma_0^2 = \sigma^2 - \sigma^2_{\text{HV}} - \sigma^2_E. \text{ [68, 171]} \tag{6.5}$$

In the summer of 2021, measurements of the N_{23} line duplet were completed. Scans were performed at 40 % column density (one day of measurements), as well as 75 % column density (25 days of measurements). To avoid condensation on the beamtube walls, krypton

[4] The presence of low-energy decay electrons and ionised molecules creates a cold-magnetised plasma within the source. The plasma can influence the starting potential of electrons inside the WGTS (for more details see section 3.7).

[5] Additional lines that are accounted for in the analysis are the N_1, N_3, as well as satellite lines such as N_{S1} and N_{S2}.

[6] The Voigt function is given by a convolution of a Cauchy-Lorentz distribution with a Gaussian distribution.

Table 6.3.: Constant factors and asymmetry values serve as inputs to calculate the energy loss shift. Values taken from [68].

Campaign	κ_1	κ_2	κ_3	ρ_{12}	ρ_{13}	ρ_{23}
KNM1	0.618	0.972	1.234	0.971	0.912	0.981
KNM2	0.746	1.227	1.617	0.959	0.893	0.982
KNM3a	0.624	0.974	1.227	0.963	0.901	0.983
KNM3b45	0.687	1.086	1.383	0.958	0.889	0.981

scans are performed at a temperature of 78.8 K. For the analysis of the data at 40 %, the integrated spectrum is fit individually for each pixel while stacking all scans. In the 75 % column density setting, the stacked data is fit with pixel-wise models, where E_2, A_2, Bg, and B_{ana} are applied individually to each pixel, while the broadening σ^2, the ratios R_{i2}, and ΔE_{i2} are applied as common parameters to all pixels within a patch. [68]

For 40 % column density, this results in a broadening of $(0.890 \pm 0.150) \times 10^{-3}\,\text{eV}^2$. With a column density of 75 %, the obtained plasma broadening is $(0.890 \pm 0.190) \times 10^{-3}\,\text{eV}^2$. [68]

The neutrino-mass measurements of KNM1 and KNM2 were performed at 30.1 K. Therefore the broadening values of krypton measured at 78.8 K can not be applied directly. Furthermore, KNM1 and KNM2 were measured at a column density of 22 % nominal and 85 % nominal, respectively. To get the broadening for KNM1 and KNM2, the broadenings at 40 % and 75 % are extrapolated to the correct column density. To account for the temperature differences (30.1 K vs 78.8 K), the uncertainties on σ_0 in additionally increased down to zero. This results in a broadening of $(0.900 \pm 0.900) \times 10^{-3}\,\text{eV}^2$ and $(0.880 \pm 0.880) \times 10^{-3}\,\text{eV}^2$ for KNM1 and KNM2, respectively. [68]

Upper limits on the energy loss shifts Δ_{i0} are constructed based on equation (3.51) [171]. Table 6.2 lists a set of effective parameters of Δ_{10} that represent the combined effect of Δ_{10}, Δ_{20}, and Δ_{30}. In the model, the individual energy loss shifts are applied using relation (3.50). The antisymmetrical factors $\hat{\rho}_i$ and the constant factors κ_i determine the energy loss shift range based on the plasma broadening. For the first three scatterings, $\hat{\rho}_i$ given by the relations derived by M. Machatschek [68], based on the "Machatschek inequality" (equation (3.51)):

$$\hat{\rho}_1(r_1) = r_1 \tag{6.6}$$

$$\hat{\rho}_2(r_2, \hat{\rho}_1) = \hat{\rho}_1\rho_{12} + r_2 \cdot \sqrt{1-\hat{\rho}_1^2} \cdot \sqrt{1-\hat{\rho}_{12}^2} \tag{6.7}$$

$$\begin{aligned}\hat{\rho}_3(r_3, \hat{\rho}_1, \hat{\rho}_2) = & -\frac{1}{1-\rho_{13}^2} \cdot \Big(\hat{\rho}_2\left(\rho_{12}\rho_{13} - \rho_{23}\right) + \hat{\rho}_1\left(\rho_{12}\rho_{23} - \rho_{13}\right) \\ & + r_3 \sqrt{\left(1-\hat{\rho}_1^2\right)\left(1-\hat{\rho}_2^2\right) - \left(\hat{\rho}_{12} - \hat{\rho}_1\hat{\rho}_2\right)^2} \\ & \cdot \sqrt{\left(1-\rho_{13}^2\right)\left(1-\rho_{23}^2\right) - \left(\rho_{12} - \rho_{13}\rho_{23}\right)^2} \Big).\end{aligned} \tag{6.8}$$

In this form r_i is bound to $\in [-1, 1]$ with a Gaussian constraint, centered around $\mu_r = 0$ and an uncertainty of $\sigma_r = 1$. All other values for κ_i and ρ_{1i} are listed in table 6.3. This

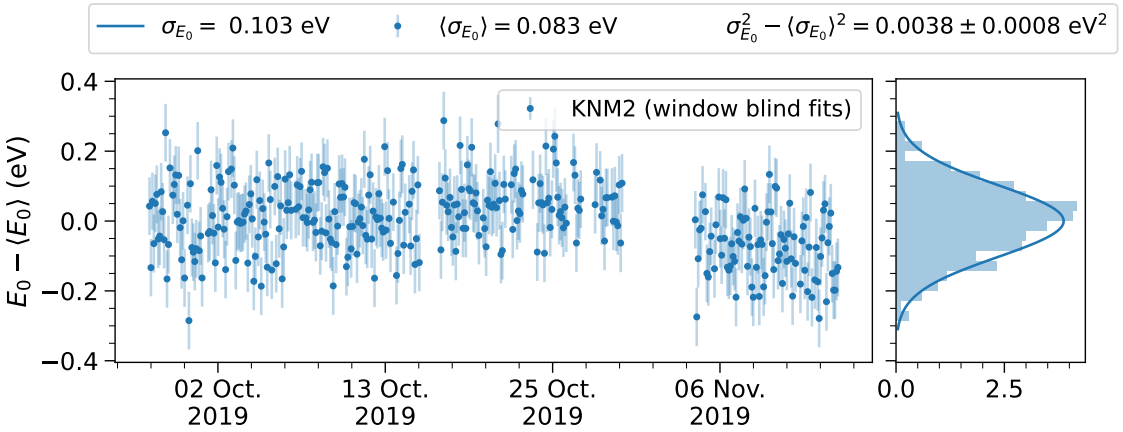

Figure 6.3.: Example of the shift and drift broadening using KNM2. The broadening is extracted from the endpoints of "window blind" fits (left). In the fits, endpoint, background and the column density are free parameters. The same fits are also used to determine the broadening due to potential shifts and drifts (see paragraph *Column density*). By subtracting the mean uncertainty of each endpoint fit from the variance of the distribution of all endpoints (right), one can extract the additional broadening due to potential shifts and drifts. During KNM2, the rear-wall voltage was adjusted twice, leading to the three distinct offsets in the fit endpoint. The same analysis is performed for each campaign.

representation also strongly correlates the $\hat{\rho}_i$ with each other. Since the neutrino-mass analysis is performed down to 40 eV below the endpoint, only Δ_{10} and Δ_{20} have a significant contribution and therefore have to be taken into account. Furthermore, the ρ_i and r_i are treated as common for all campaigns. This treatment is considered to be most conservative. [68, 171]

Source potential shifts and drifts: During measurement campaigns, shifts and drifts in the plasma potential can occur due to the rear-wall bias voltage and the general plasma conditions. These shifts and drifts manifest themselves within the endpoint fit result and are also considered in the final neutrino mass fit. The maximum possible plasma potential shift and drift is obtained from the broadening of the endpoint throghout a campaign and is determined from fits on "window blind" data. These fits are performed on a scan-wise basis, excluding the spectral data that is used for the neutrino-mass analysis. The data therefore only consists of the five background scan steps and scan steps with $qU < (E_0 - 40\,\text{eV})$.[7] The broadening on the endpoint fit result is taken into account in the KNM1-5 neutrino-mass analysis via an additional broadening $\sigma^2_{\text{shift,drift}}$.

This method involves analysis of the distribution of the scan-wise fit endpoint values, which are directly influenced by the source potential. An example of the shift and drift broadening analysis of KNM2 is displayed in figure 6.3.

To account for different scan lengths (for example, in the two periods in KNM4), the endpoint results are weighted with the corresponding effective measurement time of each

[7] The same scan-wise window blind fits are used as in the column density analysis.

scan t_i. The weights are given as follows:

$$w_i = t_i. \tag{6.9}$$

From the scan-wise endpoints, the mean weighted endpoint is given as:

$$\langle E_0 \rangle = \frac{\sum w_i \cdot E_{0,i}}{\sum w_i}. \tag{6.10}$$

The weighted standard deviation is calculated with:

$$\sigma_{E_0} = \sqrt{\frac{\sum w_i \cdot \left(E_{0,i} - \langle E_0 \rangle\right)^2}{\sum w_i}}. \tag{6.11}$$

Furthermore, the expected statistical uncertainty is given by:

$$\langle \sigma_{E_0,\mathrm{stat.}} \rangle = \frac{\sum w_i \cdot \sigma_{E_0,i}}{\sum w_i}. \tag{6.12}$$

The variance is then calculated as the difference in quadrature of the width and the expected width,

$$\sigma^2_{\mathrm{shift,drift}} = \sigma^2_{E_0} - \langle \sigma_{E_0,\mathrm{stat.}} \rangle^2. \tag{6.13}$$

This variance $\sigma^2_{\mathrm{shift,drift}}$ is interpreted as the additional broadening due to shifts or drifts of the plasma conditions or other unknown effects.

To estimate the uncertainty of the variance, the bootstrapping method is used. Random selections of endpoint values (with the same total number of values) are drawn with replacement, and the variance is calculated. This is repeated 10^5 times, and the $1\,\sigma$ width of the resulting distribution is taken as the uncertainty value.

All applied input values for $\sigma^2_{\mathrm{shift,drift}}$ and the according uncertainties are listed in table 6.2. The largest drift was observed in KNM5 due to the work function changes at the beginning of the campaign, after cleaning of the rear wall.[8] KNM2 also shows a significant shift broadening due to the different rear-wall bias voltages. It should also be noted, that negative values for $\sigma^2_{\mathrm{shift,drift}}$ are also applied in the analysis, in order not to introduce a bias by only including positive broadening values (the mathematical treatment of negative broadening values is covered by equation (6.14)). Negative values for $\sigma^2_{\mathrm{shift,drift}}$ were observed in both KNM1 and KNM3b, and can be interpreted as a statistical under fluctuation.

Time-dependent background: The Penning trap between the pre- and main spectrometer creates a background component which increases over time, as explained in section 3.8.3. If not correctly accounted for, the time-dependent background can emulate a high voltage-dependent background slope on the order of 300 mcps/keV to 500 mcps/keV close to the endpoint [89]. This leads to a neutrino mass bias on the order of $10^{-2}\,\mathrm{eV}^2$ to $10^{-1}\,\mathrm{eV}^2$. Since MTDs are optimised to be more sensitive to the neutrino mass, individual scan steps have varying lengths. Overall data points, the time-dependent background component reflects the MTD shape. The background increase is hence not equivalent for each scan

[8] Cleaning is performed by UV illumination of the rear wall surface in combination with the purging of O_2, forming ozone.

step and can vary between measurement campaigns. The Penning trap is cleaned out between scan steps by activating the Penning wiper.

To investigate the Penning trap induced background and obtain more stringent systematic input values, dedicated measurements were performed in KNM4 [106]. For the previous measurements, KNM1, KNM2, and KNM3, no dedicated measurements are available. Here, the slope is estimated from scan steps in the background region of the tritium β-decay scans. To estimate the time-dependent background slope, the background scan steps are rebinned into 1 s time intervals. For the individual scan steps, each 1 s bin of all scans is stacked, giving the rate evolution throughout every scan step. The background increase is extracted by fitting a linear slope to the rate evolution throughout a scan step. The fit is performed with one common slope for all scan steps. Values for each campaign are found in table 6.2. [164]

During KNM4 additional efforts were implemented throughout the campaign to reduce the systematic effect of the Penning trap induced background component. For each campaign segment in KNM4, individual $\mathrm{Bg}_{\mathrm{Penning}}$ are estimated. Initially, measurements were started in KNM4 with a scan length of 2 h (97 scans: $\mathrm{Bg}_{\mathrm{Penning}} = (4.8 \pm 5.2)\,\mu\mathrm{cps/s}$)[9]. The scan length was then increased to be 3 h (174 scans: $\mathrm{Bg}_{\mathrm{Penning}} = (11.4 \pm 2.1)\,\mu\mathrm{cps/s}$). An additional small modification to the MTD was that the longest scan step is smaller than 10 min (60 scans: $\mathrm{Bg}_{\mathrm{Penning}} = (6.3 \pm 5.3)\,\mu\mathrm{cps/s}$). To make the time-dependent background equal in every scan step, scan steps were further split into blocks of 100 s (123 scans: $\mathrm{Bg}_{\mathrm{Penning}} = (25.1 \pm 19.6)\,\mu\mathrm{cps/s}$) with the intermittent operation of the Penning wiper. The last 39 scans of KNM4 were performed with a grounded prespectrometer, eliminating the Penning trap, and reducing the slope to $\mathrm{Bg}_{\mathrm{Penning}} = 0.0\,\mu\mathrm{cps/s}$. When combining the five segments of KNM4 in the analysis, an effective background time slope of $(10.1 \pm 1.9)\,\mu\mathrm{cps/s}$ is applied.[10]

Since the end of KNM4, scans are only performed in the setting where the prespectrometer is grounded and hence $\mathrm{Bg}_{\mathrm{Penning}} = 0.0\,\mu\mathrm{cps/s}$.

Column density: The central values and uncertainties on the column density during the campaigns are estimated from a combination of direct measurements and relative indirect estimations on shorter time scales based on other slow control parameters. This concept is the same for all campaigns.

The weekly direct measurements of the column density are performed with the e-gun. These measurements are performed in all campaigns, hence the analysis method and procedure are the same. The measurement results define the baseline absolute column density. To measure the column density with the e-gun, 18.78 keV electrons are emitted from the rear section, traversing through the entire source length and KATRIN setup. The rates are measured at four different surplus energies (5 eV, 50 eV, 100 eV, and 200 eV). The absolute column density is obtained by fitting the e-gun specific response function to the measured rates. The analysis of the column density scans with the e-gun includes various corrections which are propagated into the final uncertainty. Systematic effects are for example the

[9] Note: For comparability between campaigns, all values given in this section are scaled to 148 pixels.

[10] In addition to the effective background time slope, also effective scan step lengths are used when modelling the Penning trap induced background. The effective scan step length ensures that the time-dependent background component is only applied to the measurement time of the first four campaign segments of KNM4.

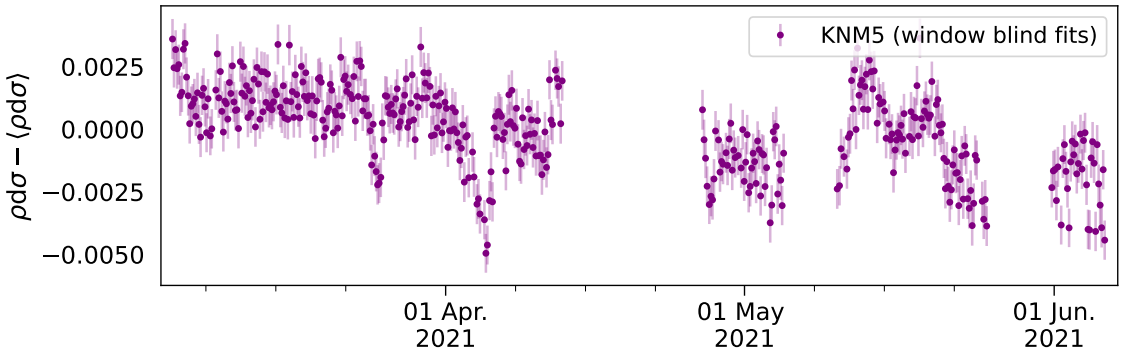

Figure 6.4.: Scan-wise column density fits of "window blind" data. In the fits, endpoint, background and the column density are free parameters. The signal is fixed to 1.0 as it is strongly correlated with the column density, and the two parameters would otherwise not be degenerate. Furthermore, in the fits, the increasing rear wall signal over time is taken into account. The fits shown here are based on KNM5. Scan-wise column density results provided by R. Salomon.

e-gun background electron model[11], as well as uncertainties on the angular distribution and emission angle of emitted electrons[12]. [65, 64]

On smaller time scales, the column density is derived from slow control parameters of various sensors or "window blind" fits. Since the circulation mode was modified between campaigns, different sensor readings or parameters provide the best accessibility for particular campaigns. For KNM3b, continuous information on the tritium flow through the WGTS is given by the tritium throughput. For KNM2 and KNM3a, continuous pressure measurements of the krypton capillary, which is directly correlated to the column density, provide the best sensitivity on relative column density changes. For KNM1, KNM4 and KNM5, relative changes are extracted from "window blind" fits of each scan. Hereby the same scans are used as for the determination of the source potential shift and drifts (previous paragraph). In the fits, the endpoint, background, and column density are kept as free parameters, whereas the signal is fixed to 1.0, as it is strongly correlated to $\rho d\sigma$. In addition, the increasing signal over time due to the rear wall spectrum is accounted for in each scan. An example of the relative changes of the column density is shown in figure 6.4. [65, 64]

For KNM2, KNM3a, and KNM3b, the column density for each scan is calculated linearly, scaling the slow control parameter by the column density of the column density measurements with the e-gun. For KNM, KNM4 and KNM5, an offset between the "window blind" results and the e-gun measurement results is fit. To obtain the mean column density for each campaign, a time-weighted average is calculated from the scan-wise column densities.

Furthermore, correlations between the column density values are propagated into the neutrino-mass analysis. These correlations result from the systematic effects previously

[11] The additional background component is manifested in a non-Poisson distribution. This component is assumed to originate from tritium ions hitting the e-gun back plate, producing electrons that are accelerated with the e-gun acceleration voltage. These background electrons furthermore have a larger angular distribution.

[12] The emission angle of electrons from the e-gun for each campaign is between 6° to 10° with an uncertainty of $\sim 1°$.

listed. KNM1 is weakly correlated with 20 % to 31 % to all other campaigns, whereas KNM2-5 are correlated with values between 50 % to 73 %. [64]

High voltage-dependent background slope: The possible existence of a background slope has been investigated in five dedicated measurements in the SAP setting and two measurements in the NAP setting. The latest estimation of the background slope in the SAP setting is based on a combined analysis of datasets collected in 2020 and additional datasets that were taken throughout 2022. The background slope estimation in the NAP configuration is based on a dataset recorded in October 2022. The measurements were performed with valve 4, between the CPS and pre-spectrometer, closed in both the NAP and SAP settings. The background rate is measured between $-18.6\,\mathrm{kV}$ to $-17.6\,\mathrm{kV}$ in steps of 100 V.

The individual scan steps of all scans are stacked, fitting the slope over the high voltage. In the analysis, the same ROI and detection efficiency corrections are applied to the recorded rates as in the neutrino-mass analysis. The fit background slope in the NAP setting scaled to 148 pixels is $(1.1 \pm 3.8)\,\mu\mathrm{cps/eV}$. The background slope is applied as a common uniform parameter to all NAP campaigns. For the SAP setting, a high voltage-dependent background slope of $(1.3 \pm 0.8)\,\mu\mathrm{cps/eV}$ is measured. Also, one common uniform parameter is applied in the analysis to all SAP campaigns. Both background slope inputs are consistent with zero. [104, 105]

Analysing plane magnetic field and transmission broadening: Both magnetic field settings, the NAP setting and the SAP setting, are described in section 5.2.1. The additional effect of the transmission broadening on the β-spectrum is described in section 6.1.2. The mean magnetic field values and mean transmission broadenings are summarised in table 6.2.

In the 6 G NAP setting (KNM1, KNM2, KNM3b), the magnetic field in the analysing plane is determined from `Kassiopeia` simulations. An example of pixel-wise simulated B_{ana} of KNM2 is illustrated in figure 5.2 (centre left). The analysing plane magnetic field in the NAP setting is applied as a uniform parameter. A source of inaccuracies of the simulated values is based on potential small misalignments or tilts of the superconducting magnets, as well as a bias due to remanent and induced magnetic fields, thus the effect is estimated to be small [57]. Systematic uncertainties on the simulated values are estimated from comparisons with the six stationary low-field magnetometers surrounding the spectrometer vessel close to the analysing plane. A comparison of measured and simulated values gives a conservative estimate of the absolute field strength uncertainty of 1 % for KNM1, KNM2, and KNM3b. In addition to the magnetic fields, the potential depression ΔU_{ana} is simulated with `Kassiopeia`. Differences in the potential depression between the inner and outer detector pixels (see figure 5.2 (lower left)) cause an overall broadening of the measured spectrum. For each campaign, a uniform transmission broadening σ^2_{ana} is applied. As this correction is only a small effect on the order of $1 \times 10^{-3}\,\mathrm{eV}^2$, no additional systematic uncertainty is applied to these three broadening parameters. [56, 57]

Dedicated measurements are performed to estimate the analysing plane characteristics in the SAP setting [65]. With $^{83\mathrm{m}}$Kr measurements, the magnetic field B_{ana} as well as the transmission broadening can be directly extracted from the krypton lines. An example of the magnetic field and the transmission broadening of KNM5 is illustrated in figure 6.5 (top right) and figure 6.5 (lower left). Within the neutrino-mass analysis, for each patch individual B_{ana} and σ^2_{ana} values are applied.

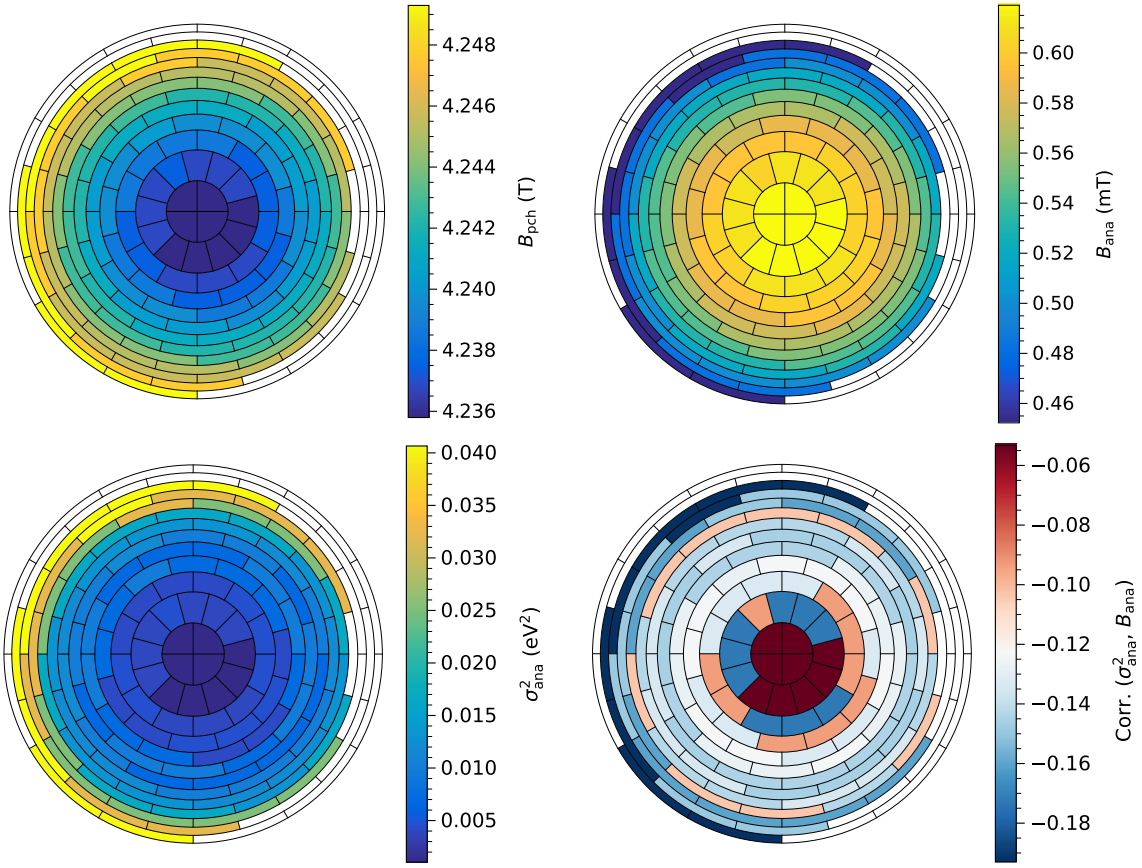

Figure 6.5.: Pinch magnetic field (top left), analysing plane magnetic field (top right), and the transmission broadening (bottom left) are applied to the integrated spectrum to account for magnetic field differences within a patch. (Bottom right) Correlation of the transmission broadening with the magnetic field in the analysing plane. The correlation for most patches is negative. The values shown here are for KNM5.

Between KNM4 and KNM5 upgrades of the low-field correction system (LFCS) resulted in an offset of the magnetic field and potential depression. Therefore B_{ana} of KNM3a and KNM4 is a common input, separate from KNM5. For KNM3a and KNM4, input values are based on K-32 line measurements and treated as fully correlated. For KNM5 inputs are derived based on measurements of the $N_{2,3}$-32 line doublet and are therefore uncorrelated to other campaigns. [57]

As depicted in figure 6.5 (lower right), the transmission broadening and the analysing plane magnetic field of each patch are anti-correlated. [65]

In general, a positive transmission broadening is observed. However, due to statistical fluctuations, two patches have negative broadenings in the KNM3a and KNM4 description[13]. The negative broadening is implemented in the integrated spectrum following the description [60]

$$N\left(\sigma^2 < 0\right) = N_0 - \left(N\left(\left|\sigma^2\right|\right) - N_0\right) = 2N_0 - N\left(\left|\sigma^2\right|\right), \quad \text{with } N_0 = N\left(\sigma^2 = 0\right). \tag{6.14}$$

[13] The broadening remains negative when combined with the Doppler broadening, which is always applied in the spectrum calculation. Only one patch overall has a negative broadening value.

The negative broadening extension is implemented in both the calculation of the krypton rate used for the field estimations [171] as well as the calculation of the integrated tritium spectrum.

Source magnetic field: The measurement principle of the source magnetic field was developed by F. Block and F. Glück and is described in more detail in [65]. The measurement is performed with electrons using the transmission characteristics and, in particular, utilises the magnetic mirror effect (equation (3.20)). The rear wall itself serves as an isotropic electron source in this measurement, as the adsorbed tritium delivers an activity of around 90 MBq.[14] The absolute electron rate measured by the FPD is reduced by applying high voltage to the main spectrometer. The relation between the pinch magnetic B_{pch} field and the source magnetic field B_{src} is proportional to the acceptance angle and therefore the number of measured electrons. For measuring the magnetic field inside the WGTS, the source magnet setting is adapted to have the largest magnetic field inside the M2 and M3 magnet, with 2.5 T. The pinch magnet at the beginning of the measurement is set to 2.3 T. By sweeping B_{pch} up to 2.7 T, two regions are observed. When $B_{\mathrm{src}} > B_{\mathrm{pch}}$, all electrons are transmitted, and a constant electron rate is expected. Once $B_{\mathrm{src}} < B_{\mathrm{pch}}$, electrons above the acceptance angle θ_{max} are magnetically reflected, and a reduction in the electron rate is observed with increasing B_{pch}. Since the rear wall is mapped to the FPD, a pixel-wise determination of B_{src} is accomplished. [57, 65]

In addition to statistical uncertainties, the uncertainty on the measured source magnetic field is due to the relative measurement with the pinch magnetic field and the accurate knowledge of B_{pch}. As described in paragraph *pinch magnetic field*, the systematic uncertainty on B_{pch} is 0.1 %.

The neutrino-mass analysis implements the source magnetic field as a longitudinally averaged value. The longitudinal magnetic field strength is determined from simulations. The longitudinal averaging is weighted by the longitudinal gas density profile [65, 154], giving regions closer to the injection capillaries a more significant weight. Based on Monte Carlo studies, the bias due to the longitudinal averaging is $3 \times 10^{-4}\,\mathrm{eV}^2$. [65]

Due to good azimuthal homogeneity inside the WGTS, the source magnetic field is applied as a uniform parameter in the neutrino-mass analysis with a central value of 2.5065 T [57]. Furthermore, B_{src} is applied as a single common parameter to all campaigns. The overall combined uncertainty on the absolute source magnetic field is estimated to be 0.006 T [57], which is taken as the systematic input for the neutrino-mass analysis.

Energy loss function: The parametrisation and characteristics of the energy loss function are summarised in section 3.4.2, with a summary of all parameter values, uncertainties, and correlations in tables 3.1 and E.6. The energy loss function was experimentally determined during the commissioning campaign [28, 206, 210, 217]. Measurements of the semi-empirical energy loss function were hereby performed with the monoenergetic angular selective electron-gun (e-gun), producing electrons with an energy of 18.6 keV. The measurement consists of seven datasets. Three of these were performed as integral measurements and four as differential (time-of-flight) measurements [28, 217].

[14] Due to the decay, the rear wall activity decreases over time. However, the rate decrease is relatively small with around 20 ppm/h and is thus negligible. [65]

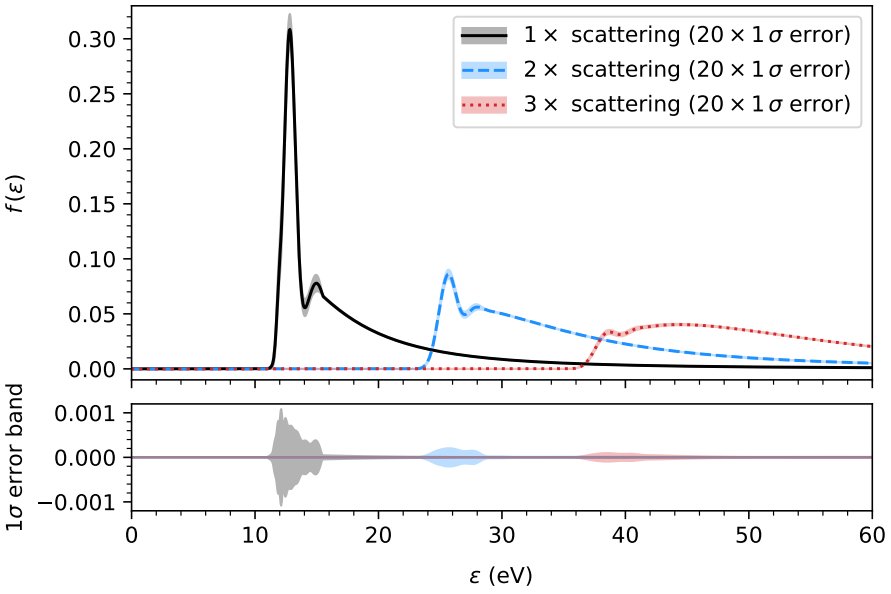

Figure 6.6.: (**Top**) Energy loss probability $f(\varepsilon)$ as it is applied in the neutrino-mass analysis with the corresponding uncertainty band. For visibility in the top plot, uncertainties have been increased by a factor of ten. (**Bottom**) energy loss function uncertainties over energy. The energy loss function has a maximum uncertainty of $\sim 1 \times 10^{-3}$. Both plots include energy loss of up to three scatterings.

For the integral measurement, the integral response function is measured at three different column densities (14 %, 41 %, and 86 %). In each column density setting, the retarding potential is kept at a constant value. At the same time, the electron energy emitted by the e-gun is changed.[15] The electrons are then recorded with the FPD. Scanning over an energy range of about 60 eV results in the integrated response function, including the superposition of n-fold scattering. To get a baseline measurement of the transmission function, which also contributes to the response characteristics, an additional measurement was performed at 0 % column density. [28, 217]

In the time of flight (TOF) mode, the laser pulse, generating the photoelectrons of the e-gun is used as a trigger applied to the measured data.[16] For each detected electron, the time difference from emission (set by the trigger) to arrival at the FPD is calculated. Electrons with larger surplus energies E_s take less time to traverse through the main spectrometer potential, therefore the flight time is directly connected to the electron energy by $\tau \sim 1/\sqrt{E_s}$ [28]. Electron events with flight times between 35 µs to 50 µs are selected for the analysis.[17] The time cut acts as a band pass filter, enabling one to measure of the differential energy spectrum. The electron events within the time band are then histogrammed over energy. The resulting differential spectrum is the superposition of the energy loss functions up to n-fold scattering. The differential TOF was performed at four column density settings: 15 %, 22 %, 39 %, and 84 % of nominal column density. [28]

[15] For the integral measurement, the laser is pulsed with a frequency of 100 kHz [28].
[16] For the TOF measurement, the laser is pulsed with a frequency of 20 kHz [28].
[17] The upper limit of τ is based on the laser frequency of 20 kHz, which only allows one to distinguish electrons in a time interval of 50 µs [28].

The analysis is performed as a combined fit of the three integral and the four differential measurements [28, 217]. The fit includes the nine parameters in the energy loss function and several nuisance parameters, such as normalisation factors and scattering probabilities. The main systematic uncertainties in the analysis are the uncertainties on the transmission function model, the pile-up correction, and the applied analysis cuts such as multiplicity cuts. In addition, minor systematic effects are connected to additional background electrons[18], the column density estimation, drifts of the rate of generated e-gun electrons, and binning effects of the continuously ramped data. In general, however, the analysis is dominated by statistical uncertainties, and no significant systematic shift was found. The uncertainties on the nine energy loss parameters are summarised by table 3.1. [28]

The propagated, correlated uncertainties on the energy loss function are illustrated with figure 6.6. In the figure, the energy loss probability is shown up to three-fold scatterings and the error bands are resulting from the parameter uncertainties. For visibility, the uncertainties have been increased by a factor 20 in the top panel.

In the context of the systematic budget for the projected final KATRIN analysis, the uncertainties on the energy loss function already meet the requirements given in [39]. [28]

Pinch magnetic field: The pinch magnetic field is generally extracted from simulations with `Kassiopeia` (see section 4.5). Within the simulation, the surface of each individual pixel of the FPD is backtracked into the pinch magnet with a fine spatial resolution. The simulation uses the `KEMField` zonal harmonic field solver to estimate the magnetic field [65]. The patch-wise values from the simulation for KNM4 and KNM5 are illustrated in figure 6.5 (top left). Due to the proximity to the windings of the superconducting magnet, the magnetic field strength on the outside is stronger by approximately 0.01 T compared to the inner part of the flux tube. The mean magnetic field throughout all campaigns is around 4.24 T.

Uncertainties on the pinch magnetic field apply to both the absolute value and the relative patch/pixel-wise values. The uncertainty on the absolute value is estimated based on measurements performed in 2015 during the commissioning of the pinch magnet [225]. Hereby measurements within the warm bore of the pinch magnet were performed with an Nuclear Magnetic Resonance (NMR) probe. Direct measurement is only possible in an open system. This standalone measurement during the commissioning was performed while operating the pinch magnet at 6 T.[19] The measurments showed an agreement on the order of 0.06 % to `Kassiopeia` simulations [65, 225].

The flux tube is misaligned from the centre axis. As can be seen in figure 6.5, the flux tube centre inside the pinch magnet is slightly misaligned towards the lower right detector quadrant. The second uncertainty component, the relative pixel-wise values, results from inaccuracies in the simulation itself. In particular, the projection of the FPD into the pinch magnet does not fully represent the misalignment of beamline components. Offsets and small rotations of the superconducting magnets result in minor shifts and distortions of the magnetic flux tube. The misalignments are estimated to be in the millimetre range.

Applying error propagation to both uncertainty components leads to a combined uncertainty of 0.1 % [57]. Furthermore, the values are highly correlated as the inputs of each campaign

[18] This additional e-gun background can, for example, be induced by ions impacting on the photocathode.
[19] During neutrino-mass measurements, the superconducting magnets along the beamline are only operated at a maximum of 70 % of the nominal magnetic field strength to reduce the risk of quenching in the transport section [43].

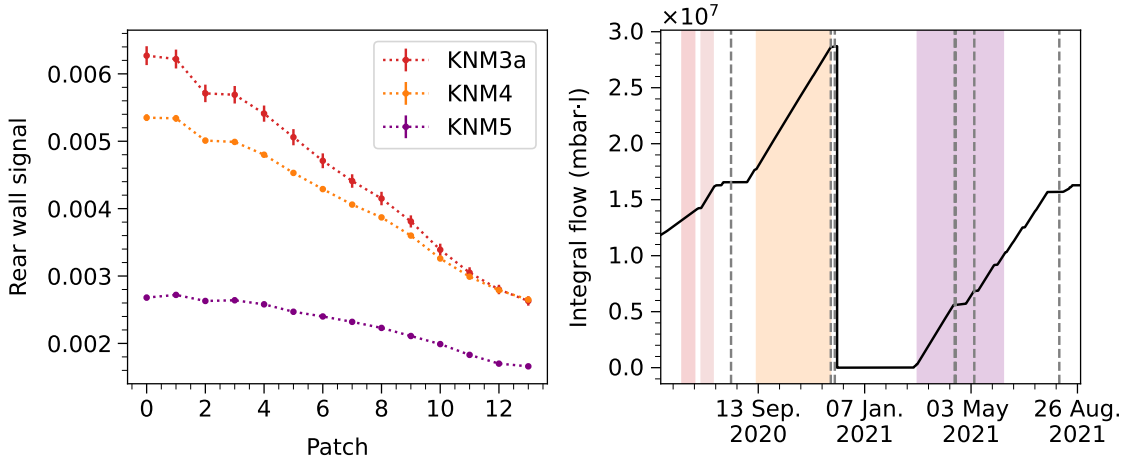

Figure 6.7.: (**Left**) Patch-wise rear wall inputs for all SAP campaigns. Due to larger accumulation in the centre, the rear wall signal is larger for central patches. The rear wall signals are scaled to the column density present in the corresponding campaign. Since KNM3a has a lower column density, the signal value is larger compared to KNM4. The absolute number of rear wall electrons in KNM3a thus is lower than in KNM4. (**Right**) Integral flow through the WGTS. The vertical dashed lines symbolise the individual measurements of the rear wall spectrum (RW1-8). The campaigns themselves are shaded in their respective colours. Between KNM4 and KNM5 (in the beginning of December 2020), the rear wall was cleaned, resulting in a reset of the integral flow seen by the rear wall. The integral throughput is further masked to only increase when the rear wall is directly exposed to tritium, rejecting periods where valve 0 sealed off the rear wall.

result from the same simulation setup. The pinch magnetic field of KNM3, KNM4, and KNM5, for example, is fully correlated. KNM1 and KNM2 each exhibit a 98 % to 99 % correlation to KNM345, and are correlated at 95 % to each other. Exchange of the detector wafer between KNM2 and KNM3 results in a different alignment of the detector, which explains the differences in the correlations.

Rear wall spectrum: Between measurement campaigns, dedicated scans of the spectrum originating from residual tritium on the rear wall are performed. The spectra are measured with an evacuated source. Between the end of KNM3 and the end of KNM5, eight datasets with a total of 175 scans were measured to characterise the rear wall spectrum. The dates of the rear wall scans are marked by the dashed vertical lines in figure 6.7. The spectra are mostly measured with a flat measurement time distribution, with retarding potential settings similar to the neutrino-mass measurements. Since rates are much lower, the rear wall spectra are analysed down to 125 eV below the endpoint to obtain better sensitivity on the fit parameters. [29]

The first dataset (RW1) was measured in the NAP settings to obtain the input values for KNM3b. All other datasets were measured in the SAP configuration. In general, the rear wall should have no bias voltage applied when rear wall scans are performed. In some instances, the bias voltage was however set to a non-zero value. In this case, the bias

voltage is accounted for in the effective rear wall endpoint:

$$E_{0,\mathrm{rw}} = E_{0,\mathrm{dataset}} - U_{\mathrm{bias,rw}}. \tag{6.15}$$

This correction has to be applied to the RW2 (+90 mV), RW4 (+300 mV), and RW6 (+300 mV) datasets.

Compared to β-electron from the WGTS, electrons from the rear wall start in a magnetic field of 1.23 T. Since the source is evacuated, the electrons do not experience scattering within the source beam tube. Rear wall spectra are fit with a reference column density $\rho \mathrm{d}\sigma_{\mathrm{ref}}$ of $3.75 \times 10^{21}\,\mathrm{m}^{-2}$ and a tritium purity of 1.00. The resulting fit signal is then rescaled to the correct column density for the neutrino mass fits for each measurement campaign.

To allow for additional uncertainty of the FSD shape, an additional parameter $w_{\mathrm{GS,rw}}$ is introduced in the fit. The rear wall FSD is based on the T_2 FSD and can be expressed as two parts:

$$\mathrm{FSD}_{\mathrm{rw}} = \begin{cases} (1 + w_{\mathrm{GS,rw}}) \cdot \mathrm{FSD}_{\mathrm{T^2}}, & E < 10\,\mathrm{eV} \\ (1 - w_{\mathrm{GS,rw}}) \cdot \mathrm{FSD}_{\mathrm{T^2}}, & E \geq 10\,\mathrm{eV}. \end{cases} \tag{6.16}$$

This parameter reweights the ground states relative to the excited states. For positive values of $w_{\mathrm{GS,rw}}$, the ground state gains in significance, reducing the mean FSD energy. For negative values of $w_{\mathrm{GS,rw}}$, the ground state probability is reduced relative to the excited states, hence increasing the mean FSD energy. The fit ground state weight is strongly anti-correlated to the rear wall endpoint with a correlation coefficient of around −96 %.

To obtain the rear wall endpoint, rear wall signal, and the ground state weighting inputs for KNM3 and KNM4, datasets RW1, RW2, and RW3 are analysed together with a common endpoint and a common ground state weighting. For KNM5, a combined fit is performed on datasets RW4-8. The corresponding input values for the endpoint and ground state weights are listed in table 6.2. The effective rear wall endpoint values are again shifted by the rear-wall bias voltage present during the respective campaign[20]. The rear wall endpoint and ground state weight inputs are listed in table 6.2.

The inputs for the rear wall signal are summarised in table 6.2. Furthermore, patch-wise inputs for KNM3a, KNM4 and KNM5 are illustrated in figure figure 6.7 (left). Since tritium on the rear wall accumulates more in the centre compared to the outside, the rear wall signal is assumed to be patch-wise for all SAP campaigns. The fit rear wall signals, on the other hand, measured only intermittently, correspond to the different accumulation of tritium on the rear wall. This accumulation is directly connected to the tritium throughput in the WGTS over time figure 6.7 (right). To obtain the appropriate representation of the rear wall signal during the measurement campaigns (shaded in colour), the rear wall signal is scaled to the effective throughput in the middle of a measurement campaign

$$\mathrm{Sig}_{\mathrm{rw,scaled}} = f \cdot \mathrm{Sig}_{\mathrm{rw,fit}}. \tag{6.17}$$

Over a longer duration, a linear increase of the rear wall signal is observed with the integral flow $\mathcal{T}$:

$$\text{KNM3-4:} \quad f(\mathcal{T}) = m \cdot \mathcal{T} + c. \tag{6.18}$$

[20] The weighted rear-wall bias voltages during the measurement campaigns are 0.175 V for KNM3a, 0.177 V for KNM3b, 0.090 V for KNM4, and 0.187 V for KNM5.

The linear growth model is estimated for each patch from rate measurements at a retarding potential of 14 kV. The mean signal increase is $m = 0.28\,(\mathrm{mbar}\cdot\mathrm{l})^{-1}$. As the input for KNM3a and KNM4 are based on the fit signal of RW2 together with RW3, both inputs are fully correlated.

After the rear wall cleaning, tritium accumulation on the rear wall surface is larger. This is taken into account by scaling the rear wall signal with a limited growth model:

$$\text{KNM5:} \quad f(\mathcal{T}) = a \cdot \exp(k \cdot (\mathcal{T} - \mathcal{T}_0)) + c. \tag{6.19}$$

Separate growth models are applied for each patch since more tritium is accumulated in the centre of the rear wall compared to the outer parts. The mean limited growth model is characterised with the scaling $a = -9.83 \times 10^{7}$ and the growth factor $k = -7.94 \times 10^{-7}\,(\mathrm{mbar}\cdot\mathrm{l})^{-1}$. Uncertainties on both growth models and the scaling are propagated via Monte Carlo sampling. In the last step, the scaled rear wall signal from the fit $\mathrm{Sig}_{\mathrm{rw,scaled}}$ further is scaled to the column density $\rho\mathrm{d}\sigma_{\mathrm{KNM}i}$ present throughout a measurement campaign, as the fits were performed at reference column density $\rho\mathrm{d}_{\mathrm{ref}}$:

$$\mathrm{Sig}_{\mathrm{rw}} = \mathrm{Sig}_{\mathrm{rw,scaled}} \cdot \frac{\rho\mathrm{d}_{\mathrm{ref}}}{\rho\mathrm{d}_{\mathrm{KNM}i}}. \tag{6.20}$$

The final scaled rear wall signal inputs are listed in table 6.2. and patch-wise inputs are illustrated in figure figure 6.7 (left). Since the input for KNM3a and KNM4 is extracted from the same fit result, the systematic input is treated as fully correlated.

The rear wall spectrum is neglected for KNM1 and KNM2. No dedicated rear wall measurements were performed pre-KNM3. Therefore no reliable estimation of the rear wall signal is possible. Since the integral flow seen by the rear wall during KNM1 and KNM2 was small, tritium accumulation was also small. The influence on m_ν^2 when neglecting the rear wall signal for KNM1 and KNM2 was estimated to be on the order of $10^{-4}\,\mathrm{eV}^2$.

Non-Poisson background: Not all ^{219}Rn from the getter pumps is retained by the baffle system. As discussed in section 3.8, radon can then migrate into the main spectrometer vessel. From this decay, primary high-energy electrons are created, which have a higher probability of being trapped [133]. The primary electrons can further ionise residual gas, leading to additional coinciding background electron chains. These electrons are manifested as an additional non-Poissonian background contribution, overall broadening the time distribution of expected background electrons. The presence of a non-Poisson background was only measured for the NAP campaign, and it was not observed anymore in the SAP campaigns, to date.

In figure 6.8, the overdispersion of the background is illustrated for the example in KNM1. The plot includes the measured number of electrons for the five background scan steps. Analysing the data with a Poisson distribution and a Gauss distribution, a 6.4 % overdispersion of the normal distribution was observed relative to the expected width of the Poisson distribution. For KNM2, a non-Poisson contribution of 11.2 % was found, and for KNM3b an increase of 10.7 % was observed.

The overdispersion of the background is accounted for in the fit by an increase of the background variance. The uncertainty σ_i enters the χ^2 and is given as the square root of

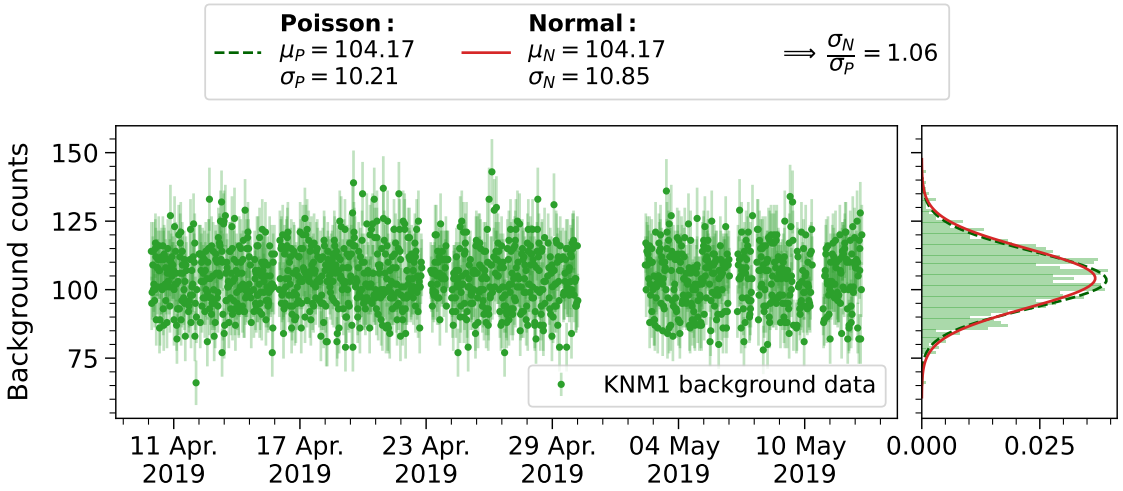

Figure 6.8.: Non-Poisson over dispersion of the background as measured during KNM1. The counts are summed over all golden pixels for each of the five background scan steps. The width of the Poisson distribution and the standard deviation are compared. The KNM1 data shows an overdispersion of 6 %.

the theoretical number of expected electrons,

$$\sigma_i = \sqrt{N_{\text{total},i}} = \sqrt{N_{\text{Sig},i} + N_{\text{Bg},i}}. \tag{6.21}$$

When including the expected overdispersion, the background fraction $N_{\text{Bg},i}$ of the variance is scaled with the non-Poisson background fraction $\text{Bg}_{\text{non-Poi}}$. The increased variance then becomes

$$\sigma_i^2 = N_{\text{total},i} - N_{\text{Bg},i} + \text{Bg}^2_{\text{non-Poi}} \cdot N_{\text{Bg},i} \text{ [155]}. \tag{6.22}$$

6.3.3.2. Impact of systematic uncertainties

Including systematics in the analysis is crucial for determining the neutrino mass. Systematic effects can influence different parts of the model (for example the scattering probability, transmission, or integrated spectrum), and therefore the impact of each is investigated individually. To get a complete picture, figures 6.9 and 6.10 summarise the impact of each systematic on both the individual campaigns and the combined analysis. Here, the systematic impact was estimated based on the measured data. As previously introduced with equation (4.19), the isolated systematic impact is given by

$$\sigma_{\text{syst}} = \sqrt{\sigma^2_{\text{stat \& syst}} - \sigma^2_{\text{stat}}}. \tag{6.23}$$

The systematic effects in both figures are separated into the ten previously introduced categories, as well as the statistical sensitivity and the total sensitivity, including all systematics simultaneously. The plot is further divided into three panels. Effects that influence the model itself (top), effects that influence the uncertainties of data points (middle), and the combination with σ_{total} (bottom). Note that the panels showing 1σ statistical sensitivity and 1σ total sensitivity share the same x-axis and can therefore be directly compared. However, the systematic error contribution is displayed in a smaller

x-range to have a more detailed comparison between systematics. The figure is further split into two columns. The left column, showing the impact on the sensitivity, is based on the mean uncertainty

$$\langle\sigma\rangle = \frac{|\sigma_{\text{upper}}| + |\sigma_{\text{ lower}}|}{2}. \tag{6.24}$$

As the parameter space is slightly asymmetric, a difference in the upper error, σ_{upper}, and lower error, σ_{lower}, is expected.[21] A listing of the detailed values is given in addition to the bars for each systematic. If a systematic does not apply to a given campaign (for example, due to successive improvements in the experimental conditions), the affected systematic is labelled with *n.a.* Subplots in the right column all share the same x-scale and illustrate the relative change in central value when introducing a systematic parameter as a constrained nuisance parameter. The values in this column are hence given relative to $m^2_{\nu,\text{stat}}$. The systematic impacts in both figures are further sorted according to the impact size in the KNM1-5 combined analysis (top to bottom). Additional studies investigating the impact of the individual systematics on the endpoint and signal amplitude are presented in appendix F.

Looking closer at figure 6.9, each colour represents the results of one campaign. The statistical sensitivity σ_{stat} of KNM4 and KNM5 is predominant to other data sets, with $0.169\,\text{eV}^2$ and $0.180\,\text{eV}^2$, respectively. In contrast, due to its comparatively small statistics, KNM1 has a substantially worse sensitivity of $0.980\,\text{eV}^2$. The statistical sensitivity of the individual also indicates the significance of the respective campaign in the combined analysis. Furthermore, it represents the weighing of the systematic error contributions of each campaign in the combined KNM1-5 analysis, giving KNM4 and KNM5 the most substantial weighting, in contrast to the statistical significance of KNM1, KNM2, KNM3a, and KNM3b.

The source potential broadening due to plasma and the energy loss shift is present in the analysis of all six data sets. As it is present in all campaigns, it is the most significant systematic overall. The systematic uncertainties lead to an error contribution on the order of $1 \times 10^{-2}\,\text{eV}^2$ to $3 \times 10^{-2}\,\text{eV}^2$, with a slightly larger contribution for KNM3b and KNM5. The central value is mostly unaffected by the introduction of plasma systematics.

On a similar level is the Penning trap induced time-dependent background. As discussed previously, this background contribution was eliminated during KNM4. The most significant Penning-trap error contribution is in KNM1 and KNM3a with $-1.315\,\text{eV}^2$ and $-0.097\,\text{eV}^2$, respectively. Sizable shifts in the central values are also observed. This shift is positive in KNM2 to KNM4 and negative for KNM1. Due to the fact that one of the datasets with the largest statistics (KNM5) is not impacted by the systematic effect, the error contribution in the combined fit is only the second largest.

The third largest contribution is the column density with a systematic impact between $0.022\,\text{eV}^2$ and $0.030\,\text{eV}^2$. For the column density, a moderate shift of the fit m^2_ν is observed. The shift is of negative sign with the most pronounced value of $-0.007\,\text{eV}^2$ in KNM4.

Accounting for a high voltage-dependent background slope, mostly NAP campaigns are affected due to the comparatively large uncertainty of $5.848\,\mu\text{cps/eV}$. Furthermore, the fit m^2_ν of KNM2 is shifted towards smaller values. This is explained by the preference for statistical fluctuations in the data and the highest background point acting as leverage, leading to a preferably larger central value of the background slope. The background slope is more precisely determined for SAP campaigns, resulting in a reduced error contribution.

[21] The asymmetric errors are obtained from profiling the parameter space, using the `MINOS` routine.

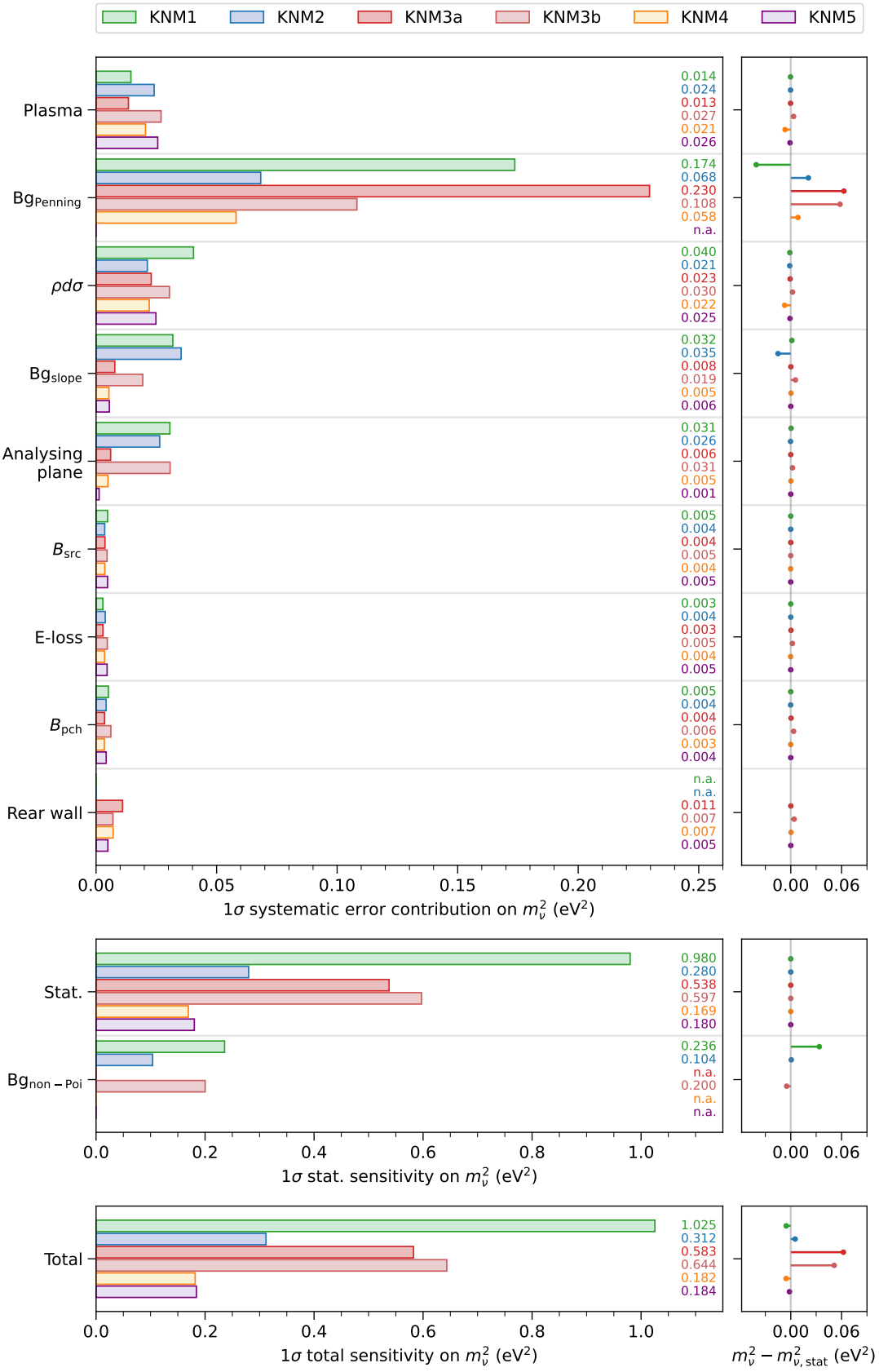

Figure 6.9.: Systematic breakdown of each campaign individually. The plot is separated into systematic error contribution (top), statistical uncertainty (middle), and the total uncertainty, including all systematics (bottom). The right panels show the central m_ν^2 relative to the statistics-only fit. More details are given in the text.

The systematic error contribution of the analysing plane magnetic field in combination with the transmission broadening is much smaller for SAP campaigns compared to the NAP campaigns. This is due to the strong anticorrelation between B_{ana} and σ^2_{ana} in SAP campaigns. The introduced σ^2_{ana} can directly compensate for increases in B_{ana}. Increasing the magnetic field strength widens the transmission edge, which reduces the transmission broadening due to the anticorrelation, leaving the neutrino mass square unaffected.

Systematic contributions with only a small impact are the magnetic field in the source system, B_{src}, uncertainties on the energy loss function, and magnetic field in the pinch magnet, B_{pch}. All three systematics have error contributions on the order of $\leq 0.005\,\mathrm{eV}^2$. Furthermore, only minimal differences in the m^2_ν central value are observed. It should be mentioned that minor fluctuations of small error contributions can occur. This effect is connected to the asymmetric nature of the χ^2 for positive and negative m^2_ν values. If the central value shifts, the mean uncertainty $\sigma_{\mathrm{stat\ \&\ syst}}$ can change. Subtraction of σ_{stat} consequently can thus lead to a slightly different value of σ_{syst}.

The additional spectrum from the rear wall is only accounted for in KNM3-5. The uncertainty is connected to the uncertainties on the rear wall signal amplitude, the effective endpoint of the rear wall, and the additional uncertainty on the FSD shape. Here, the systematic error contribution is between $0.005\,\mathrm{eV}^2$ and $0.011\,\mathrm{eV}^2$ for the different campaigns. The effect on the central values is only minimal. This systematic effect has the smallest impact.

Introducing a non-Poisson background component is considered a change of statistical sensitivity, as only the background uncertainty increases in the constructed χ^2. The non-Poisson background component is only applied to NAP campaigns. Due to proportionally smaller increases in the background variance in longer scan steps, the central value is expected to change when fitting data. This is due to the fact that scan steps are reweighted with $\mathrm{Bg}_{\mathrm{non\text{-}Poi}}$, giving statistical fluctuations a modified influence compared to the statistics-only fit. Here, the largest change in the m^2_ν central value is observed in KNM1 with $0.034\,\mathrm{eV}^2$. The increase in statistical uncertainty is on the order of $1 \times 10^{-2}\,\mathrm{eV}^2$ to $2 \times 10^{-2}\,\mathrm{eV}^2$.

Figure 6.10 is structured in the same way as figure 6.9. The systematic breakdown uses the same inputs as for the individual campaigns. In addition, correlations between campaigns are introduced, and some parameters are applied as common to more than one campaign. In general, the systematic breakdown of the combined analysis is approximately the contribution of the individual campaigns weighted by their respective statistics. By combining parameters for different campaigns into a common parameter, or with additional correlations, greater statistical power is achieved on the parameters.

The statistical sensitivity of the combined analysis is $0.105\,\mathrm{eV}^2$. As the systematic effect due to variations in the source potential is present in all campaigns, it is manifested as the largest systematic with a contribution of $0.025\,\mathrm{eV}^2$. In this case, the plasma parameters between KNM3b, KNM4, and KNM5 are common parameters. The second largest contribution to the systematic error is the time-dependent Penning background. This has an error contribution of $0.024\,\mathrm{eV}^2$. The central value of the fit is shifted by $0.005\,\mathrm{eV}^2$ towards larger masses. The third largest systematic is the column density with $0.023\,\mathrm{eV}^2$. Here, the central value shifts most compared to that statistics-only fit by $-0.008\,\mathrm{eV}^2$. Accounting for the high voltage-dependent background slope, the background slope is common for KNM1, KNM2, and KNM3b as well as for KNM3a, KNM4, and KNM5. This leads to a contribution of $0.008\,\mathrm{eV}^2$.

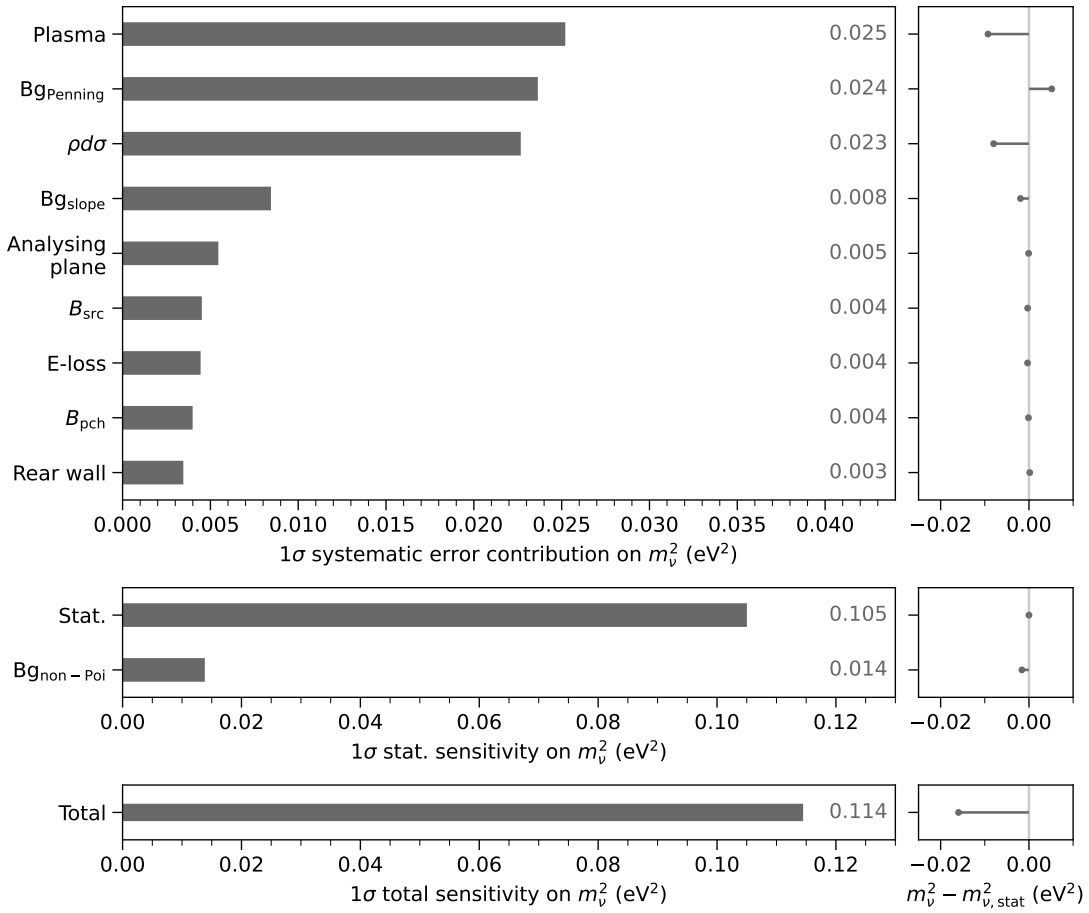

Figure 6.10.: Systematic breakdown of the combined KNM1-5 analysis. The plot is separated into systematic error contribution (top), statistical uncertainty (middle), and the total uncertainty including all systematics (bottom). The right panels show the central m_ν^2 relative to the statistics-only fit. Systematics are sorted by their impact on the squared neutrino mass. The corresponding systematic inputs are summarised in table 6.2.

Systematics of the analysing plane (magnetic field and transmission broadening) are shared between KNM3a and KNM4. The other parameters are set independently. The resulting error contribution is then $0.005\,\mathrm{eV}^2$. B_{pch} is considered to be common for KNM3, KNM4, and KNM5, which is in addition correlated to KNM1 and KNM2. The same energy loss function is applied to all campaigns, leading to common model parameters and a systematic contribution of $0.004\,\mathrm{eV}^2$. The systematic uncertainty on the source magnetic field is treated as a common parameter for all campaigns. The error contributions from the pinch magnet and source magnetic field are $0.004\,\mathrm{eV}^2$ and $-0.034\,\mathrm{eV}^2$, respectively. The rear wall spectrum overall has the smallest systematic error contribution of $0.003\,\mathrm{eV}^2$. This assumes a common rear wall endpoint of KNM3a and KNM3b and further includes correlations between the patch-wise rear wall signals of KNM3a and KNM4. The non-Poisson background contribution is only applied to NAP campaigns. Due to the comparatively smaller statistical power of the NAP campaigns, the statistical error contribution of the non-Poisson background contribution is only $0.014\,\mathrm{eV}^2$. Overall, the combined total sensitivity for KNM1-5 is $0.114\,\mathrm{eV}^2$. The central value, including all systematic effects, shifts by $-0.016\,\mathrm{eV}^2$ compared to the statistics-only result.

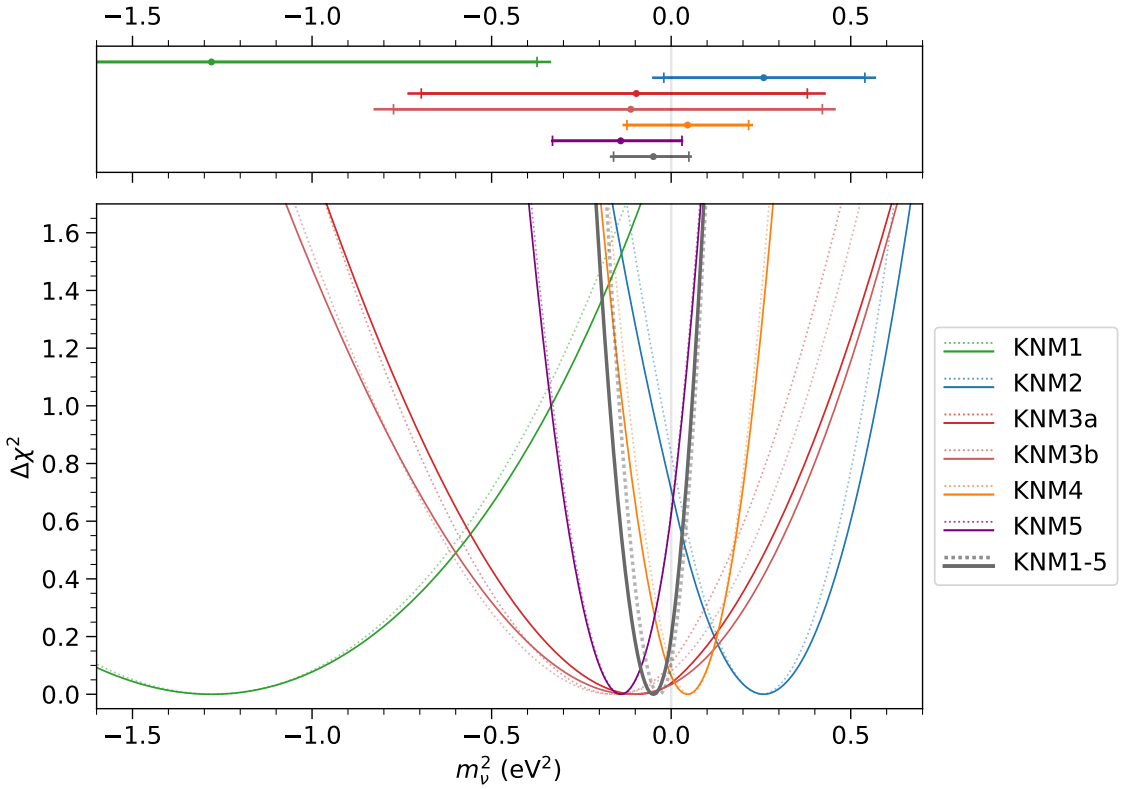

Figure 6.11.: (**Top**) Neutrino mass results of the individual campaigns as well as the combined analysis. The analysis includes all systematic uncertainties. The error bars are split by vertical lines into the statistical uncertainty and the systematic error contribution. The split error bars illustrate that the uncertainties are statistics dominated.
(**Bottom**) χ^2 profiles of the neutrino mass analyses. The profiles are shown for the analysis of each individual campaign and the combined analyis (grey). The plot includes both the statistics-only profiles (dotted) and including all systematic effects (solid). For comparison, values are shown relative to the minimum $\Delta\chi^2 = \chi^2 - \chi^2_{\text{min}}$.

Additional systematic effects that have been previously applied in the KNM1 and KNM2 analyses [25, 22], such as activity fluctuations, the high voltage stability and reproducibility, uncertainties on the detection efficiency, or uncertainties on theoretical corrections are negligible and therefore not included in the KNM1-5 analysis. Previous analyses further included uncertainties on the FSD. In the previous approach described in [25, 22], conservative uncertainties were considered for the FSD, which led to a systematic error contribution $\mathcal{O}(10^{-2}\,\text{eV}^2)$. However, recent methods rely on theoretical calculations as input and a reevaluation of the accuracy of the FSD shows that its systematic impact is $< 0.001\,\text{eV}^2$ [220, 224].

6.3.4. Analysis results

Following the discussion of systematic impacts on the neutrino mass analysis, the actual inference results will now be presented in this section.

Table 6.4.: Summary of squared neutrino masses obtained from the fits. The table compares the results with only statistical uncertainties and including all systematics. Furthermore, for each result, the asymmetric error estimation is listed.

Campaign	**Stat.: m_ν^2 (eV^2)**		**Total: m_ν^2 (eV^2)**	
KNM1	-1.275	$^{+0.907}_{-1.053}$	-1.280	$^{+0.946}_{-1.105}$
KNM2	$+0.252$	$^{+0.282}_{-0.278}$	$+0.258$	$^{+0.313}_{-0.311}$
KNM3a	-0.159	$^{+0.476}_{-0.599}$	-0.097	$^{+0.528}_{-0.637}$
KNM3b	-0.164	$^{+0.533}_{-0.661}$	-0.112	$^{+0.571}_{-0.717}$
KNM4	$+0.051$	$^{+0.170}_{-0.169}$	$+0.046$	$^{+0.183}_{-0.181}$
KNM5	-0.139	$^{+0.171}_{-0.190}$	-0.141	$^{+0.174}_{-0.194}$
KNM1-5	$\mathbf{-0.034}$	$\mathbf{^{+0.099}_{-0.111}}$	$\mathbf{-0.050}$	$\mathbf{^{+0.107}_{-0.121}}$

The neutrino mass results for each individual campaign, as well as the combined KNM1-5 analysis, are illustrated in figure 6.11, and listed in table 6.4, where the additional columns show the asymmetric errors obtained with `Minos`. The table is split into fits considering only statistical uncertainties, and fits with all systematic effects included. As discussed in the previous section, one can see the larger statistical power of KNM4 and KNM5. Furthermore, it can be observed that the uncertainties become more asymmetric with more negative central values. Here, the asymmetry of KNM1 is most prominent (as can be seen in table 6.4). On the other hand, with positive central values, as in KNM2 and KNM4, the upper and lower errors are more symmetric.

Looking at the central values of the squared neutrino mass, no particular preference for positive or negative central values is present. The most strongly negative result is obtained from the KNM1 dataset with $-1.280\,^{+0.946}_{-1.105}\,\mathrm{eV}^2$. Thus, this result, with larger uncertainties, is still consistent with zero within $1.4\,\sigma$. The largest positive squared neutrino mass value is extracted from KNM2 with a central value of $+0.258\,^{+0.313}_{-0.311}\,\mathrm{eV}^2$, which is consistent with a zero neutrino mass within $0.8\,\sigma$.

A combined fit of all campaigns together, accounting for all systematics, results in a central value of

$$m_\nu^2 = -0.050\,^{+0.107}_{-0.121}\,\mathrm{eV}^2. \tag{6.25}$$

The fit result of this analysis is consistent with zero within $0.5\,\sigma$. Comparing the statistics-only fits with the results with systematics, shifts of the central values in both positive and negative directions are present. As discussed in the previous section, the change in the central value results from the extra freedom of the model by the addition of pull terms.

Next to the neutrino mass, it is also interesting to look at the behaviour of the nuisance parameters of the fit. The number of free fit parameters is comparatively large (see table 6.1); therefore, if patch-wise parameters are fit, only the mean parameter values are compared. Table 6.5 compares the endpoint, signal, and background of the individual fits to the combined multi-fit. When fitting all datasets together, the individual parameters become correlated through the squared neutrino mass and shared/correlated systematic parameters. Additional information about the resulting parameter correlations is given in

Table 6.5.: Fit parameter summary for the individual analyses and combined analysis. The combined analysis shares one squared neutrino mass for all campaigns, whereas the individual analysis allows a free squared neutrino mass per campaign. In the case of KNM3a, KNM4, and KNM5, the mean of the 14 patch-wise parameters is given for both the central values and uncertainties. Note that the uncertainties are based on estimations from the Hesse matrix and might hence not be fully reliable. The table summarises fit results accounting for all systematics.

Camp.	Individual			Combined		
	$\langle E_0 \rangle - 18573$ (eV)	⟨Sig⟩	⟨Bg⟩ (cps)	$\langle E_0 \rangle - 18573$ (eV)	⟨Sig⟩	⟨Bg⟩ (mcps)
KNM1	0.800 ± 0.021	1.077 ± 0.003	370.5 ± 0.4	0.871 ± 0.005	1.072 ± 0.002	370.8 ± 0.4
KNM2	0.675 ± 0.009	1.047 ± 0.001	278.6 ± 0.3	0.651 ± 0.004	1.050 ± 0.001	278.4 ± 0.3
KNM3a	0.566 ± 0.024	1.016 ± 0.003	136.6 ± 0.9	0.569 ± 0.022	1.017 ± 0.003	136.6 ± 0.9
KNM3b	0.605 ± 0.017	1.010 ± 0.002	258.8 ± 0.5	0.609 ± 0.005	1.010 ± 0.001	258.9 ± 0.5
KNM4	0.703 ± 0.012	1.010 ± 0.001	150.4 ± 0.4	0.696 ± 0.012	1.011 ± 0.001	150.3 ± 0.4
KNM5	0.664 ± 0.008	1.011 ± 0.001	160.9 ± 0.4	0.669 ± 0.007	1.011 ± 0.001	161.0 ± 0.4

appendix G.

The smallest changes are expected to be observed in the background since it has no strong correlation with the neutrino mass squared. This can also be confirmed by comparing the mean background values in table 6.5. No visible changes, or only small changes, are observed. Due to the strong correlation of the squared neutrino mass with the endpoint and a strong anticorrelation of the signal and the squared neutrino mass, larger changes are expected in these parameters. This is confirmed by comparing the $\langle E_0 \rangle$ and ⟨Sig⟩ columns. With a difference of 0.071 eV, changes in the endpoint are largest for KNM1. This is expected since the central value of the separate KNM1 analysis has the largest difference to the neutrino mass squared of the combined fit. The fit compensates for the positive difference of $1.226\,\mathrm{eV}^2$ by increasing the endpoint. On the other hand, the signal decreases due to its anticorrelation with the neutrino mass squared. The second largest change is in KNM2, here we observe the opposite behaviour. In this case, the neutrino mass squared becomes more negative by $0.211\,\mathrm{eV}^2$, leading to a decrease in the mean endpoint value by 0.024 eV and an increase in the signal amplitude by 0.003.

It should further be noted that the spread of the patch-wise values is less affected by changes of the fit neutrino mass squared. Radial and azimuthal dependencies of the nuisance parameters are described in more detail in section 6.3.4.2.

It is also interesting to compare the goodness-of-fit obtained from the best fits. This is summarised in tables 6.6 and 6.7, for the statistics-only fits and the fits with all systematics included. The tables show the χ^2 values, reduced χ^2, and p-values. Due to the statistically fluctuated nature of the data, reduced χ^2 values around 1.0 are expected, whereas p values should be uniformly distributed in a range of $(0.0, 1.0)$. In both the statistics-only case and with systematics this is indeed observed. Some fluctuations are present which are compatible with statistical fluctuations. The reduced χ^2 values range between 0.89 and 1.47 in the statistics-only fits, and between 0.89 to 1.34 when including systematics.

Comparing table 6.6 to table 6.7, small improvements in the χ^2 are observed. Adding additional constrained parameters gives the model more freedom to describe the data

Table 6.6.: Goodnes of fit summary for the individual campaigns as well as the combined KNM1-5 analysis. The values presented here correspond to the fit results assuming only statistical uncertainties. For the combined analysis, the goodness-of-fit quantities $\bar{\chi}^2$ as well as $\hat{p}_{\mathrm{PG}}$ are given according to [174].

Campaign	χ^2	dof	χ^2/dof	p	$\bar{\chi}^2$	$\hat{p}_{\mathrm{PG}}$
KNM1	22.327	23	0.971	0.501	–	–
KNM2	30.113	24	1.255	0.181	–	–
KNM3a	311.508	349	0.893	0.926	–	–
KNM3b	35.192	24	1.466	0.066	–	–
KNM4	388.722	348	1.114	0.065	–	–
KNM5	309.240	349	0.886	0.938	–	–
KNM1-5	1100.931	1123	0.980	0.675	3.829	0.700

Table 6.7.: Goodnes of fit summary for the individual campaigns as well as the combined KNM1-5 analysis. The fits were performed including systematics. For the combined analysis, the goodness-of-fit quantities $\bar{\chi}^2$ as well as $\hat{p}_{\mathrm{PG}}$ are given according to [174].

Campaign	χ^2	dof	χ^2/dof	p	$\bar{\chi}^2$	$\hat{p}_{\mathrm{PG}}$
KNM1	21.264	23	0.925	0.565	–	–
KNM2	27.712	24	1.155	0.272	–	–
KNM3a	311.420	349	0.892	0.927	–	–
KNM3b	32.046	24	1.335	0.126	–	–
KNM4	388.428	349	1.113	0.072	–	–
KNM5	309.237	349	0.886	0.938	–	–
KNM1-5	1093.638	1123	0.974	0.729	3.530	0.619

better. Since the statistics-only fits already describe the data well, the changes are small. For the combined fit, also the goodness-of-fit quantities $\bar{\chi}^2$ as well as $\hat{p}_{\mathrm{PG}}$, according to [174], are given. Since the combined fit has one common squared neutrino mass, compared to the six independent squared neutrino masses of the individual fits, $\bar{\chi}^2$ is expected to be distributed around 5.0. This applies in particular to the combined fit with systematics.

The best-fit spectra of the combined analysis with systematics are presented in figure 6.12. The figure is split into four subplots, with two panels each. Each subplot displays the spectra (top panels) and the residuals (lower panels). The spectra panels include the measured data points (solid points) and the fit spectra calculated from the model (solid lines). The top left plot shows the spectra of all NAP campaigns. The spectra of KNM3a (top right), KNM4 (bottom left), and KNM5 (bottom right) are shown as patch-wise spectra. Spectra of the inner patches are displayed in lighter shades, and patches comprising outer pixels

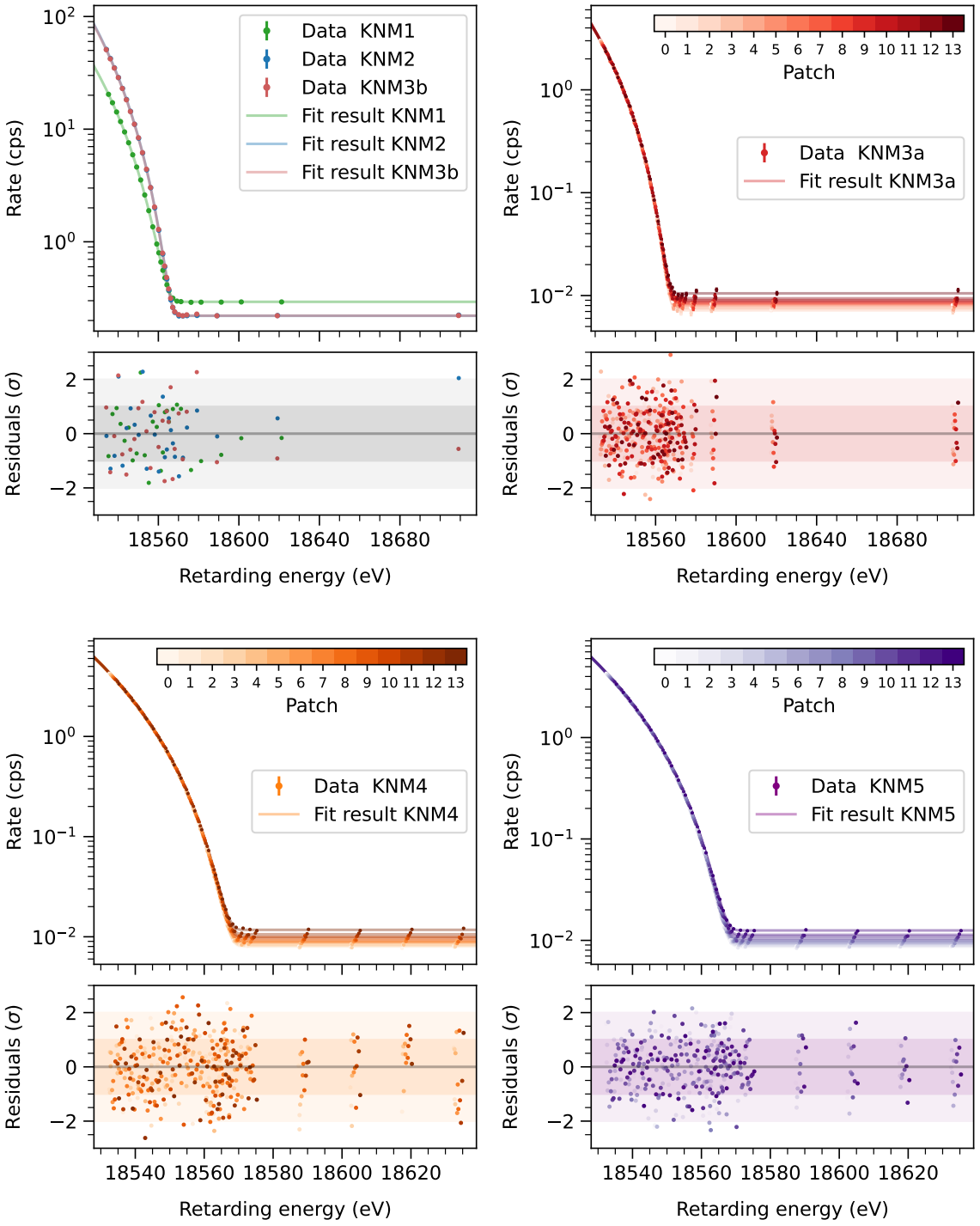

Figure 6.12.: Fit spectra of the combined analysis including all systematic uncertainties. The multi-fit of all spectra has one shared neutrino mass squared. Each quadrant of the figure is divided into the spectra on top and residuals at the bottom. The upper left quadrant shows the spectra and fit result of all NAP campaigns. The three other quadrants each show the spectra and residuals of the SAP campaigns. For the SAP spectra, the patches are shaded in lighter colours for the central patches and darker for the outer patches. No structure is observed in the residuals.

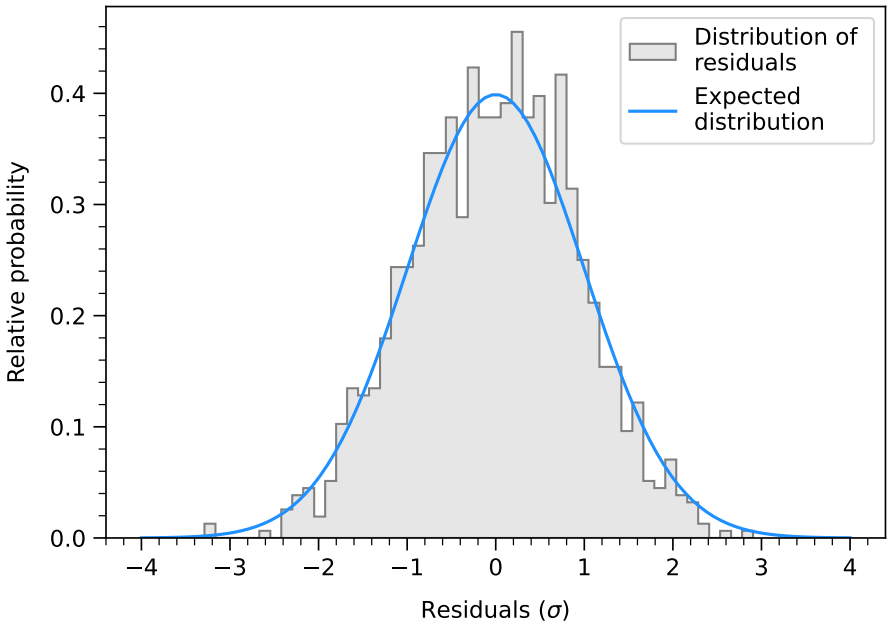

Figure 6.13.: Comparison of the residual distribution to the expected width. The residuals are combined from all 1259 data points that are displayed in figure 6.12. The histogram of the residuals is displayed relative to the expected distribution – a Gaussian pdf with a central value of 0.0 and width of 1.0.

are in darker shades. By comparing the scale of the background region, one can see the effect of the measures taken to reduce the background (see section 5.3), which are improved surface conditions due to the bakeout after KNM1, and the introduction of the SAP field configuration (see section 5.2.1) after KNM2. The background level on the outer patches is approximately 1.3× larger than the centre of the FPD due to a radially increasing component, related to the conditions on the inner surface of the main spectrometer vessel.

The residuals (lower panel of each subplot) are given relative to the 1σ uncertainty of each data point. This is only a first-order approximation assuming a Gaussian distribution of the residuals for illustration. The pdf applied to the SAP datasets in the fit is Poisson distributed, which has asymmetric uncertainties. The residuals do not show any structure and are randomly distributed around zero.

To further investigate if the residuals follow the expected distribution, they are histogrammed and compared to the predicted distribution (see figure 6.13). The standard deviation of the residuals is 0.94, which is a statistical under fluctuation to the expected width of 1.0 due to the Gaussian approximation.

6.3.4.1. Scan-wise parameters

Individual fits are performed scan-wise to obtain information about temporal stability. The results are shown in figure 6.14. The data of all detector pixels in each scan are stacked into a uniform spectrum. An increased transmission broadening is applied to the spectrum to account for the increased differences in the transmission in SAP campaigns between the inner and outer pixels. All fits are performed with a fixed neutrino mass squared, set to $m_\nu^2 = 0.0\,\mathrm{eV}^2$, while the endpoint, the signal amplitude, and the background are kept

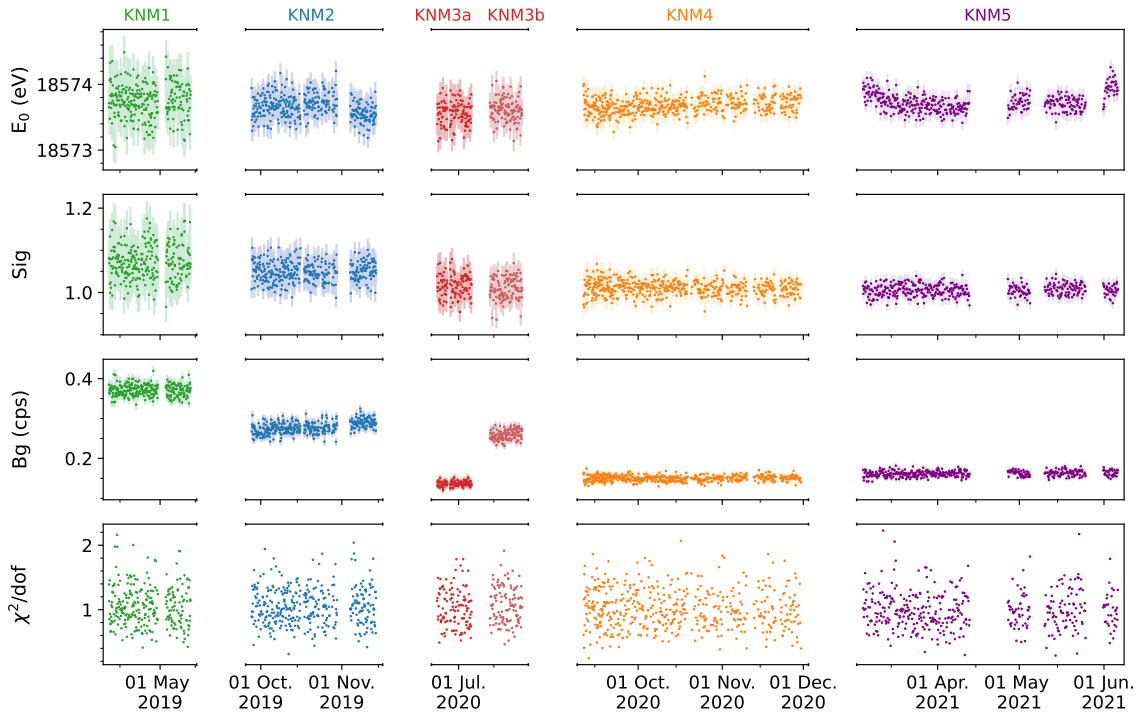

Figure 6.14.: Scan-wise fit parameters. For each scan, a uniform fit is performed. Only statistical uncertainties are considered in the fits. As there is no sensitivity to the neutrino mass in individual scans, the squared neutrino mass is set to a fixed value of $m_\nu^2 = 0.0\,\mathrm{eV}^2$. All other parameters are free, uniform parameters. An increased transmission broadening accounts for spatial variations in the magnetic field.

free in the fit. From top to bottom, figure 6.14 displays the resulting endpoints, signals, background levels, and the corresponding normalised χ^2: (χ^2/dof).

The rear-wall bias voltage directly influences the electron starting potential and, consequently, the measured endpoint. If the rear-wall bias changes over time, we expect shifts in the endpoint. The most significant changes are anticipated for KNM2 and KNM5 due to resetting of the rear-wall bias voltage (see section 5.2.2). In KNM2, the rear-wall bias changed twice. In KNM5, four different rear-wall bias voltages were applied. In addition to this, changes in the work function can also lead to drifts in the observed endpoints. These drifts are also prominent at the beginning of KNM5. Due to the cleaning of the rear wall between KNM4 and KNM5, a fractionally larger accumulation of tritium on the rear wall leads to changes in the work function. As the accumulation is a continuous process, a drift in the endpoint is observed.

An overview of the estimated endpoint evolution is shown in table 6.8. The table compares two scenarios to extract the endpoint drift over time. In the second column (with U_{RW}), a common slope and a common offset was fit to the scan-wise results of each campaign. When fitting the time evolution, this method does not account for different rear-wall bias voltage set-points, which were applied in the course of a given campaign. In the second column (without U_{RW}), a common slope is fit while allowing for different endpoint offsets for different parts of the campaigns when the rear-wall voltage was changed. Hence, increasing the rear-wall voltage twice in KNM2 results in lower endpoints for the second

Table 6.8.: Endpoint evolution over time. The evolution is analysed for two scenarios. With U_{RW}: Here, a slope is fit to the scan-wise E_0 results of each campaign. Without U_{RW}: A common slope is fit to the scan-wise E_0 results of each campaign. In addition, for the different rear-wall bias voltages, individual endpoint offsets are fit, allowing the extraction of the endpoint slope independent of U_{RW}.

Campaign	**With U_{RW}**		**Without U_{RW}**	
	Slope (meV/day)		**Slope (meV/day)**	
KNM1	-0.339	± 1.548	-0.339	± 1.548
KNM2	-2.416	± 0.570	-0.375	± 1.845
KNM3a	-0.125	± 3.670	-0.125	± 3.670
KNM3b	-6.160	± 3.909	-6.160	± 3.909
KNM4	$+1.335$	± 0.231	$+1.335$	± 0.231
KNM5	$+0.649$	± 0.186	-3.647	± 0.540

Table 6.9.: Background increase over time. The increase is both given as relative and absolute values. Note that the slope of KNM1 is slightly negative but consistent with zero. A significant increase of the background is oberved in the case of all other campaigns.

Campaign	**Rel. slope (%/day)**	**Slope (mcps/day)**	**Uncertainty (mcps/day)**
KNM1	-0.007	-0.026	± 0.078
KNM2	$+0.171$	$+0.476$	± 0.038
KNM3a	$+0.159$	$+0.217$	± 0.174
KNM3b	$+0.304$	$+0.789$	± 0.245
KNM4	$+0.014$	$+0.021$	± 0.014
KNM5	$+0.025$	$+0.041$	± 0.012

and third part of KNM2. Globally, this decrease is fit as a significant negative slope of $(-2.416 \pm 0.570)\,\mathrm{meV/day}$. By contrast, using the second method, a much smaller drift of $(-0.375 \pm 1.845)\,\mathrm{meV/day}$ was observed. For KNM5, resetting of the rear-wall bias voltage results in the opposite behaviour. Here, the rear-wall voltage was decreased three times. This would generally result in an increasing endpoint after each adaptation of the rear wall setting. Opposing this is the accumulation of tritium on the rear wall and resulting changes in the work function, causing the endpoint to decrease over time. Fitting the endpoint evolution with the first method, therefore, results in a positive slope of $(0.649 \pm 0.186)\,\mathrm{meV/day}$ since both effects partially compensate each other. The second method disentangles drifts from the rear-wall bias voltage set points. In this case, a

significant negative drift of $(-3.647 \pm 0.540)\,\mathrm{meV/day}$ is fit to the scan-wise endpoints. The rear-wall bias voltage does not affect the fit slope for the other campaigns (KNM1, KNM3a, KNM3b, and KNM5), as the set rear-wall voltage remained mostly constant in these campaigns. Therefore, both methods are consistent. Negative endpoint slopes are further present in KNM1, KNM3a, and KNM3b, which are compatible with zero within the uncertainties or related to additional drifts of the work function. An endpoint increase was fit to the KNM4 scan-wise endpoints.

When stacking scans, the shifts and drifts are correctly accounted for by the $\sigma^2_{\mathrm{shift,drift}}$ (for more details, see section 6.3.3.1). Other than the endpoint changes that are understood and are explained, the endpoint shows good stability and agreement with the expected statistical uncertainties.

The signal is slightly higher in KNM1, KNM2, and KNM3b compared to the other campaigns. This is as described earlier and is due to the larger ROIs chosen in KNM1 and KNM2 campaigns. The signal also shows good stability, which is in agreement with the expected statistical uncertainties.

The largest changes are seen in the background between campaigns. The prominent decreases reflect the measures taken to reduce the overall background level, namely baking of the main spectrometer and the introduction of the SAP setting. Overlayed to these features, a gradual increase in the background rate can be observed throughout the individual campaigns. This increase is due to the slow, gradual deterioriationg surface conditions of the. An overview of the measured background increase inferred from the data is shown in table 6.9. The maximum increase that was observed occured between KNM2 and KNM3b with 0.2 %/day to 0.3 %/day. In the fit combining scans, the background increase over time is fully absorbed in the absolute background rate.

6.3.4.2. Spatial dependencies

Since the squared neutrino mass is an experiment-independent quantity, no spatial dependence of the parameter is expected. KNM4 and KNM5 are the two datasets with the largest statistics. For this reason, they provide a good basis for investigating spatial dependencies of the inferred squared neutrino mass. Figures 6.15 and 6.16 show the results of the analysis investigating both the radial and azimuthal dependencies.

The radial analysis uses the same patches that are also applied in the standard analysis. In addition, the neutrino mass squared is fit as a patch-wise parameter. Figure 6.15 shows the results of the patch-wise fits of both campaigns. The panels of the plot show the fit neutrino mass squared, endpoint, signal, and background. In addition to this, each of the resulting parameter sets is fit with a first-order polynomial to extract the patch-dependent slope. The slopes' corresponding uncertainties are listed in the legend of each panel. For some of the parameters, radial dependencies are expected. The most significant radial dependency is observable for the background parameter. This radially increasing component is due to the proximity to the spectrometer walls and the conditions on the inner surface of the main spectrometer vessel. In addition to this, a slope of the signal parameter is present. This implies radial inhomogeneities of the column density, with higher column density in the central parts of the WGTS. The endpoint also shows a minor radial dependency. A smaller effective endpoint is fit for the central patches. The endpoint's radial dependency can be interpreted as radially different starting conditions of the electrons in the source. This can either be due to the presence of the source plasma or radially dependent coupling

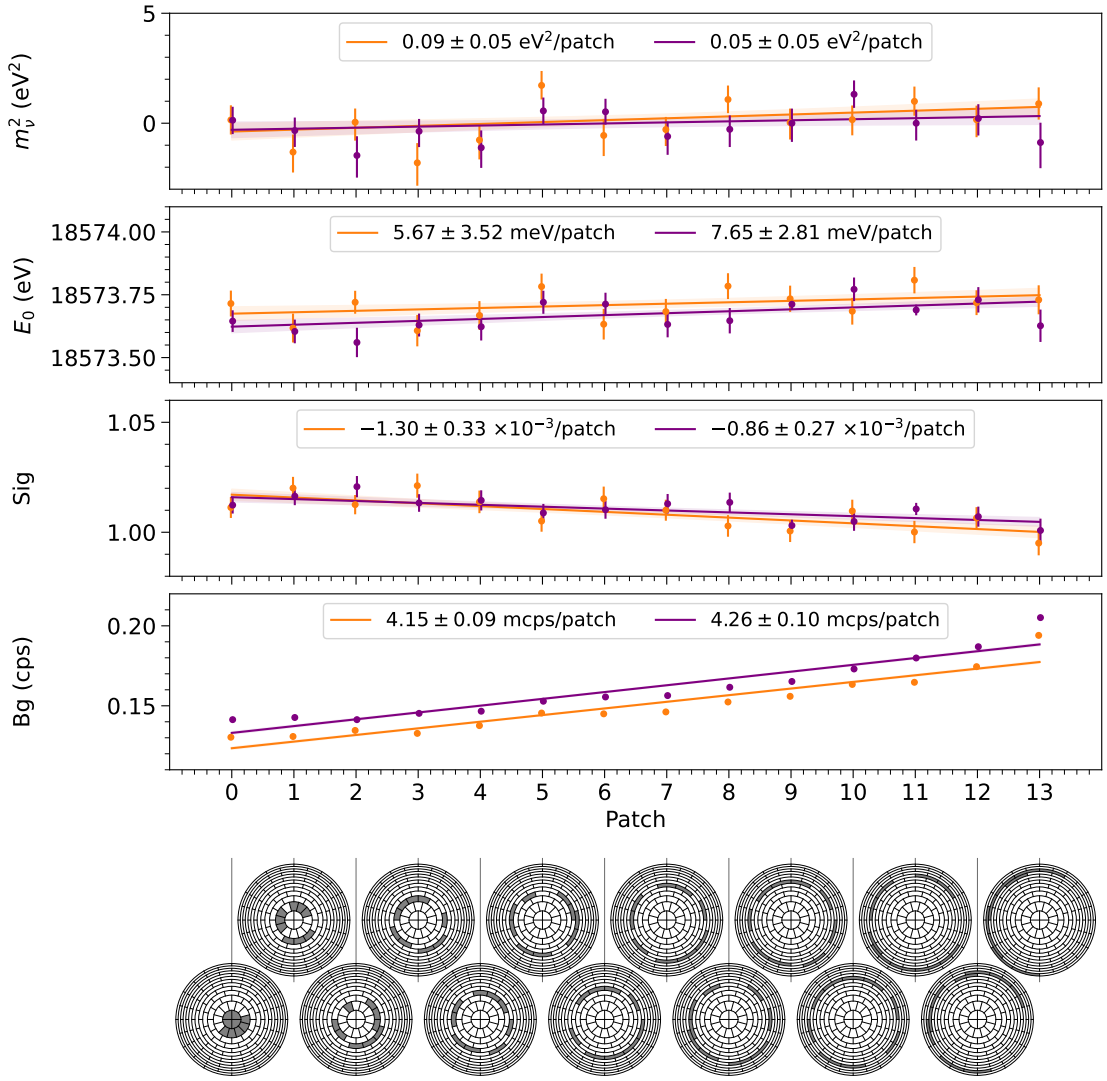

Figure 6.15.: Investigations of radial dependencies. The fits are performed with a free neutrino mass squared and patch-wise models. The results of KNM4 (orange) and KNM5 (purple) are, in addition, fit with a first-order polynomial to estimate the slope significance over patches.

conditions of the rear wall. No significant slope is observed in the fit patch-wise neutrino mass squared values, as the fit m_ν^2 slope is consistent with zero.

Azimuthal dependencies are investigated by segmenting the detector into four quadrants: left, right, top, and bottom. The quadrants coincide with the four cards of the readout electronics of the focal-plane detector system. Therefore, the presence of an azimuthal pattern could also reflect dependencies of the spectral shape to the readout electronics[22]. To further account for radially dependent parameters, such as magnetic fields, the transmission broadenings, or the potential depression, patch-wise models and patch-wise parameters (endpoints, signals, and backgrounds) are used in the analysis of each detector quadrant. The results are shown in figure 6.16. Similarly to the radial case, the fit squared neutrino masses, endpoints, signals, and backgrounds are shown in the plots. Besides the individual

[22]The readout cards are physically situated next to each other and could potentially exhibit a temperature gradient.

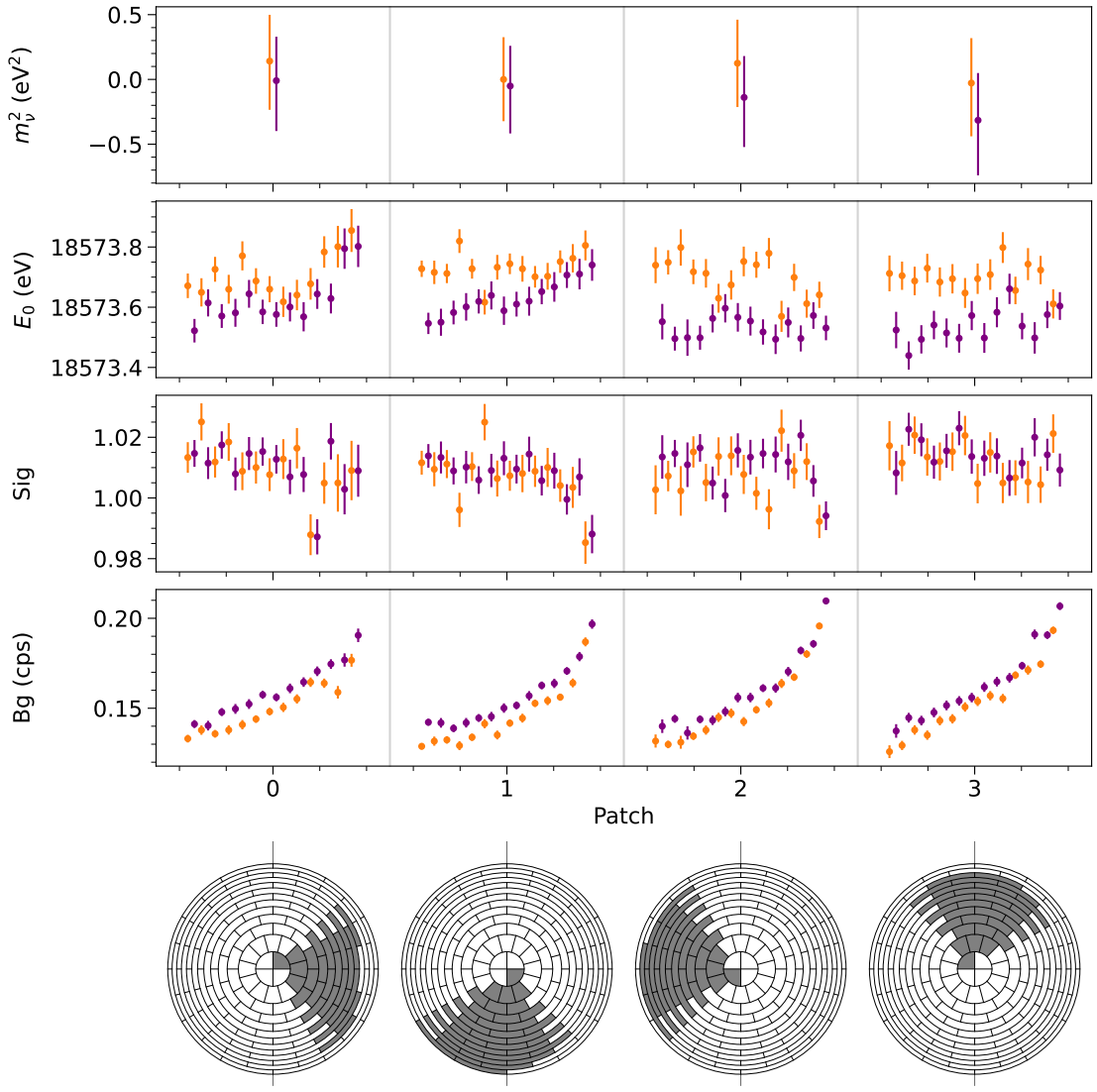

Figure 6.16.: Investigations of azimuthal dependencies. The fits are performed with a free neutrino mass squared and radial patch-wise models for each detector quadrant. The results from each detector quarter of KNM4 (orange) and KNM5 (purple) consist of 14 endpoints, 14 signal parameters, 14 background parameters, and a single neutrino mass squared.

m_ν^2 per readout segment, the plot has 14 endpoints, signals, and backgrounds in each sector according to the 14 patches. Some expected dependencies are observed, similar to those visible in figure 6.15. Azimuthally, the neutrino mass squared does not show any dependency over the different detector quadrants. The values agree with each other within the uncertainties. Also, the other parameters do not show any significant differences amongst the readout segments.

6.3.4.3. Scan-order dependency

The squared neutrino mass is a parameter that remains experimentally independent, thus no scan-order dependence is foreseen. As summarised in chapter 5 and in table 5.1, three

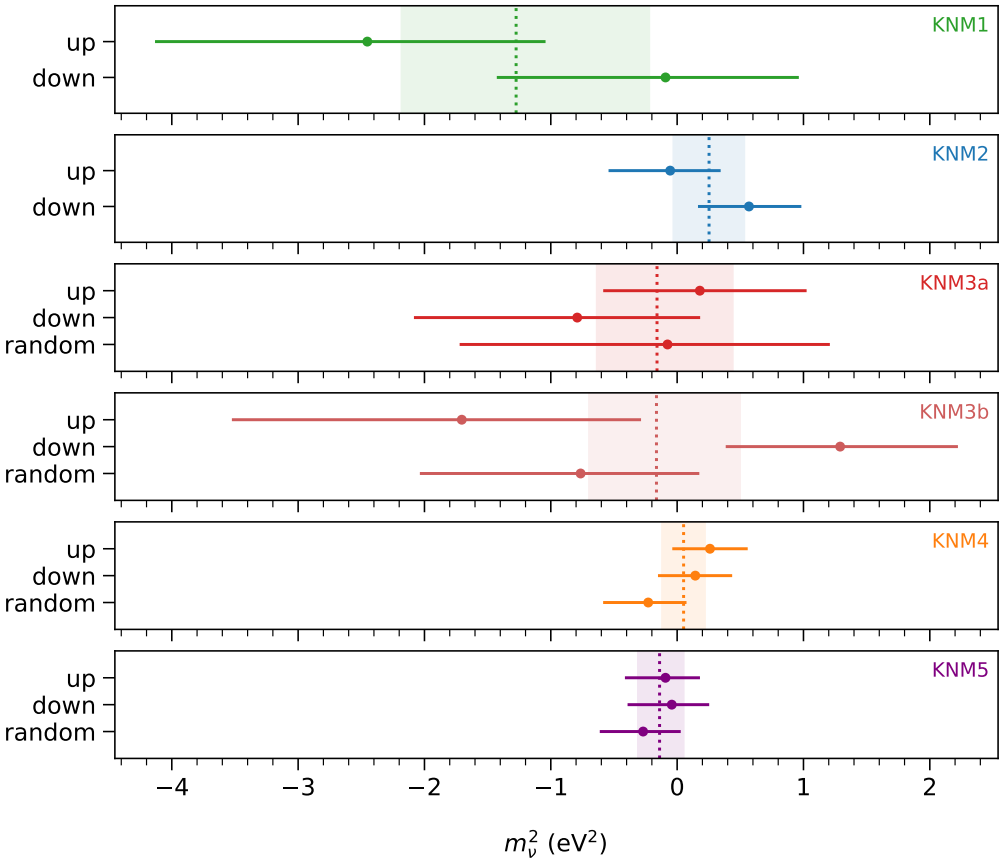

Figure 6.17.: Scan-order dependency of m_ν^2. For each campaign, the scans are separated by their scan direction (up, down, and random) and fit together. The results are compared to the combined fit (central value given by the dashed vertical line and uncertainties represented by the shaded range).

different scan modes are applied when measuring the spectrum. The data can therefore be split into up, down, and random scans.[23] It is also investigated if there is a dependency of the neutrino mass squared on the scan order by analysing the three scanning modes independently from each other. The uncertainties generally increase when splitting the data since the statistics are reduced by a factor of ~ 3.

The result of this study is summarised in figure 6.17. For comparison, the plot also shows the results when combining all scans (dashed vertical lines and shaded range). Overall there is no recurring structure for the different scan orders. Furthermore, the individual results are consistent within their uncertainties. The largest outlier is the combination of all KNM3b down scans, however this is still compatible with the other scan directions and explained by statistical fluctuations of the data.

Separating the datasets into NAP and SAP campaigns, the up and down scans of the NAP campaigns might indicate a preference for a smaller neutrino mass squared inferred from upward scans. This could be due to a minor scan dependency of the collected background depending on the scan direction. Trapped low-energy background electrons can be accelerated when reducing the retarding energy and hence increase the background

[23] For KNM1 and KNM2 only unidirectional up and down scans were recorded.

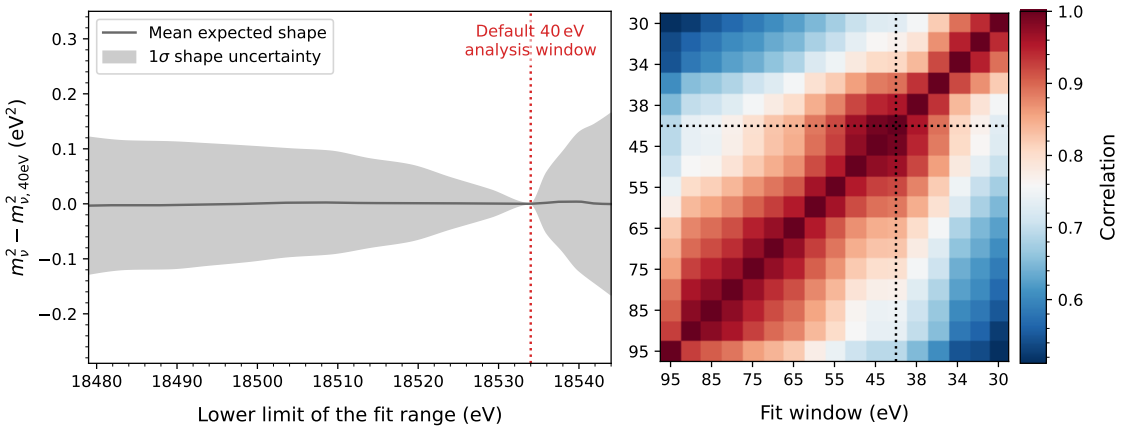

Figure 6.18.: Expected shape uncertainty of the squared neutrino mass over the fit range. The study is based on 500 statistically fluctuated KNM5 Monte Carlo samples. For each of the statistically fluctuated samples, a qU scan was performed. The left subplot summarises the expected shape uncertainty when performing a qU scan on fluctuated data. The x-axis represents the lower limit of the fit range. The dotted red line shows the standard fit range. The right subplot illustrates the correlation between the results of different fit ranges. Hereby, the x- and y-axis represent the fit range relative to the endpoint. The m_ν^2 results of different fit ranges for the same data set are highly correlated, as the majority of the statistics is shared between different fit ranges. The dotted black lines show the standard 40 eV fit range.

contribution for successive scan steps. To counteract the danger of this effect, the usage of the different scan directions was introduced, mitigating potential bias when stacking the data [171]. Since only three datasets in the NAP setting are available for this comparison, it is not possible to confirm this hypothesis. Furthermore, the datasets taken in the SAP setting do not show this behaviour.

6.3.4.4. Fit-range dependence

The neutrino-mass analyses presented in the previous sections are based on the default fit interval, extending to 40 eV below the endpoint. However, further data points are recorded below this range, which are used to study systematic effects (see section 6.3.3.1). The additional spectral data points can also be used to check for dependencies of the squared neutrino mass on the fit range. As the neutrino mass is an experiment-independent property, it should not exhibit any changes when changing the analysis range. Similar analyses were also performed by the Mainz experiment [151]. If a dependence on the fit interval of the squared neutrino mass is detected, it may suggest either an unaccounted systematic effect or a discrepancy between the model inputs and the true experimental conditions.

An interesting study is to quantify if the fit neutrino mass squared has a significant dependence on the energy range used in the spectrum fit (so-called "qU scans"). For this study, the analyses are repeated with data ranges between ~ 30 eV and ~ 100 eV below the endpoint (10 eV smaller than the default fit range and up to 60 eV larger, respectively).

First, to quantify the range in which deviations are expected, a study is performed on 500 statistically fluctuated Monte Carlo samples. For each Monte Carlo sample, a qU scan is performed. From all qU scans, the expected relative shape of the fit result deviations over the fit range is calculated. The results of the study are summarised in figure 6.18. The study is based on KNM5-like Monte Carlo. The left panel of figure 6.18 gives the expected qU scans shape relative to the squared neutrino mass extracted from the default 40 eV fit range. On average (grey solid line), a flat structure is expected. The 1σ spread of the deviations is shaded in grey. Structures are expected to increase with a wider fitting range due to the addition of statistically independent data points in the individual fits. Fits with much smaller fit ranges are expected to deviate more from the 40 eV reference fit result due to the rapidly decreasing statistics. The correlations between the results of different fit ranges are illustrated in the right panel of figure 6.18. Fit results with similar fit ranges are extremely correlated (with values close to 1.0) since most of the data in the fit is shared and hence is statistically dependent. Fit results with fit ranges that are more different (such as 30 eV versus 95 eV) are more uncorrelated since only a smaller fraction of the data is shared. The correlation is still on the order of 0.5. For the example of KNM5, deviations on the order of $\sim 0.1\,\mathrm{eV}^2$ are expected based on the Monte Carlo simulation within the $1\,\sigma$ band.

In a second step, the qU scans are performed for each individual campaign and the combined KNM1-5 analysis. In addition to the spread of the qU scan, it is also interesting to investigate if any patterns are reappearing between the campaigns. Reappearing structures could imply a missing systematic effect. The results of the qU scans are shown in figure 6.19. Studies investigating the fit range dependence include both the statistics-only fits (lighter colours and central values marked by crosses in figure 6.19) and fits including all systematic uncertainties (darker colours and central values marked by the filled circles in figure 6.19). The same systematic inputs are applied to all fit ranges, and the FSD was precisely calculated for the 40 eV fit range. An increasing fraction of the electronically excited states contribute to the measured spectrum for larger fit ranges. For wider ranges, it would hence be adequate also to assume an additional uncertainty impact that is currently not taken into account.

The qU scan results of the combined fit are given in the top panel of figure 6.19. This is effectively the combined result of all individual campaign-wise qU scans (lower panels). For smaller fit ranges of the combined analysis, more negative squared neutrino masses are observed, whereas, for increased fit ranges, the fit squared neutrino masses remain mostly constant. The results are all compatible within their error bars. When including systematic uncertainties, the results only change on a small scale. The combined fit only shows small changes in the central value when extending the fit range. Comparing to the standard 40 eV range, the central value changes by $-0.001\,\mathrm{eV}^2$ for the 60 eV fit range and by $-0.002\,\mathrm{eV}^2$ for the 90 eV fit range.[24] Comparing the individual campaigns, no significant deviations within the uncertainties are observed. Furthermore, also in the individual scans, no reoccurring structure is observed. There are only minor changes for the individual

[24] The FSD applied in the KATRIN neutrino-mass analysis is available up to excitation energies of ∼240 eV. The ground state probabilities (<10 eV) are based on ab initio calculations [213]. The representation of the electric ground state is based on calculations by Seanz et al. and Fackler et al. [99, 213](≲40 eV), with good agreement of both calculations. States of the electronic continuum (≳40 eV), on the other hand, show more significant differences between different approaches. Following this, the FSD is considered to be theoretically well described in the default 40 eV fit interval [224]. The small changes in the central value of the squared neutrino mass over large fit ranges indicate that the FSD is already describing the measured data in a range wider than 40 eV below the endpoint with high precision.

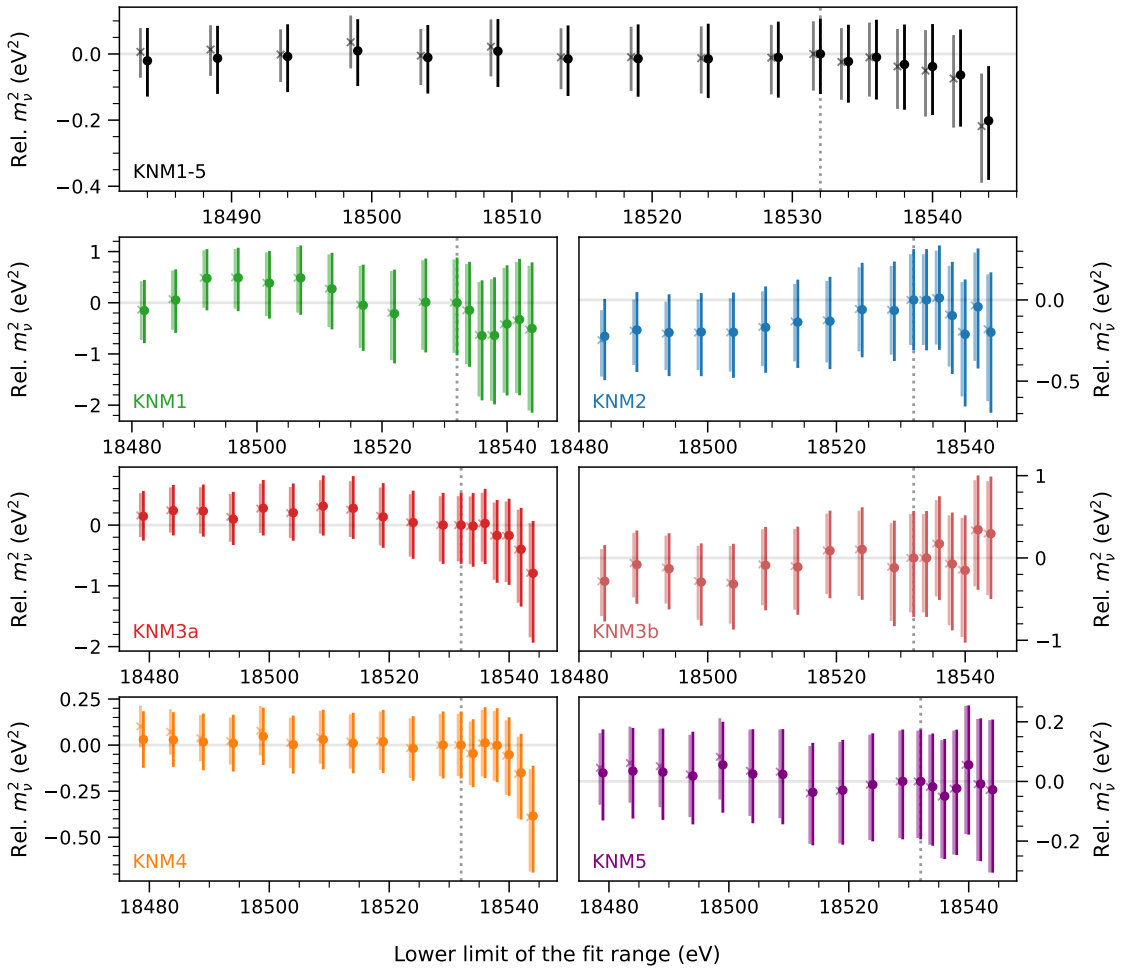

Figure 6.19.: Fit range dependence of m_ν^2. The results are based on fits considering only statistical uncertainties (marked by the crosses and lighter colours), and fits considering statistical and systematematic uncertainties (marked by the filled circles and darker colours). The values are given relative to the result obtained from the standard 40 eV fit range. The top panel represents the combined KNM1-5 analysis. The lower six panels illustrate the fit range dependence for each campaign individually. As neighbouring points share a significant amount of statistics, the results are strongly correlated. Due to the superior statistical power of KNM4 and KNM5, the combined shape is mainly dominated by these two campaigns.

campaigns when considering systematic uncertainties. For KNM4 and KNM5, the central values become more consistent with the default 40 eV fit range for increasing fit ranges when including systematic uncertainties. Summarising the results of the qU scans, no prominent reoccurring structure was observed, and the shape lies within the expected spread, illustraded by the KNM5 based Monte Carlo simulation.

Similar to section 6.3.3.2, the impact of the individual systematic effects is also investigated over the fit range. The results of the KNM1-5 statistics-only fits, as well as the impact of individual systematic effects, and fits including all systematics, are shown in figure 6.20. The top panel shows the absolute uncertainty on m_ν^2 of the statistics-only fit and the fit

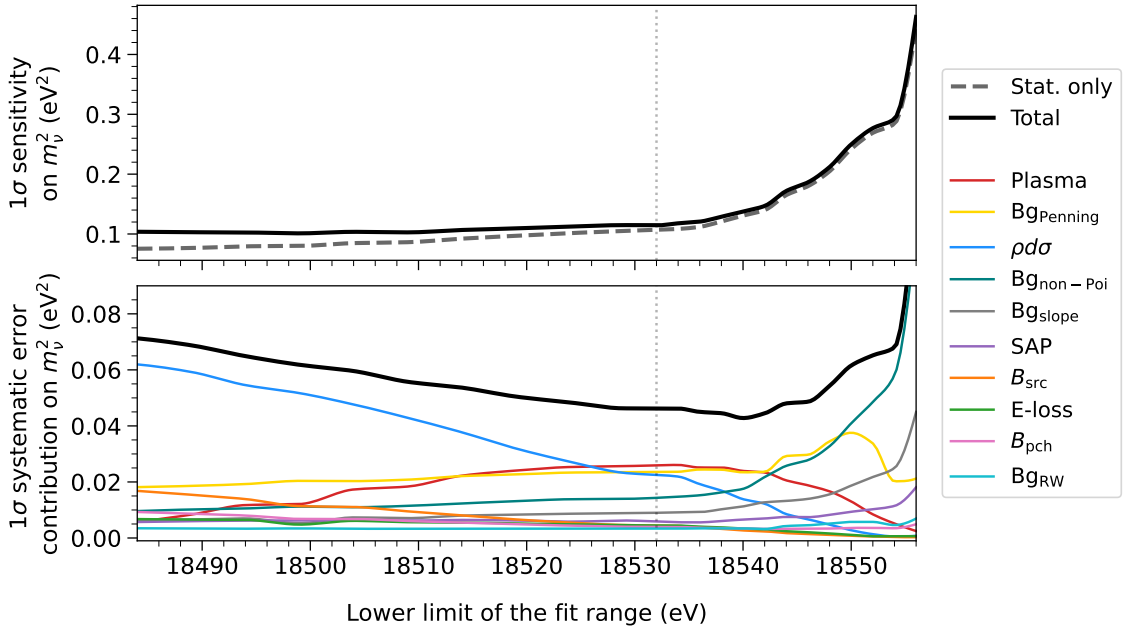

Figure 6.20.: Fit-range dependence of systematics, based on the combined KNM1-5 fit. In the top panel, the statistics-only fits and fits including all systematics are shown. The lower panel outlines the impact of each systematic individually. The systematic impact is calculated as described in section 6.3.3.2. The systematics are sorted according to their impact in the standard 40 eV analysis interval (vertical dotted line).

with all systematics. The bottom panel of figure 6.20 illustrates the systematic contribution, according to equation (4.19).

Background systematics, such as the non-Poisson background and the background slope have larger impact on smaller fit ranges. This can be explained as the relative background fraction of the measured data is larger for smaller fit ranges. Deeper into the spectrum, the signal contribution increases, reducing relative influences of the background systematic. The systematic effect due to Penning-induced background has a slight increase for small ranges and then mostly remains constant for wider ranges. In contrast to this, the column density has an increasing impact on wider fit ranges. By increasing the fit range, the influence of scattering effects becomes more prominent, which is directly connected to the column density. This behaviour, on a much smaller scale, can also be observed for systematic effects such as the energy loss function, the source magnetic field and the pinch magnetic field. The energy loss function also gains in significance since, with wider rages, more electrons are measured which scattered once or multiple times. Also connected to the scattering are the uncertainties due to the source potential and plasma. Here the uncertainty reaches a maximal value in the 40 eV fit window, which is then reduced for wider fit ranges. This structure is explained due to the effect of the energy loss function shifts. This has the largest impact on the one-times scattered electrons, resulting in the maximal contribution in the 40 eV fit range. The effects on the squared neutrino mass were also investigated in [171]. The increasing impact of the pinch magnetic field and the source magnetic field is connected to the acceptance angle. An increase in the energy range corresponds to a higher probability of measuring scattered electrons. Hereby, electrons with large pitch angles θ are more likely to undergo multiple scattering as they travel a longer distance

through the source. The electrons can further experience angular changes after scattering and consequently fall into the angular range of the acceptance angle. These effects are more significant deeper in the spectrum. Systematic uncertainties on the analysing plane magnetic fields and the transmission broadening have a lager effect for small fit ranges since the systematic mainly influences the transmission edge shape. This especially has a direct effect on unscattered electrons with small surplus energies. Lastly, the smallest effect overall is the systematic effect of the additional β-spectrum. The systematic error contribution from the rear wall increases slightly with wider fitting ranges.

All systematic uncertainties combined is shown by the black lines in figure 6.20. The systematic contribution, including all effects, reflects features of the dominating systematic for certain regions. The short-range, for example, is dominated by the contribution of $\mathrm{Bg}_{\text{non-Poi}}$ and $\mathrm{Bg}_{\text{Penning}}$. Fit ranges between 35 eV to 55 eV below the endpoint are mainly affected by $\mathrm{Bg}_{\text{Penning}}$, the source potential (plasma), and $\rho\mathrm{d}\sigma$. The combined systematic error contribution is smallest for an analysis window of ∼32 eV below the endpoint. However, combined with the statistical uncertainty, the overall sensitivity on m_ν^2 is considerably larger compared to the default 40 eV fit range. Wider fit ranges (more than 55 eV below the endpoint) are dominated by the systematic uncertainty on $\rho\mathrm{d}\sigma$. Overall, comparing the statistics-only sensitivity to the total sensitivity (top panel of figure 6.20), the fit is dominated by statistical uncertainties for all fit ranges. The default analysis window is a good choice, given the robustness of the FSD in the 40 eV range and the fact that the overall sensitivity only marginally improves with a wider analysis range.

6.3.4.5. Neutrino mass Limit

Based on the results of the combined neutrino-mass analysis of KNM1-5 (presented in section 6.3.4), the result is consistent with $0.0\,\mathrm{eV}^2$ within $0.5\,\sigma$. Based on this, an upper limit on the squared neutrino mass is calculated. In the following, the upper limit on the neutrino mass is presented following the Lokhov-Tkachov method and the Feldman-Cousins construction as described in section 4.4. The two belts constructed with both methods are presented in figure 6.21: the Lokhov-Tkachov belt is shown in blue, and the Feldman-Cousins belt is shown in grey. The upper limit on the squared neutrino mass is calculated for the best-fit value of the combined analysis $m_\nu^2 = -0.050\,^{+0.107}_{-0.121}\,\mathrm{eV}^2$. In figure 6.21, this value is marked by the vertical orange line. A more detailed illustration of the belt construction is presented in appendix H.

The Feldman-Cousins belt construction returns,

$$m^2_{\nu,\,\mathrm{FC}} < 0.14\,\mathrm{eV}^2 \quad (90\,\%\ \text{C.L.}), \tag{6.26}$$

$$m_{\nu,\,\mathrm{FC}} < 0.37\,\mathrm{eV} \quad (90\,\%\ \text{C.L.}), \tag{6.27}$$

since the best fit has a slightly negative squared neutrino mass value. While the Feldman-Cousins approach has a misleading benefit when obtaining more negative squared neutrino mass results in the unphysical region, the Lokhov-Tkachov approach is more robust as it returns a consistent upper limit for the negative region.

For the Lokhov-Tkachov method, the new limit on the squared effective neutrino mass is

$$m^2_{\nu,\,\mathrm{LT}} < 0.18\,\mathrm{eV}^2 \quad (90\,\%\ \text{C.L.}). \tag{6.28}$$

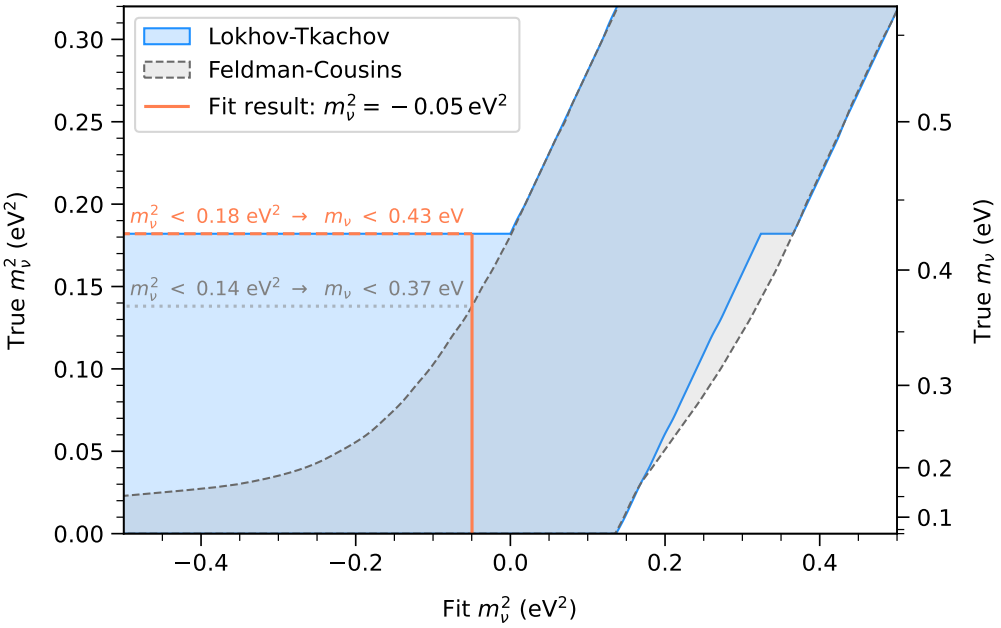

Figure 6.21.: Confidence belt and upper limit on the squared neutrino mass based on the combined KNM1-5 analysis. The plot shows both the Lokhov-Tkachov belt (blue) and Feldman-Cousins belt (grey) construction. The best-fit value is marked by the solid vertical orange line. Based on the best-fit value, the upper limits on the squared neutrino mass are determined from the intersections with the lower bound for the constructed Lokhov-Tkachov belt (dashed orange line) and the constructed Feldman-Cousins belt (dotted grey line). The limits on m_ν are derived, By taking the square root of the calculated m_ν^2-limits.

Taking the square root, this translates to a limit on the effective neutrino mass of

$$m_{\nu,\,\mathrm{LT}} < 0.43\,\mathrm{eV} \quad (90\,\%\ \mathrm{C.L.}). \tag{6.29}$$

Concluding, with the more robust Lokhov-Tkachov method, the combined analysis of KNM1-5 is able to constrain the neutrino mass to less than $m_{\nu,\,\mathrm{KNM1\text{-}5}} < 0.43\,\mathrm{eV}$ (90 % C.L.). Following the previous two neutrino-mass results released by KATRIN collaboration, in 2019 with $m_{\nu,\,\mathrm{KNM1}} < 1.1\,\mathrm{eV}$ [22], and in 2022 with $m_{\nu,\,\mathrm{KNM1\text{-}2}} < 0.75\,\mathrm{eV}$ [25], this is yet again the current best limit on the neutrino mass from direct measurements. The result is, in particular, of great significance as it is model-independent in comparison to limits obtained through observational cosmology and does not rely on assumptions on the Majorana or Dirac nature of the neutrino.

6.3.4.6. Outlook – influence of different priors

With more statistics and correspondingly more stringent results, alternative inference methods obtain a stronger appeal. In particular Bayesian analysis (more details in section 4.3.2) could become more relevant as it allows a straightforward treatment of prior assumptions. These assumptions can limit the physical parameter space, and can also further incorporate external information from other experiments (this will, in particular, become interesting

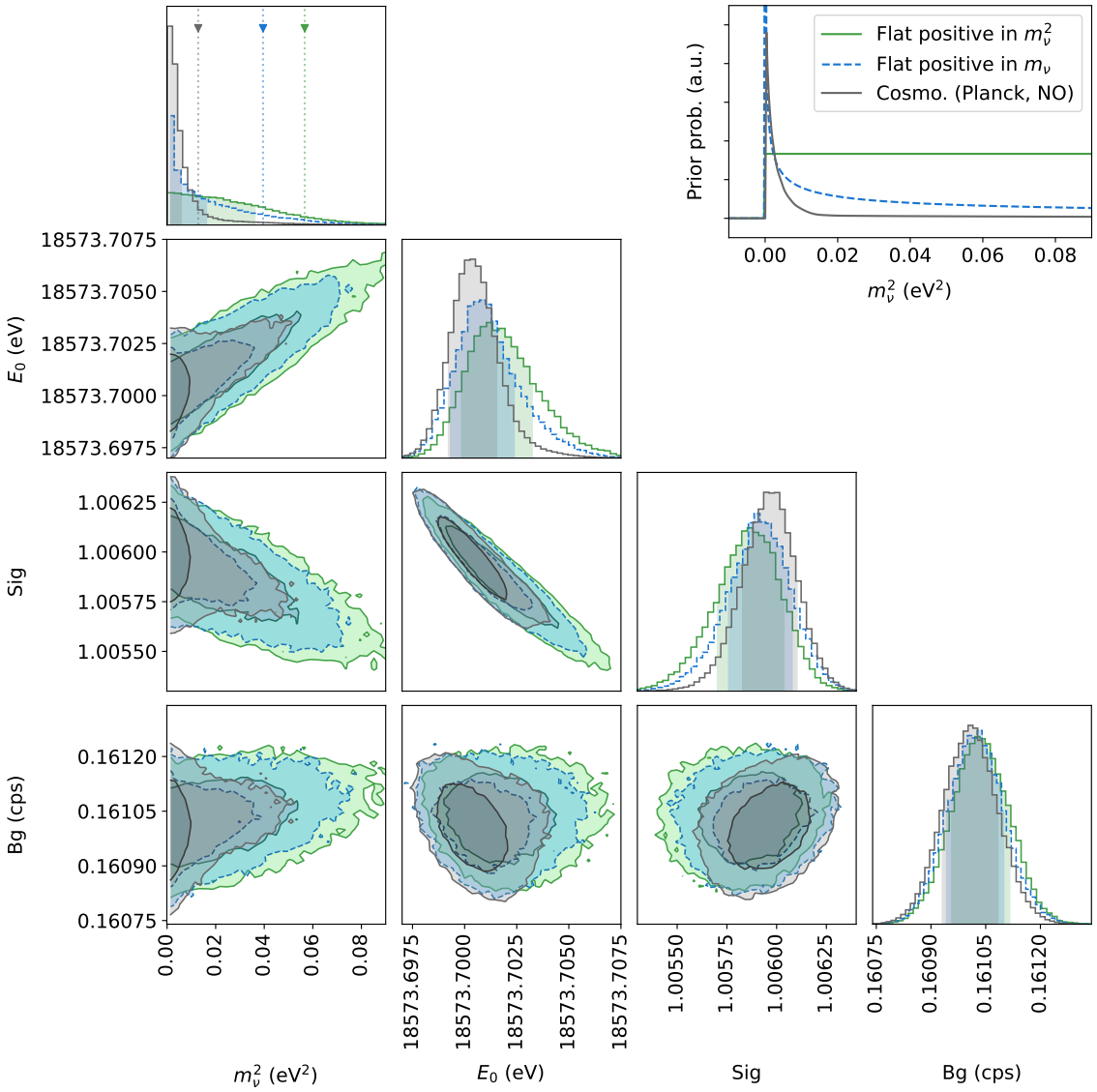

Figure 6.22.: Influence of different priors on the squared neutrino mass limit. The Bayesian analysis study is based on 1000 days of simulated KATRIN spectra, with conditions similar to KNM5. The plot includes three different prior scenarios: A flat positive prior on the m_ν^2 parameter space (green), a flat prior on the m_ν parameter space (blue), and an example prior extracted from the cosmological posterior distribution of the Planck analysis (grey). The three different prior scenarios are illustrated in the top right panel. The transformation from the $\sum m_\nu$ space of the cosmological posterior distribution into the m_ν^2 parameter space is done assuming normal ordering. The diagonal panels show the marginalised posterior distributions. The 1σ credibility intervals (C.I.s) (given by the hdi) are shaded in the respective colour. The 90 % C.L. upper bounds on the squared neutrino mass are marked by the vertical dotted lines and arrows. The panels below the diagonal show the two-dimensional posterior distributions and the parameter correlations. The contours are shown for 1σ and 2σ.

when other laboratory experiments such as Project 8 or holmium-based neutrino mass searches start providing competitive results). Based on simulated spectra, a set of different example priors is shown in figure 6.22 and appendix I. The studies are based on 1000 days of simulated KATRIN data, with conditions that are modeled on KNM5. To approach the Bayesian inference, a Markov Chain Monte Carlo (MCMC) method is employed for the studies. Figure 6.22 is based on an input neutrino mass squared of $m_\nu^2 = 0.0\,\mathrm{eV}^2$. To demonstrate this technique for a positive neutrino squared mass sign, further studies are shown with $m_\nu^2 = 0.1\,\mathrm{eV}^2$ (see appendix I). The plots include the two-dimensional parameter contours ($1\,\sigma$ and $2\,\sigma$) over m_ν^2, E_0, Sig, and Bg, as well as the marginalised histograms of each parameter. The marginalised 68 % C.I. of the parameters is shaded, whereas in figure figure 6.22 the 90 % C.I. on the squared neutrino mass is marked by the vertical dotted line.

The most natural prior in the case of KATRIN is a flat positive prior in the m_ν^2 parameter space (green). This prior restricts the ensemble of resulting chains to only explore the physical parameter space. Since the squared neutrino mass is the observable in the measured integrated spectrum, this prior does not modify the parameter space and only excludes the negative parameter space. For squared neutrino mass values close to zero, the flat positive prior results in an upper limit. When applying the prior, the distribution on the endpoint and signal furthermore becomes more asymmetric.

An alternative prior is the assumption that the probability density is equal in m_ν. Here, it also makes sense to restrict the parameters space to physical values $m_\nu \geq 0$. To construct the prior distribution in m_ν^2, we utilise that the total probability is conserved in both the m_ν^2 and the m_ν parameter space. This can be written as

$$P\left(m_\nu\right) \mathrm{d}m_\nu = \pi\left(m_\nu^2\right) \mathrm{d}m_\nu^2, \tag{6.30}$$

where $P\left(m_\nu\right) = \text{const.}$ Solving the equation for the prior probability π on the squared neutrino mass leads to

$$\pi\left(m_\nu^2\right) = P\left(m_\nu\right) \cdot \left(\frac{\mathrm{d}m_\nu^2}{\mathrm{d}m_\nu}\right)^{-1} = \frac{\text{const.}}{2 \cdot \sqrt{m_\nu^2}}. \tag{6.31}$$

Since no normalisation of the pdf is required for the MCMC, the constant can be chosen as const. $= 1.0$ for $m_\nu^2 \geq 0$ and const. $= 0.0$ for $m_\nu^2 < 0$. The application of this prior is illustrated in blue in figure 6.22. The prior favours squared neutrino masses close to zero. Overall, this leads to more stringently constrained parameter regions compared to the flat positive prior in m_ν^2. Furthermore, the upper limit is more stringent in the case of a true m_ν^2 close to zero.

A comparison of both flat priors for the example of a positive squared neutrino mass of $m_\nu^2 = 0.1\,\mathrm{eV}^2$ is shown in appendix I. In this case, the influence on the contours is only small. The flat prior in m_ν also here gives masses close to zero larger probability and hence increases the lower uncertainty on the neutrino mass squared.

The third example shows a prior based on results from cosmology. The prior is hereby based on the posterior distribution obtained from Planck data [16]. The likelihood is extracted from one of the baseline likelihoods (TT, TE, EE, with lowℓ, and lensing) from the data release of the Planck 2018 dataset. The posterior distribution on $\sum m_\nu$ is extracted using the `MONTEPYTHON` framework [69]. Samples of the resulting Markov chain are further

converted into the m_ν^2 parameter assuming normal ordering.[25] This naturally limits the prior distribution to

$$m_\nu^2 \geq |U_{21}|^2 \Delta m_{21}^2 + [U_{13}]^2 e^{2i\delta_{\mathrm{CP}}} \left(\Delta m_{21} + \Delta m_{23}\right)^2 , \tag{6.32}$$

at $m_{\mathrm{light}} = 0.0\,\mathrm{eV}$. The resulting prior is shown in the top right panel in figure 6.22 (grey). By combining the KATRIN analysis with a cosmology likelihood, the prior becomes the dominant factor in the analysis due to its strong constraints. This leads to an upper limit that is largely determined by the prior assumption. The results from cosmology have to be interpreted with caution due to the inherent model dependence and reliance on the ΛCDM assumption. Currently, cosmological results are much more constraining than results from direct measurements, even tackling the inverted hierarchy scale. As illustrated in section 1.5, these constraints thus strongly depend on the combined data and the choice of free parameters. If direct, kinematics-based experiments find a neutrino mass within the cosmology-excluded range, this would call into question the validity of cosmological models. There are also non-standard cosmological models that would allow for larger neutrino masses in the sensitivity reach of KATRIN. Cosmological bounds can significantly increase when incorporating modifications to the neutrino sector. Some conceivable non-standard processes are, for example, the invisible neutrino decay ($\sum m_i < 0.42\,\mathrm{eV}$ to $1\,\mathrm{eV}$) [8, 95], time-dependent neutrino masses ($\sum m_i < 1.4\,\mathrm{eV}$ to $3\,\mathrm{eV}$) [85, 98, 110, 168], or non-standard neutrino populations ($\sum m_i < 3\,\mathrm{eV}$) [95, 100, 185].

Additional parameters in the analysis could further be constrained by informed priors in a Bayesian analysis. Limiting parameters, such as the transmission broadening or shift and drift broadenings to the positive physical region, would further help to constrain the neutrino mass. Since the neutrino mass is strongly correlated with the effective endpoint, more precise measurements of the Q-value would also further constrain the neutrino mass. The Q-value can, for instance, be extracted from Penning trap experiments[26]. Combined with better knowledge of the absolute energy scale of the KATRIN setup [210, 67], stronger constraints of the Q-value could enter the analysis. The current uncertainty on the Q-value is $(18\,575.72 \pm 0.07)\,\mathrm{eV}$ [181, 210]. Figure I.12 illustrates the effect of a hypothetical constraint of the endpoint with an uncertainty of $0.001\,\mathrm{eV}$.

Summarising, section 6.4.3 provided an overview of the neutrino-mass analysis procedure. Ten significant systematic effects were identified, along with their impact on the squared neutrino mass. The main results of the individual campaigns and the combined KNM1-5 analysis were presented, which yielded a result of $m_\nu^2 = -0.050^{+0.107}_{-0.121}\,\mathrm{eV}^2$. Additional studies were performed to check the robustness of the result by studying the dependencies of m_ν^2 on different parameters, including radial and azimuthal dependencies, scan-order dependencies, and analysis-range dependencies. No indication of significant dependencies was found. The conversion of the neutrino-mass result into an upper bound yields a limit of $m_\nu < 0.43\,\mathrm{eV}$ (90 % C.L.) using the Lokhov-Tkachov construction. This is the current best limit on the neutrino mass from a model-independent approach. The final subsection presented a perspective on how the incorporation of priors could affect future analyses

[25] The conversion applies the mixing matrix elements of the normal ordering as listed in table 1.1. A CP violating phase of $\delta_{\mathrm{CP}} = 0.0$ is assumed in this example.

[26] High precision measurements of the Q-value with Penning trap measurements compare the atomic mass difference of ^{3}He and T [181].

6.4. Sterile neutrino analysis

The spectra measured with the KATRIN experiment are not only used to search for the effective neutrino mass of the light active neutrinos [22, 25], but can also in parallel be used to search for physics beyond the Standard Model.[27] As presented in section 1.3, the νMSM framework introduces additional heavy sterile neutrinos. In the most simple case, this leads to the $(3\nu + 1)$ extension. In the standard neutrino-mass analysis spectral data is fit in a 40 eV range below the endpoint. Using the same data, further analysis of the spectrum also allows us to search for sterile neutrino masses in the eV mass range, with m_4^2 up to 1600 eV^2 [26, 24]. The search for eV-scale sterile neutrinos is well motivated by long-standing observations of anomalies encountered in neutrino oscillation experiments, such as the reactor antineutrino anomaly (RAA) [177], the gallium anomaly (GA) [122, 3, 53], and tentative observations of a sterile neutrino signal by the Neutrino-4 experiment [228, 229] (for more details see section 1.6).

The differential spectrum of the $(3\nu + 1)$ model consists of two branches, as described in section 3.1. One of the branches is characterised by the effective squared mass m_ν^2 and the amplitude of the active branch $(1 - |U_{e4}|^2)$, whereas the second component is calculated with the squared sterile neutrino mass m_4^2 and the sterile-mixing amplitude $|U_{e4}|^2$. The imprint of a sterile neutrino is manifested as a kink-like distortion of the spectrum, with the position of the kink at m_4^2 (see figure 3.2).

The following sections will summarise the analysis results of the eV-scale sterile neutrino analysis for the KNM1 and KNM2 data. The fitting procedure is recapped in section 6.4.1. Results and exclusion contours are presented in section 6.4.3, while also illustrating the effects and the interplay with the active neutrino. The results are put into the context of other experiments and the observed anomalies in section 6.4.3.3.

6.4.1. Analysis procedure

In contrast to the neutrino-mass analysis presented in the previous section, the sterile neutrino analysis is carried out in a 2-dimensional parameter space $(m_4^2, |U_{e4}|^2)$. The analysis is performed as a grid scan. The grid is typically chosen as 50×50 grid with an equidistant logarithmic spacing in both parameters. The parameter grid in the log-log parameter space is illustrated by the grey points in figure 6.23. The mass range of the grid is limited by the range of the analysis energy interval $(E_0 - m_4 < qU_{max})$.

A fit is carried out for every combination of m_4^2 and $|U_{e4}|^2$, which involves minimizing the χ^2 for the nuisance parameters E_0, Sig, and Bg.[28] From the resulting grid of χ^2 values (illustrated by the colour scale in figure 6.23), the exclusion (marked as a white contour in figure 6.23) contour is drawn based on the $\Delta\chi^2$, relative to the minimum $\Delta\chi^2 = \chi^2 - \chi^2_{min}$. Similarly to the uncertainty estimation in the neutrino-mass analysis (see section 4.3.1), exclusion contours within the sterile parameters space follow Wilks' theorem for two degrees of freedom [256]. The critical $\Delta\chi^2$ for two degrees of freedom is $\Delta\chi^2 = 5.991$ at 95 % C.L.. Since sterile neutrino contours are commonly given at a 95 % C.L. in the literature, the sensitivities and exclusion contours shown here follows this convention. The application

[27] Additional physics searches in KATRIN range from searches for sterile neutrinos [26, 32, 24], over the imprint from right-handed currents [234, 66], or even a completely generalisation of neutrino interactions [63], to searches for relic neutrinos [27] and Lorentz-invariance violation [30].

[28] In particular cases, also the active neutriono mass m_ν^2 is kept as a free parameter in the fits.

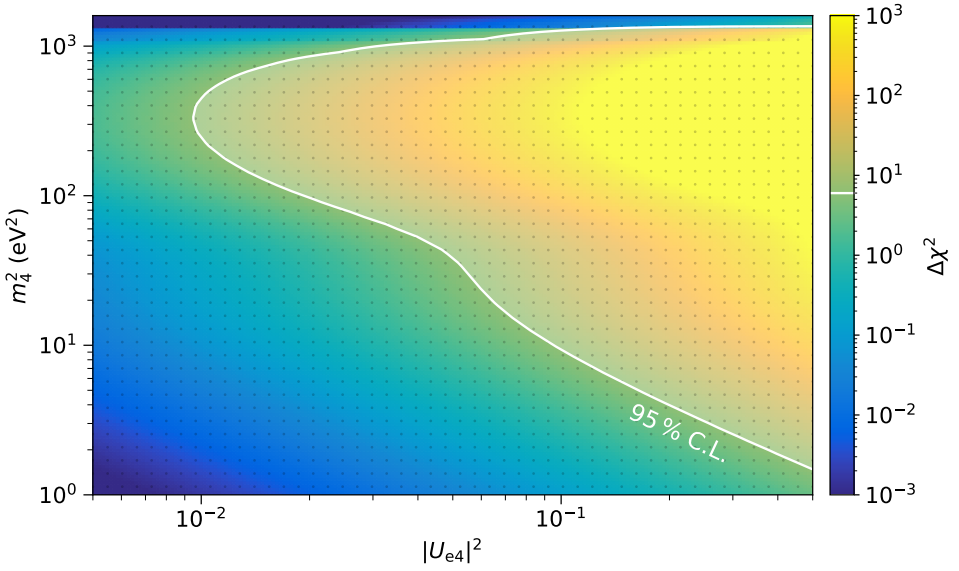

Figure 6.23.: Illustration of the grid scans performed in sterile neutrino analyses. In this case, fits are performed on a logarithmically spaced 50×50 grid within the (m_4^2, $|U_{e4}|^2$) parameter space (light grey points). From the resulting χ^2 values, the sensitivity or exclusion contour is drawn (solid white line), excluding the paramameterspace shaded in white. The sensitivity is based on a KNM2-like simulated spectrum.

of Wilks' theorem is justified for the sterile neutrino analysis in the case of KATRIN has been shown in [219].

The KNM2 based example figure 6.23 further shows some characteristic features that are expected for the sensitivity on m_4^2 and $|U_{e4}|^2$. For very small sterile masses ($m_4^2 \to 0.0\,\mathrm{eV}^2$) and large sterile masses ($m_4^2 > 1600\,\mathrm{eV}^2$), the spectrum is not sensitive to the distortion by the fourth neutrino mass state. For $m_4^2 \to 0\,\mathrm{eV}^2$, the sterile imprint is very close to the endpoint and can effectively not be resolved in the measured data, similarly to a very small active neutrino mass. For large sterile masses, the kink-like feature is too close or even outside the range of the measured spectrum and hence is not constrained by any of the data points. The active-to-sterile mixing enhances the spectral distortion for larger $|U_{e4}|^2$. Hence, the sensitivity for $|U_{e4}|^2 \to 0.0$ reduces. Within the excluded region (for large $|U_{e4}|^2$), the χ^2 steeply increases due to the more pronounced spectral imprint.

The sterile neutrino analysis follows the same blinding procedure as applied in the neutrino-mass analysis (see section 6.3.2). Analysis techniques and procedures are first tested on simulated spectra by individual teams. After agreement between the teams and after freezing all cuts and analysis procedures, the data is analysed using the same framework. This ensures an unbiased analysis and calculation of exclusion limits. A summary of the run and period summary versions for the sterile neutrino analysis are listed appendix E.2.

6.4.2. Impact of systematic uncertainties

Since the sterile neutrino analysis requires a large number of fits (2500 fits per grid scan), the covariance matrix approach is ideal for this type of analysis (see section 4.2.1). As mentioned

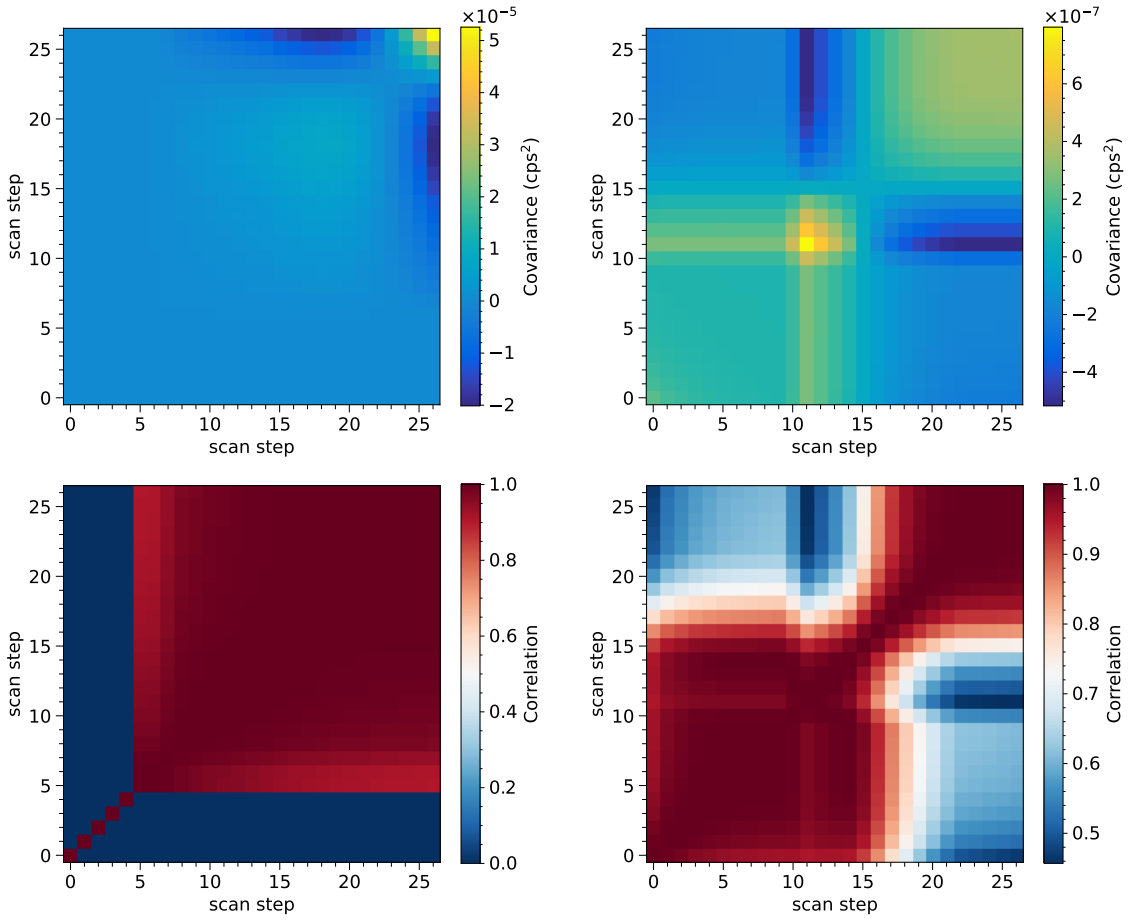

Figure 6.24.: KNM1 normalised covariance matrices (top) and correlation matrices (bottom). The panels on the left represent the covariances and correlation when fluctuating systematic parameters that influence the spectrum. The panels on the right represent the covariances and correlation when fluctuating systematic parameters connected to the background model. Scan steps with indices between 0 and 4 refer to the scan steps in the background region, while scan steps with indices ≥ 5 are scan steps measuring the β-spectrum.

in section 4.2.1, covariance matrices can only be applied under the assumption of a Gaussian pdf. The impact of systematics is precalculated once, a priori. The matrices are then included in the χ^2-minimisation at each grid point. For each fit, only the signal, endpoint, background and in some cases the active neutrino mass squared (see section 6.4.3.2) are fit.

Systematic inputs are based on previous estimations, as documented in [22, 23, 25]. The covariance matrices are calculated based on 10^4 tritium spectra. When calculating the simulated spectra, model parameters representing systematic effects are fluctuated and sampled according to their central values and uncertainties. Independent systematic parameters, such as parameters only affecting the β-spectrum or parameters only affecting the background component, are sampled separately. The combined systematic covariance is then calculated by combining the individual covariance matrices:

$$C_{\text{syst}} = C_{\text{syst, spec}} + C_{\text{syst, bg}}. \tag{6.33}$$

The covariance matrix summarising all systematic effects is then added to the statistical

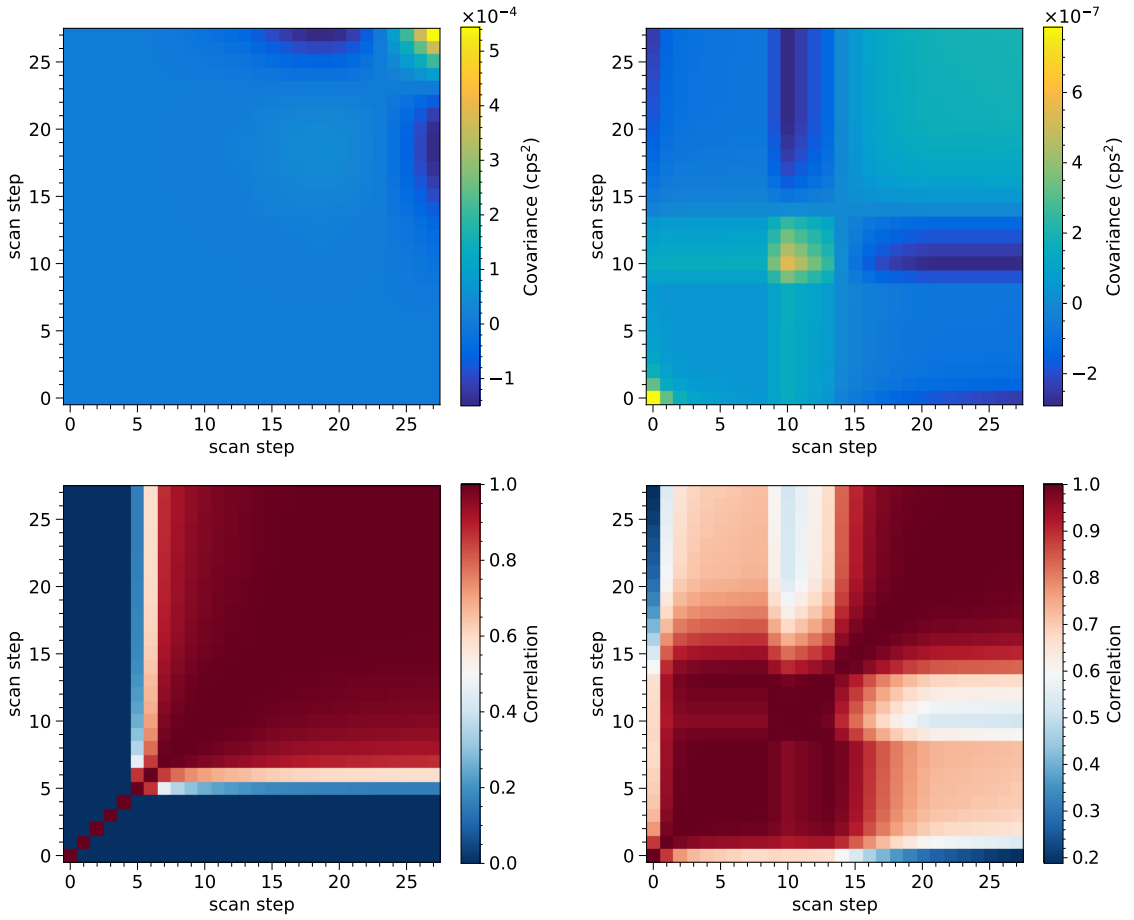

Figure 6.25.: KNM2 normalised covariance matrices (top) and correlation matrices (bottom). The panels on the left represent the covariances and correlation when fluctuating systematic parameters that influence the spectrum. The panels on the right represent the covariances and correlation when fluctuating systematic parameters connected to the background model. Scan steps with indices between 0 and 4 refer to the scan steps in the background region, while scan steps with indices ≥ 5 are scan steps measuring the β-spectrum.

uncertainties, following equation (4.14). The normalised covariance matrices for KNM1 and KNM2, respectively, are shown in the top panels of figures 6.24 and 6.25. The covariance matrices shown are given in units of cps^2 (according to equation (4.12)). When applying the covariance matrices in the χ^2 minimisation, each entry is scaled by the measurement time of the corresponding scan step t_i (see equation (4.13))[29]. In addition to the covariance matrices, figures 6.24 and 6.25 (bottom panels) also include the correlations between the scan steps for the two campaigns.

In both figures, the covariance and correlation matrix in the left panels summarise all systematics connected to the β-spectrum, whereas the matrices in the right panels summarise the systematics connected to the background. The systematic uncertainties on the signal in sum have the largest absolute impact on scan steps deeper in the spectrum. From the correlation, one can also see that the background region (scan steps 0 to 5) is uncorrelated to the other scan steps. When varying spectrum-relevant parameters, the background

[29]The covariance matrix then has the unit of square counts.

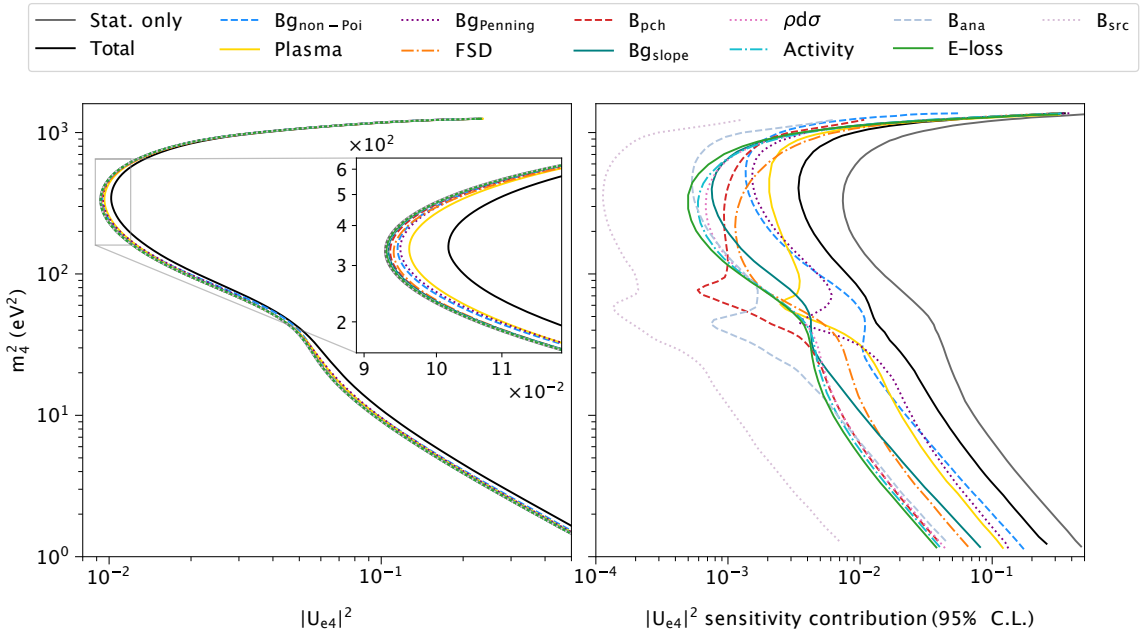

Figure 6.26.: Left: KNM2 systematic breakdown on the $(m_4^2, |U_{e4}|^2)$ parameter space. The 95 % C.L. sensitivity is based on the $\Delta\chi^2_{\text{crit}} = 5.991$ (for 2 dof). Systematic uncertainties are applied individually (coloured lines) as well as via a combined total covariance matrix (solid black). The statistics-only sensitivity in comparison is shown in grey. **Right:** Estimation of the systematics-only contribution on the sensitivity. The systematic contribution is extracted from a raster scan. The 95 % C.L. systematics contribution is based on the $\Delta\chi^2_{\text{crit}} = 3.841$ (for 1 dof). The systematics-only contributions are shown in comparison to the statistics-only sensitivity on $|U_{e4}|^2$ (solid grey). Both plots show that the KNM2 dataset is dominated by statistical uncertainties.

region remains unchanged, hence these scan steps are not correlation. In comparison to this, the underlying background in KATRIN is present in all scan steps above and below the endpoint. Therefore the background systematics are correlated between all scan steps. The systematic contributions of scan steps closely neighbouring show a stronger correlation than scan steps further apart. The largest absolute impact in the normalised covariance matrix is at scan step number 10/11 (and scan step number 0 in KNM1), which is due to the time-dependent background component, indirectly reflecting the MTD. For KNM2, the impact of individual systematics is shown in figure 6.26. To investigate the impact of systematic effects individually, covariance matrices are generated for each systematic separately and then applied in the fit. In figure 6.26, two methods are shown to quantify the systematic impact. The left panel shows the absolute impact on the 95 % C.L. sensitivity. The right panel shows the isolated systematic impact. To get the isolated impact, a raster scan is performed. For different fixed m_4^2, the sensitivity on $|U_{e4}|^2$ is calculated at 95 % C.L..[30] Similarly to the systematic breakdown in section 6.3.3.2, the error contribution is

[30] For the raster scan, $\Delta\chi^2_{\text{crit}}$ is based on 1 dof. Hence the $\Delta\chi^2_{\text{crit}} = 3.841$ (95 % C.L.).

Table 6.10.: Summary of the best fit results of the sterile neutrino analysis, as well as the goodness of fit. Furthermore, the best fit χ^2 is compared to the χ^2 of the null hypothesis. For the combined analysis, the goodness-of-fit quantities $\bar{\chi}^2$ as well as $\hat{p}_{\mathrm{PG}}$ are given according to [174].

Campaign	m_4^2	$\lvert U_{e4}\rvert^2$	χ^2_{best}	dof	p	$\chi^2_{\mathrm{null}} - \chi^2_{\mathrm{best}}$	$\bar{\chi}^2$	$\hat{p}_{\mathrm{PG}}$
KNM1	$77.5\,\mathrm{eV}^2$	0.031	21.40	22	0.50	1.43	–	–
KNM2	$0.27\,\mathrm{eV}^2$	1.0	27.48	23	0.24	0.74	–	–
KNM1-2	$59.9\,\mathrm{eV}^2$	0.011	50.39	47	0.34	0.68	1.52	0.47

calculated by subtraction of the statistical sensitivity (solid grey line) in quadrature

$$\sigma_{\mathrm{syst}}(|U_{e4}|^2) = \sqrt{\left(\sigma_{\mathrm{syst}}(|U_{e4}|^2)\right)^2 - \left(\sigma_{\mathrm{stat}}(|U_{e4}|^2)\right)^2}. \tag{6.34}$$

Both plots illustrate that the sensitivity is statistics dominated. Systematic effects with the largest impact are the non-Poisson background, uncertainties on the source potential, and the time-dependent background component. Note that the impact is dependent on the mass range. Peak-like structures in the raster scan are indirectly related to the shape of the MTD, resulting in an increased sensitivity for $40\,\mathrm{eV}^2 \lesssim m_4^2 \lesssim 100\,\mathrm{eV}^2$. Here, the spread of contours, including systematic uncertainties, is reduced, resulting in smaller systematic contributions in this region when subtracting in quadrature.

6.4.3. Analysis results

The following sections summarise the sterile neutrino analysis results of the KNM1 and KNM2 datasets. The sterile neutrino analyses are divided into scans where the active neutrino mass is kept fixed to 0.0 eV (section 6.4.3.1) and an extended analysis, where the active neutrino mass is added as a free fit parameter (section 6.4.3.2). No light sterile neutrino was found, hence the analysis provides information about excluded parameter regions. Finally, the obtained exclusion contours are compared to and interpreded in the light of the results of other experiments (section 6.4.3.3).

6.4.3.1. Exclusion contours

In the main sterile neutrino analysis, the active neutrino mass is kept fixed at zero. This is justified by the hierarchical scenario $m_{1,2,3} \ll m_4$. The assumption of zero is further supported by the lower bound on m_ν of 0.009 eV derived from neutrino oscillation [188]. Furthermore, since systematic uncertainties are propagated with covariance matrices, only the signal, endpoint, and background are minimised for each grid point.

The resulting 95 % C.L. exclusion contours are shown in figure 6.27. A summary of the best-fit values, as well as the χ^2 of the null hypothesis, is shown in table 6.10.

Focussing on the statistically less dominant KNM1 data set, the KNM1 data excludes a smaller region (outlined by the dotted green line in figure 6.27). From the KNM1 data, the active-to-sterile mixing is constrained down to 0.017 at a sterile neutrino mass of

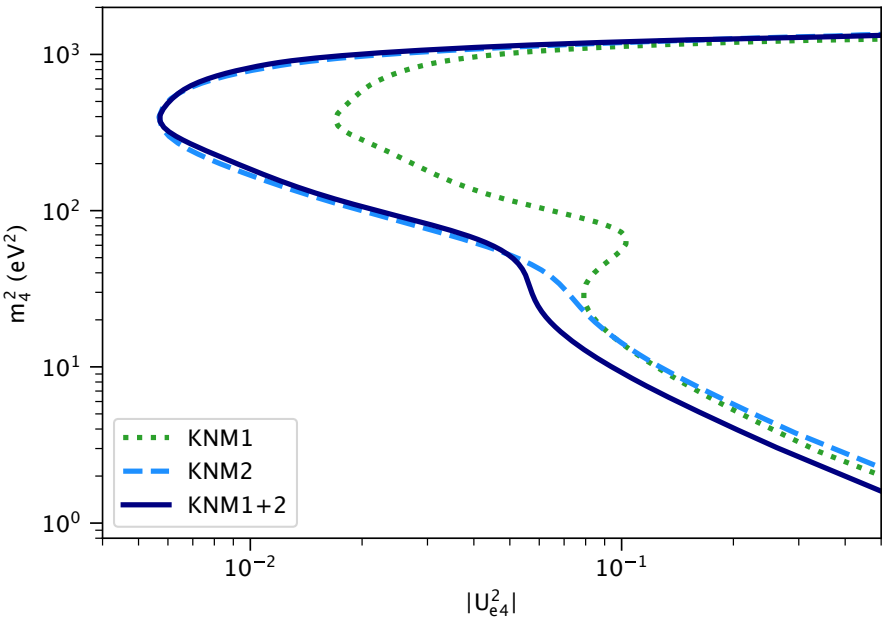

Figure 6.27.: Sterile exclusion contours (95 % C.L.) for KNM1 (dotted green), KNM2 (dashed blue), and both datasets combined (solid dark blue). Regions to the right of the contours are excluded. The analysis includes systematic uncertainties.

$m_4^2 = 381.9\,\mathrm{eV}^2$. The contour further shows an indentation at $m_4^2 \approx 70\,\mathrm{eV}^2$. This is explained by the location of the best fit, which for KNM1 falls to $m_4^2 = 77.5\,\mathrm{eV}^2$ with a sterile mixing of $|U_{e4}|^2 = 0.031$. The best-fit differs from the null hypothesis with $\chi^2_{\mathrm{null}} - \chi^2_{\mathrm{best}} = 1.4$.

KNM2 has approximately twice the statistics compared to KNM1, therefore a larger region of the $(m_4^2, |U_{e4}|^2)$ parameter space is excluded by the KNM2 data (outlined by the dashed blue line in figure 6.27). From the data, $|U_{e4}|^2$ is excluded down to 0.006 at $m_4^2 = 391.7\,\mathrm{eV}^2$. In the case of the KNM2 analysis, the global best fit is found at $m_4^2 = 0.27\,\mathrm{eV}^2$ with a mixing of $|U_{e4}|^2 = 1.0$. This is in agreement with the best fit of the neutrino-mass analysis, published in [25]. Hence, the best fit can be interpreted as the imprint of the active neutrino branch with a free m_ν^2. The best fit also agrees well with the null hypothesis, with only a difference of $\chi^2_{\mathrm{null}} - \chi^2_{\mathrm{best}} = 0.7$.

Lastly, the χ^2-values of the KNM1 grid scan and the KNM2 grid scan can be combined to calculate the joint exclusion limit from both datasets[31]

$$\chi^2_{\mathrm{comb.}}(m_4^2, |U_{e4}|^2) = \sum_{i\in[1,2]} \chi^2_{\mathrm{N},i}\left(m_\nu^2 = 0\,\mathrm{eV}^2, m_4^2, |U_{e4}|^2, E_{0i}, \mathrm{Sig}_i, \mathrm{Bg}_i\right). \tag{6.35}$$

The combined KNM1 and KNM2 contour is shown by the dark blue line in figure 6.27. The combined contour further improves on the one from KNM2 below $\sim 70\,\mathrm{eV}^2$. Similarly to the KNM2-only contour, a minimal axtive-to-sterile mixing of 0.006 is excluded at $m_4^2 = 389.3\,\mathrm{eV}^2$. The best fit is located at $m_4^2 = 59.9\,\mathrm{eV}^2$ with $|U_{e4}|^2 = 0.011$. The χ^2

[31] The combination of the individual grid scans in this way is only possible because m_ν^2 is fixed to zero (there are no common parameters) and systematics are treated via covariance matrices.

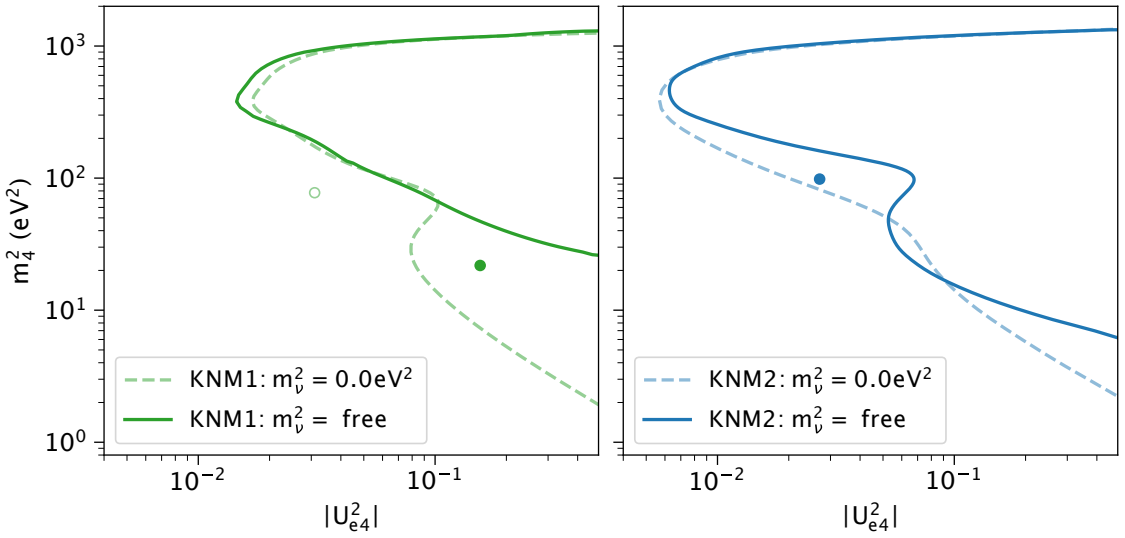

Figure 6.28.: Influence of a free active neutrino on the sterile neutrino exclusion bound. Analyses for KNM1 (left panel) and KNM2 (right panel) are presented. In both cases, the exclusion contour with a fixed neutrino mass is indicated by the dashed line, whereas the exclusion contour with a free active neutrino mass is outlined by the solid line. In addition, the best-fit locations are indicated by the solid markers for the free neutrino mass case and open markers for the fixed $m_\nu^2 = 0.0\,\mathrm{eV}$ case. The best fit of KNM2 ($m_\nu^2 = 0.0\,\mathrm{eV}$) is outside the plot range, at $m_4^2 = 0.27\,\mathrm{eV}^2$.

of the null hypothesis only varies by $\chi^2_{\mathrm{null}} - \chi^2_{\mathrm{best}} = 0.7$ from the best fit. In conclusion, no significant sterile neutrino signal was found in the data of the first two measurement campaigns.

6.4.3.2. Interplay with the active neutrinos

As an extension to the analysis presented in the previous section, one can further add the active neutrino mass as a free fit parameter in the grid scan. Apart from this change, the analysis is identical. The exclusion contours for KNM1 and KNM2 of the free-mass case is shown in figure 6.28. By adding another free fit parameter, the model is able to compensate for the sterile neutrino imprint by varying the active neutrino mass. This results in a loss of sensitivity in the $(m_4^2, |U_{e4}|^2)$ parameter space. The exclusion contours are particularly shifted at small m_4^2, as this is the region, the active neutrino compensates most of the sterile shape distortion. For larger masses ($m_4^2 \gtrsim 400\,\mathrm{eV}^2$), further away from the endpoint, the sensitivity is less affected.

The introduction of the active neutrino also results in a shift of the best-fit location. In the case of KNM1, the best-fit shifts towards larger mixing amplitudes and smaller sterile neutrino masses: $m_4^2 = 21.84\,\mathrm{eV}^2$ and $|U_{e4}|^2 = 0.155$. The active neutrino mass at this location is fit to a rather large negative value of $m_\nu^2 = -5.34\,\mathrm{eV}^2$. The χ^2 improves by 1.5 compared to the best fit of the $m_\nu^2 = 0.0\,\mathrm{eV}^2$ case. Comparing the best fit to the null hypothesis gives $\chi^2_{\mathrm{null}} - \chi^2_{\mathrm{best}} = 1.3$.

For KNM2 on the other hand, the best fit is located at $m_4^2 = 98.34\,\mathrm{eV}^2$ and $|U_{e4}|^2 = 0.027$. In this case, the χ^2 improves by 2.5 compared to the best fit of the $m_\nu^2 = 0.0\,\mathrm{eV}^2$ case. The

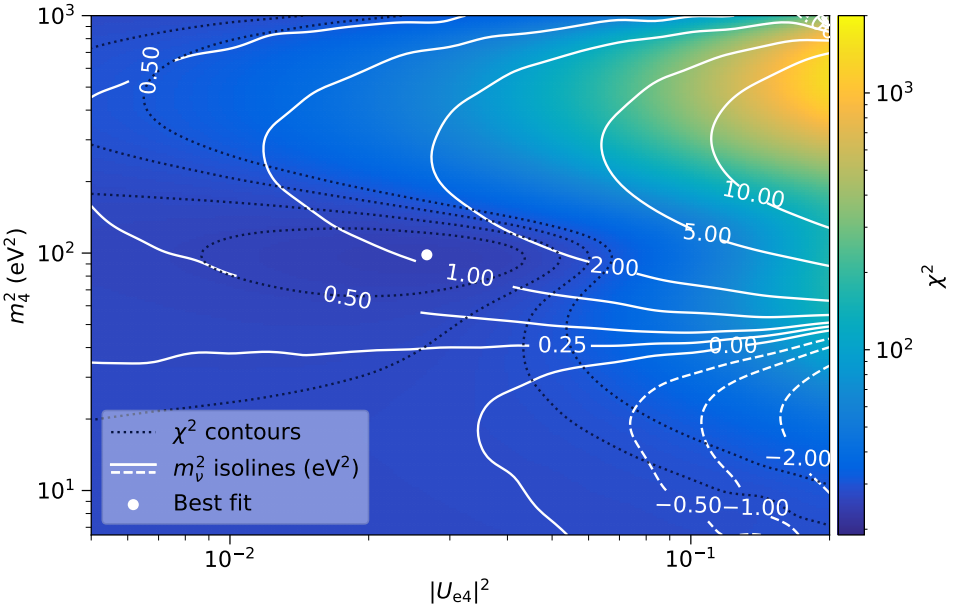

Figure 6.29.: Interplay between sterile neutrino parameters and the active neutrino mass in KNM2. In the background the colour-coded χ^2 map is shown. For orientation, the $0.5\,\sigma$, $1\,\sigma$, $1.5\,\sigma$, and $2\,\sigma$ exclusion contours are outlined by dotted dark blue lines. The white lines indicate the m_ν^2 isolines over m_4^2 and $|U_{e4}|^2$. A small region around the best fit is shown (white marker) for better visibility.

best fit further has a difference of $\chi^2_{\text{null}} - \chi^2_{\text{best}} = 2.5$ to the null hypothesis of the m_ν^2 = free case. This corresponds to a 71 % significance for 2 dof.

To further investigate the interplay between the sterile neutrino and active neutrino mass, the m_ν^2 isolines are illustrated in figure 6.29. The isolines over m_4^2 and $|U_{e4}|^2$ highlight how the active neutrino mass compensates for the sterile neutrino signature. For small m_4^2 ($\lesssim 40\,\text{eV}^2$), m_ν^2 is also fit with a value close to zero. With larger $|U_{e4}|^2$ ($\gtrsim 0.04$), the sterile imprint is enhanced, which is counteracted by an increasingly more negative neutrino mass. On the other hand, for larger masses ($40\,\text{eV}^2 \gtrsim m_4^2 \lesssim 500\,\text{eV}^2$) the fit active neutrino mass squared generally increases. With even larger m_4^2 ($\gtrsim 500\,\text{eV}^2$), the fit active neutrino mass squared decreases again as the sterile neutrino signature is shifted further out of the analysis window, only influencing the last spectral points. The active neutrino mass is fit to a value close to the fit result of the standard neutrino-mass analysis.

Naturally, the introduction of sterile neutrinos also impacts the neutrino-mass result. The best fit of m_ν^2 found in the KNM2 analysis with the $3+1\nu$ is $m_\nu^2 = (1.05 \pm 0.60)\,\text{eV}^2$ (marked by the white dot in figure 6.29). From the same grid scan, one can also extract the χ^2 profile over m_ν^2. In figure 6.30, the χ^2 profile of the standard 3ν case (red) is compared to the χ^2 profile of the $3+1\nu$ framework (blue). The plot shows the significant change in the central value (from $(0.25 \pm 0.32)\,\text{eV}^2$ to $(1.05 \pm 0.60)\,\text{eV}^2$).[32] Furthermore, the uncertainty on the neutrino mass significantly increases within the $3+1\nu$ case. Here, the mean uncertainty increases from $0.32\,\text{eV}^2$ to $0.60\,\text{eV}^2$. For negative m_ν^2, the χ^2 profile of the $3+1\nu$ case flattens, diminishing the sensitivity in this region. Due to the additional

[32] The same systematic treatment and systematic inputs are applied in the χ^2 calculation of both profiles. The inputs are based on [25].

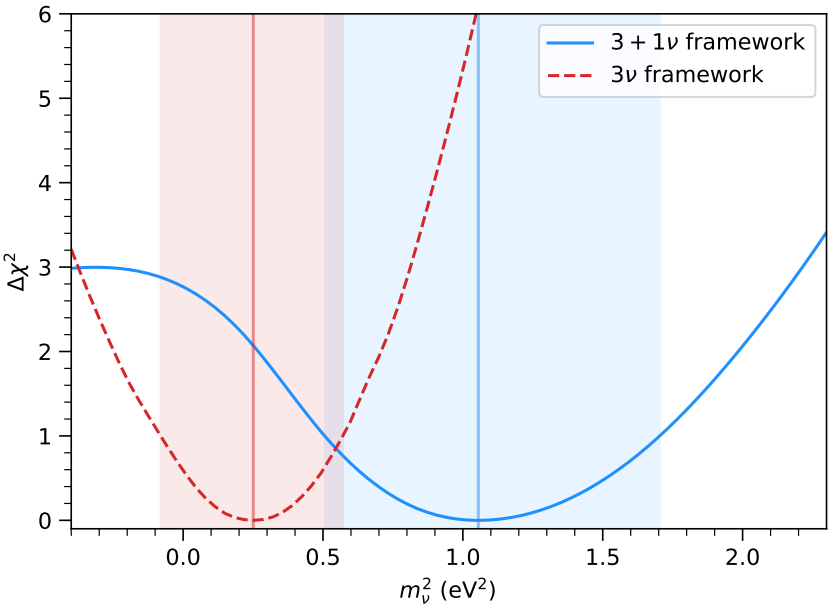

Figure 6.30.: Influence of sterile neutrinos on the neutrino-mass result. The KNM2 χ^2 profile over m_ν^2 is shown for the 3ν case (red) and the $3\nu + 1$ case (blue). Both profiles include the same systematic inputs (as published in [25]). The vertical line marks the best-fit value, the 1σ uncertainty is shaded.

freedom within the model caused by the minimization of the sterile neutrino parameters, the sensitivity to m_ν^2 is reduced.

6.4.3.3. Comparison to oscillation experiments

Converting the observables m_4^2 and $|U_{e4}|^2$ of the β-spectrum to the observables Δm_{41}^2 and $\sin^2 2\theta_{ee}$, which is typically measured in oscillation experiments, the resulting KATRIN exclusion contours can be put into context of other experiments.[33] The conversion follows the approximation described in the last part of section 3.1. The KATRIN results are particularly interesting since they are complementary to short-baseline experiments, and KATRIN is probing relevant regions that are observed by the reactor antineutrino anomaly (RAA) [177], the gallium anomaly (GA) [53], or the Neutrino-4 experiment [229].

Furthermore, short-baseline experiments are susceptible to deviations from Wilks' theorem as statistical fluctuations can emulate high-frequency oscillation, which can be interpreted as a sterile neutrino [19]. In the case of KATRIN however, the imprint of sterile neutrinos affects the shape of the entire spectrum and is hence constrained by all data points. This makes the analysis of the β-spectrum less vulnerable to deviations from Wilks' theorem or a mimicking of a sterile neutrino signature by statistical fluctuations of data points. The validity of Wilks' theorem has been tested for different scenarios in [219]. No significant discrepancy from Wilks' theorem was observed.

The comparison of the KATRIN exclusion contours compared to the contours of other experiments is presented in figure 6.31. The KATRIN contours are displayed in shades of

[33] Comparisons to other β-decay experiments such as the Mainz and Troitsk experiments can be performed without the parameter transformation, but will in the context of this section also be compared in the $(\Delta m_{41}^2, \sin^2 2\theta_{ee})$ parameter space.

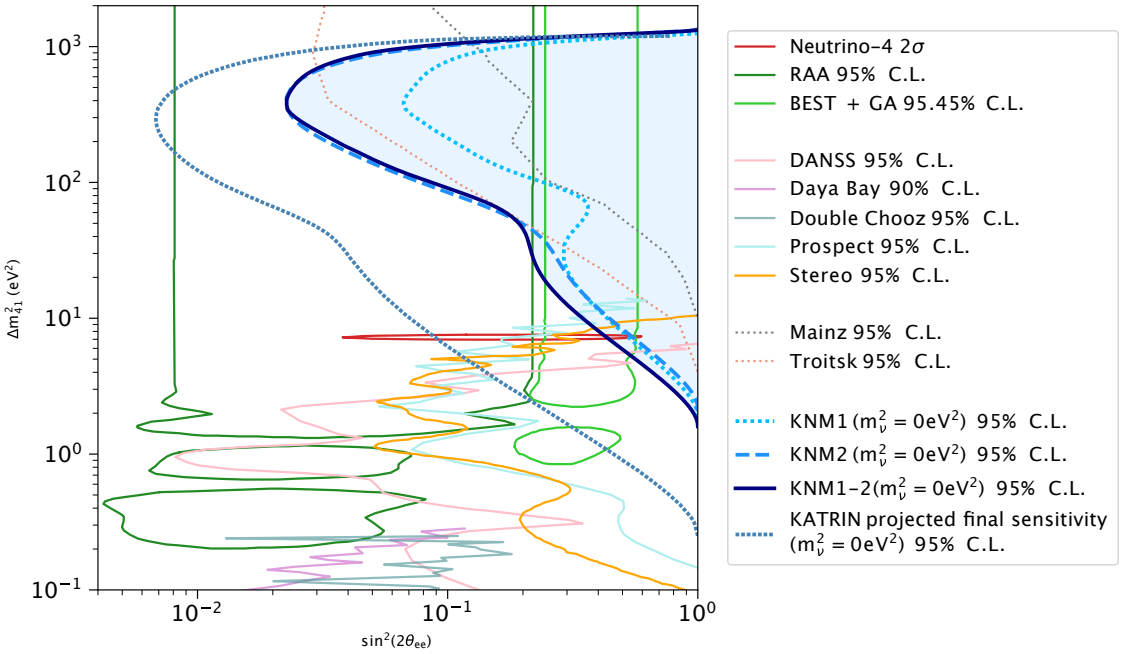

Figure 6.31.: Comparison of the KATRIN results from KNM1 (dotted light blue line), from KNM2 (dashed blue line), and from KNM1-2 combined (solid dark blue outline and shaded) compared to other experiments. The contours are shown over Δm^2_4 and $\sin^2(2\theta_{ee})$. The figure includes the RAA [177] and GA [53] anomalies, as well as the measured signal from Neutrino-4 [229]. Further exclusion contours are shown for different short baseline experiments [9, 12, 35, 38, 80]. Exclusion contours from other tritium β-decay experiments are published by the Mainz [152] and the Troitsk experiments [59]. The projected sensitivity of final KATRIN (as published in [24]) is marked by the (dotted dark blue line). Figure similar to [26].

blue. The KNM1 contour is marked by the dotted light-blue line, the KNM2 by the dashed blue line, and the combined exclusion from the KNM1 and KNM2 data is outlined by the solid blue line and shaded in blue. The combined analysis improves on previous β-decay results by Mainz (dash-dotted pink) and Troitsk (dashed black) for $\Delta m^2_{41} \gtrsim 300\,\mathrm{eV}^2$. The KATRIN results are complementary to short-baseline oscillation experiments (solid lines), excluding additional regions of the (Δm^2_{41}, $\sin^2 2\theta_{ee}$) parameter space for $\Delta m^2_{41} \gtrsim 10\,\mathrm{eV}^2$. The exclusion contour of KNM1-2 disfavours large parts of the Baksan Experiment on Sterile Transitions (BEST) and GA findings for $20\,\mathrm{eV}^2 \lesssim \Delta m^2_{41} \lesssim 1000\,\mathrm{eV}^2$. Furthermore a significant fraction of the RAA is excluded $50\,\mathrm{eV}^2 \lesssim \Delta m^2_{41} \lesssim 1000\,\mathrm{eV}^2$ and $\sin^2 2\theta_{ee} \gtrsim 0.02$. Lastly, the KATRIN results disfavour parts of the Neutrino-4 solution for $\sin^2 2\theta_{ee} \gtrsim 0.4$.

Comparing the extrapolated final sensitivity for KATRIN (based on [24]) shows that constraints will improve further, excluding wider regions of the BEST and GA and RAA. The projected sensitivity is, in addition, able to probe almost the entire range of the Neutrino-4 solution[34].

The analysis of KATRIN data presents an independent approach to exclude parts of the

[34] The Neutrino-4 solution published in 2022 [229] extends to smaller $\sin^2 2\theta_{ee}$ compared to the solution published in 2019 [228]. The 2019 Neutrino-4 solution can fully be probed with the projected final KATRIN sensitivity.

sterile neutrino parameter space complementary to the oscillation experiments. This will, in particular, be of relevance in the future, probing further regions suggested by different anomaly observations.

7. Summary and conclusion

The KATRIN experiment was designed with the aim of determining the effective electron antineutrino mass from measurements of the T_2 β-decay spectrum with a final sensitivity of 0.2 eV (90 % C.L.) [39]. To realise this goal, the experiment started operation with tritium in the middle of 2018. Since April 2019, successive measurement campaigns have improved the statistical precision. As of the submission of this thesis, a total of nine measurement campaigns have been successfully completed. As statistics continue to increase, thus leading to higher precision, an ever more precise characterisation of the experimental conditions and improvements to the operational settings are required.

This thesis follows a set of four main objectives. The first one is to provide a detailed description of the underlying physics model and analysis strategies developed and employed in the KATRIN data analysis. The second objective is to summarise the characterisation of systematic effects and how these are incorporated in the data analysis. The third is to present the results of the neutrino-mass analysis of the first five measurement campaigns. Intermediate neutrino-mass analyses of the first and second campaigns, of which the work presented in this thesis forms an integral part, were published in [22, 23, 25], providing leading neutrino mass limits. The last objective is to present the results of the light sterile neutrino search based on the first and second campaigns. Sterile neutrino analysis was presented in this thesis and contributed to two KATRIN publications. The analysis of the first campaign served as a crosscheck for [24], and the analysis of the second campaign is one of the main analysis results published in [26].

A detailed overview of the model composition was given in chapter 3. In addition to this, the statistical methods and software infrastructure were introduced in chapter 4. The relevant measurement campaigns were summarised in chapter 5. The analyses presented within this thesis were performed with the `KaFit` framework, calculations of the integrated β-spectrum were based on the `SSC` model.

In the following two sections, key results of the neutrino-mass analysis and sterile neutrino analysis will be presented in more detail. Furthermore, an outlook on future perspectives will be outlined for both cases.

7.1. Neurtino-mass analysis

Several approaches are being pursued to determine the absolute mass scale of neutrinos, including determination from cosmological observations, the search for neutrinoless double β-decay, and kinematic measurements of the single β-decay spectrum. From previous laboratory experiments, a long-standing upper bound on the effective neutrino mass at 2 eV

was set by the Mainz and Troitsk groups [46, 121, 151]. With the start of the KATRIN experiment, data is continuously aggregated, resulting in an improving sensitivity on m_ν. From only approximately one month of operation within the first campaign, KATRIN was able to provide its first upper limit of $m_\nu < 1.1\,\mathrm{eV}$ (90 % C.L.) [22]. This was an improvement by approximately a factor of two compared to the previous kinematic bound. With the combination of the KNM1 and KNM2 data sets, the bound was further narrowed to $m_\nu < 0.75\,\mathrm{eV}$ (90 % C.L.) [25]. This was the first sub-eV probe of the effective neutrino mass from a laboratory experiment. Neutrino-mass analyses conducted within the course of the thesis contributed to the previous results of both publications. Furthermore, in this thesis, the combined analysis of the first five campaigns KNM1 to KNM5 was presented. This included the analysis of a total of 1757 scans of the integrated β-spectrum.

The analysis of multiple datasets obtained under different operating conditions requires a combined analysis strategy. A common χ^2 function was constructed for the parameter inference, which was minimised with one common m_ν^2. To guarantee an unbiased neutrino mass result, a prerequisite for the combined analysis was the careful treatment of systematic effects and uncertainties. Hereby systematic uncertainties were included as pull terms. This led to the analysis of 45 stacked β-spectra with 281 fit parameters, where 145 of the parameters were constrained externally, and 136 were free fit parameters, leading to 1123 degrees of freedom.

The combined KNM1-5 fit, including all systematic uncertainties, resulted in a best-fit value of

$$m_\nu^2 = -0.050\,^{+0.107}_{-0.121}\,\mathrm{eV}^2. \tag{7.1}$$

The fit result of this analysis is consistent with zero within $0.5\,\sigma$. Furthermore, the influence of systematic effects was investigated in great detail, showing that the analysis is dominated by the statistical uncertainty. Studies on fit range dependencies, spatial dependencies, and time dependence of the neutrino-mass estimator were conducted. No significant influence on the results was found, underlining the robustness of the analysis.

From the fit result, an upper limit on the effective neutrino mass was constructed using the Lokhov-Tkachov and Feldman-Cousins approaches. As the main result, the limit based on the Lokhov-Tkachov construction is

$$m_\nu^2 < 0.18\,\mathrm{eV}^2 \quad \Rightarrow \quad m_\nu < 0.43\,\mathrm{eV} \quad (90\,\%\ \text{C.L.}). \tag{7.2}$$

Alternatively, from the Feldman-Cousins belt construction, an upper limit of

$$m_\nu^2 < 0.14\,\mathrm{eV}^2 \quad \Rightarrow \quad m_\nu < 0.37\,\mathrm{eV} \quad (90\,\%\ \text{C.L.}) \tag{7.3}$$

was calculated. The Lokhov-Tkachov based result is quoted as the main limit, as it provides a conservative upper bound which does not further tighten with increasingly negative values. This is the current best limit on the neutrino mass from a model-independent approach. To put this result into a broader context, the central values and derived upper limits of previous laboratory experiments are shown in figure 7.1 in comparison to the three results provided by KATRIN up to now. The figure illustrates how the upper bound tightened from the KNM1 dataset to the KNM1-5 analysis presented in this thesis.

With more campaigns, and thus more data points and parameters, the analysis will continue to become more challenging. Going towards a combined analysis of more campaigns in the following years, and the use of different approaches, such as Bayesian analysis, means that computational improvements and optimised analysis strategies will have increasing

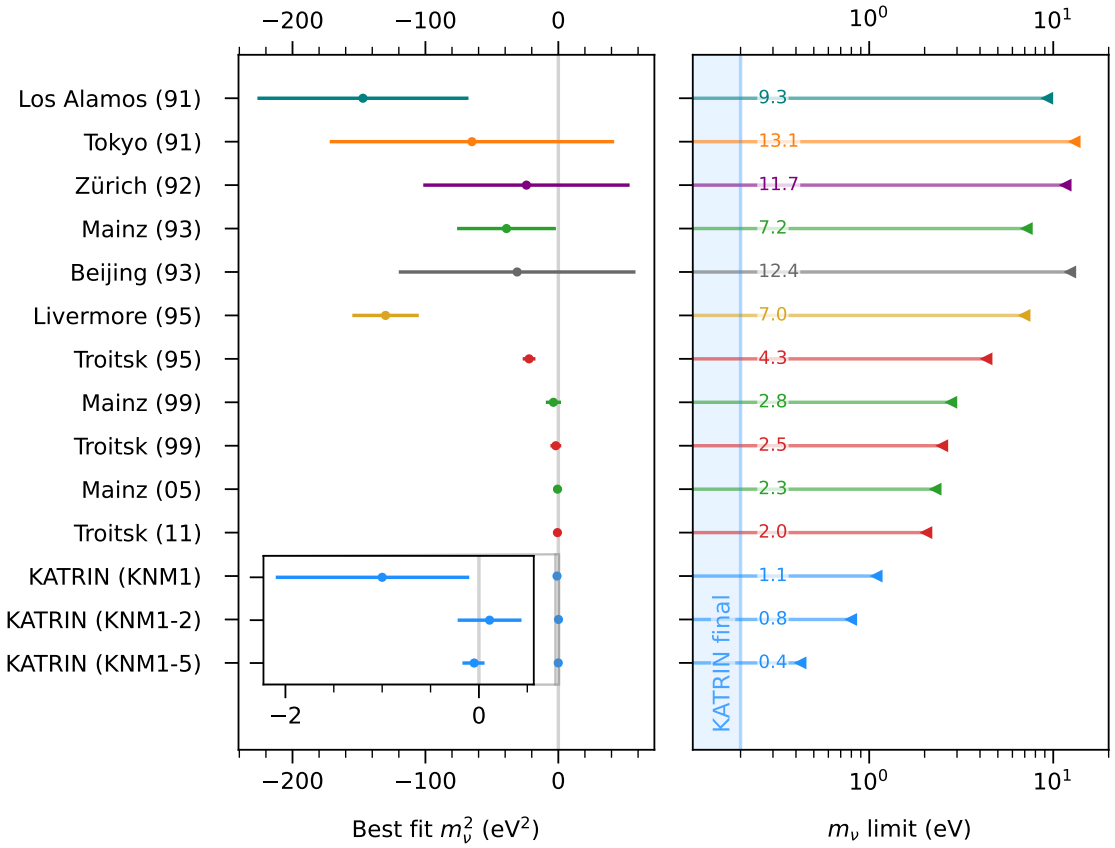

Figure 7.1.: KATRIN neutrino mass results to date in the context of previous experiments. The left panel shows the m_ν central values and uncertainties, including a zoom into the region close to zero. The right panel summarises the corresponding improvement of the upper limits on the neutrino mass, and furthermore shows the final sensitivity goal of KATRIN [39] (blue shaded band). The results are sorted by the respective publication date and are taken from the following references: Published results from Robertson et al. [203], Kawakami et al. [144], Holzschuh et al. [135], Weinheimer et al. [254], Sun et al. [124], Stoeffl et al. [235], Belesev et al. [61], Weinheimer et al. [255], Lobashev et al. [161], Kraus et al. [151], Aseev et al. [46], and Aker et al. [22, 23, 25], as well as the latest KATRIN results from this work (bottom blue markers). Note that the KATRIN limits are given with 90 % C.L., whereas other limits are quoted at 95 % C.L.

relevance. Improved performance can, for example, be achieved by the integration of caching in more parts of the model calculation (see section 4.5.1). Since the neutrino-mass inference is susceptible to approximations within the model, optimisations are extensively tested to avoid potential biases.

The allowed region for the neutrino mass is steadily shrinking, and KATRIN is on track towards the 0.2 eV sensitivity goal. Currently, observational cosmology points to a neutrino mass below the KATRIN design sensitivity. On the other hand, if KATRIN finds a neutrino mass within the cosmology-excluded range, this would call into question the validity of cosmological models [94].

Following the thesis submission, several refinements and corrections were implemented in the neutrino mass analysis for journal publication, as outlined in [33], without altering the thesis's core conclusions. Adjustments included data reclassification of KNM4 to account for endpoint value variations, corrections to column density, an increased uncertainty to the energy loss function, alongside a revision of the background model for the Penning trap induced background to a non-linear description, and a minor correction of the rear wall background. Although these changes were implemented after unblinding, they were motivated as improved inputs to the analysis and not based on the central value of the squared neutrino mass. Post-unblinding modifications resulted in an updated estimation of the squared neutrino mass and a revised upper bound. The revised analysis shifted the best-fit value of the squared neutrino mass from $m_\nu^2 = -0.05\,^{+0.11}_{-0.12}\,\mathrm{eV}^2/\mathrm{c}^4$ to a new best-fit value of $m_\nu^2 = -0.14\,^{+0.13}_{-0.15}\,\mathrm{eV}^2/\mathrm{c}^4$. Consequently, the upper limit on the neutrino mass was adjusted from $m_\nu < 0.43\,\mathrm{eV/c}^2$ (90 % C.L.) to a revised upper limit of $m_\nu < 0.45\,\mathrm{eV/c}^2$ (90 % C.L.). [33]

7.2. Sterile neutrino analysis

The same data sets used for the neutrino-mass analysis can also be used to search for sterile neutrinos in the eV-mass range. In this thesis, the search for sterile neutrinos in the KNM1 and KNM2 datasets was shown. The sterile neutrino analyses were based on grid scans up to a maximum sterile neutrino mass of $m_4 \approx 40\,\mathrm{eV}$. Similar to the neutrino-mass analysis, the sterile neutrino search is currently dominated by statistical uncertainties. In the main sterile neutrino search, the active neutrino mass is fixed at $m_\nu = 0.0\,\mathrm{eV}$. Neither of the two individual campaigns showed a sterile neutrino signal. Likewise, no significant sterile neutrino signal was found in the combined analysis. From the combined analysis a minimal mixing amplitude of $|U_{\mathrm{e}4}|^2 \approx 0.03$ at $m_4^2 \approx 70\,\mathrm{eV}^2$ was excluded at 95 % C.L.. Furthermore, the interplay between sterile and active neutrinos in the integrated β-spectrum was investigated. Allowing the active neutrino to be an additional free fit parameter in the sterile neutrino analysis resulted in a reduced sensitivity and thus reduced excluded parameter space. This, in particular, impacted the range of small sterile neutrino masses ($m_4^2 \lesssim 20\,\mathrm{eV}^2$). Conversely, the neutrino mass sensitivity is also affected by the sterile parameters m_4^2 and $|U_{\mathrm{e}4}|^2$. For example, in KNM2, it was shown that the best-fit value of m_ν^2 shifts to larger masses and increases the uncertainty by approximately a factor of two in the $(3\nu + 1)$ active-sterile model.

A comparison of the KATRIN exclusion contours to other experiments (see figure 1.4) showed that KATRIN is probing the sterile neutrino parameter space in regions complementary to short-baseline oscillation experiments excluding additional regions for $\Delta m_{41}^2 \gtrsim 10\,\mathrm{eV}^2$. The combined analysis improved on previous β-decay results by Mainz and Troitsk for $\Delta m_{41}^2 \gtrsim 300\,\mathrm{eV}^2$. The contour excluded large parts of the BEST and GA findings for $20\,\mathrm{eV}^2 \lesssim \Delta m_{41}^2 \lesssim 1000\,\mathrm{eV}^2$. Furthermore a significant fraction of the RAA was excluded at $50\,\mathrm{eV}^2 \lesssim \Delta m_{41}^2 \lesssim 1000\,\mathrm{eV}^2$ and $\sin^2 2\theta_{\mathrm{ee}} \gtrsim 0.02$. Lastly, the results disfavoured parts of the Neutrino-4 solution for $\sin^2 2\theta_{\mathrm{ee}} \gtrsim 0.4$.

Adding further measurement campaigns to the sterile neutrino analysis will improve the sensitivity and will also bring new challenges. Since the sterile neutrino analysis requires grid scans with $\mathcal{O}(2500)$ fits within the $(m_4^2, |U_{\mathrm{e}4}|^2)$ parameter space, even moderate improvements in the computation time can beneficially impact the feasibility of the analysis. Optimisations, such as additional caching, are therefore crucial, looking towards the future.

In the future, one of the goals of KATRIN is to conduct sterile neutrino searches in the keV mass range. Extending the light sterile neutrino search, first KATRIN keV-scale sterile neutrino exclusion contours were published in [30] from initial measurements with reduced column density during commissioning operations in 2018. Probing a wider region requires improved knowledge of the underlying spectral shape and consideration of additional systematic effects. Furthermore, the new TRISTAN detector system [241] as an upgrade of the focal-plane detector currently in use will enable a highly sensitive search for sterile neutrinos in the keV-mass range with the KATRIN experiment. The detector system is expected to be able to reach a statistical sensitivity on the order of $|U_{e4}|^2 = 10^{-8}$ [241]. Including systematic uncertainties, the target sensitivity is expected to be $|U_{e4}|^2 = 10^{-6}$ [241].

In conclusion, the results of this thesis showed the important role of KATRIN in the determination of the neutrino mass. The combined analysis presented in this work provides a substantially tightened direct neutrino-mass bound compared to KATRIN's early results. This underlines the prospects of ongoing data-taking with increasing statistical power. KATRIN also has the precision, stability, and versatility to provide competitive results in a number of physics cases beyond the standard neutrino-mass analysis.

Appendix

A. Operational settings for neutrino-mass measurements

In appendix A.1, the inner electrode settings in the main spectrometer are summarised. In appendix A.1, the LFCS and EMCS settings are given. The inner electrode voltages and air coil currents are listed for the NAP and the SAP settings.

A.1. Inner electrode settings

Table A.1.: Voltage setpoints of the inner electrodes during neutrino-mass measurements. The coil voltages are given for NAP and SAP settings. The table is subdivided into steep cones, flat cones, and the central part.

	Ring	$U_{\mathbf{NAP}}$ **(V)**	$U_{\mathbf{SAP}}$ **(V)**
Steep cone	2	−160.0	−80.0
	3	−160.0	−80.0
Flat cone	4	−200.0	−180.0
	5	−200.0	−180.0
	6	−200.0	−180.0
Central part	7	−200.0	−195.0
	8	−200.0	−195.0
	9	−200.0	−195.0
	10	−200.0	−195.0
	11	−200.0	−195.0
Flat cone	12	−200.0	−203.0
	13	−200.0	−205.0
	14	−200.0	−203.0
Steep cone	15	−160.0	−80.0
	16	−160.0	−80.0

A.2. LFCS and EMCS settings

Table A.2.: Current setpoints of LFCS coils during neutrino-mass measurements. The coil currents are given for NAP and SAP settings.

LFCS coil	$I_{\mathbf{NAP}}$ **(A)**	$I_{\mathbf{SAP}}$ **(A)**
1	50.0	120
2	0.0	−4.0
3	44.6	116.0
4	45.4	70.0
5	24.6	70.0
6	37.0	70.0
7	14.7	70.0
8	52.8	110.0
9	34.9	110.0
10	38.7	110.0
11	9.2	−60.0
12	35.9	−28.0
13	92.7	58.0
14	13.2	5.0
15	0.0	120.0
16	0.0	120.0
17	0.0	−120.0
18	0.0	−119.0
19	0.0	−120.0
20	0.0	−120.0

Table A.3.: Current setpoints of EMCS coils during neutrino-mass measurements. The coil currents are given for NAP and SAP settings.

EMCS coil	$I_{\mathbf{NAP}}$ **(A)**	$I_{\mathbf{SAP}}$ **(A)**
EMCS-horizontal	0.0	0.0
EMCS-vertical	45.0	45.0

B. Statistics and analysis

The following appendices illustrate the differences and impact when assuming a Gaussian or a Poisson approximation for the measured statistics (appendix B.1). Furthermore, information is given about the numerical stability and reproducibility that is achieved with the analysis code (appendix B.2).

B.1. Gauss vs. Poisson

As described in section section 4.1, with sufficient statistics, the Poissonian pdf can be approximated by a Gaussian distribution with mean $\mu = N$ and width $\sigma = \sqrt{N}$. In figure B.1, the difference between the distributions is shown for the cases where $N = [10, 50, 100, 150]$.

If data is combined to a uniform detector, the scan step with the least amount of statistics is on the order of $N \sim 3 \times 10^4$ counts, justifying the usage of the normal distribution.

In the data is partitioned into detector patches, the scan step with the smallest number of counts is $N \sim 300$ counts for a single detector patch. In this case, the Gaussian approximation is insufficient and leads to a systematic neutrino mass bias on the order of $0.01\,\mathrm{eV}^2$.

The comparison of fits assuming Gaussian and Poisson pdf is depicted in figure B.2. The study is based on 500 statistically fluctuated Monte Carlo spectra. The spectra are fit

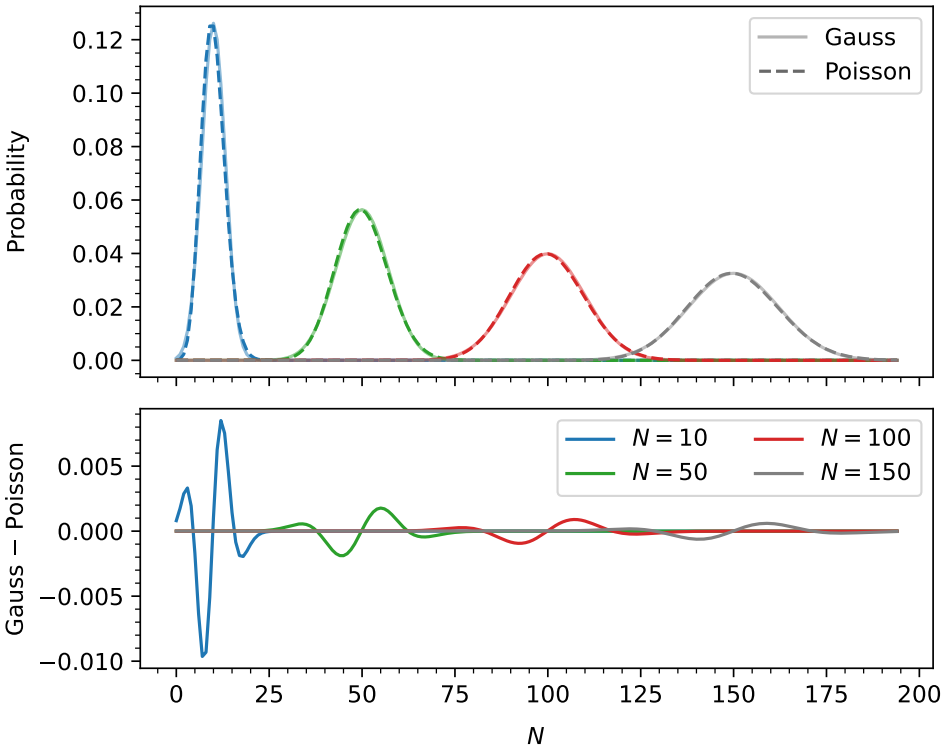

Figure B.1.: (**Top**) Direct comparison of Gaussian distributions (solid) and Poisson distributions (dashed). (**Bottom**) Difference between Gaussian and Poisson distributions.

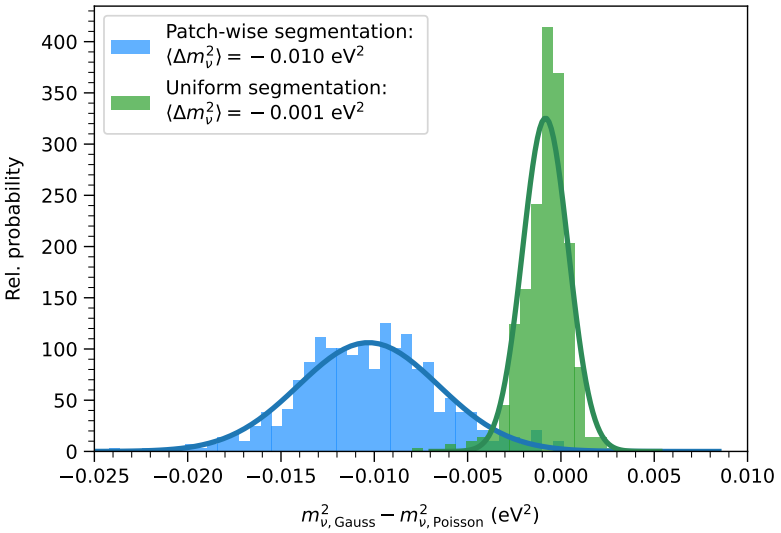

Figure B.2.: Neutrino mass bias due to Gaussian pdf approximation. The Monte Carlo study includes 500 statistically fluctuated datasets based on KNM5 that are fit with Gaussian and Poisson pdf with uniform (green) and patch-wise (blue) data segmentation. The bias is extracted by subtracting the fit results assuming a Poisson pdf from the results assuming a Gauss pdf. The broadening of the distribution is partially caused by numerical stability and convergence precision $\mathcal{O}(10^{-3}\,\mathrm{eV}^2)$ (for more details, see appendix B.2).

as a uniform dataset (green) and with patch-wise detector segmentation (blue). When subtracting the result of the fits using Poisson pdf, one can extract the expected neutrino mass bias due to pdf approximation. In the case of uniform data combination, the bias is on the order of $10^{-3}\,\mathrm{eV}^2$. When splitting the data and consequently reducing the statistics of individual spectra, the bias increases to $10^{-2}\,\mathrm{eV}^2$.

B.2. Numerical stability and reproducibility

To determine the numerical stability and reproducibility of fit results, fits have been performed on a statistically fluctuated Monte Carlo spectrum while varying the initial start parameter. The study is depicted in figure B.3. The initial m_ν^2 has been varied 500 times in the range of $[-0.5\,\mathrm{eV}^2, 0.5\,\mathrm{eV}^2]$. The fit m_ν^2 values show a reproducibility with a standard deviation of $9 \times 10^{-5}\,\mathrm{eV}^2$ and a maximum deviation of $6 \times 10^{-4}\,\mathrm{eV}^2$.

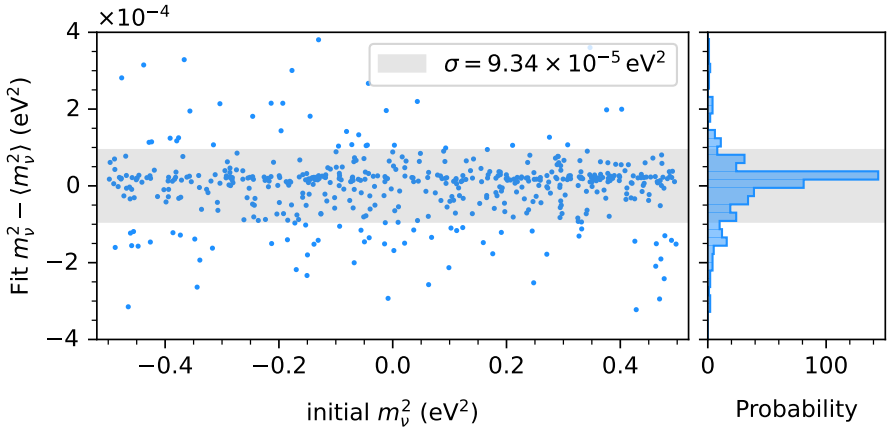

Figure B.3.: Illustration of the numerical stability and reproducibility of m_ν^2. Each point represents a fit result, given a certain initial m_ν^2.

C. Data selection and data combination

Due to the magnetic field settings, alignment, and the usage of different detector wafers, a different pixel selection is applied for each campaign. The pixel selection is summarised in appendix C.1. For the SAP campaigns, pixels are further grouped into 14 detector patches. The patch grouping is given in appendix C.2.

C.1. Pixel selection

Table C.4.: Pixel exclusion for each campaign. The exclusion is mainly based on three criteria: High noise or damage of a pixel, shadowing by the FBM, or alignment of the fluxtube onto the detector. All analyses presented in this work take into account the pixel exclusions listed in the table.

Campaign	Excluded	Reason	Pixel numbers of excluded pixels
KNM1	31 pixels	Wafer noise	97, 98, 110, 111, 121, 122
		FBM shadowing	99, 100, 112, 123
		Alignment	99, 112, 123, 124, 125, 126, 127, 128, 129, 130, 134, 135, 136, 137, 138, 139, 140, 141, 142, 143, 144, 145, 146, 147
KNM2	31 pixels	Wafer noise	97, 98, 110, 111, 121, 122
		FBM shadowing	100
		Alignment	112, 113, 123, 124, 125, 126, 127, 128, 129, 130, 134, 135, 136, 137, 138, 139, 140, 141, 142, 143, 144, 145, 146, 147
KNM345	22 pixels	FBM shadowing	100
		Alignment	112, 113, 123, 124, 125, 126, 127, 128, 129, 134, 135, 136, 137, 138, 139, 140, 141, 142, 145, 146, 147

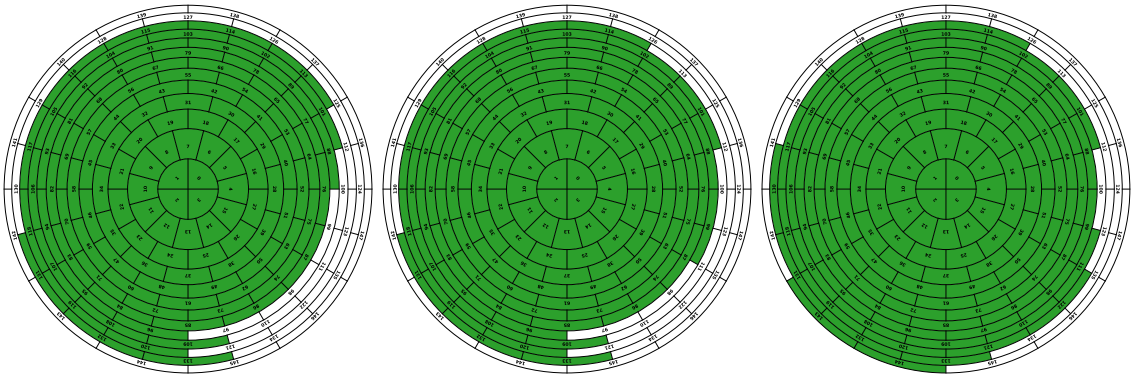

(a) KNM1 **(b)** KNM2 **(c)** KNM345

Figure C.4.: "Golden" detector pixel selections for neutrino-mass measurements. KNM1 and KNM2 includes 117 active pixels, KNM3, 4, and 5 include 126 active pixels in the pixel selection. Pixels are excluded as shown in table C.4.

C.2. SAP patch grouping

Table C.5.: Grouping of detector pixels into SAP-patches. The pixel grouping is based on the similarity of the transmission behaviour of electrons from the source to the detector. The transmission behaviour is mainly affected by the retarding potential and magnetic field in the analysing plane. The detector is segmented into 14 patches, each with 9 pixels.

Patch	Pixel numbers
0	0, 1, 2, 3, 4, 12, 13, 14, 15
1	5, 6, 7, 9, 10, 11, 24, 25, 26
2	8, 16, 17, 22, 23, 27, 37, 38, 39
3	18, 19, 20, 21, 28, 35, 36, 49, 50
4	29, 30, 31, 33, 34, 47, 48, 51, 62
5	32, 40, 46, 41, 45, 52, 60, 61, 63
6	42, 43, 44, 53, 59, 72, 73, 74, 75
7	54, 55, 57, 58, 64, 71, 85, 86, 87
8	56, 65, 69, 70, 76, 83, 84, 97, 98
9	66, 67, 68, 77, 82, 95, 96, 99, 110
10	78, 79, 80, 81, 88, 94, 108, 109, 111
11	89, 90, 93, 92, 107, 119, 120, 121, 122
12	91, 101, 102, 103, 105, 106, 118, 132, 133
13	104, 114, 115, 116, 117, 130, 131, 143, 144

D. Fit configuration

To initialise the model, data, and fit configuration, the `KaFit` framework is set up by xml configuration files. The following two sections provide more details on the `KaFit` configuration (appendix D.1) and `SSC` configuration (appendix D.1) used in the neutrino-mass analysis.

D.1. KaFit configuration

The following xml-code shows the `KaFit` configurations to run the neutrino mass fits. Settings to define the location of run and period summaries are provided externally as a `runRegister.xml`. Model settings to configure the integrated spectrum are given in the `ssc.xml` (see appendix D.2). Additionally, a model for rear wall electrons is set by the `ssc-rw.xml` config, which takes into account a separate FSD and different transmission properties, as electrons have to travel through the entire source length.

```
<!-- Definition of external variables -->

<external_define name="runlist"       value="runRegister.xml"          />
<external_define name="window"        value="42.0"                     />
<external_define name="bg"            value="0.137"                    />
<external_define name="NPfactor"      value="1.00"                     />
<external_define name="BgTimeSlope"   value="0.0"                      />
<external_define name="BgSlope"       value="0.0"                      />
<external_define name="BgRWSig"       value="0.0"                      />
<external_define name="firstrun"      value="0"                        />
<external_define name="runs"          value="0"                        />
<external_define name="seg"           value="uniform"                  />
<external_define name="patches"       value="None"                     />
<external_define name="analysisType"  value="Stacked"                  />
<external_define name="smartStacking" value="true"                     />
<external_define name="paramDoc"      value="ExtendedParameterDoc.ktf" />
<external_define name="minosParam"    value="0"                        />

<kafit>

<!-- Definition of qU-cuts, pixel-cuts and definition of patches -->

  <QUCuts
      Name="myQUCuts"
      LowerQURange="{18574.0-[window]}"
      UpperQURange="19000.0" />

  <PixelCuts
      Name="myPixelCutsKNM1"
      MeasurementCampaign="KNM1" />
```

```
31
32    <PixelCuts
33        Name="myPixelCutsKNM2"
34        MeasurementCampaign="KNM2" />
35
36    <PixelCuts
37        Name="myPixelCutsKNM345"
38        MeasurementCampaign="KNM345" />
39
40    <Patches
41        Name="myPatchesSAP"
42        Configuration="KNM345" />
43
44    <Patches
45        Name="myPatchesUniform"
46        Configuration="Uniform" />
47
48  </kafit>
49
50  <!-- Include additional xml files to setup model and define data -->
51
52  <include base="ssc.xml" />
53  <include base="ssc-rw.xml" />
54  <include base="[runlist]" />
55
56  <kafit>
57
58    <Random
59        Seed="[seed:12345]" />
60
61    <!-- Configure the background -->
62
63    <BackgroundPoissonTimeDep
64        Name="myTimeDepBackground"
65        TotalRate="[bg]"
66        ScaleError="[NPfactor]"
67        TotalTimeSlope="[BgTimeSlope]" />
68
69    <BackgroundSlope
70        Name="myBackgroundSlope"
71        ReferenceEnergy="{18573.7 + 15.0}"
72        Slope="[BgSlope]" />
73
74    <BackgroundBeta
75        Name="myRWBackground"
76        Spectrum="myIntSpecRW"
```

```
77      SharedParams="2-6,8-55,57-173"
78      Signal="[BgRWSig]" />
79
80  <!-- Configure the integrated beta spectrum -->
81
82  <SpectrumSimulator
83      Name="mySpecSim"
84      Spectrum="myIntSpec"
85      Caching="true" >
86      <Background Name="myTimeDepBackground" />
87      <Background Name="myBackgroundSlope" />
88      <Background Name="myRWBackground" />
89  </SpectrumSimulator>
90
91  <!-- Manage runs that are fit -->
92
93  <RunSummarySheaf
94      Name="myRunSummarySheaf" >
95      <loop variable="index" start="[firstrun]" end="[runs]" step="1" >
96          <Run Name="myRunSummary[index]" />
97      </loop>
98  </RunSummarySheaf>
99
100 <RunManager
101     Name="myRunManager"
102     RunSource="myRunSummarySheaf"
103     Segmentation="[seg]"
104     QUCuts="myQUCuts"
105     Patches="[patches]"
106     AnalysisType="[analysisType]"
107     GroupByVoltage="[smartStacking]" >
108 </RunManager>
109
110 <RunSummaryMerger
111     Name="myRunSummaryMerger"
112     RunManager="myRunManager" >
113 </RunSummaryMerger>
114
115 <!-- Manage fit parameters, penalties and correlations -->
116
117 <ParameterManager
118     Name="myParameterManager"
119     RunSource="myRunManager"
120     File="[paramDoc]" >
121 </ParameterManager>
122
```

```
<LoglikelihoodKatrinMulti
    Name="myKatrinLogLMulti"
    PDF="[pdf:Poisson]"
    RunSource="myRunManager"
    SpectrumSimulator="mySpecSim"
    SlowControlLevel="Run"
    ParameterManager="myParameterManager" >
</LoglikelihoodKatrinMulti>

<!-- Minuit settings -->

<Minuit
    Name="myMinuit2Multi"
    Function="myKatrinLogLMulti"
    RandomizeStartValues="0.0"
    Minimizer="migrad"
    MaxFcnCalls="500000000"
    Tolerance="[tolerance:0.01]"
    ParameterManager="myParameterManager"
    PrintLevel="1" >
</Minuit>

<!-- Execute fit -->

<EnsembleTest
    Name="myTester"
    OutputFilename="[output_name:kafit].root"
    NumberOfFits="1"
    Minimizer="myMinuit2Multi"
    MinosParameters="[minosParam]"
    ConfidenceLevel="1.0"
    SystematicError="0.0"
    Debug="False" />

<!-- KaFigure configuration to export the final spectrum,
the data, or model components -->

<Kafigure
    Name="myKafigure"
    OutputPrefix="[output_name:kafit]"
    RunSource="myRunManager"
    FitResultFileName="[output_name:kafit].root"
    DrawingObjects="[objects:data]"
    Likelihood="myKatrinLogLMulti"
    StepSize="0.2"
    LowerRange="{18574.0-[window]-5.0}"
```

```
      UpperRange="18710.0" >
  </Kafigure>

</kafit>
```

D.2. SSC configuration

The following xml-code block defines the SSC configurations to set up the model used in the neutrino-mass analysis. The integrated spectrum is mainly composed of the differential spectrum and response function.

```
<ssc>

    <!-- Defining source -->

    <GasDynamicsConstant
        Name="myGasDynamicsConstant"
        Temperature="[temp:80.0]"
        ColumnDensity="[cd:3.78E21]" />

    <WGTS
        Name="myWGTS"
        BSource="2.5065"
        Flux="[flux:{153.0*1E-4}]"
        BeamtubeLengthFront="5.0075"
        BeamtubeLengthRear="5.0745"
        BeamtubeRadius="0.045"
        NSlices="1" NRings="1" NSegments="1" NCenterSegments="1"
        SegmentationType="detector">
        <GasDynamics Name="myGasDynamicsConstant" />
    </WGTS>

    <!-- FSD settings (for both parametrised and discrete FSD) -->

    <FinalStatesGauss
        Name="myFsdGauss"
        ReducedTritiumPurity="0.98"
        DTvsHTFraction="0.2"
        EmulateDoppler="True"
        Temperature="[temp:80.0]"
        OrthoParaRatio="0.75"
        Model="[FsdModel]"
        GaussModel="Combined" />
```

```
33
34      <FinalStatesRebinned
35          Name="myFsdSaenzRebinned"
36          ReducedTritiumPurity="0.98"
37          DTvsHTFraction="0.2"
38          Binning="1000.0:-10.0:90.0"
39          EmulateDoppler="True"
40          Temperature="[temp:80.0]"
41          OrthoParaRatio="0.75"
42          Model="[FsdModel]" />
43
44      <!-- Settings for differential spectrum -->
45
46      <DifferentialSpectrum
47          Name="myDiffSpec"
48          Endpoint="[E0:18573.7]"
49          NeutrinoMassesSquared="[mnu2:0.0]"
50          MixingParametersSquared="1.0"
51          FinalStatesName="myFsdSaenzRebinned"
52          NegMNuSqMode="phys"
53          CorrectionMode="endpoint"
54          Corrections="G"
55          FermiFunctionMode="rel" />
56
57      <!-- Settings for response function -->
58
59      <ElossInelasticKatrinParametrization
60          Name="myElossInelasticKatrin"
61          Configuration="KNM3_T2" />
62
63      <TransmissionAnalyticalSynchrotron
64          Name="myTransmissionSync"
65          BA="6.3E-4"
66          BS="2.5065"
67          BMax="4.24"
68          Relativistic="true"
69          BTrans="3.6"
70          l1="5.041"
71          l2="14.0"
72          UseCaching="True" />
73
74      <ScatCrossSecInelasConst
75          Name="myConstInelasScatCrossSec"
76          CrossSection="3.63704E-22" />
77
78      <ScatCrossSecInelasEnergyDep
```

```
79          Name="myEnergyDependentInelasScatCrossSec"
80          Configuration="Glueck2019_T2" />
81
82      <ElossShiftHandler
83          Name="myElossShiftHandler" >
84          <Configuration ColumnDensityRange="0.00E21 1.50E21" Kappa="0.618 0.972"
            ↪  Correlation="0.971" />
85          <Configuration ColumnDensityRange="4.00E21 5.00E21" Kappa="0.746 1.227"
            ↪  Correlation="0.959" />
86          <Configuration ColumnDensityRange="1.50E21 2.75E21" Kappa="0.624 0.974"
            ↪  Correlation="0.963" />
87          <Configuration ColumnDensityRange="2.75E21 4.00E21" Kappa="0.687 1.086"
            ↪  Correlation="0.958" />
88      </ElossShiftHandler>
89
90      <Response
91          Name="myResponse"
92          InelasticCrossSecName="[cross_sec:myEnergyDependentInelasScatCrossSec]"
93          EnergyLossName="myElossInelasticKatrin"
94          EnergyLossBinWidth="0.01"
95          EnergyLossRange="0.0;{[window]+5.0}"
96          TransmissionName="myTransmissionSync"
97          NScatterings="7"
98          ElossShiftHandlerName="myElossShiftHandler"
99          DetailedTransmissionForNScatterings="[det_trans:1]"
100         AngularChange="False"
101         UseScatteringCaching="[scat_cache:True]"
102         UseResponseCaching="[resp_cache:True]"
103         CacheEnergyLowerBound="{18574.0-[window]-10.0}"
104         CacheEnergyUpperBound="18580.0"
105         ConvolutionMethod="[conv_method:Direct]" />
106
107     <!-- Settings of detection efficiency -->
108
109     <AngularDetectionEfficiency
110         Name="myAngularEfficiency" />
111
112     <Detector
113         Name="myDetector"
114         Efficiency="0.95"
115         DetectorPositionZ="13.98" />
116
117     <!-- Settings for final integrated spectrum -->
118
119     <IntegratedSpectrum
120         Name="myIntSpec"
```

```
121         SourceName="myWGTS"
122         ResponseName="myResponse"
123         DetectorName="myDetector"
124         DopplerMode="off"
125         TritiumPurity="0.98"
126         IntegrationMinSteps="64"
127         IntegrationPrecision="1E-6"
128         IntegrationMethod="[IntMethod:Legendre]" >
129         <Spectrum Name="[DiffSpec:myDiffSpec]" />
130     </IntegratedSpectrum>
131
132 </ssc>
```

E. Parameter and data inputs

The following appendices provide more details on applied parameter correlations for the energy loss function (appendix E.1). Furthermore, the applied run summary versions and period summary versions are listed in appendix E.2.

E.1. Energy loss correlations

Table E.6.: Parameters correlations of the energy loss function as it is used in the neutrino-mass analysis. Note that the values here are rounded to three digits. [28, 217]

	a_1	μ_1	σ_1	a_2	μ_2	σ_2	a_3	μ_3	σ_3
a_1									
μ_1	+0.450								
σ_1	+0.294	+0.781							
a_2	+0.119	−0.115	−0.002						
μ_2	+0.523	+0.585	+0.559	+0.158					
σ_2	−0.666	−0.440	−0.589	−0.349	−0.261				
a_3	−0.101	−0.021	−0.072	+0.196	+0.242	+0.304			
μ_3	−0.205	−0.100	−0.167	−0.047	+0.086	+0.392	−0.414		
σ_3	+0.217	+0.076	+0.169	−0.233	−0.318	−0.546	−0.883	−0.043	

E.2. Run and period summary versions

The following four tables summarise the versions of run and period summaries used in the analyses.

E.2.1. Run summaries

Run summaries are versioned, including major and minor releases. `Durable` versions of the run summaries are processed offline after the data taking has been finished and the calibration data has been processed. Major releases correspond to the number and are increased if an analysis strategy changes when post-processing the data. Minor releases include minor changes or bug fixes and are represented by the letter. The `Fitting` version is produced for the neutrino-mass analysis, setting the column density according to the expert input.

Table E.7.: Run summary versions used in the neutrino-mass analysis.

Campaign	Run summary version
KNM1	`Durable3a-Fitting3`
KNM2	`Durable5j-Fitting2`
KNM3a	`Durable10a-Fitting2`
KNM3b	`Durable10a-Fitting2`
KNM4	`Durable10aRev2-Fitting3`
KNM5	`Durable10a-Fitting3`

Table E.8.: Run summary versions used in the sterile neutrino analysis.

Campaign	Run summary version
KNM1	`Durable3a`
KNM2	`Durable5i`

E.2.2. Period summaries

Period summaries can either be produced from simulations or based on measurements with krypton. This is reflected in the naming, where period summaries from simulations contain `GlobalKNMXSimulation-PeriodSummary` in the naming, and period summaries that are created based on additional measurements contain `SAP_KNMX_KryptonPeriodSummary` in their name.

Table E.9.: Period summary versions used in the neutrino-mass analysis.

Campaign	Period summary version
KNM1	`GlobalKNM1Simulation-PeriodSummary-Fitting_Feb2021b-ActualCurrent_18600V_6.0G-000001_1432ROI.ktf`
KNM2	`GlobalKNM2Simulation-PeriodSummary-Fitting_Feb2021b-ActualCurrent_18600V_6.0G-000001_1432ROI.ktf`
KNM3a	`SAP_KNM3_KryptonPeriodSummary_2022-12-19_2234ROI (_IE200).ktf`*
KNM3b	`GlobalKNM3Simulation-PeriodSummary-Fitting_Jan2022b-Actual-Knm3b_18600V_6.0G-000001_2234ROI.ktf`
KNM4	`SAP_KNM3_KryptonPeriodSummary_2022-12-19_2234ROI.ktf`
KNM5	`SAP_KNM5_KryptonPeriodSummary_2023-02-13_Patchwise_2234ROI.ktf`

*) The addition in the bracket denotes two separate period summary versions that reflect a time-weighted differences in the inner electrode settings. In the analysis of KNM3a data, average of both period summaries is used.

Table E.10.: Period summary versions used in the sterile neutrino analysis.

Campaign	Period summary version
KNM1	`GlobalKNM1Simulation-PeriodSummary-Fitting_Mar2019c-200V_18600V_6.0G-000001.ktf`
KNM2	`GlobalKNM2Simulation-PeriodSummary_Jun2020b-Actual_18600V_6.0G-000001.ktf`

F. Impact of systematic uncertainties on the endpoint, signal, and background

In addition to the systematic breakdown on m_ν^2, one can also investigate the effects of systematic uncertainties on other nuisance parameters such as the endpoint and signal. Symmetric uncertainties on these parameters are estimated by the Hesse matrix alongside the asymmetric uncertainty on the neutrino mass in the fits. In figures F.5 and F.6 the systematic breakdown for the NAP campaigns (KNM1, KNM2, KNM3b) is presented. Investigating the effects on these campaigns is motivated since the data is stacked into a single spectrum, fitting one endpoint and one signal per campaign. Consequently, the robustness of the uncertainties from the Hesse matrix is guaranteed due to higher statistics and less numerical noise. In both figures, the uncertainties are ordered by the impact of the systematic effect on the neutrino mass, which is the same order as presented in section 6.3.3.

The breakdown for the endpoint uncertainty is presented in figure F.5. Alongside the uncertainties, changes in the central values are summarised in the right panels. For the endpoint, uncertainties on the analysing plane fields give the largest systematic error contribution, followed by the impact of the non-Poisson background. In comparison, the impact of all other systematic effects is on a much smaller level. On the other hand, the largest change in the central values is observed for the Penning trap induced background.

The breakdown for the signal amplitude uncertainty is presented in figure F.6. For the signal, the largest systematic error contribution is from the uncertainties on the column density. In the case of KNM1, the impact is even larger than the statistical uncertainty. This can be explained, since the column density not only changes the scattering probabilities but also enters the integrated spectrum as a scaling factor (see equations (3.45) and (3.46)), resulting in a strong correlation of $\rho d\sigma$ and Sig. Similarly, uncertainties on the pinch and source magnetic fields influence the acceptance angle, increasing the uncertainty on Sig.

The breakdown for the background uncertainty is presented in figure F.7. As expected, the background uncertainty is only affected by background-related systematic effects. The largest systematic error contribution is posed by the Penning trap induced background. The contribution is even larger than the statistical uncertainty on the background. For the Penning trap induced background, the central value is also affected when applying the systematic uncertainty. The second largest contribution is the non-Poissonian background uncertainty. The high voltage dependence of the background only has a minor error contribution.

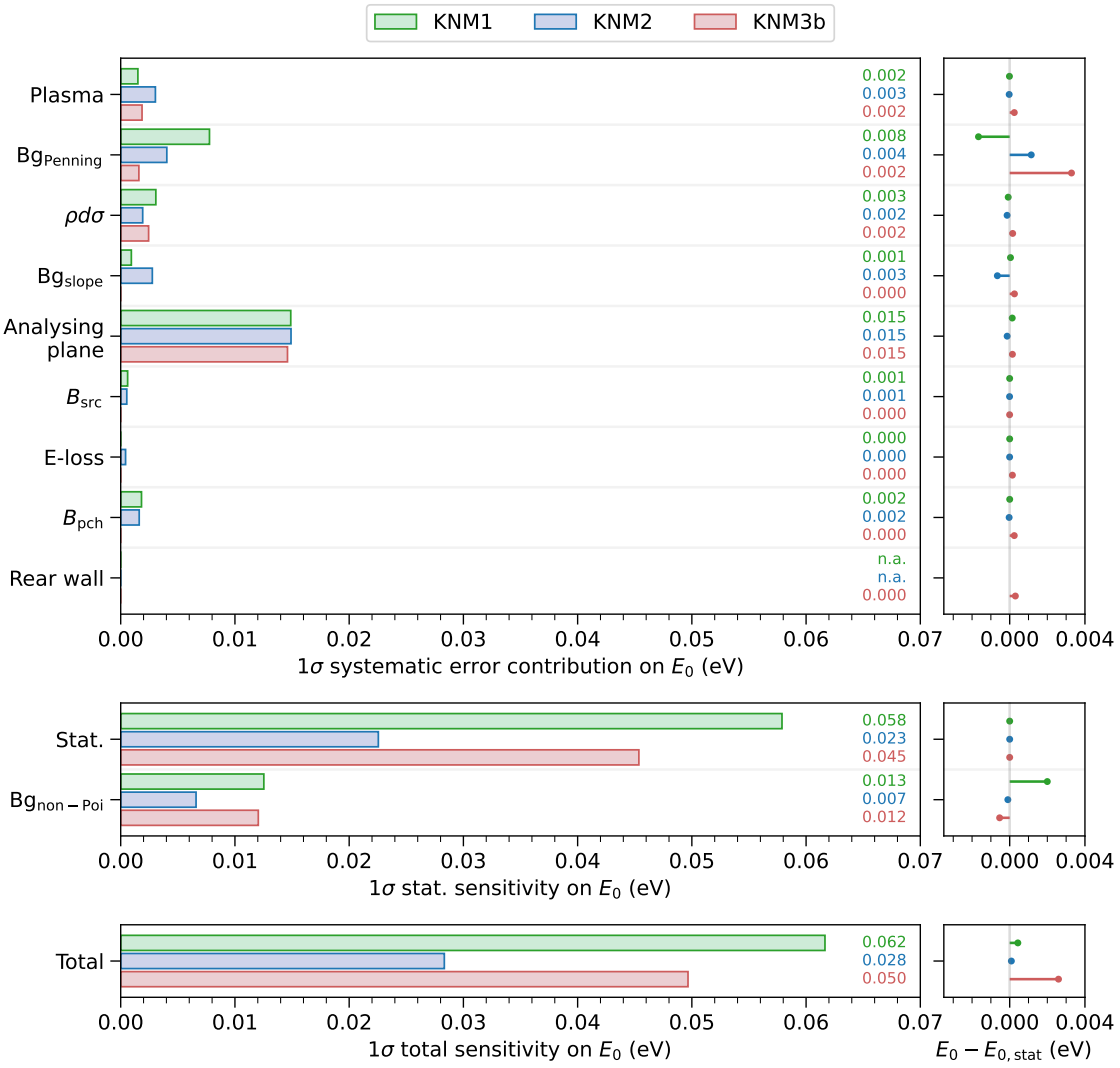

Figure F.5.: Systematic breakdown for the effective endpoint. The breakdown is displayed for all NAP campaigns since the data is stacked into a uniform spectrum, resulting in a single endpoint for each campaign. The uncertainties displayed here have been estimated from the Hesse matrix. The plot is separated into systematic error contribution (top), statistical uncertainty (middle), and the total uncertainty, including all systematics (bottom). The right panels show the central E_0 relative to the statistics-only fit.

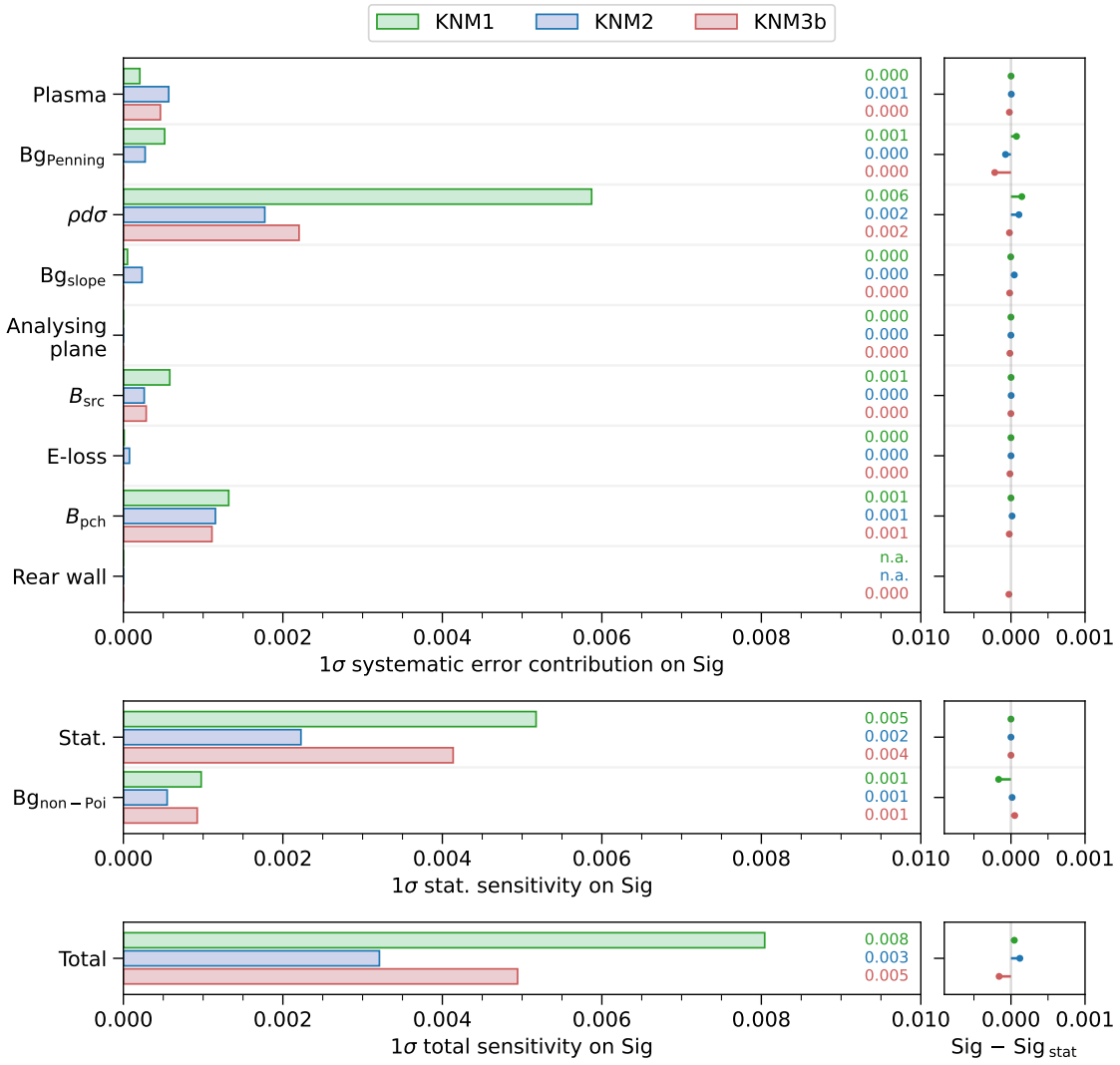

Figure F.6.: Systematic breakdown for the signal amplitude. The breakdown is displayed for all NAP campaigns since the data is stacked into a uniform spectrum, resulting in a single fit signal for each campaign. The uncertainties displayed here have been estimated from the Hesse matrix. The plot is separated into systematic error contribution (top), statistical uncertainty (middle), and the total uncertainty, including all systematics (bottom). The right panels show the central value of the signal relative to the statistics-only fit.

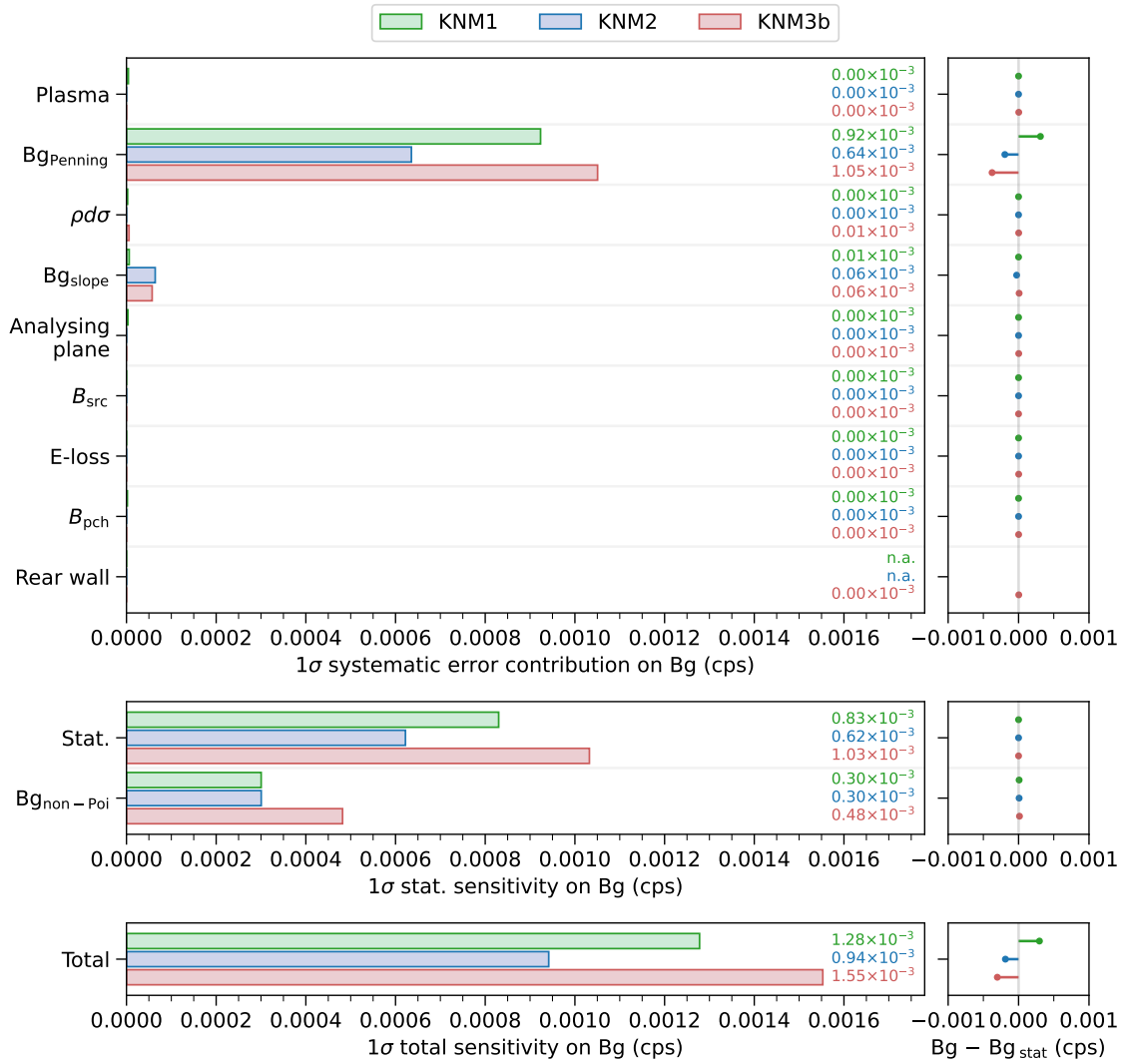

Figure F.7.: Systematic breakdown for the background. The breakdown is displayed for all NAP campaigns since the data is stacked into a uniform spectrum, resulting in a single fit background for each campaign. The uncertainties displayed here have been estimated from the Hesse matrix. The plot is separated into systematic error contribution (top), statistical uncertainty (middle), and the total uncertainty, including all systematics (bottom). The right panels show the central value of the signal relative to the statistics-only fit.

G. Fit-parameter correlations

The resulting correlations for the fit parameters form the combined KNM1-5 neutrino-mass analysis and from the analyses of the individual campaigns are shown in figures G.8 and G.9.

Constrained fit parameters are partially already connected by the correlated pull terms, such as the inserted correlation between B_{ana} and σ_{trans}. These correlations are also retrieved from the fit.

Thus it is, in particular, interesting to look at the correlations that are calculated for the free fit parameters (m_ν^2, E_0, Sig, and Bg). Hereby the neutrino mass is strongly correlated to the endpoints and strongly anti-correlated to the signals. There is a small correlation between the neutrino mass and the background. Furthermore, the endpoint and signal have a strong anti-correlation. In the case of a combined analysis of several spectra (like the combined fit of patches or campaigns), fit parameters become correlated through the neutrino mass. This can be observed for the endpoints and signal amplitudes.

Other correlations that emerge from the fit are, for example, a correlation between E_0 and B_{ana}. An anti-correlation of Sig and $\rho \mathrm{d}\sigma$ is observed, as the column density is also applied in the scaling factor of the spectrum. The signal is further correlated with B_{pch}, which also scales the spectrum with the acceptance angle in the model calculation. The Penning trap induced background is correlated to both m_ν^2 and E_0, and has a strong anticorrelation with Bg, as an increase of $\mathrm{Bg}_{\mathrm{Penning}}$ als overall increases the absolute background rate, which is compensated by Bg.

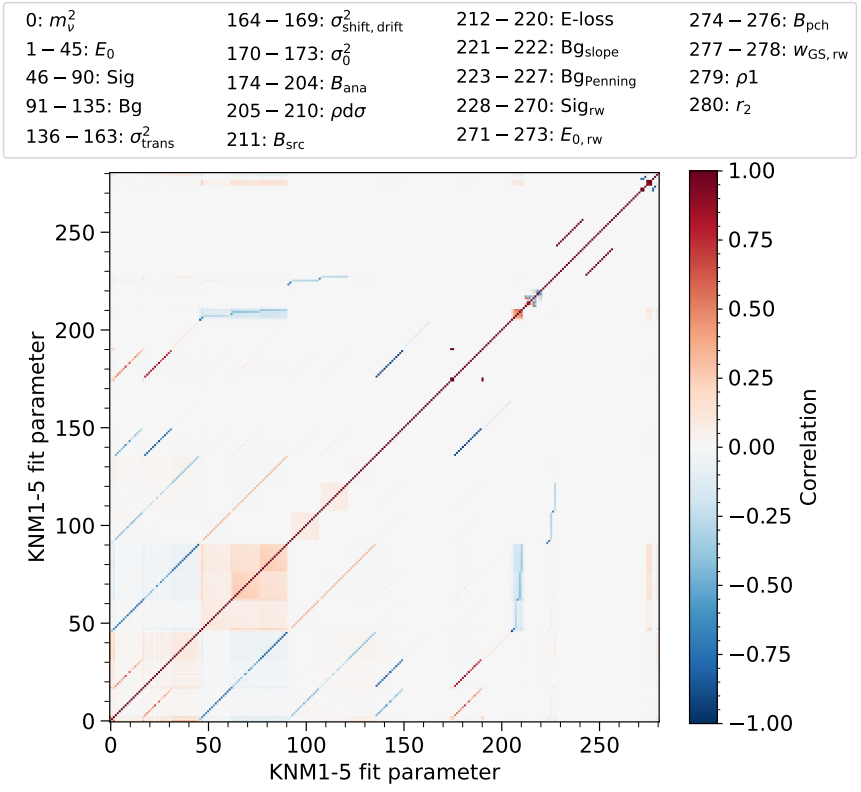

Figure G.8.: Fit parameter correlations of the combined KNM1-5 analysis, including all systematic uncertainties. The parameter index ranges and corresponding parameter names are listed in the legend.

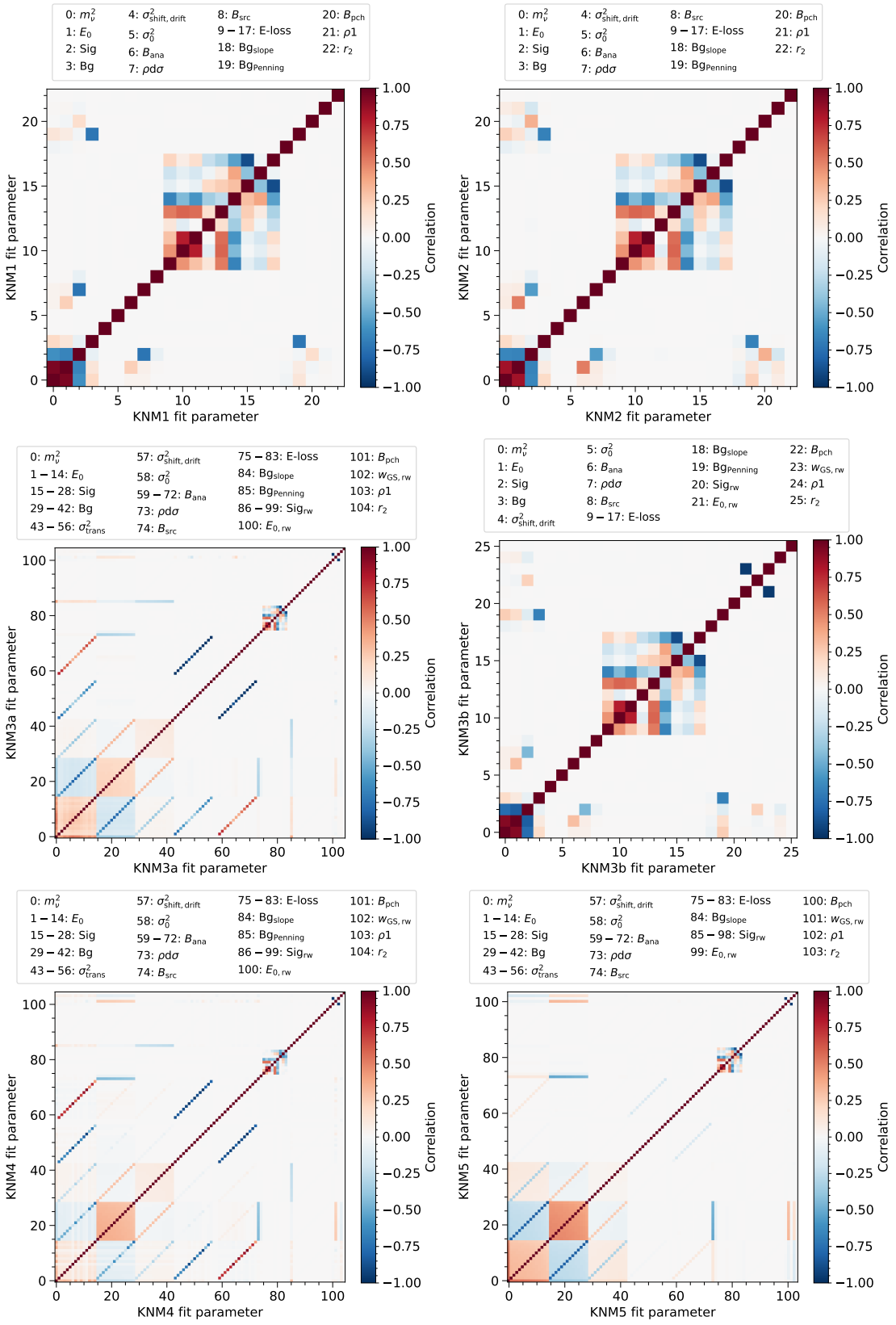

Figure G.9.: Fit parameter correlations of the analysis of each campaign including all systematic uncertainties. The parameter index ranges and corresponding parameter names are listed in the legend.

H. KNM1-5 confidence belt construction

The Lokhov-Tkachov belt and Feldman-Cousins belt are constructed based on generated Asimov datasets. The spectra are simulated based on the fit signal, background, and endpoint of the KNM1-5 analysis, including all systematic uncertainties. The spectra are further generated for fifferent $m^2_{\nu,\,\mathrm{true}}$ in between $0.00\,\mathrm{eV}^2$ and $0.35\,\mathrm{eV}^2$ in steps of $0.01\,\mathrm{eV}^2$. For each Asimov dataset, the χ^2 profile is calculated over $m^2_{\nu,\,\mathrm{fit}}$ (first panel of figure H.10). The resulting χ^2 is then converted into the profile likelihood $\mathcal{L}$, using equation (4.6) (second panel of figure H.10).

From the profile likelihood, the one-sided and two-sided 90 % C.L. bounds are estimated for the Lokhov-Tkachov method blue dotted and blue sold horizontal lines in the bottom panel of figure H.10). The Lokhov-Tkachov belt is outlined by the solid blue line.

For the Feldman-Cousins construction, the likelihood ratio R is further required (third panel of figure H.10).[1] Resorting by the likelihood ratio, the two-sided bounds are calculated for each $m^2_{\nu,\,\mathrm{true}}$ (solid grey horizontal lines in the bottom panel). The Feldman-Cousins belt is outlined by the dashed grey line.

[1] The likelihood ratio is defined by equation (4.23).

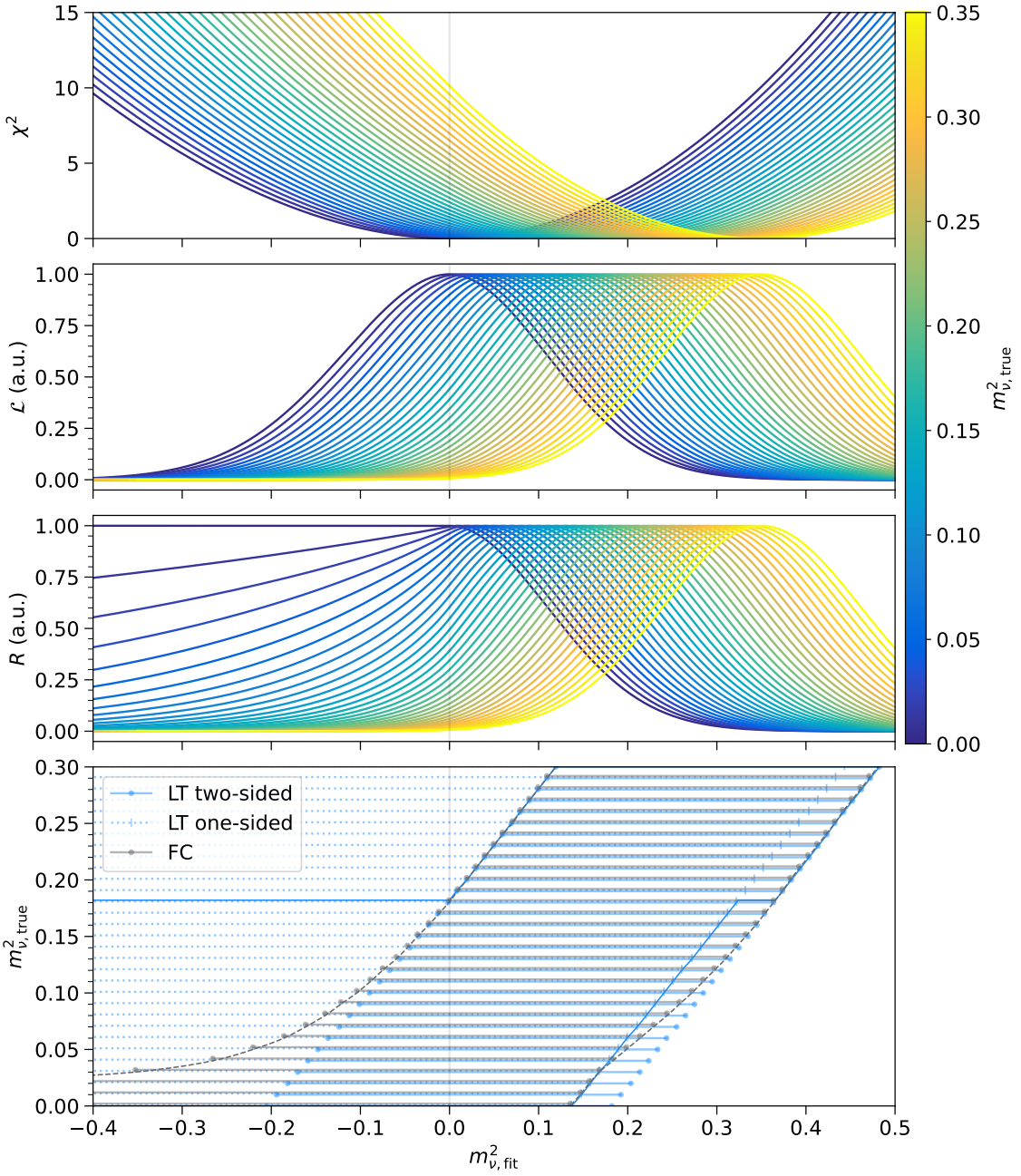

Figure H.10.: Detailed illustration of the KNM1-5 belt construction. The top panel show the χ^2 profiles for different $m^2_{\nu,\,\mathrm{true}}$. The χ^2 is then translated into the profile likelihood $\mathcal{L}$ (second panel). For the Feldman-Cousins construction, the likelihood ratio R is further required (third panel). From the profile likelihood, the different confidence intervals are estimated (bottom panel).

I. Influence of different prior distributions

The following two plots show the influence of additional priors on the neutrino mass, signal and endpoint. In figure I.11 a flat positive prior in m_ν^2 (blue) and a flat positive prior in m_ν (grey) are compared to the scenario with no additional prior. The study is performed on 1000 days of simulated KATRIN spectra, with conditions similar to KNM5. In the simulated spectrum, the neutrino mass is set to $m_\nu^2 = 0.1\,\mathrm{eV}^2$. For a positive neutrino mass significantly different from zero, the different prior scenarios only have a small impact on the resulting Markov chains. A flat positive prior in m_ν gives slightly more preference to values close to zero compared to the other two cases.

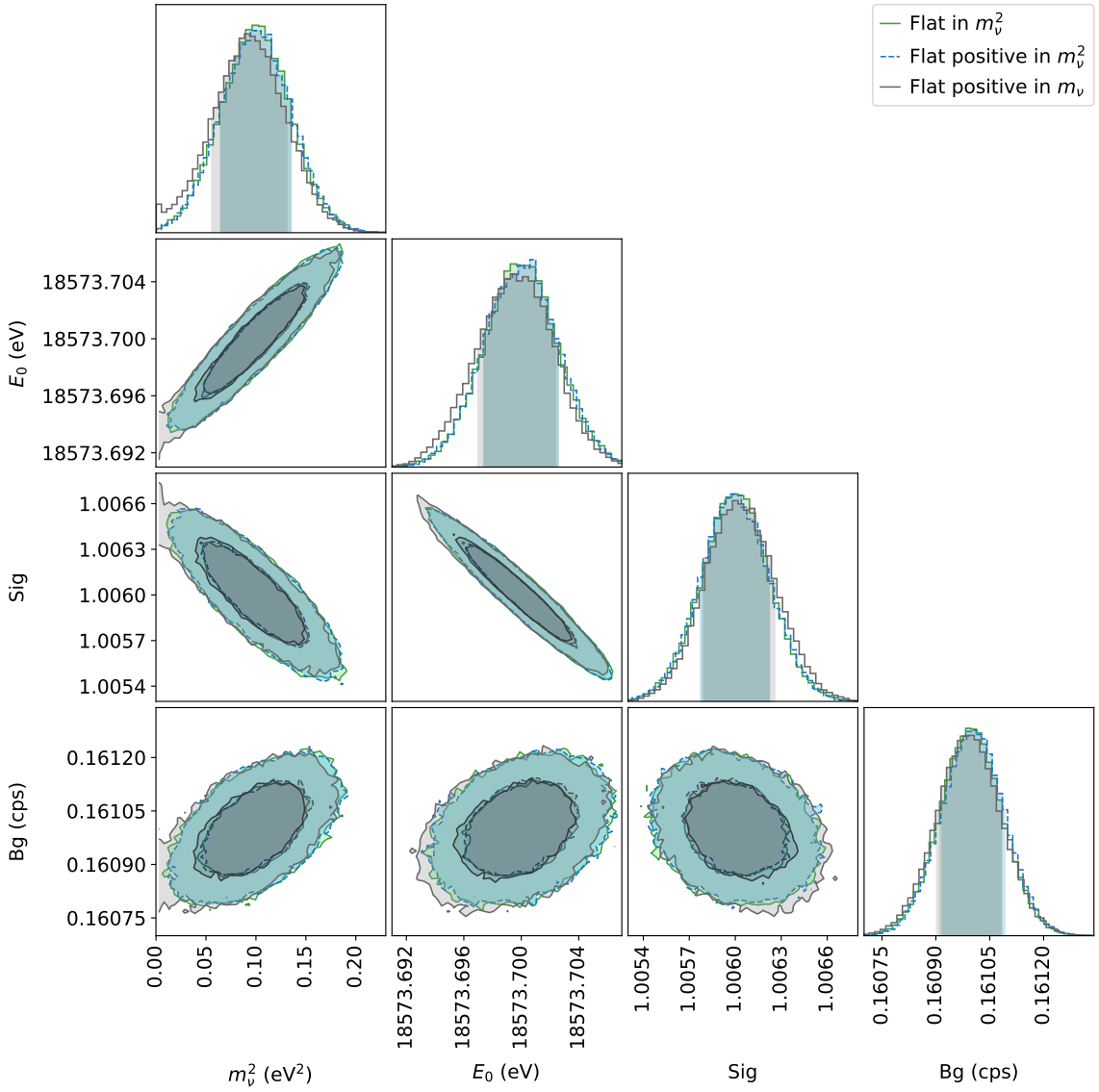

Figure I.11.: Influence of different priors for a positive neutrino mass. The study is based on 1000 days of simulated KATRIN spectra, with conditions similar to KNM5.

In figure I.12 an additional constraint is set to the endpoint value ($\sigma = 0.001\,\mathrm{eV}$). Also, here the study is performed on 1000 days of simulated KATRIN spectra, with conditions similar to KNM5. In the simulated spectrum, the neutrino mass is set to $m_\nu^2 = 0.0\,\mathrm{eV}^2$. Due to the strong correlation between the endpoint and the neutrino mass, this also improves the sensitivity on the neutrino mass significantly. This study is shown to illustrate how improved external knowledge of the Q-value and better knowledge of the absolute potential could impact the neutrino mass.

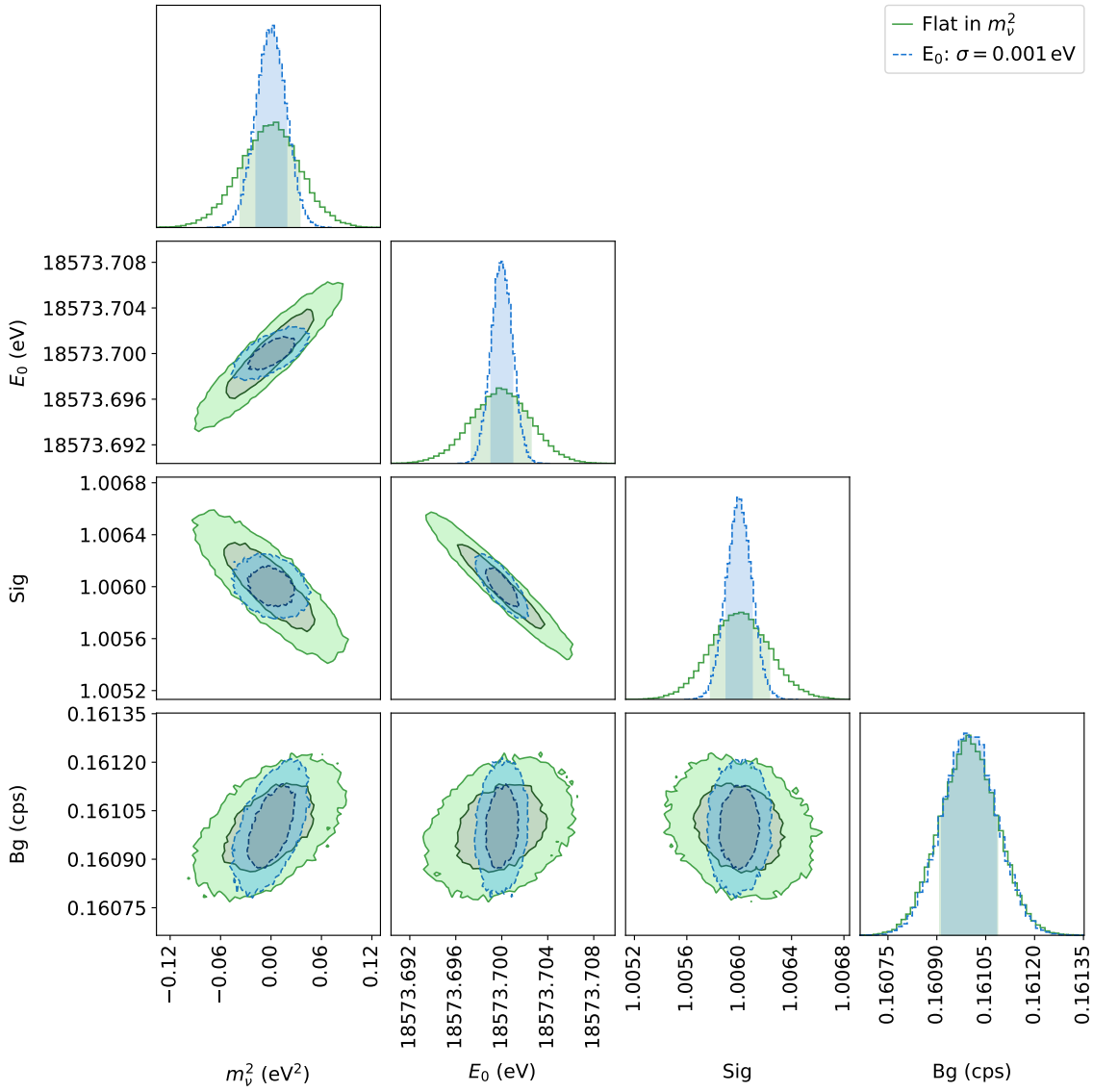

Figure I.12.: Influence of stronger constraints on the endpoint. The study is based on 1000 days of simulated KATRIN spectra, with conditions similar to KNM5.

List of acronyms

BAO	baryon acoustic oscillations
BED	binary-encounter-dipole
BEST	Baksan Experiment on Sterile Transitions
BFGS	Broyden–Fletcher–Goldfarb–Shanno
BIXS	beta induced X-ray spectroscopy
BOSS	Baryon Oscillation Spectroscopic Survey
CAD	computer-aided design
C.I.	credibility interval
C.L.	confidence level
CMB	cosmic microwave background
CνB	cosmic neutrino background
CP	charge-parity
CPS	cryogenic pumping section
cps	counts per second
CRES	Cyclotron Radiation Emission Spectroscopy
CUORE	Cryogenic Underground Observatory for Rare Events
DAQ	data acquisition system
`DeSASTER`	Detector Section Analysis Suite – Temporary Evaluation Revision
dof	degrees of freedom
`DRIPS`	Detector readout simulation
DPS	differential pumping section
e-gun	electron-gun
ECHo	Electron CaptureHolmium
EMCS	earth magnetic field compensation system
EXO	Enriched Xenon Observatory
FBM	forward beam monitor
FPD	focal plane detector
FSD	final states distribution
FWHM	full width half maximum
GA	gallium anomaly
GALLEX	Gallium-Experiment
GERDA	Germanium Detector Array
hdi	highest density interval
HLL	Halbleiter Labor
`IDLE`	intermediate data layer
IO	inverted ordering
ISW	integrated Sachs-Wolfe effect
`KaFit`	Fit environment for KATRIN-spectra
`KaLi`	KATRIN library

KamLAND	Kamioka Liquid Scintillator Antineutrino Detector
KARMEN	KArlsruhe Rutherford Medium Energy Neutrino experimen
`KASPER`	KATRIN C++ software package
KATRIN	KArlsruhe TRItium Neutrino experiment
`KESS`	KATRIN electron silicon scattering
KIT	Karlsruhe Institute of Technology
KNM	KATRIN neutrino-mass measurement
`Kommon`	`KASPER`-common
`KTrap`	KATRIN transmission analysing package
LARA	laser Raman spectroscopy system
LFCS	low-field correction system
LSND	Liquid Scintillator Neutrino Detector
MAC-E	magnetic adiabatic collimation with electrostatic
MARE	Microcalorimeter Arrays for a Rhenium Experiment
MCMC	Markov Chain Monte Carlo
MINOS	Main Injector Neutrino Oscillation Search
MiniBooNE	Mini Booster Neutrino Experiment
MLE	maximum likelihood estimation
MS	main spectrometer
MTD	measuring time distribution
NAP	nominal analysing plane
NEG	non-evaporating getter pump
NMR	Nuclear Magnetic Resonance
NO	normal ordering
NOMAD	neutrino oscillation magnetic detector
NOνA	Neutrinos at the Main Injector Off-Axis ν_e Appearance
PAE	post acceleration electrode
pdf	probability density function
PIN	positive intrinsic negative
PMNS	Pontecorvo-Maki-Nakagawa-Sakata neutrino mixing matrix
PROSPECT	Precision Oscillation and Spectrum Experiment
PS	pre-spectrometer
PS1	upstream pre-spectrometer magnet
PS2	downstream pre-spectrometer magnet
QCD	quantum chromodynamics
RAA	reactor antineutrino anomaly
RENO	Reactor Experiment for Neutrino Oscillation
ROI	region of interest cut applied to FPD data
RS	rear section
SAP	shifted analysing plane
SAGE	Soviet–American Gallium Experiment
SBL	short-baseline
SDD	silicon drift detector
SDS	spectrometer and detector section
SNO	Sudbury Neutrino Observatory
SQUID	superconducting quantum interference device
`SSC`	Source and Spectrum Calculation
STEREO	Search for Sterile Reactor Neutrino Oscillations
STS	source and transport section

T2K	Tokai to Kamioka
TOF	time of flight
TLK	Tritium Laboratory Karlsruhe
TMP	turbo-molecular pump
TRISTAN	tritium beta decay to search for sterile neutrinos
WGTS	windowless gaseous tritium source
ΛCDM	Λ cold dark matter
νMSM	neutrino minimal extension of the Standard Model

List of Figures

List of Tables

Bibliography

[1] M. G. Aartsen et al. “Measurement of Atmospheric Neutrino Oscillations at 6–56 GeV with IceCube DeepCore”. In: *Phys. Rev. Lett.* 120.7 (2018), p. 071801. DOI: 10.1103/PhysRevLett.120.071801.

[2] D. N. Abdurashitov et al. “Electron scattering on hydrogen and deuterium molecules at 14–25 keV by the “Troitsk nu-mass” experiment”. In: *Physics of Particles and Nuclei Letters* 14.6 (2017), pp. 892–899. DOI: 10.1134/S1547477117060024.

[3] J. Abdurashitov et al. “Measurement of the solar neutrino capture rate with gallium metal. III. Results for the 2002–2007 data-taking period”. In: *Phys. Rev. C* 80.1 (2009), p. 015807. DOI: 10.1103/PhysRevC.80.015807.

[4] K. Abe et al. “Atmospheric neutrino oscillation analysis with external constraints in Super-Kamiokande I-IV”. In: *Phys. Rev. D* 97.7 (2018), p. 072001. DOI: 10.1103/PhysRevD.97.072001.

[5] K. Abe et al. “Solar Neutrino Measurements in Super-Kamiokande-IV”. In: *Phys. Rev. D* 94.5 (2016), p. 052010. DOI: 10.1103/PhysRevD.94.052010.

[6] K. Abe et al. “Constraint on the matter–antimatter symmetry-violating phase in neutrino oscillations”. In: *Nature* 580.7803 (2020), pp. 339–344. DOI: 10.1038/s41586-020-2177-0.

[7] S. Abe et al. “Search for the Majorana Nature of Neutrinos in the Inverted Mass Ordering Region with KamLAND-Zen”. In: *Phys. Rev. Lett.* 130.5 (2023), p. 051801. DOI: 10.1103/PhysRevLett.130.051801.

[8] G. F. Abellán et al. “Improved cosmological constraints on the neutrino mass and lifetime”. In: *Journal of High Energy Physics* 2022.8 (2022), p. 76. DOI: 10.1007/JHEP08(2022)076.

[9] T. Abrahão et al. “Search for Signatures of Sterile Neutrinos with Double Chooz”. In: (2020). arXiv: 2009.05515 [hep-ex].

[10] M. A. Acero et al. “First Measurement of Neutrino Oscillation Parameters using Neutrinos and Antineutrinos by NOvA”. In: *Phys. Rev. Lett.* 123.15 (2019), p. 151803. DOI: 10.1103/PhysRevLett.123.151803.

[11] P. Adamson et al. “Precision Constraints for Three-Flavor Neutrino Oscillations from the Full MINOS+ and MINOS Dataset”. In: *Phys. Rev. Lett.* 125.13 (2020), p. 131802. DOI: 10.1103/PhysRevLett.125.131802.

[12] P. Adamson et al. “Improved Constraints on Sterile Neutrino Mixing from Disappearance Searches in the MINOS, MINOS+, Daya Bay, and Bugey-3 Experiments”. In: *Phys. Rev. Lett.* 125.7 (2020), p. 071801. DOI: 10.1103/PhysRevLett.125.071801.

[13] E. G. Adelberger et al. “Solar fusion cross sections. II. The *pp* chain and CNO cycles”. In: *Rev. Mod. Phys.* 83.1 (2011), pp. 195–245. DOI: 10.1103/RevModPhys.83.195.

[14] D. Adey et al. “Measurement of the Electron Antineutrino Oscillation with 1958 Days of Operation at Daya Bay”. In: *Phys. Rev. Lett.* 121.24 (2018), p. 241805. DOI: 10.1103/PhysRevLett.121.241805.

[15] R. Adhikari et al. “A White Paper on keV sterile neutrino Dark Matter”. In: *Journal of Cosmology and Astroparticle Physics* 2017.01 (2017), pp. 025–025. DOI: 10.1088/1475-7516/2017/01/025.

[16] N. Aghanim et al. “Planck 2018 results. VI. Cosmological parameters”. In: *Astron. Astrophys.* 641 (2020), A6. DOI: 10.1051/0004-6361/201833910.

[17] M. Agostini et al. “Experimental evidence of neutrinos produced in the CNO fusion cycle in the Sun”. In: *Nature* 587.7835 (2020), pp. 577–582.

[18] M. Agostini et al. “Final Results of GERDA on the Search for Neutrinoless Double-β Decay”. In: *Phys. Rev. Lett.* 125.25 (2020), p. 252502. DOI: 10.1103/PhysRevLett.125.252502.

[19] M. Agostini and B. Neumair. “Statistical methods applied to the search of sterile neutrinos”. In: *Eur. Phys. J. C* 80.8 (2020), p. 750. DOI: 10.1140/epjc/s10052-020-8279-x.

[20] A. Aguilar et al. “Evidence for neutrino oscillations from the observation of $\overline{\nu}_e$ appearance in a $\overline{\nu}_\mu$ beam”. In: *Phys. Rev. D* 64.11 (2001), p. 112007. DOI: 10.1103/PhysRevD.64.112007.

[21] A. Aguilar-Arevalo et al. “Significant Excess of Electronlike Events in the MiniBooNE Short-Baseline Neutrino Experiment”. In: *Phys. Rev. Lett.* 121.22 (2018), p. 221801. DOI: 10.1103/physrevlett.121.221801.

[22] M. Aker et al. “An improved upper limit on the neutrino mass from a direct kinematic method by KATRIN”. In: *Phys. Rev. Lett.* 123 (2019), p. 221802. DOI: 10.1103/PhysRevLett.123.221802.

[23] M. Aker et al. “Analysis methods for the first KATRIN neutrino-mass measurement”. In: *Phys. Rev. D* 104 (2021), p. 012005. DOI: 10.1103/PhysRevD.104.012005.

[24] M. Aker et al. “Bound on 3+1 active-sterile neutrino mixing from the first four-week science run of KATRIN”. In: *Phys. Rev. Lett.* 126 (2021), p. 091803. DOI: 10.1103/PhysRevLett.126.091803.

[25] M. Aker et al. “Direct neutrino-mass measurement with sub-electronvolt sensitivity”. In: *Nature Physics* 18.2 (2022), pp. 160–166. DOI: 10.1038/s41567-021-01463-1.

[26] M. Aker et al. “Improved eV-scale sterile-neutrino constraints from the second KATRIN measurement campaign”. In: *Physical Review D* 105.7 (2022). DOI: 10.1103/physrevd.105.072004.

[27] M. Aker et al. “New Constraint on the Local Relic Neutrino Background Overdensity with the First KATRIN Data Runs”. In: *Phys. Rev. Lett.* 129.1 (2022), p. 011806. DOI: 10.1103/PhysRevLett.129.011806.

[28] M. Aker et al. “Precision measurement of the electron energy loss function in tritium and deuterium gas for the KATRIN experiment”. In: *Eur. Phys. J. C* 81.7 (2021). DOI: 10.1140/epjc/s10052-021-09325-z.

[29] M. Aker et al. *Rear wall report for the KNM1-5 neutrino-mass analysis*. Internal technical report. 2022. URL: https://ikp-katrin-wiki.ikp.kit.edu/katrin/images/d/dc/RW-combined-tech-report.pdf.

[30] M. Aker et al. *Search for keV-scale Sterile Neutrinos with first KATRIN Data*. 2022. arXiv: 2207.06337 [nucl-ex].

[31] M. Aker et al. "The design, construction, and commissioning of the KATRIN experiment". In: *Journal of Instrumentation* 16.08 (2021), T08015. DOI: 10.1088/1748-0221/16/08/t08015.

[32] M. Aker et al. "First operation of the KATRIN experiment with tritium". In: *Eur. Phys. J. C* 80.3 (2020). DOI: 10.1140/epjc/s10052-020-7718-z.

[33] M. Aker et al. "Probing the absolute neutrino mass scale with KATRIN". In submission. 2024.

[34] H. Almazan et al. "Improved sterile neutrino constraints from the STEREO experiment with 179 days of reactor-on data". In: *Phys. Rev. D* 102.5 (2020), p. 052002. DOI: 10.1103/PhysRevD.102.052002.

[35] H. Almazán et al. "STEREO neutrino spectrum of ^{235}U fission rejects sterile neutrino hypothesis". In: *Nature* 613.7943 (2023), pp. 257–261. DOI: 10.1038/s41586-022-05568-2.

[36] J. Amsbaugh et al. "Focal-plane detector system for the KATRIN experiment". In: *Nuclear Instruments and Methods in Physics Research Section A: Accelerators, Spectrometers, Detectors and Associated Equipment* 778 (2015), pp. 40–60. DOI: 10.1016/j.nima.2014.12.116.

[37] F. P. An et al. "New measurement of θ_{13} via neutron capture on hydrogen at Daya Bay". In: *Phys. Rev. D* 93.7 (2016), p. 072011. DOI: 10.1103/PhysRevD.93.072011.

[38] M. Andriamirado et al. "Improved short-baseline neutrino oscillation search and energy spectrum measurement with the PROSPECT experiment at HFIR". In: *Phys. Rev. D* 103.3 (2021), p. 032001. DOI: 10.1103/PhysRevD.103.032001.

[39] J. Angrik et al. *KATRIN design report 2004*. Tech. rep. 2005. DOI: 10.5445/IR/270060419.

[40] G. Anton et al. "Search for Neutrinoless Double-β Decay with the Complete EXO-200 Dataset". In: *Phys. Rev. Lett.* 123.16 (2019), p. 161802. DOI: 10.1103/PhysRevLett.123.161802.

[41] M. Archidiacono et al. "Physical effects involved in the measurements of neutrino masses with future cosmological data". In: *Journal of Cosmology and Astroparticle Physics* 2017.02 (2017), pp. 052–052. DOI: 10.1088/1475-7516/2017/02/052.

[42] M. Arenz et al. "Commissioning of the vacuum system of the KATRIN Main Spectrometer". In: *Journal of Instrumentation* 11 (2016), P04011. DOI: 10.1088/1748-0221/11/04/P04011.

[43] M. Arenz et al. "The KATRIN superconducting magnets: overview and first performance results". In: *Journal of Instrumentation* 13.08 (2018), T08005. DOI: 10.1088/1748-0221/13/08/T08005.

[44] B. Armbruster et al. "Upper limits for neutrino oscillations $\overline{\nu}_\mu \to \overline{\nu}_e$ from muon decay at rest". In: *Phys. Rev. D* 65.11 (2002), p. 112001. DOI: 10.1103/PhysRevD.65.112001.

[45] V. N. Aseev et al. “Energy loss of 18 keV electrons in gaseous T_2 and quench condensed D_2 films”. In: *Eur. Phys. J. D* 10 (2000), pp. 39–52. DOI: 10.1007/s100530050525.

[46] V. N. Aseev et al. “Upper limit on the electron antineutrino mass from the Troitsk experiment”. In: *Phys. Rev. D* 84.11 (2011), p. 112003. DOI: 10.1103/PhysRevD.84.112003.

[47] P. Astier et al. “Search for $\nu_\mu \to \nu_e$ oscillations in the NOMAD experiment”. In: *Physics Letters B* 570.1 (2003), pp. 19–31. DOI: 10.1016/j.physletb.2003.07.029.

[48] M. Babutzka. “Design and development for the Rearsection of the KATRIN experiment”. PhD thesis. Karlsruher Institut für Technologie (KIT), 2014. DOI: 10.5445/IR/1000045598.

[49] J. N. Bahcall. “Solar Neutrinos. I. Theoretical”. In: *Phys. Rev. Lett.* 12.11 (1964), pp. 300–302. DOI: 10.1103/PhysRevLett.12.300.

[50] J. N. Bahcall and R. Davis. “Solar Neutrinos: A Scientific Puzzle”. In: *Science* 191.4224 (1976), pp. 264–267. URL: http://www.jstor.org/stable/1741261.

[51] G. Bak et al. “Measurement of Reactor Antineutrino Oscillation Amplitude and Frequency at RENO”. In: *Phys. Rev. Lett.* 121.20 (2018), p. 201801. DOI: 10.1103/PhysRevLett.121.201801.

[52] S. Baker and R. D. Cousins. “Clarification of the use of CHI-square and likelihood functions in fits to histograms”. In: *Nuclear Instruments and Methods in Physics Research* 221.2 (1984), pp. 437–442. DOI: 10.1016/0167-5087(84)90016-4.

[53] V. V. Barinov et al. “Results from the Baksan Experiment on Sterile Transitions (BEST)”. In: *Physical Review Letters* 128.23 (2022). DOI: 10.1103/physrevlett.128.232501.

[54] G. Beamson, H. Q. Porter, and D. W. Turner. “The collimating and magnifying properties of a superconducting field photoelectron spectrometer”. In: *Journal of Physics E: Scientific Instruments* 13.1 (1980), pp. 64–66. DOI: 10.1088/0022-3735/13/1/018.

[55] H. Becquerel. “On the rays emitted by phosphorescence”. In: *Compt. Rend. Hebd. Seances Acad. Sci.* 122.8 (1896), pp. 420–421.

[56] J. Behrens and F. Block. *KATRIN First Tritium Reference Report Systematic Uncertainty of Magnetic Field in the Analyzing Plane*. Internal technical report. 2022. URL: https://ikp-katrin-wiki.ikp.kit.edu/katrin/images/9/92/FT_syst_uncertainty_Bana_030419.pdf.

[57] J. Behrens and F. Block. *KNM3/4/5 Systematic Uncertainties Uncertainties of magnetic field in analyzing plane, pinch magnet and WGTS*. Internal technical report. 2022. URL: https://ikp-katrin-wiki.ikp.kit.edu/katrin/images/d/dc/KNM3_4_5_MagFieldReport-2022-04-20.pdf.

[58] J. D. Behrens. “Design and commissioning of a mono-energetic photoelectron source and active background reduction by magnetic pulse at the KATRIN spectrometers”. PhD thesis. Westfälische Wilhelms-Universität Münster, 2016. URL: https://www.uni-muenster.de/imperia/md/content/physik_kp/agweinheimer/theses/phd-behrens.pdf.

[59] A. I. Belesev et al. “An upper limit on additional neutrino mass eigenstate in 2 to 100 eV region from “Troitsk nu-mass” data”. In: *JETP Lett.* 97 (2013), pp. 67–69. DOI: 10.1134/S0021364013020033.

[60] A. I. Belesev et al. “Investigation of space-charge effects in gaseous tritium as a source of distortions of the beta spectrum observed in the Troitsk neutrino-mass experiment”. In: *Physics of Atomic Nuclei* 71.3 (2008), pp. 427–436.

[61] A. Belesev et al. “Results of the Troitsk experiment on the search for the electron antineutrino rest mass in tritium beta-decay”. In: *Physics Letters B* 350.2 (1995), pp. 263–272. DOI: 10.1016/0370-2693(95)00335-I.

[62] L. Bergström and A. Goobar. *Cosmology and Particle Astrophysics*. Springer Berlin Heidelberg, 2004. DOI: 10.1007/3-540-37719-0.

[63] I. F. Bischer. “Effective Neutrino Interactions: Origins and Phenomenology”. PhD thesis. 2021. DOI: 10.11588/heidok.00030163.

[64] F. Block et al. *KATRIN column denisty report for KNM1-5*. Internal technical report. 2022. URL: https://ikp-katrin-wiki.ikp.kit.edu/katrin/images/6/67/ColumnDensity_KNM_1_5_2023-01-15.pdf.

[65] F. Block. “Determination of Electromagnetic Fields and Tritium Column Density for Neutrino Mass Analysis with KATRIN”. PhD thesis. Karlsruher Institut für Technologie (KIT), 2021. DOI: 10.5445/IR/1000127553.

[66] J. Bonn et al. “The KATRIN sensitivity to the neutrino mass and to right-handed currents in beta decay”. In: *Physics Letters B* 703.3 (2011), pp. 310–312. DOI: 10.1016/j.physletb.2011.08.005.

[67] M. Böttcher. *KNM1-5 Q value analysis note*. Internal technical report. 2022. URL: https://ikp-katrin-wiki.ikp.kit.edu/katrin/images/2/22/Q_KNM1to5_14Dec2022.pdf.

[68] M. Böttcher et al. *Analysis note – KNM1-5 plasma inputs*. Internal technical report. 2022. URL: https://nuserv.uni-muenster.de:8443/machatschek/krypton-v-analysis/-/blob/master/KNM1to5_Plasma_Inputs_Analysis_Note.pdf.

[69] T. Brinckmann and J. Lesgourgues. *MontePython 3: boosted MCMC sampler and other features*. 2018. arXiv: 1804.07261 [astro-ph.CO].

[70] J. Chadwick. “Intensitätsverteilung im magnetischen Spektrum von β-Strahlen von Radium B+C”. In: *Verhandlungen der Deutschen Physikalischen Gesellschaft* 16 (1914), pp. 383–391.

[71] J. Chadwick. “Possible Existence of a Neutron”. In: *Nature* 129.3252 (1932), pp. 312–312. DOI: 10.1038/129312a0.

[72] Y. Chikashige, R. Mohapatra, and R. Peccei. “Are there real goldstone bosons associated with broken lepton number?” In: *Physics Letters B* 98.4 (1981), pp. 265–268. DOI: 10.1016/0370-2693(81)90011-3.

[73] W. Choi, F. Leven, and L. Schimpf. *Theoretical Corrections / Synchrotron considerations for KNM1*. Internal report. 2019. URL: https://ikp-katrin-wiki.ikp.kit.edu/katrin/images/a/a3/Systematics_TheoCor_Sync_120219_WQ.pdf.

[74] B. T. Cleveland et al. “Measurement of the solar electron neutrino flux with the Homestake chlorine detector”. In: *Astrophys. J.* 496 (1998), pp. 505–526. DOI: 10.1086/305343.

[75] T. J. Corona. “Methodology and Application of High Performance Electrostatic Field Simulation in the KATRIN Experiment”. PhD thesis. University of North Carolina at Chapel Hill, 2014. URL: https://cdr.lib.unc.edu/record/uuid:6f44a9c2-f053-404a-b726-b960d5772619.

[76] C. L. Cowan et al. “Detection of the Free Neutrino: a Confirmation”. In: *Science* 124.3212 (1956), pp. 103–104. DOI: 10.1126/science.124.3212.103.

[77] G. Cowan et al. “Asymptotic formulae for likelihood-based tests of new physics”. In: *Eur. Phys. J. C* 71.1554 (2011), pp. 1434–6052. DOI: 10.1140/epjc/s10052-011-1554-0.

[78] G. Danby et al. “Observation of High-Energy Neutrino Reactions and the Existence of Two Kinds of Neutrinos”. In: *Phys. Rev. Lett.* 9.1 (1962), pp. 36–44. DOI: 10.1103/PhysRevLett.9.36.

[79] M. V. Danilov and N. A. Skrobova. “Comment on “Analysis of the Results of the Neutrino-4 Experiment on the Search for the Sterile Neutrino and Comparison with Results of Other Experiments”(JETP Letters 112, 199 (2020))”. In: *JETP Letters* 112.7 (2020), pp. 452–454. DOI: 10.1134/S0021364020190066.

[80] M. Danilov. *Recent results of the DANSS experiment*. 2019. arXiv: 1911.10140 [hep-ex].

[81] D. DeCamp et al. “Determination of the number of light neutrino species”. In: *Phys. Lett. B* 231.4 (1989), pp. 519–529. DOI: 10.1016/0370-2693(89)90704-1.

[82] DONUT Collaboration. “Observation of tau neutrino interactions”. In: *Physics Letters B* 504.3 (2001), pp. 218–224. DOI: 10.1016/S0370-2693(01)00307-0.

[83] N. Doss and J. Tennyson. “Excitations to the electronic continuum of $^{3}HeT^{+}$ in investigations of T_2 β-decay experiments”. In: *J. Phys. B* 41.12 (2008), pp. 125701+. DOI: 10.1088/0953-4075/41/12/125701.

[84] N. Doss et al. “Molecular effects in investigations of tritium molecule β decay endpoint experiments”. In: *Physical Review C* 73 (2006), p. 025502. DOI: 10.1103/PhysRevC.73.025502.

[85] G. Dvali and L. Funcke. “Small neutrino masses from gravitational θ-term”. In: 93.11 (2016). DOI: 10.1103/physrevd.93.113002.

[86] R. Dvornický et al. “Absolute mass of neutrinos and the first unique forbidden β decay of ^{187}Re”. In: *Phys. Rev. C* 83.4 (2011), p. 045502. DOI: 10.1103/PhysRevC.83.045502.

[87] S. Dyba. “Background reduction by the inner wire electrode and set-up of the condensed krypton source at the neutrino mass experiment KATRIN”. PhD thesis. Westfälische Wilhelms-Universität Münster, 2019. URL: https://nbn-resolving.de/urn:nbn:de:hbz:6-15149612886.

[88] E. Ellinger. “Development and Investigation of the Forward Beam Monitor for the KATRIN experiment”. PhD thesis. Bergische Universität Wuppertal, 2019. DOI: 10.25926/r160-7a40.

[89] E. Enomoto. *Penning trap background and MTD*. Presentation. 2020. URL: https://ikp-katrin-wiki.ikp.kit.edu/katrin/images/7/7b/201013-PenningTrapBG-v4.pdf.

[90] S. Enomoto. *New Run Summary Contents for KNM3-Durable and KNM4/5*. https://ikp-katrin-wiki.ikp.kit.edu/katrin/images/a/a6/20200908v2-RunSummary.pdf. 2020.

[91] S. Enomoto. “FPD analysis”. In: *40th KATRIN Collaboration Meeting* (2021). URL: https://ikp-katrin-wiki.ikp.kit.edu/katrin/images/7/77/FPD-210308v3.pdf.

[92] M. Erhard et al. “High-voltage monitoring with a solenoid retarding spectrometer at the KATRIN experiment”. In: *Journal of Instrumentation* 9.6 (2014), P06022. DOI: 10.1088/1748-0221/9/06/P06022.

[93] M. Erhard et al. “Technical design and commissioning of the KATRIN large-volume air coil system”. In: *Journal of Instrumentation* 13.02 (2018), P02003. DOI: 10.1088/1748-0221/13/02/P02003.

[94] M. Escudero, T. Schwetz, and J. Terol-Calvo. “A seesaw model for large neutrino masses in concordance with cosmology”. In: *JHEP* 02 (2023), p. 142. DOI: 10.1007/JHEP02(2023)142.

[95] M. Escudero et al. “Relaxing cosmological neutrino mass bounds with unstable neutrinos”. In: *Journal of High Energy Physics* 2020.12 (2020). DOI: 10.1007/jhep12(2020)119.

[96] A. A. Esfahani et al. *The Project 8 Neutrino Mass Experiment*. 2022. arXiv: 2203.07349 [nucl-ex].

[97] A. A. Esfahani et al. *Tritium Beta Spectrum and Neutrino Mass Limit from Cyclotron Radiation Emission Spectroscopy*. 2022. arXiv: 2212.05048 [nucl-ex].

[98] I. Esteban and J. Salvado. “Long range interactions in cosmology: implications for neutrinos”. In: *Journal of Cosmology and Astroparticle Physics* 2021.05 (2021), p. 036. DOI: 10.1088/1475-7516/2021/05/036.

[99] O. Fackler et al. “Accurate Theoretical β-Decay Energy Spectrum of the Tritium Molecule and Its Neutrino Mass Dependence”. In: *Phys. Rev. Lett.* 55.13 (Sept. 1985), pp. 1388–1391. DOI: 10.1103/PhysRevLett.55.1388.

[100] Y. Farzan and S. Hannestad. “Neutrinos secretly converting to lighter particles to please both KATRIN and the cosmos”. In: *Journal of Cosmology and Astroparticle Physics* 2016.02 (2016), pp. 058–058. DOI: 10.1088/1475-7516/2016/02/058.

[101] G. J. Feldman and R. D. Cousins. “Unified approach to the classical statistical analysis of small signals”. In: *Physical Review D* 57.7 (1998), pp. 3873–3889. DOI: 10.1103/physrevd.57.3873.

[102] E. Fermi. “Versuch einer Theorie der β-Strahlen.” In: *Zeitschrift für Physik* 88.3–4 (1934), pp. 161–177. DOI: 10.1007/BF01351864.

[103] D. Foreman-Mackey et al. “emcee: The MCMC Hammer”. In: *Publications of the Astronomical Society of the Pacific* 125.925 (2013), pp. 306–312. DOI: 10.1086/670067.

[104] F. Fränkle. *Background dependence on retarding potential - update*. Presentation. 2022. URL: https://ikp-katrin-wiki.ikp.kit.edu/katrin/images/b/b5/BGSlopeFraenkle221018.pdf.

[105] F. Fränkle. *KNM3b background dependence on retarding potential*. Presentation. 2022. URL: https://ikp-katrin-wiki.ikp.kit.edu/katrin/images/2/2c/BGSlopeFraenkle221025.pdf.

[106] F. Fränkle. *Penning Trap measurements*. Presentation. 2020. URL: https://ikp-katrin-wiki.ikp.kit.edu/katrin/images/3/3d/PenningTrapMeasurements201103.pdf.

[107] F. Fränkle et al. “Radon induced background processes in the KATRIN pre-spectrometer”. In: *Astroparticle Physics* 35.3 (2011), pp. 128–134. DOI: 10.1016/j.astropartphys.2011.06.009.

[108] F. M. Fränkle. "Background Investigations of the KATRIN Pre-Spectrometer". PhD thesis. Karlsruher Institut für Technologie (KIT), 2010. DOI: 10.5445/IR/1000019392.

[109] F. Friedel et al. "Time-dependent simulation of the flow reduction of D_2 and T_2 in the KATRIN experiment". In: *Vacuum* 159 (2019), pp. 161–172. DOI: 10.1016/j.vacuum.2018.10.002.

[110] F. Führer and C. Wetterich. "Backreaction in Growing Neutrino Quintessence". In: *Phys. Rev. D* 91.12 (2015), p. 123542. DOI: 10.1103/PhysRevD.91.123542.

[111] D. Furse. "Techniques for direct neutrino-mass measurement utilizing tritium β-decay". PhD thesis. Massachusetts Institute of Technology, 2015. URL: http://hdl.handle.net/1721.1/99313.

[112] D. Furse et al. "Kassiopeia: a modern, extensible C++ particle tracking package". In: *New Journal of Physics* 19.5 (2017), p. 053012. DOI: 10.1088/1367-2630/aa6950.

[113] A. Gando et al. "Reactor On-Off Antineutrino Measurement with KamLAND". In: *Phys. Rev. D* 88.3 (2013), p. 033001. DOI: 10.1103/PhysRevD.88.033001.

[114] L. Gastaldo et al. "The Electron Capture ^{163}Ho Experiment ECHo". In: *Journal of Low Temperature Physics* 176.5-6 (2014), pp. 876–884. DOI: 10.1007/s10909-014-1187-4.

[115] G. Gelmini and M. Roncadelli. "Left-handed neutrino mass scale and spontaneously broken lepton number". In: *Physics Letters B* 99.5 (1981), pp. 411–415. DOI: 10.1016/0370-2693(81)90559-1.

[116] C. Giunti et al. "Reactor antineutrino anomaly in light of recent flux model refinements". In: *Physics Letters B* 829 (2022), p. 137054. DOI: 10.1016/j.physletb.2022.137054.

[117] F. Glück et al. "Electromagnetic design of the large-volume air coil system of the KATRIN experiment". In: *New Journal of Physics* 15.8 (2013), p. 083025. DOI: 10.1088/1367-2630/15/8/083025.

[118] M. Goeppert-Mayer. "Double Beta-Disintegration". In: *Phys. Rev.* 48.6 (1935), pp. 512–516. DOI: 10.1103/PhysRev.48.512.

[119] S. Görhardt. "Background Reduction Methods and Vacuum Technology at the KATRIN Spectrometers". PhD thesis. Karlsruher Institut für Technologie (KIT), 2014. DOI: 10.5445/IR/1000038050.

[120] S. Groh. "Modeling of the response function and measurement of transmission properties of the KATRIN experiment". PhD thesis. Karlsruher Institut für Technologie (KIT), 2015. DOI: 10.5445/IR/1000046546.

[121] P. D. Group. "Review of Particle Physics". In: *Phys. Rev. D* 98.3 (2018), p. 030001. DOI: 10.1103/PhysRevD.98.030001.

[122] W. Hampel et al. "Final results of the 51Cr neutrino source experiments in GALLEX". In: *Phys. Lett. B* 420.1 (1998), pp. 114–126. DOI: 10.1016/S0370-2693(97)01562-1.

[123] W. Hampel et al. "GALLEX solar neutrino observations: results for GALLEX IV". In: *Physics Letters B* 447.1 (1999), pp. 127–133. DOI: 10.1016/S0370-2693(98)01579-2.

[124] S. Hancheng, L. Dongqi, and C. Shiping. "An upper limit for the electron anti-neutrino mass". In: *Chinese Journal of Nuclear Physics* 15.3 (1993), pp. 261–268. URL: http://inis.iaea.org/search/search.aspx?orig_q=RN:25075641.

[125] W. D. Harkins. "XXXIX. The constitution and stability of atom nuclei. (A contribution to the subject of inorganic evolution.)" In: *The London, Edinburgh, and Dublin Philosophical Magazine and Journal of Science* 42.249 (1921), pp. 305–339. DOI: 10.1080/14786442108633770.

[126] F. Harms. "Characterization and Minimization of Background Processes in the KATRIN Main Spectrometer". PhD thesis. Karlsruher Institut für Technologie (KIT), 2015. DOI: 10.5445/IR/1000050027.

[127] W. K. Hastings. "Monte Carlo sampling methods using Markov chains and their applications". In: *Biometrika* 57.1 (1970), pp. 97–109. DOI: 10.1093/biomet/57.1.97.

[128] F. Heizmann. "Analysis tools and methods for tritium data taking with the KATRIN experiment". PhD thesis. Karlsruher Institut für Technologie (KIT), 2018. DOI: 10.5445/IR/1000093536.

[129] S. Hickford. *KNM2 MTD*. Presentation. 2019. URL: https://ikp-katrin-wiki.ikp.kit.edu/katrin/images/1/1c/Knm2-mtd.pdf.

[130] S. Hickford. *KNM3 MTD*. Presentation. 2020. URL: https://ikp-katrin-wiki.ikp.kit.edu/katrin/images/5/53/Mtd-slides.pdf.

[131] S. Hickford and F. Heizmann. *KNM1 Measurement Time Distribution*. Presentation. 2019. URL: https://ikp-katrin-wiki.ikp.kit.edu/katrin/images/1/12/KNM1-MTD-final.pdf.

[132] S. Hickford and F. Heizmann. *MTD for KNM1, v0*. Presentation. 2018. URL: https://ikp-katrin-wiki.ikp.kit.edu/katrin/images/f/f9/2018-02-05-MTDforKNM1.pdf.

[133] D. F. Hinz. "Background systematics and extensions to the KATRIN background model". PhD thesis. Karlsruher Institut für Technologie (KIT), 2022. 157 pp. DOI: 10.5445/IR/1000151022.

[134] K. S. Hirata et al. "Experimental Study of the Atmospheric Neutrino Flux". In: *Phys. Lett. B* 205 (1988). Ed. by J. Tran Thanh Van, p. 416. DOI: 10.1016/0370-2693(88)91690-5.

[135] E. Holzschuh, M. Fritschi, and W. Kuendig. "Measurement of the electron-neutrino mass from tritium beta decay". In: *Phys. Lett. B* 287 (1992), pp. 381–388. DOI: 10.1016/0370-2693(92)91000-Y.

[136] M. Hötzel. "Simulation and analysis of source-related effects for KATRIN". PhD thesis. Karlsruher Institut für Technologie (KIT), 2012. DOI: 10.5445/IR/1000031259.

[137] W. Hu, D. J. Eisenstein, and M. Tegmark. "Weighing Neutrinos with Galaxy Surveys". In: *Physical Review Letters* 80.24 (1998), pp. 5255–5258. DOI: 10.1103/physrevlett.80.5255.

[138] W. Huang et al. "The AME 2020 atomic mass evaluation (I). Evaluation of input data, and adjustment procedures*". In: *Chinese Physics C* 45.3 (2021), p. 030002. DOI: 10.1088/1674-1137/abddb0.

[139] M. Inokuti. “Inelastic Collisions of Fast Charged Particles with Atoms and Molecules—The Bethe Theory Revisited”. In: *Rev. Mod. Phys.* 43.3 (1971), pp. 297–347. DOI: 10.1103/RevModPhys.43.297.

[140] F. James and M. Roos. “Minuit - a system for function minimization and analysis of the parameter errors and correlations”. In: *Computer Physics Communications* 10.6 (1975), pp. 343–367. DOI: 10.1016/0010-4655(75)90039-9.

[141] T. M. James et al. “Automated Quantitative Spectroscopic Analysis Combining Background Subtraction, Cosmic Ray Removal, and Peak Fitting”. In: *Applied Spectroscopy* 67.8 (2013). PMID: 23876734, pp. 949–959. DOI: 10.1366/12-06766.

[142] W. Käfer. “Sensitivity studies of the KATRIN experiment”. PhD thesis. Karlsruher Institut für Technologie (KIT), 2012. DOI: 10.5445/IR/1000026021.

[143] C. Karl, P. Eller, and S. Mertens. “Fast and precise model calculation for KATRIN using a neural network”. In: *Eur. Phys. J. C* 82.5 (2022), p. 439. DOI: 10.1140/epjc/s10052-022-10384-z.

[144] H. Kawakami et al. “New upper bound on the electron anti-neutrino mass”. In: *Phys. Lett. B* 256 (1991), pp. 105–111. DOI: 10.1016/0370-2693(91)90226-G.

[145] H. de Kerret et al. “Double Chooz θ_{13} measurement via total neutron capture detection”. In: *Nature Phys.* 16.5 (2020), pp. 558–564. DOI: 10.1038/s41567-020-0831-y.

[146] Y.-K. Kim, J. P. Santos, and F. Parente. “Extension of the binary-encounter-dipole model to relativistic incident electrons”. In: *Phys. Rev. A* 62.5 (2000), p. 052710. DOI: 10.1103/PhysRevA.62.052710.

[147] M. Kleesiek et al. “β-Decay spectrum, response function and statistical model for neutrino-mass measurements with the KATRIN experiment”. In: *Eur. Phys. J. C* 79.3 (2019). DOI: 10.1140/epjc/s10052-019-6686-7.

[148] M. Kleesiek. “A Data-Analysis and Sensitivity-Optimization Framework for the KATRIN Experiment”. PhD thesis. Karlsruher Institut für Technologie (KIT), 2014. DOI: 10.5445/IR/1000043301.

[149] M. Klein. “Tritium ions in KATRIN: blocking, removal and detection”. PhD thesis. Karlsruher Institut für Technologie (KIT), 2018. DOI: 10.5445/IR/1000093526.

[150] V. Kopeikin, M. Skorokhvatov, and O. Titov. “Reevaluating reactor antineutrino spectra with new measurements of the ratio between ^{235}U and ^{239}Pu β spectra”. In: *Phys. Rev. D* 104.7 (2021), p. L071301. DOI: 10.1103/PhysRevD.104.L071301.

[151] C. Kraus et al. “Final results from phase II of the Mainz neutrino mass searchin tritium β decay”. In: *Eur. Phys. J. C* 40.4 (2005), pp. 447–468. DOI: 10.1140/epjc/s2005-02139-7.

[152] C. Kraus et al. “Limit on sterile neutrino contribution from the Mainz Neutrino Mass Experiment”. In: *Eur. Phys. J. C* 73.2 (2013), p. 2323. DOI: 10.1140/epjc/s10052-013-2323-z.

[153] P. Kruit and F. H. Read. “Magnetic field paralleliser for 2π electron-spectrometer and electron-image magnifier”. In: *Journal of Physics E: Scientific Instruments* 16.4 (1983), pp. 313–324. DOI: 10.1088/0022-3735/16/4/016.

[154] L. Kuckert. “The Windowless Gaseous Tritium Source of the KATRIN Experiment – Characterisation of Gas Dynamical and Plasma Properties”. PhD thesis. Karlsruher Institut für Technologie (KIT), 2016. DOI: 10.5445/IR/1000065077.

[155] T. Lasserre, L. Schlueter, and J. Dai. *KNM1 Background: SubRun-wise Analysis and Background Rate Systematics.* Internal technical report. 2019. URL: https://ikp-katrin-wiki.ikp.kit.edu/katrin/images/3/37/KATRIN_KNM1_SubRunWiseBackground.pdf.

[156] J. Lesgourgues and S. Pastor. "Neutrino Mass from Cosmology". In: *Advances in High Energy Physics* 2012 (2012), pp. 1–34. DOI: 10.1155/2012/608515.

[157] J. Lesgourgues et al. *Neutrino Cosmology.* Cambridge University Press, 2013. DOI: 10.1017/CBO9781139012874.

[158] J. Lesourges and S. Pastor. "Massive neutrinos and cosmology". In: *Physics Reports* 429.6 (2006), pp. 307–379. DOI: 10.1016/j.physrep.2006.04.001.

[159] J. W. Liu. "Total cross sections for high-energy electron scattering by H_2 ($^1\Sigma_g^+$), N_2 ($^1\Sigma_g^+$), and O_2 ($^3\Sigma_g^-$)". In: *Phys. Rev. A* 35.2 (1987), pp. 591–597. DOI: 10.1103/PhysRevA.35.591.

[160] J. W. Liu. "Total Inelastic Cross Section for Collisions of H_2 with Fast Charged Particles". In: *Phys. Rev. A* 7.1 (1973), pp. 103–109. DOI: 10.1103/PhysRevA.7.103.

[161] V. Lobashev et al. "Direct search for mass of neutrino and anomaly in the tritium beta-spectrum". In: *Physics Letters B* 460.1 (1999), pp. 227–235. DOI: 10.1016/S0370-2693(99)00781-9.

[162] V. Lobashev and P. Spivak. "A method for measuring the electron antineutrino rest mass". In: *Nuclear Instruments and Methods in Physics Research Section A: Accelerators, Spectrometers, Detectors and Associated Equipment* 240.2 (1985), pp. 305–310. DOI: 10.1016/0168-9002(85)90640-0.

[163] A. Lokhov. *SAP operation and further Background measures.* Presentation at the 38th KATRIN Collaboration Meeting. 2020. URL: https://fuzzy.fzk.de/bscw/bscw.cgi/1318584?op=preview&back_url=15294%5C%3fclient_size%5C%3d1632x945.

[164] A. Lokhov and M. Slezák. *Analysis note: Time-dependent background in KNM1/2 subruns.* Internal technical report. 2021. URL: https://ikp-katrin-wiki.ikp.kit.edu/katrin/images/0/00/2021-01-22_Time-slope_KNM2_analysis_note.pdf.

[165] A. Lokhov and C. Weinheimer. *Transmission function for pixels and patches in SAP configuration.* Presentation. 2020. URL: https://ikp-katrin-wiki.ikp.kit.edu/katrin/images/1/15/2020-06-30_sap_transmission.pdf.

[166] A. V. Lokhov and F. V. Tkachov. "Confidence intervals with a priori parameter bounds". In: *Physics of Particles and Nuclei* 46.3 (2015), pp. 347–365. DOI: 10.1134/s1063779615030089.

[167] A. Lokhov et al. "Background reduction at the KATRIN experiment by the shifted analysing plane configuration". In: *Eur. Phys. J. C* 82.3 (2022), p. 258. DOI: 10.1140/epjc/s10052-022-10220-4.

[168] C. S. Lorenz et al. "Reconstruction of the neutrino mass as a function of redshift". In: *Physical Review D* 104.12 (2021). DOI: 10.1103/physrevd.104.123518.

[169] M. R. Lovell et al. "The haloes of bright satellite galaxies in a warm dark matter universe". In: *Monthly Notices of the Royal Astronomical Society* 420.3 (2012), pp. 2318–2324. DOI: 10.1111/j.1365-2966.2011.20200.x.

[170] E. Ma. "Verifiable radiative seesaw mechanism of neutrino mass and dark matter". In: *Phys. Rev. D* 73.7 (2006), p. 077301. DOI: 10.1103/PhysRevD.73.077301.

[171] M. Machatschek. "A Phenomenological Theory of KATRIN Source Potential Systematics and its Application in Krypton-83m Calibration Measurements." PhD thesis. Karlsruher Institut für Technologie (KIT), 2021. DOI: 10.5445/IR/1000132391.

[172] E. Majorana. "Teoria simmetrica dell'elettrone e del positrone". In: *Nuovo Cim.* 14 (1937), pp. 171–184. DOI: 10.1007/BF02961314.

[173] Z. Maki, M. Nakagawa, and S. Sakata. "Remarks on the Unified Model of Elementary Particles". In: *Progress of Theoretical Physics* 28.5 (1962), pp. 870–880. DOI: 10.1143/PTP.28.870.

[174] M. Maltoni and T. Schwetz. "Testing the statistical compatibility of independent datasets". In: *Phys. Rev. D* 68.3 (2003). DOI: 10.1103/physrevd.68.033020.

[175] A. Marsteller. "Characterization and optimization of the KATRIN tritium source". PhD thesis. Karlsruher Institut für Technologie (KIT), 2020. DOI: 10.5445/IR/1000127553.

[176] A. Marsteller. "FPD angular dependence". In: *KATRIN Analysis Report* (2022). URL: https://ikp-katrin-wiki.ikp.kit.edu/katrin/images/4/44/2022_09_22_AnalysisNote_FPD_Angular_Dependence.pdf.

[177] G. Mention et al. "Reactor antineutrino anomaly". In: *Phys. Rev. D* 83.7 (2011), p. 073006. DOI: 10.1103/PhysRevD.83.073006.

[178] S. Mertens et al. "Background due to stored electrons following nuclear decays in the KATRIN spectrometers and its impact on the neutrino mass sensitivity". In: *Astroparticle Physics* 41 (2013), pp. 52–62. DOI: 10.1016/j.astropartphys.2012.10.005.

[179] S. Mertens. "Study of Background Processes in the Electrostatic Spectrometers of the KATRIN experiment". PhD thesis. Karlsruher Institut für Technologie (KIT), 2012. DOI: 10.5445/IR/1000027058.

[180] S. Mertens et al. "A novel detector system for KATRIN to search for keV-scale sterile neutrinos". In: *Journal of Physics G: Nuclear and Particle Physics* 46.6 (2019), p. 065203. DOI: 10.1088/1361-6471/ab12fe.

[181] E. G. Myers et al. "Atomic Masses of Tritium and Helium-3". In: *Phys. Rev. Lett.* 114.1 (2015), p. 013003. DOI: 10.1103/PhysRevLett.114.013003.

[182] J. Neyman. "Outline of a Theory of Statistical Estimation Based on the Classical Theory of Probability". In: *Philosophical Transactions of the Royal Society of London. Series A, Mathematical and Physical Sciences* 236.767 (1937), pp. 333–380. DOI: 10.1098/rsta.1937.0005.

[183] Nobel Prize Outreach AB 2023. *The Nobel Prize in Physics 2015 was awarded jointly to Takaaki Kajita and Arthur B. McDonald "for the discovery of neutrino oscillations, which shows that neutrinos have mass."* URL: https://www.nobelprize.org/prizes/physics/2015/press-release//.

[184] A. Nucciotti et al. "Status of the HOLMES Experiment to Directly Measure the Neutrino Mass". In: *Journal of Low Temperature Physics* 193.5-6 (2018), pp. 1137–1145. DOI: 10.1007/s10909-018-2025-x.

[185] I. M. Oldengott et al. "How to relax the cosmological neutrino mass bound". In: *Journal of Cosmology and Astroparticle Physics* 2019.04 (2019), p. 049. DOI: 10.1088/1475-7516/2019/04/049.

[186] E. W. Otten and C. Weinheimer. "Neutrino mass limit from tritium β decay". In: *Reports on Progress in Physics* 71.8 (2008), p. 086201. DOI: 10.1088/0034-4885/71/8/086201.

[187] N. Palanque-Delabrouille et al. "Hints, neutrino bounds and WDM constraints from SDSS DR14 Lyman-α and Planck full-survey data". In: *JCAP* 04 (2020), p. 038. DOI: 10.1088/1475-7516/2020/04/038.

[188] Particle Data Group. "Review of Particle Physics". In: *Progress of Theoretical and Experimental Physics* 2020.8 (2020). DOI: 10.1093/ptep/ptaa104.

[189] W. E. F. Pauli, R. Kronig, and V. F. Weisskopf. *Collected scientific papers*. Offener Brief an die Gruppe der Radioaktiven bei der Gauvereinstagung zu Tübingen (datiert 4. Dez. 1930). New York, NY: Interscience, 1964.

[190] P. F. Pérez and M. B. Wise. "On the origin of neutrino masses". In: *Phys. Rev. D* 80.5 (2009), p. 053006. DOI: 10.1103/PhysRevD.80.053006.

[191] M. L. Perl et al. "Evidence for Anomalous Lepton Production in $e^+ - e^-$ Annihilation". In: *Phys. Rev. Lett.* 35.22 (1975), pp. 1489–1492. DOI: 10.1103/PhysRevLett.35.1489.

[192] A. Picard et al. "A solenoid retarding spectrometer with high resolution and transmission for keV electrons". In: *Nuclear Instruments and Methods in Physics Research Section B: Beam Interactions with Materials and Atoms* 63.3 (1992), pp. 345–358. DOI: 10.1016/0168-583X(92)95119-C.

[193] R. L. Plackett. "Karl Pearson and the Chi-Squared Test". In: *International Statistical Review / Revue Internationale de Statistique* 51.1 (1983), pp. 59–72. URL: http://www.jstor.org/stable/1402731.

[194] B. Pontecorvo. "Mesonium and anti-mesonium". In: *Sov. Phys. JETP* 6 (1957), p. 429.

[195] M. Prall et al. "The KATRIN pre-spectrometer at reduced filter energy". In: *New Journal of Physics* 14.7 (2012), p. 073054. DOI: 10.1088/1367-2630/14/7/073054.

[196] F. Priester and B. Bornschein. "TriToP - A compatibility experiment with turbomolecular pumps under tritium atmosphere". In: *Vacuum* 98.0 (2013), pp. 22–28. DOI: 10.1016/j.vacuum.2012.09.006.

[197] F. Priester, M. Sturm, and B. Bornschein. "Commissioning and detailed results of KATRIN inner loop tritium processing system at Tritium Laboratory Karlsruhe". In: *Vacuum* 116 (2015), pp. 42–47. DOI: 10.1016/j.vacuum.2015.02.030.

[198] F. Priester et al. "Tritium Processing Systems and First Tritium Operation of the KATRIN Experiment". In: *Fusion Science and Technology* 76.4 (2020), pp. 600–604. DOI: 10.1080/15361055.2020.1730118.

[199] G. Racah. "Sulla Simmetria Tra Particelle e Antiparticelle". In: *Il Nuovo Cimento* 14.7 (1937), pp. 322–328. DOI: 10.1007/BF02961321.

[200] P. C. .-O. Ranitzsch et al. "Characterization of the ^{163}Ho Electron Capture Spectrum: A Step Towards the Electron Neutrino Mass Determination". In: *Phys. Rev. Lett.* 119.12 (2017), p. 122501. DOI: 10.1103/PhysRevLett.119.122501.

[201] W. Repko and C.-E. Wu. "Radiative corrections to the endpoint of the tritium β decay spectrum". In: *Phys. Rev. C* 28.6 (1983), pp. 2433–2436. DOI: 10.1103/physrevc.28.2433.

[202] A. G. Riess et al. “A Comprehensive Measurement of the Local Value of the Hubble Constant with 1 km s^{-1} Mpc^{-1} Uncertainty from the Hubble Space Telescope and the SH0ES Team”. In: *The Astrophysical Journal Letters* 934.1 (2022), p. L7. DOI: 10.3847/2041-8213/ac5c5b.

[203] R. G. H. Robertson et al. “Limit on $\overline{\nu}_e$ mass from observation of the β decay of molecular tritium”. In: *Physical Review Letters* 67.8 (1991), pp. 957–960. DOI: 10.1103/PhysRevLett.67.957.

[204] W. Rodejohann. “Neutrino-less double beta decay and particle physics”. In: *International Journal of Modern Physics E* 20.09 (2011), pp. 1833–1930. DOI: 10.1142/s0218301311020186.

[205] C. Rodenbeck et al. “Wideband precision stabilization of the -18.6kV retarding voltage for the KATRIN spectrometer”. In: *Journal of Instrumentation* 17.06 (2022), P06003. DOI: 10.1088/1748-0221/17/06/P06003.

[206] C. Rodenbeck. “Inelastic electron scattering in tritium gas and ppm-precise energy scale at the KATRIN experiment”. PhD thesis. Westfälische Wilhelms-Universität Münster, 2023. URL: https://nbn-resolving.de/urn:nbn:de:hbz:6-27978340837.

[207] W. Romberg. “Vereinfachte numerische Integration”. In: *Det Kongelige Norske Videnskabers Selskab Forhandlinger* 28 (1955), pp. 30–36.

[208] C. Röttele. “Tritium suppression factor of the KATRIN transport section”. PhD thesis. Karlsruher Institut für Technologie (KIT), 2019. DOI: 10.5445/IR/1000096733.

[209] E. Rutherford. “VIII. Uranium radiation and the electrical conduction produced by it”. In: *The London, Edinburgh, and Dublin Philosophical Magazine and Journal of Science* 47.284 (1899), pp. 109–163. DOI: 10.1080/14786449908621245.

[210] R. Sack. “Measurement of the energy loss of 18.6 keV electrons on deuterium gas and determination of the tritium Q-value at the KATRIN experiment”. PhD thesis. Westfälische Wilhelms-Universität Münster, 2020. URL: https://nbn-resolving.de/urn:nbn:de:hbz:6-59069498754.

[211] A. Saenz and P. Froelich. “Effect of final-state interactions in allowed β decays. II. Reliability of the β-decay spectrum for T_2”. In: *Physical Review C* 56 (1997), pp. 2162–2184. DOI: 10.1103/PhysRevC.56.2162.

[212] A. Saenz, S. Jonsell, and P. Froelich. “Improved Molecular Final-State Distribution of HeT^+ for the β-Decay Process of T_2”. In: *Physical Review Letters* 84 (2000), pp. 242–245. DOI: 10.1103/PhysRevLett.84.242.

[213] A. Saenz, S. Jonsell, and P. Froelich. “Improved Molecular Final-State Distribution of HeT^+ for the β-Decay Process of T_2”. In: *Phys. Rev. Lett.* 84.2 (Jan. 2000), pp. 242–245. DOI: 10.1103/PhysRevLett.84.242.

[214] A. K. Schaller. “Characterization and mitigation of the background in KATRIN”. PhD thesis. Technical University of Munich, 2020. URL: http://nbn-resolving.de/urn/resolver.pl?urn:nbn:de:bvb:91-diss-20200828-1553598-1-6.

[215] J. Schechter and J. W. F. Valle. “Neutrino masses in SU(2)×U(1) theories”. In: *Phys. Rev. D* 22.9 (1980), pp. 2227–2235. DOI: 10.1103/PhysRevD.22.2227.

[216] L. Schimpf. “Characterisation of energy loss processes of 18.6 keV electrons inside the windowless tritium source of KATRIN”. PhD thesis. Karlsruher Institut für Technologie (KIT), 2021. 232 pp. DOI: 10.5445/IR/1000131810.

[217] L. Schimpf. *KNM3 energy loss parametrisation*. Internal report. 2021. URL: https://nuserv.uni-muenster.de:8443/katrin-git/KATRIN-eloss/-/blob/master/parameters/KNM3/t2-eloss_parameterization_v5_chisq1/fit_result.txt.

[218] M. Schlösser et al. "Accurate calibration of the laser Raman system for the Karlsruhe Tritium Neutrino Experiment". In: *Journal of Molecular Structure* 1044.0 (2013), pp. 61–66. DOI: 10.1016/j.molstruc.2012.11.022.

[219] L. Schlüter. "Neutrino-Mass Analysis with sub-eV Sensitivity and Search for Light Sterile Neutrinos with the KATRIN Experiment". PhD thesis. Technische Universität München, 2022. URL: https://mediatum.ub.tum.de/?id=1661391.

[220] S. Schneidewind et al. "Uncertainties of the molecular final states used in the first KATRIN neutrino mass campaign". In: *KATRIN analysis report* (2022). URL: https://ikp-katrin-wiki.ikp.kit.edu/katrin/images/7/7b/FSD_KMN1_uncertainties_2022_12_05.pdf.

[221] S. Schneidewind. "Improvement of the neutrino mass sensitivity and background reduction of the KATRIN experiment". Thesis in submission. PhD thesis. Westfälische Wilhelms-Universität Münster, to be published in 2024.

[222] S. Schneidewind. *MTD Optimisations*. Presentation. 2020. URL: https://ikp-katrin-wiki.ikp.kit.edu/katrin/images/e/e1/MTDOptimisation_KNM4.pdf.

[223] S. Schneidewind. *Update from MTD working group*. Presentation. 2021. URL: https://ikp-katrin-wiki.ikp.kit.edu/katrin/images/6/6e/Update_from_MTD_working_group_-_Status_of_KNM5_MTD.pdf.

[224] S. Schneidewind et al. "Uncertainties of the molecular final states used in the first KATRIN neutrino mass campaign". In preparation. 2023.

[225] C. Schönfeld. "Commissioning of the KATRIN Pinch Magnet". Bachelor thesis. Karlsruher Institut für Technologie (KIT), 2015. URL: https://fuzzy.fzk.de/bscw/bscw.cgi/d1236629/BA2015-Sch%C3%B6nfeld.pdf.

[226] K. Schönung. "Development of a Rear Wall for the KATRIN Rear Section and investigation of tritium compatibility of Rear Section components". PhD thesis. Karlsruher Institut für Technologie (KIT), 2016. 336 pp. DOI: 10.5445/IR/1000056077.

[227] J. S. Schwarz. "The Detector System of the KATRIN Experiment - Implementation and First Measurements with the Spectrometer". PhD thesis. Karlsruher Institut für Technologie (KIT), 2014. DOI: 10.5445/IR/1000042772.

[228] A. P. Serebrov et al. "First Observation of the Oscillation Effect in the Neutrino-4 Experiment on the Search for the Sterile Neutrino". In: *Pisma Zh. Eksp. Teor. Fiz.* 109.4 (2019), pp. 209–218. DOI: 10.1134/S0021364019040040.

[229] A. P. Serebrov et al. "Search for sterile neutrinos with the Neutrino-4 experiment and measurement results". In: *Phys. Rev. D* 104.3 (2021), p. 032003. DOI: 10.1103/PhysRevD.104.032003.

[230] C. D. Shin et al. "Observation of reactor antineutrino disappearance using delayed neutron capture on hydrogen at RENO". In: *JHEP* 04 (2020), p. 029. DOI: 10.1007/JHEP04(2020)029.

[231] M. Slezák et al. "Electron line shape of the KATRIN monitor spectrometer". In: *Journal of Instrumentation* 8.12 (2013), T12002. DOI: 10.1088/1748-0221/8/12/T12002.

[232] M. Slezák. "The source of monoenergetic electrons for the monitoring of spectrometer in the KATRIN neutrino experiment". Diploma Thesis. Charles University in Prague, 2011. URL: http://www.katrin.kit.edu/publikationen/dth-slezak.pdf.

[233] F. Soddy. "The Radio-Elements and the Periodic Law". In: *Nature* 91.2264 (1913), pp. 57–58. DOI: 10.1038/091057a0.

[234] N. M. Steinbrink et al. "Statistical sensitivity on right-handed currents in presence of eV scale sterile neutrinos with KATRIN". In: *Journal of Cosmology and Astroparticle Physics* 2017.06 (2017), p. 015. DOI: 10.1088/1475-7516/2017/06/015.

[235] W. Stoeffl and D. J. Decman. "Anomalous Structure in the Beta Decay of Gaseous Molecular Tritium". In: *Phys. Rev. Lett.* 75.18 (1995), pp. 3237–3240. DOI: 10.1103/PhysRevLett.75.3237.

[236] C. A. Ternes. "Current Status of Neutrino Oscillations". In: *Moscow University Physics Bulletin* 77.2 (2022), pp. 411–414. DOI: 10.3103/S0027134922020977.

[237] The ALEPH Collaboration, the DELPHI Collaboration, the L3 Collaboration, the OPAL Collaboration, the SLD Collaboration, the LEP Electroweak Working Group, the SLD Electroweak and Heavy Flavour Groups. "Precision electroweak measurements on the Z resonance". In: *Physics Reports* 427.5 (2006), pp. 257–454. DOI: 10.1016/j.physrep.2005.12.006.

[238] The Kassiopeia developers. *Kassiopeia documentation*. URL: http://katrin-experiment.github.io/Kassiopeia/index.html.

[239] T. Thümmler. *Spectrometer and Detector System Status Update*. Presentation at the 38th KATRIN Collaboration Meeting. 2020. URL: https://fuzzy.fzk.de/bscw/bscw.cgi/1318629?op=preview&back_url=1318494.

[240] E. Tiesinga et al. "CODATA recommended values of the fundamental physical constants: 2018". In: *Rev. Mod. Phys.* 93.2 (2021), p. 025010. DOI: 10.1103/RevModPhys.93.025010.

[241] TRISTAN group. *Conceptual Design Report: KATRIN with TRISTAN modules*. 2022. URL: https://www.katrin.kit.edu/downloads/TRISTAN__Technical_Design_Report%20(10).pdf.

[242] N. R.-M. Trost. "Modeling and measurement of Rydberg-State mediated Background at the KATRIN Main Spectrometer". PhD thesis. Karlsruher Institut für Technologie (KIT), 2019. DOI: 10.5445/IR/1000090450.

[243] K. Urban et al. "Characterization measurements of the TRISTAN multi-pixel silicon drift detector". In: *Journal of Instrumentation* 17.09 (2022), p. C09020. DOI: 10.1088/1748-0221/17/09/C09020.

[244] K. Urban. "Application of a TRISTAN Silicon Drift Detector as Forward Beam Monitor in KATRIN". Master Thesis. Technical University of Munich, 2019. URL: https://publications.mppmu.mpg.de/2019/MPP-2019-356/FullText.pdf.

[245] E. D. Valentino, A. Melchiorri, and J. Silk. "Cosmological constraints in extended parameter space from the Planck 2018 Legacy release". In: *Journal of Cosmology and Astroparticle Physics* 2020.01 (2020), p. 013. DOI: 10.1088/1475-7516/2020/01/013.

[246] K. Valerius. "Electromagnetic design and inner electrode for the KATRIN main spectrometer". In: *Progress in Particle and Nuclear Physics* 57.1 (2006). International Workshop of Nuclear Physics 27th course: Neutrinos in Cosmology, in Astro, Particle and Nuclear Physics, pp. 58–60. DOI: 10.1016/j.ppnp.2005.11.011.

[247] K. Valerius. “Spectrometer-related background processes and their suppression in the KATRIN experiment”. PhD thesis. Westfälische Wilhelms-Universität Münster, 2009. URL: http://nbn-resolving.de/urn:nbn:de:hbz:6-28479494638.

[248] D. Vénos et al. “Properties of ^{83m}Kr conversion electrons and their use in the KATRIN experiment”. In: *Journal of Instrumentation* 13.02 (2018), T02012. DOI: 10.1088/1748-0221/13/02/T02012.

[249] N. Wandkowsky. “Study of background and transmission properties of the KATRIN spectrometers”. PhD thesis. Karlsruher Institut für Technologie (KIT), 2013. DOI: 10.5445/IR/1000036631.

[250] K. C. Wang. “A Suggestion on the Detection of the Neutrino”. In: *Physical Review* 61.1-2 (1942), pp. 97–97. DOI: 10.1103/PhysRev.61.97.

[251] P. Weck, B. Joulakian, and P. A. Hervieux. “Fivefold differential cross section of fast $(e, 2e)$ ionization of H_2, D_2, and T_2 by a Franck-Condon approach”. In: *Phys. Rev. A* 60.4 (1999), pp. 3013–3019. DOI: 10.1103/PhysRevA.60.3013.

[252] S. Weinberg. “A Model of Leptons”. In: *Phys. Rev. Lett.* 19.21 (1967), pp. 1264–1266. DOI: 10.1103/PhysRevLett.19.1264.

[253] C. Weinheimer et al. *Background and counter measures: Rydberg background*. 2019. URL: https://fuzzy.fzk.de/bscw/bscw.cgi/1253179?op=preview&back_url=15294.

[254] C. Weinheimer et al. “Improved limit on the electron anti-neutrino rest mass from tritium beta decay”. In: *Phys. Lett. B* 300 (1993), pp. 210–216. DOI: 10.1016/0370-2693(93)90355-L.

[255] C. Weinheimer et al. “High precision measurement of the tritium β spectrum near its endpoint and upper limit on the neutrino mass”. In: *Physics Letters B* 460.1 (1999), pp. 219–226. DOI: 10.1016/S0370-2693(99)00780-7.

[256] S. S. Wilks. “The Large-Sample Distribution of the Likelihood Ratio for Testing Composite Hypotheses”. In: *The Annals of Mathematical Statistics* 9.1 (1938), pp. 60–62. DOI: 10.1214/aoms/1177732360.

[257] R. L. Workman et al. “Review of Particle Physics”. In: *PTEP* 2022 (2022), p. 083C01. DOI: 10.1093/ptep/ptac097.

[258] W. Xu. *KaFit optimizations: Potential on Bayesian analysis*. Presentation at the 43rd KATRIN Collaboration Meeting. 2022. URL: https://indico.scc.kit.edu/event/2895/contributions/11320/attachments/5440/8373/Optimization_CM43.pdf.

[259] T. Yanagida. “Horizontal Symmetry and Masses of Neutrinos”. In: *Progress of Theoretical Physics* 64.3 (1980), pp. 1103–1105. DOI: 10.1143/PTP.64.1103.

[260] K. Zuber. *Neutrino Physics (3rd ed.)* CRC Press, 2020. DOI: 10.1201/9781315195612.

Acknowledgements

This work would not have been possible without the help and support of many people. I am very thankful to have experienced such a friendly work environment and to be part of the collaborative work spirit in KATRIN over the past couple of years. In particular, I want to give thanks to:

- Prof. Dr Kathrin Valerius, for the excellent supervision and continuous support, which has been invaluable to my work. I am grateful for all of the opportunities I was given, sending me to conferences, workshops and summer schools. In particular, I would also like to thank her for making my stay in Berkeley at LBL possible.
- Prof. Dr Christian Weinheimer for the evaluation of this thesis as a second reviewer and, in this context, the interest he showed throughout the course of my thesis.
- Dr Alan Poon for inviting me to stay at LBL and for the hospitality in his working group. Here I would also like to thank Dr Björn Lehnert and Dr Ann-Kathrin Schütz for the great time I had in the U.S.
- Benedikt Bieringer, Dr Wonqook Choi, Dr Stephanie Hickford, Dr Moritz Machatschek, Dr Alexey Lokhov, Weiran Xu representative for the `KaFit`-Team. I learned a lot in all of our discussions and enjoyed the close work together, analysing and solving problems as a team. It has been a privilege to be a part of such a supportive and collaborative team.
- The many people who proofread different parts of this thesis: Dr Fabian Block, Dr Stephanie Hickford, Dr Dominic Hinz, Dr Anton Huber, and Dr Moritz Machatschek.
- Dr Anton Huber, Dr Dominic Hinz, Dr Moritz Machatschek, Dr Fabian Block, Dr Alexey Lokhov, Martin Descher, Dr Sanshiro Enomoto, and Dr Wonqook Choi for the friendships that developed throughout the years and went further than work. Thank you for all of the activities – from climbing and skiing to many nights of good food and drinks.
- Dr Oliver Kalsbach for our long-lasting close friendship and being there as a brother with whom I started my journey in Karlsruhe.

Special gratitude goes to my family, Dr Cornelia Köllenberger and Elisabeth Köllenberger, for their unwavering support throughout my studies and for giving me the opportunity to follow my interests. I cannot thank you enough for everything you have done. I would also like to commemorate my father, Hans Jakob Köllenberger, who could not take part in the adventure of this thesis but who always supported my curiosity in my youth.

Last and most important, I would like to thank Dr Stephanie Hickford. Thank you for being a wonderful and loving partner. I am grateful for all of the tireless encouragement, the support in times of doubt and for working together with you as a team.